TECHNISCHE UNIVERSITÄT MÜNCHEN

Fakultät Wissenschaftszentrum Weihenstephan für Ernährung, Landnutzung und Umwelt

Lehrstuhl für Atmosphärische Umweltforschung

Airborne observations of black carbon aerosol layers at mid-latitudes

Florian Dahlkötter

Vollständiger Abdruck der von der Fakultät Wissenschaftszentrum Weihenstephan für Ernährung, Landnutzung und Umwelt der Technischen Universität München zur Erlangung des akademischen Grades eines

Doktors der Naturwissenschaften (Dr. rer. nat.)

genehmigten Dissertation.

Vorsitzende:

Univ.-Prof. A. Menzel

Prüfer der Dissertation:

1. Univ.-Prof. Dr. H. P. Schmid
2. Univ.-Prof. Dr. B. Weinzierl (Ludwig-Maximilians-Universität München)

Die Dissertation wurde am 26.11.2013 bei der Technischen Universität München eingereicht und durch die Fakultät Wissenschaftszentrum Weihenstephan für Ernährung, Landnutzung und Umwelt am 05.05.2014 angenommen.

Abstract

Model studies show that black carbon (BC) is, after CO_2, the second strongest component of current global warming. However, data from in-situ measurement are sparse and BC in atmospheric aerosol layers is insufficiently investigated. Thus, the investigation of the aerosol layer distribution and the microphysical and optical properties of particle layers at mid-latitudes containing BC, based on airborne in-situ observations with the research aircraft Falcon during the aircraft field experiment CONCERT 2011, contributes valuable facts to clarify the relevance of absorbing aerosol layers in the atmosphere. For this field experiment, the Single Particle Soot Photometer (SP2), based on the measurement principle laser-induced incandescence, was for the first time operated onboard the Falcon. The results benefit the understanding of the characteristics of atmospheric aerosol layers at mid-latitudes. Especially information about BC in aerosol layers assessed in this thesis provides a comprehensive data set for the estimation of their impact on the climate.

Based on 11 research flights, the average aerosol burden within the vertical column of the troposphere and the lower stratosphere for Central Europe in September 2011 was derived. Highly variable aerosol layers were observed in roughly 10% of the flight time, predominantly at altitudes < 7 km and with vertical depths < 4 km. These aerosol layers were characterized according to their origin, BC mass size distributions, total BC mass concentrations, number size distributions and mixing states. At standard temperature and pressure (stp), the BC mass concentrations observed in the aerosol layers ranged from < 5 ng m^{-3} to > 400 ng m^{-3}. The total number concentrations of the layers varied almost by two orders of magnitude. The results of this study suggest three specific coating thickness distributions, characteristic for fresh planetary boundary layer aerosol, aged elevated aerosol layers and forest fire aerosol layers, implying different modifications in the absorption of BC particles.

Among the observed aerosol layers, an elevated concentrated forest fire aerosol layer was observed at 10–12 km altitude. The total BC mass concentration of this aged (3–4 days old) forest fire aerosol layer was 0.033–0.348 µg m^{-3} (stp), comparable to BC mass concentrations which are typical for moderately polluted planetary boundary layers. The individual BC particles in this layer, predominantly smaller than 130 nm in diameter, exhibited coating thicknesses of roughly 40–200 nm (calculated assuming a core-shell structure), while the majority of coated particles in the planetary boundary layer had coatings of less than 50 nm. Additionally, the data set gives evidence that a large fraction of the BC-containing particles disintegrated in the SP2 laser beam, implicating relevant information on the structure of the BC-containing particles in that fire plume. Besides the structure of the particles, the contribution of different particle components and mechanisms to the light absorption of the forest fire aerosol layer is discussed. Finally, the BC mass import of this forest fire into the free troposphere is estimated, and found to be comparable to the averaged global daily aviation-related BC emissions.

Kurzfassung

Modellstudien zeigen, dass Ruß nach CO_2 den zweitstärksten Beitrag zur globalen Erderwärmung aufweist. Allerdings gibt es nicht ausreichend viele in-situ Messdaten und Ruß in atmosphärischen Aerosolschichten ist somit nur unzureichend erforscht. Daher liefert die in dieser Arbeit behandelte Untersuchung der Verteilung und der mikrophysikalischen und optischen Eigenschaften von rußenthaltenden Aerosolschichten in den mittleren Breiten, basierend auf flugzeuggetragenen in-situ Beobachtungen auf dem Forschungsflugzeug Falcon im Rahmen des Feldexperiments CONCERT 2011, wertvolle Informationen, um die Bedeutung von absorbierenden Aerosolschichten in der Atmosphäre zu klären. Dafür wurde das Single Particle Soot Photometer (SP2), das Messprinzip der laser-induzierten Inkandeszenz verwendend, erstmals auf der Falcon betrieben. Die Ergebnisse tragen zum Verständnis der Eigenschaften von atmosphärischen Aerosolschichten in den mittleren Breiten bei. Dabei stellen insbesondere die Informationen über Ruß in Aerosolschichten einen umfassenden Datensatz für die Beurteilung der Auswirkungen von Ruß auf das Klima bereit.

Basierend auf elf Forschungsflügen wurde die durchschnittliche Aerosolbelastung innerhalb der vertikalen Säule der Troposphäre und der unteren Stratosphäre für Mitteleuropa im September 2011 bestimmt. Dabei wurden hochvariable Aerosolschichten während rund 10% der Flugzeit beobachtet, vorwiegend in Höhen < 7 km und mit vertikalen Ausdehnungen < 4 km. Diese Aerosolschichten wurden anhand ihrer Herkunft, Ruß-Massen-Konzentrationen und -Verteilungen, Anzahl-Größenverteilungen und Mischungszuständen charakterisiert. Bei Normbedingungen (stp) wiesen die Aerosolschichten Ruß-Massen-Konzentrationen im Bereich von < 5 ng m^{-3} bis > 400 ng m^{-3} auf und variierten um fast zwei Größenordnungen in ihren Gesamt-Anzahlkonzentrationen. Weiterhin wurden drei spezifische Verteilungen von Beschichtungsdicken auf Rußpartikeln beobachtet, die für frisches Grenzschicht-Aerosol, gealterte abgehobene Aerosolschichten und Waldbrand-Aerosolschichten unterschieden werden können. Sie implizieren verschiedenartige Modifikationen der Absorption von Rußpartikeln.

Eine der beobachteten Aerosolschichten war eine abgehobene, konzentrierte Waldbrand-Aerosolschicht in 10–12 km Höhe. Die Ruß-Massenkonzentration dieser 3–4 Tage alten Aerosolschicht war 0,033–0,348 µg m^{-3} (stp), vergleichbar mit typischen Konzentrationen in der mäßig verschmutzten planetaren Grenzschicht. Die Rußpartikel waren überwiegend kleiner als 130 nm mit Beschichtungsdicken von etwa 40–200 nm (unter Annahme einer Kern-Schalen-Struktur). In der Grenzschicht wies der Großteil der Partikel dagegen Beschichtungen von weniger als 50 nm auf. Zusätzlich gibt der Datensatz Hinweise darauf, dass ein Großteil der rußenthaltenden Partikel in dem Laserstrahl des SP2 zerfielen, was relevante Informationen über die Struktur der rußenthaltenden Partikel liefert. Neben der Partikelstruktur, wird der Beitrag verschiedener Partikelkomponenten und Mechanismen zur Absorption der Waldbrand-Aerosolschicht diskutiert. Schließlich wird der Ruß-Massen-Eintrag dieses Waldbrands in die freie Troposphäre abgeschätzt. Dies ist vergleichbar mit den mittleren globalen luftfahrtbezogenen Ruß-Emissionen pro Tag.

Contents

1 Introduction

1.1 Relevance of atmospheric aerosol

Within the last decades, significant changes of parameters representative for the climate change, e.g. surface temperature, sea level or snow cover, were observed (Figure 1). Predictions suggest that these changes will continue and potentially increase. Based on the assessments of the Intergovernmental Panel on Climate Change (IPCC), it is very unlikely that these changes are exclusively of natural origin or attributable to the natural variability of the climate system (IPCC, 2007). Thus, besides natural radiative forcing, from solar irradiance and volcanic aerosol, for instance, a major reason for the change is the anthropogenic radiative forcing driven by human activities. These activities causes the increase of concentrations of long-living greenhouse gases such as carbon dioxide (CO_2), methane (CH_4), nitrous oxide (N_2O), halocarbons and sulfur hexafluoride (SF_6), and significant changes in ozone (O_3), water vapor, and aerosols (IPCC, 2007).

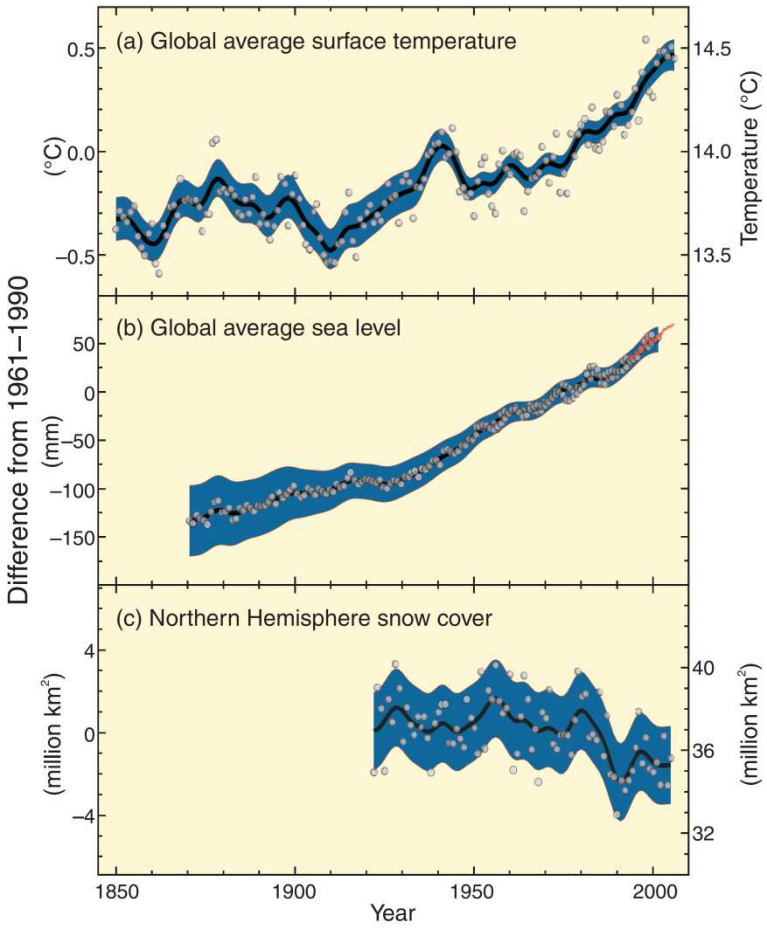

Figure 1. *Observed changes in global average surface temperature (top panel), global average sea level (middle panel), and northern hemisphere snow cover for March to April (bottom panel) relative to corresponding averages for the period 1961–1990 (IPCC, 2007) as average (black line), yearly values (white circles), and estimated uncertainties (shaded areas). Adopted from IPCC (2007).*

One of the largest uncertainties in the characterization of climate change is the impact of aerosol[1] particles on the radiative budget and aerosol-cloud-interactions (e.g. Satheesh and Moorthy, 2005; IPCC, 2007). The individual effects of aerosol particles are schematically shown in Figure 2: the *direct effects* describe the interactions of particles with the incoming solar radiation, where the radiation is either scattered or partly absorbed[2] and the heat is redistributed in the atmosphere and at the surface, causing major changes in the earth's radiation budget (e.g. Haywood and Boucher, 2000; IPCC, 2007). The total direct radiative forcing of aerosol particles, a combination of light scattering and absorbing effects, is estimated to be negative (-0.5±0.4 W m^{-2}), i.e. to be a cooling effect. Based on the distribution, the abundance, and microphysical and optical properties, different aerosol species have varying direct radiative forcings, e.g. sulfate aerosol -0.4±0.2 W m^{-2}, fossil fuel organic carbon (OC) -0.05±0.05 W m^{-2}, fossil fuel black carbon (BC) +0.2±0.15 W m^{-2}, biomass burning +0.03±0.12 W m^{-2}, nitrate -0.1±0.1 W m^{-2}, or mineral dust -0.1±0.2 W m^{-2} (IPCC, 2007). For BC recently the value of the direct radiative forcing was reviewed to be +0.71 (+0.09 to +1.26) W m^{-2} (Bond et al., 2013).

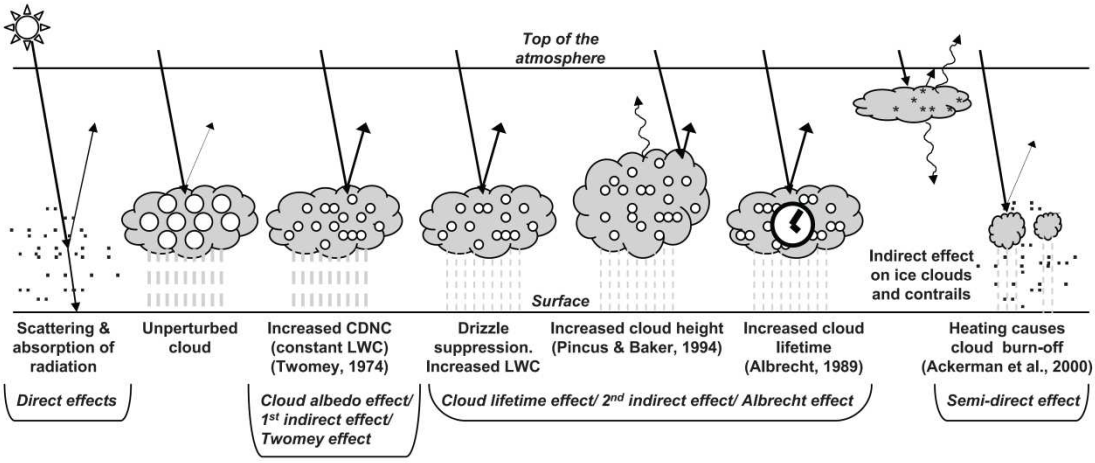

Figure 2. *Schematic view of the various radiative mechanisms associated with aerosols. Small black dots: aerosol particles; white dots: cloud droplets; straight lines: incident and reflected solar radiation; waved lines: terrestrial (long wave) radiation. (LWC: liquid water content; CDNC: cloud droplet number concentration). Adopted from IPCC (2007), modified from Haywood and Boucher (2000).*

In addition to the direct effects, aerosol particles act as cloud condensation nuclei (CCN) (e.g. Quinn et al., 2008) or ice nuclei (IN) (e.g. Hoose and Möhler, 2012), causing changes in droplet size, number concentration, and the lifetime of cloud droplets, and thus lead to *indirect effects* on the radiative budget (e.g. Pöschl, 2005; Andreae and Rosenfeld, 2008): in the present day, more particles exist in the atmosphere as compared to preindustrial times. The more aerosols there are in the atmosphere, the smaller the developing cloud droplets (Twomey, 1977), resulting in an increased brightness of the cloud and causing the clouds to reflect more solar radiation (*first indirect effect* or *Twomey effect)*. Besides that, clouds with smaller droplets may exhibit a longer lifetime as compared to clouds with large droplets

[1] Technically, aerosol is defined as a suspension of solid or liquid particles in a gas (e.g. Seinfeld and Pandis, 2006). However, aerosol is often used as a synonym only for the particles themselves.

[2] During absorption, solar radiation energy is converted to thermal radiation energy, causing absorbing particles to change their temperature during the interaction with light.

(*second indirect effect*), due to a reduction or delay of precipitation (e.g. Andreae et al., 2004; Lohmann and Feichter, 2005). Besides that, aerosol particles can cause a *semi-direct effect* on clouds (e.g. Ackerman et al., 2000): absorbing aerosols such as soot can induce a heating of the upper parts of the cloud, which can result in a decrease of relative humidity associated with a modified cloud formation and lifetime or a dispersal of the cloud, counteracting the *first* and *second indirect effect* (e.g. Lohmann and Hoose, 2009 and references therein).

However, despite elaborate studies, the magnitude of aerosol climate forcing is uncertain with a low to medium level of scientific understanding (e.g. IPCC, 2007; Hansen et al., 2011). The uncertainties arise from the highly variable and heterogeneous properties of aerosol particles, such as their size, their chemical composition, their morphology, their heterogeneous vertical and horizontal distribution within the atmosphere, and their various and manifold interactions with other constituents of the atmosphere (e.g. Kaufman et al., 2002). Furthermore, the size, chemical composition and morphology of aerosol particles can change during their atmospheric lifetime, due to the process of mixing inside the population of aerosol particles (Fenn et al., 1981; IPCC, 2007). Consequently, the broad spectrum of aerosol particle properties and interactions forms a complex system of aerosols affecting the atmosphere. Due to the described heterogeneous mixing and aging processes, its formation and alteration, this system is not yet fully understood and is difficult to determine though the investigation of aerosol particles is a key parameter for the quantification of the effects of aerosols on climate change (Schmale, 2011). To differentiate the impact of different aerosols on the atmosphere, aerosol particles are classified in specific aerosol types, exhibiting specific optical and microphysical properties.

1.2 Aerosol types and processes with focus on black carbon

Figure 3 shows a global distribution of aerosol particles calculated with the Goddard Earth Observing System Model, Version 5 (GEOS-5). There, the aerosols are separated into four major categories: mineral dust (orange), mainly originating from the Saharan desert and Arabia, sea salt aerosol (blue), industrial and volcanic sulfate emissions (white), and biomass burning emissions (green), mainly from fires in the rain forests and boreal forests. The variety of aerosol particles includes predominantly light scattering particles, like sulfate aerosol or sea salt, and particles with a considerably enhanced absorbing component, like black carbon (BC).

The aerosol type with the highest emissions with respect to mass is sea salt due to the large source area of the ocean, which covers approximately 70% of the Earth's surface (Winter and Chýlek, 1997). Sea salt is highly hygroscopic and has a refractive index[3] with a negligible imaginary part ($1.381\text{-}4.26\cdot10^{-9}i$), i.e. with a negligible absorption (Takemura et al., 2005). In contrast to sea salt particles, absorbing aerosol particles result in an increase of the temperature of the particle and thus of the surrounding air. Hence, absorbing aerosol species contribute, to a large part, to the positive radiative forcing, i.e. warming, attributed

[3] The key quantities of the optical properties of aerosol particles are defined in Section 2.3.

to aerosol particles (Jacobson, 2001). An absorbing but less abundant component of atmospheric aerosol is volcanic ash, contributing only up to 1% of the total mass of emitted aerosol (e.g. Hinds, 1999). Weinzierl et al. (2012) report values at 550 nm for the real part of the refractive index *n* of 1.56–1.60 and for the imaginary part *k* 0.002–0.015 for volcanic ash from the Eyjafjalla volcano. The occurrence and concentrations of volcanic ash are highly variable in space and time due to its irregular emissions during volcanic eruptions. More details on volcanic ash properties are described, for example, in Volz (1973), Patterson (1981), Patterson et al. (1983), Clarke et al. (1983), and Corradini et al. (2008).

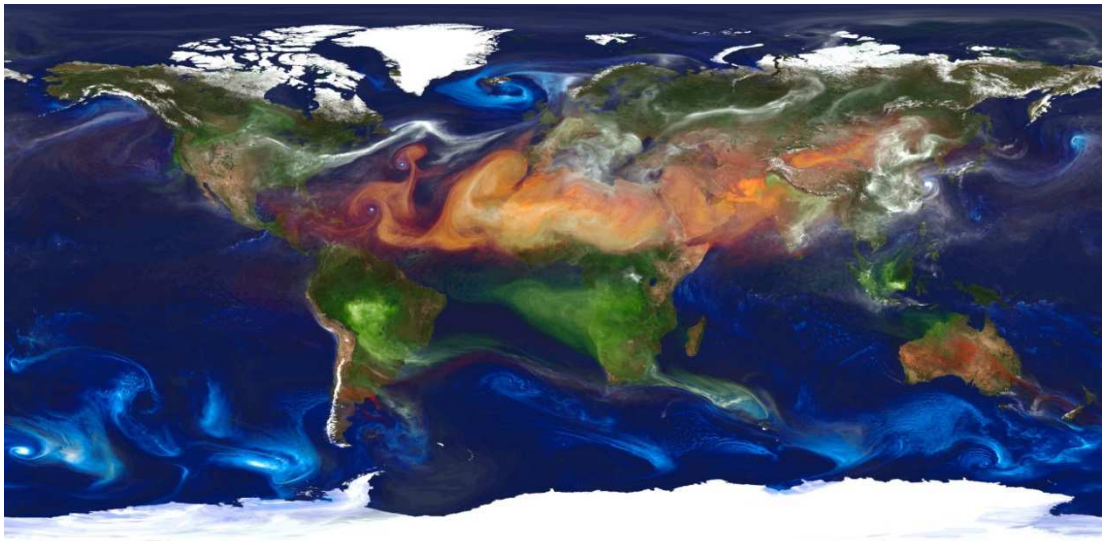

Figure 3. *Portrait of Global Aerosols (source: www.nasa.gov; Image credit: William Putman, NASA/Goddard). High-resolution global atmospheric modeling run at 10 km resolution based on the Goddard Earth Observing System Model, Version 5 (GEOS-5), showing dust lifted from the surface (red), sea salt swirls inside cyclones (blue), smoke arising from biomass burning (green), and sulfate particles stream from volcanoes and fossil fuel emissions (white).*

In addition to volcanic ash aerosol, weakly absorbing mineral dust contributes partially to the absorption of aerosols due to the high amounts of emitted material (Satheesh and Moorthy, 2005). The main sources for mineral dust, which is often non-spherical and irregularly shaped (Moosmüller et al., 2009), are the North African and Asian deserts (Prospero et al., 2002), where the dust is mechanically emitted by wind erosion. Weinzierl et al. (2011), determined at 530 nm for the real part of the refractive index *n* 1.54–1.56 and for the imaginary part *k* 0.000–0.008. Mineral dust and volcanic ash do not absorb light comparably efficiently as BC[4] due to the lower mass absorption cross-sections (e.g. 0.02–

[4] The terminology used in the literature for the carbonaceous particles from combustion emission is often ambiguous and not clear (Petzold et al., 2013). Besides BC, other terms like soot or light absorbing carbon (LAC) (Bond and Bergstrom, 2006) are used to describe this strongly absorbing material arising from combustion processes. Here the term "BC" is used exclusively for the most refractory and light absorbing component of carbonaceous combustion particles, which is essentially pure carbon, not including organic carbon (OC), brown carbon (BrC) or inorganic aerosol components. Furthermore, the more specific term refractory black carbon is used (rBC; see Petzold et al., 2013), whenever it is referred to quantitative measurements of the rBC mass (or quantities inferred from rBC mass measurements) performed, using the Single Particle Soot Photometer (SP2; Schwarz et al., 2006). However, Bond et al. (2013) recommend the consistent use of the term rBC for future work. Further recommendations for the interpretation of BC measurements and the terminology to clarify the terms used for BC in atmospheric research are presented in Petzold et al. (2013).

0.1 $m^2 g^{-1}$ for mineral dust) (Moosmüller et al., 2009) compared to BC (6.3–8.7 $m^2 g^{-1}$) (Bond and Bergstrom, 2006). This difference is also reflected by a higher single-scattering albedo ω_0 of mineral dust (0.5–0.97) (Lafon et al., 2006) compared to BC (0.2–0.3) (Bond and Bergstrom, 2006), as it is compared in Heimerl (2011). BC is the dominant solar radiation absorbing component in the visible spectrum in the atmosphere and recent modeling studies suggest that BC is the second strongest source of global warming after CO_2 (Ramanathan and Carmichael, 2008). Because the exact effects of absorbing aerosols on the climate are poorly understood (e.g. Bond et al., 2013), this study focusses on strongly absorbing BC, representing the key type of absorbing aerosol in the atmosphere.

BC forms by fuel molecules being pyrolyzed and split during incomplete combustion[5]. The formed radicals build polycyclic aromatic hydrocarbons (PAH), which grow due to the chemical reactions and condensation (e.g. Seinfeld and Pandis, 2006). After growing to particles > 10 nm and transition to the solid phase, the soot spherules coagulate and form fractal-like aggregates (Moosmüller et al., 2009), which are hydrophobic (Takemura et al., 2005). The particle structure and optical properties of the soot agglomerates depend on the fuel type and combustion conditions (Slowik et al., 2007b). Thus, the refractive index of BC is determined to be in a range from 1.75-0.63i to 1.95-0.79i at 550 nm (Bond and Bergstrom, 2006). This range indicates that even within aerosol types the absorbing properties can vary widely due to different source materials or different emission processes.

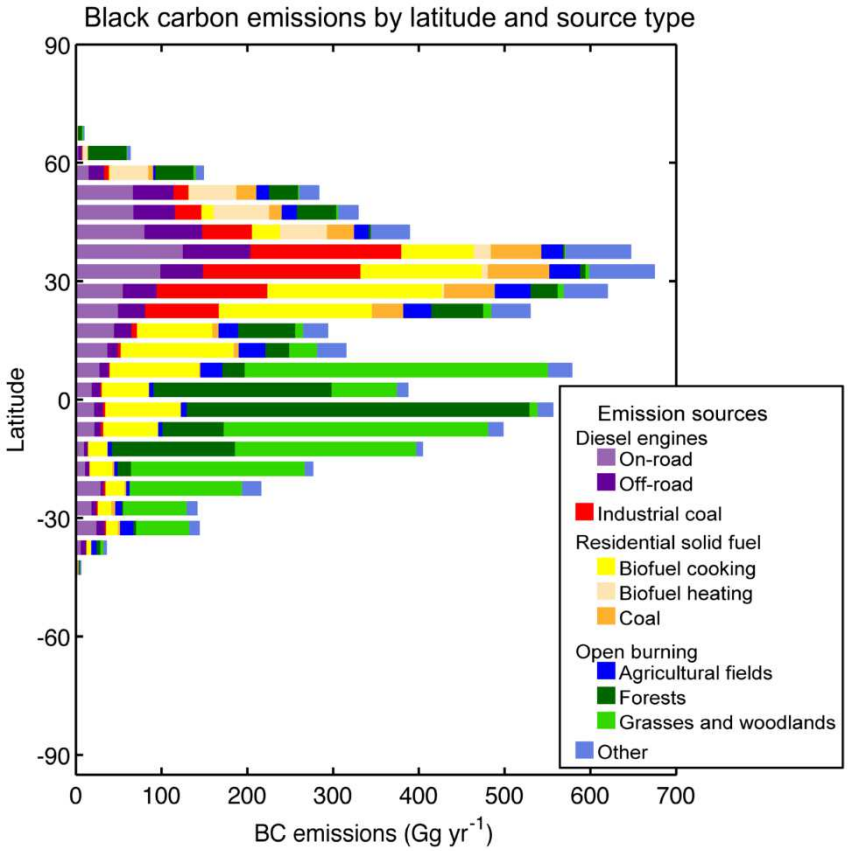

Figure 4. *Emission rates of BC in the year 2000 by latitude, indicating major source categories for each 5°-latitude bin. Adopted from Bond et al. (2013).*

[5] Details on the formation processes of BC are described in e.g. Moosmüller et al. (2009).

BC is emitted by anthropogenic sources, like the combustion of fossil fuels, or natural sources, like biomass burning induced by lightning strike. Especially in industrialized parts of the world, anthropogenic emissions are relevant sources for BC particles in the troposphere. Figure 4 shows the latitudinal distribution of BC emissions divided into major source categories. In the northern hemisphere BC emissions are dominated by traffic, industry related sources and residential solid fuel combustion, while in the southern hemisphere open burning dominates the total BC emissions.

In contrast to the variety of aerosol sources on the ground, aviation is the only source emitting primary aerosol particles, including BC, directly to the upper troposphere and lower stratosphere (UTLS) region. Though BC emissions of aviation accounts only for a minor fraction to BC (< 5% in terms of BC mass) in the UTLS region (e.g. Hendricks et al., 2004), aviation is of certain relevance for the BC load at higher altitudes (e.g. Petzold et al., 1999; Righi et al., 2013). Aviation emits, globally averaged, roughly 0.006 Tg soot (Lee et al., 2009) to 0.02 Tg BC (Bond et al., 2013) per year to the atmosphere with a major part being emitted directly to the UTLS region. The fresh combustion particles are emitted in the size range of roughly 20–60 nm (Petzold et al., 2003), depending on engine type and operating conditions. The emitted particles may become coated with condensable gases in the expanding and cooling exhaust and, thus, can grow further by hygroscopic growth and may induce contrail formation, depending on the atmospheric conditions (Schumann et al., 2012).

Among the various sources of BC, biomass burning[6] is of major relevance (e.g. Lavoue et al., 2000). Figure 5 shows a generic global fire map for the period 8–17 September 2011. The fires are detected by Moderate Resolution Imaging Spectroradiometer (MODIS) onboard the Terra and Aqua satellites. Each dot indicates a fire during the period with the color ranging from red to yellow with increasing number of fires (e.g. Justice et al., 2002; Giglio et al., 2003; http://rapidfire.sci.gsfc.nasa.gov). This figure, which just shows the fires during a ten-day period, illustrates the quantity of biomass burning events and thus their relevance as an aerosol source. Underlining this, the Canadian Forest Service states that over the last 25 years, forest fires across Canada have consumed an average of 2.3 million hectares a year (http://cfs.nrcan.gc.ca). Besides aerosol particles such as BC, biomass burning emits atmospheric trace compounds like OC, CO_2, CO, CH_4, H_2, NO_x, NO, NO_2, non-methane organic compounds and hydrocarbons, SO_2, NH_3, etc. (Akagi et al., 2011; Wiedinmyer et al., 2011) throughout to the atmosphere. On a global scale, in the global troposphere biomass burning is the second largest source of trace gases and the largest source of primary fine carbonaceous particles (Akagi et al., 2011). Barnaba et al. (2011) estimate that up to 35% of the European fine particle fraction (< 1 µm) aerosol optical thickness is attributable to wild land fire aerosol particles. Depending on the burning conditions and type of fuel material, properties of aerosol particles from biomass burning can vary widely. Diehl et al. (2012) estimate the global BC emissions from biomass burning to be 1.8–7.0 Tg a^{-1}, while OC[7] emissions range from 14–57 Tg a^{-1}. Findings of Reid et al. (2005b) show that biomass

[6] Biomass burning is defined as the sum of all open or quasi-open natural and anthropogenic combustion processes using non-fossilized vegetative or organic fuels, such as open fires in forests, savannas, crop residues, causing the major part of biomass burning emissions, and biofuel burning, such as cooking fires or dung burning (Akagi et al., 2011).

[7] OC is a carbonaceous, non-BC material absorbing little or no light and is a byproduct emitted by combustion processes (Bond et al., 2013).

burning emissions contain roughly 50–60% OC and 5–10% BC. In addition to BC, in forest fire aerosols enhanced concentrations of brown carbon (BrC), an absorbing OC, are observed (e.g. Lukacs et al., 2007) as a result of smoldering combustion of biomass (Andreae and Gelencser, 2006; Moosmüller et al., 2009), which can contribute significantly to light absorption (e.g. Andreae and Gelencser, 2006; Alexander et al., 2008; Moosmüller et al., 2009; Lack and Langridge, 2013). A difference between BrC and BC is the wavelength-dependent light absorption of BrC, compared to the wavelength-independent absorption of BC. In biomass plumes even mineral dust particles are observed, possibly lifted together with the smoke particles at the source of the biomass burning due to the intense heat at the source of the fire (Tesche et al., 2011). A future increase in forest fire events, and generally biomass burning, might be of great importance on the (BC) aerosol import into the atmosphere. Consequently, biomass burning has a major, possibly growing, impact on the radiative budget of the atmosphere (Knorr et al., 2012) and a better understanding of the microphysical properties of biomass burning layers is essentially required.

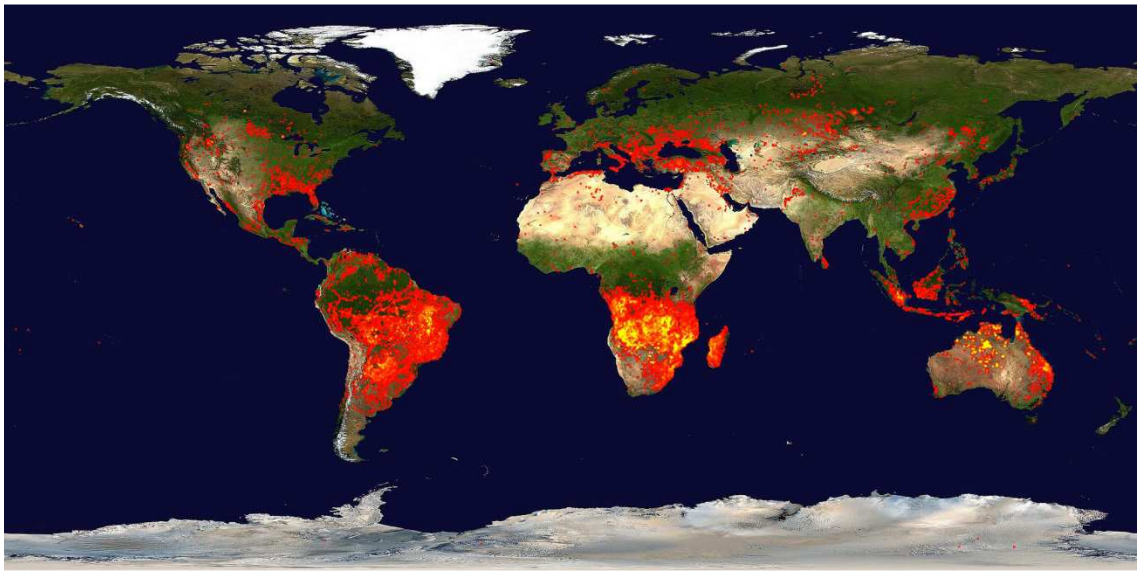

Figure 5. *Example of the global fire distribution for the period 8–17 September 2011 (source: http://rapidfire.sci.gsfc.nasa.gov). The fires are detected by Moderate Resolution Imaging Spectroradiometer (MODIS) onboard the Terra and Aqua satellites. Each dot indicates a fire during the period with the color ranging from red to yellow with the increasing number of fires (e.g. Justice et al., 2002; Giglio et al., 2003).*

Though most sources of BC are ground-based (Figure 6) and BC is predominantly agglomerate in the planetary boundary layer (PBL), the impact of BC in the climate system extends throughout the entire atmosphere, because parts of the emissions are transported to the free troposphere or even to the stratosphere (e.g. Trickl et al., 2013), contributing to the BC burden at higher altitudes (besides direct emissions of aviation). Such elevated aerosol layers[8] in the atmosphere above the boundary layer occur frequently and can be transported over long distances, even on global scales in transcontinental plumes (Damoah et al., 2004; Spichtinger et al., 2004; Mattis et al., 2008) on time scales of days to weeks (e.g. Damoah et al., 2004) and mix with other aerosols during the transport (e.g. Ramanathan and

[8] In this study, an elevated aerosol layer is defined as a vertically extended layer containing enhanced aerosol particle concentrations compared to the background situated above the planetary boundary layer.

Carmichael, 2008; Petzold et al., 2011; Weinzierl et al., 2011). Consequently, the transport of aerosol is of enormous importance for the temporal and spatial variability of aerosols and the atmospheric burden (e.g. Vignati et al., 2004; Weinzierl, 2007). As also indicated in Figure 3, such long-range transport can significantly influence remote regions with originally low particle emissions, like the Arctic (e.g. Stohl et al., 2006; Browse et al., 2012), and is frequently observed for, e.g., mineral dust plumes, anthropogenic emitted aerosols or biomass burning emissions and was reported by, among others, Fiebig et al. (2003), Petzold et al. (2007), e.g. Stohl et al. (2007), Quennehen et al. (2011), Weinzierl et al. (2011) and Quennehen et al. (2012).

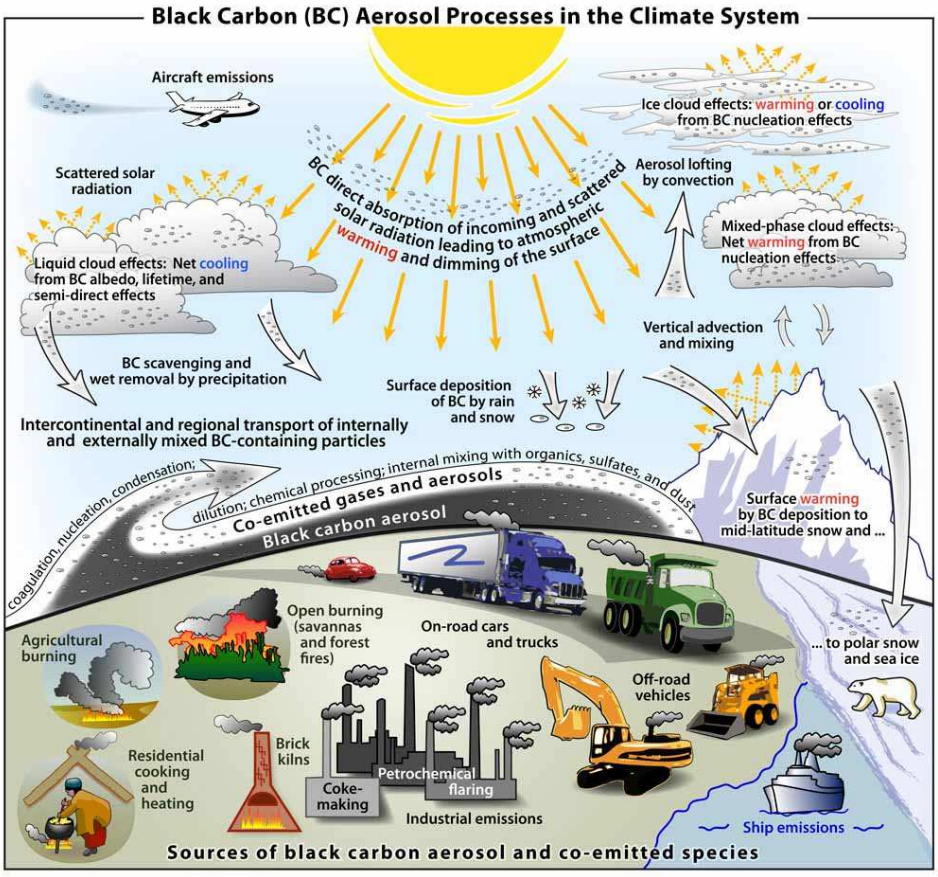

Figure 6. *Schematic overview of the primary black carbon emission sources, the processes controlling the distribution of black carbon in the atmosphere and its role in the climate system. Adopted from Bond et al. (2013).*

Mattis et al. (2008) observed, for instance, free-tropospheric aerosol layers over central Europe based on ten years of ground-based multi-wavelength Raman lidar (light detection and ranging) observations. They report pollution above the continental boundary layer in 43% of their measurements, with a maximum from June to August. In 19% of all measurements, they found forest fire smoke advected from Canada and anthropogenic pollution advected from urban areas of the USA and Canada (Mattis et al., 2008). The distribution of the aerosol layers within the free troposphere (Figure 7) shows that the layers were found in altitudes between 0 km and 8 km with a layer depth of predominantly 0–4 km (Mattis et al., 2008). This vertical distribution of aerosols is relevant for the impact on the radiative budget, because, e.g., the surface temperature change caused by BC is dependent on the altitude of BC (Ban-Weiss et al., 2012). However, the distribution and

burden of BC in the atmosphere is strongly influenced by the emissions and the removal of BC. Atmospheric BC is removed efficiently by wet removal (Oshima et al., 2012; Moteki et al., 2012), due to mixing of the hydrophobic BC with hydrophilic materials during aging (e.g. Liu et al., 2010). In addition, at high altitudes BC particles can also be scavenged by ice particles (Baumgardner et al., 2008). Even after removal, BC can influence the radiative budget by a decrease of the surface albedo, particularly relevant for BC deposition on snow and ice, enhancing the absorption and potentially causing an accelerated melting (e.g. Kaspari et al., 2011).

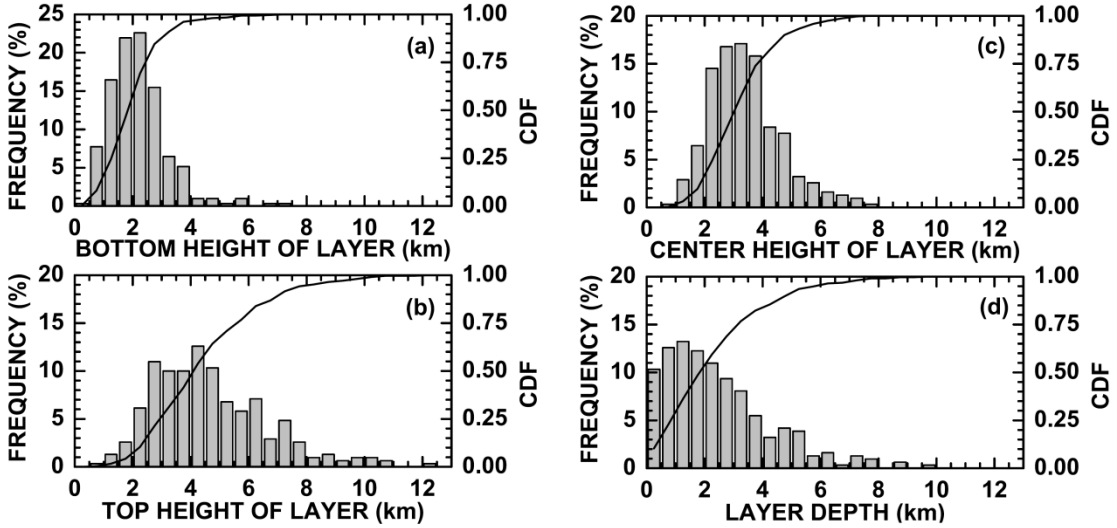

Figure 7. *Frequency distribution of aerosol layers observed in Central Europe based on ten years (1997–2006) of multi-wavelength Raman lidar observations. (a) bottom height, (b) top height, (c) center height, and (d) geometrical depth of the aerosol layers. Adopted from Mattis et al. (2008).*

The described processes of BC in the atmosphere are not understood quantitatively. Even the knowledge on the horizontal and vertical distribution of BC still comprises large uncertainties (e.g. IPCC, 2007), though representing the basic element for the described processes and sensitively affecting the radiative budget directly. To be able to assess the manifold of effects of (BC) aerosols, the atmospheric (BC) aerosol particles need to be characterized and quantified. In contrast to satellite measurements providing column integrated aerosol optical properties or lidar measurements, airborne measurements deliver essential in-situ data on the vertical distribution of aerosol particle properties in the atmosphere (e.g. Weinzierl, 2007) and important input data for models and emission databases and can improve them significantly (e.g. Hamburger, 2010). Recent studies focused on the distribution of aerosol particles in the troposphere assessed by airborne measurements (e.g. McMeeking et al., 2010; Schwarz et al., 2010b). However, despite of a multitude of measurements, many processes of (BC) aerosol particles in the atmosphere have not yet been investigated in detail and have only been quantified and characterized insufficiently. Therefore, further vertically and horizontally resolved airborne in-situ measurements of (BC) aerosol are essential, representing the scientific basis to decrease uncertainties in radiative budget estimations.

1.3 Scientific objectives

Bond et al. (2013) give a comprehensive overview on black carbon (BC) in the atmosphere and its role in the climate system and assembles some major issues of the BC quantification. Major uncertainties caused by BC are based on

- not sufficiently described processes of BC like e.g. its interactions with other aerosol components;
- the underestimation of the global atmospheric absorption caused by BC by many global aerosol models compared to results from remote sensing measurements;
- the insufficiently accomplished attribution of the measured absorptions to the specific absorbing components, like BC, dust or OC;
- uncertainties in the distribution of BC and the underlying emission factors from biomass burning and fossil fuel combustion (Bond et al., 2013).

This listing shows that BC aerosol in the atmosphere is still insufficiently described, though many studies have addressed atmospheric (BC) aerosol. Especially single-particle properties like mixing states and BC contents are usually disregarded due to measurement difficulties, e.g. problems in the determination of mixing states based on filter-based measurements. Thus, the gaps in the knowledge on strongly absorbing BC and its mixing state in aerosol layers contributes significantly to uncertainties of the impact of BC aerosol in the atmosphere. To improve the understanding of BC-containing aerosol layers, following open scientific questions are addressed by this study based on airborne in-situ measurements during the CONCERT 2011 field experiment[9]:

- **How are aerosols and aerosol layers distributed in the atmosphere at mid-latitudes in September 2011?**
  - Are measured vertical (BC) aerosol profiles comparable to model results?
  - How frequently and at which altitudes were elevated aerosol layers observed at mid-latitudes during CONCERT 2011?
  - Which types of aerosol layers were observed during CONCERT 2011?

- **Which characteristics describe the observed aerosol layers at mid-latitudes in September 2011?**
  - How do elevated aerosol layers differ regarding their optical and microphysical properties?
  - What are the microphysical properties of BC in aerosol layers at mid-latitudes?
  - What mixing states of BC-containing particles are observed in aerosol layers at mid-latitudes?

[9] Airborne in-situ data from the ACCESS field experiment are used for comparison.

- **Which characteristics describe strongly absorbing forest fire aerosol layers?**
  - Are some of the observed aerosol layers identified as forest fire aerosol plumes?
  - Do forest fire aerosol exhibit different characteristics regarding their optical and microphysical properties in comparison to other elevated aerosol layers?

- **Which sources contribute to the BC load in the UTLS region?**
  - Do fires in boreal forests act as a significant source for BC load within the UTLS region, and how relevant are they compared to other sources of BC, like aviation?

To answer these scientific questions, in this study BC is measured directly using a Single Particle Soot Photometer (SP2), which was prepared, characterized and operated for the first time on the DLR research aircraft Falcon as crucial part of this study. Based on that, the characterization and quantification of elevated BC aerosol layers at mid-latitudes, according to their optical properties, microphysics and mixing state, is addresses. Such expensive and sophisticated airborne in-situ measurements of aerosol layers can provide in-depth examinations of aerosol properties and transformation processes (e.g. Bond et al., 2013). The analyzed microphysical and optical aerosol properties are combined with air mass transport calculations to differentiate the layers with respect to their sources.

This work[10] provides a comprehensive and unique data set allocating new, single-particle information on BC-containing aerosol layers for the wide area of Europe throughout the whole vertical column of the troposphere and UTLS region. The results obtained within this study, investigated in the framework of the Helmholtz young investigators group AerCARE, represent spadework and a scientific basis to assess the impact of elevated absorbing aerosol layers at mid-latitudes within the atmosphere.

In the following section the fundamentals of atmospheric aerosol are explained (Section 2), in particular aerosol particle properties treated in this study. Afterwards, the measurement campaigns, the applied techniques of aerosol in-situ measurements, the associated analysis methods and the accuracy and the quality of the data are described (Section 3). The results of this study are presented and discussed in Section 4 starting with the general vertical aerosol distribution (Section 4.1). The characteristics of the entire data set of observed aerosol layers will be described in Sections 4.1.4 and 4.2. A case study on long-range transport forest fire plumes observed over Germany is presented in Section 4.3. In Section 4.4, the contribution of different sources to the BC load in the UTLS region is discussed.

[10] Parts of this study are published in Dahlkötter et al. (2014).

2 Basics of atmospheric (black carbon) aerosol

This section addresses the fundamentals of aerosol particles in the atmosphere. Aerosol particle sources, the particle aging processes during the transport and sinks are described. In addition, the relevant parameters of aerosol size distributions and mixing states are defined. Finally, the theoretical background on optical properties of aerosol particles needed for this study is presented. Further details on aerosol theory are given in Bohren and Huffman (1983), Hinds (1999), Seinfeld and Pandis (2006), or Kulkarni et al. (2011), for example.

2.1 Sources, sinks and aging of aerosol particles

Aerosol particles in the atmosphere arise from various sources, which are divided into *natural* and *anthropogenic* sources. Aerosol particles emitted from natural sources include mechanically wind-borne mineral dust, aerosol particles emitted by volcanic eruptions, oceanic sea spray or biologically formed particles (Figure 8). Main anthropogenic emissions are related to combustion processes from industry and traffic, creating urban areas as a major source in terms of particle number (e.g. Dahlkötter et al., 2010), from aviation, and mechanically emitted road dust, wind erosion of cropland, etc. (Seinfeld and Pandis, 2006). In contrast, biomass burning can be caused naturally, for instance, by lightning strikes or anthropogenically, by fire clearance. An estimate of the annual global emissions of the particular sources is given in Table 1 (Raes et al., 2000 and references therein). Associated with the sources and source processes, aerosol particles exhibit diverging shapes, ranging from a spherical shape, e.g. liquid particles, to aspherical shapes, e.g. mineral dust or volcanic ash or clusters of nano-particles typical for soot.

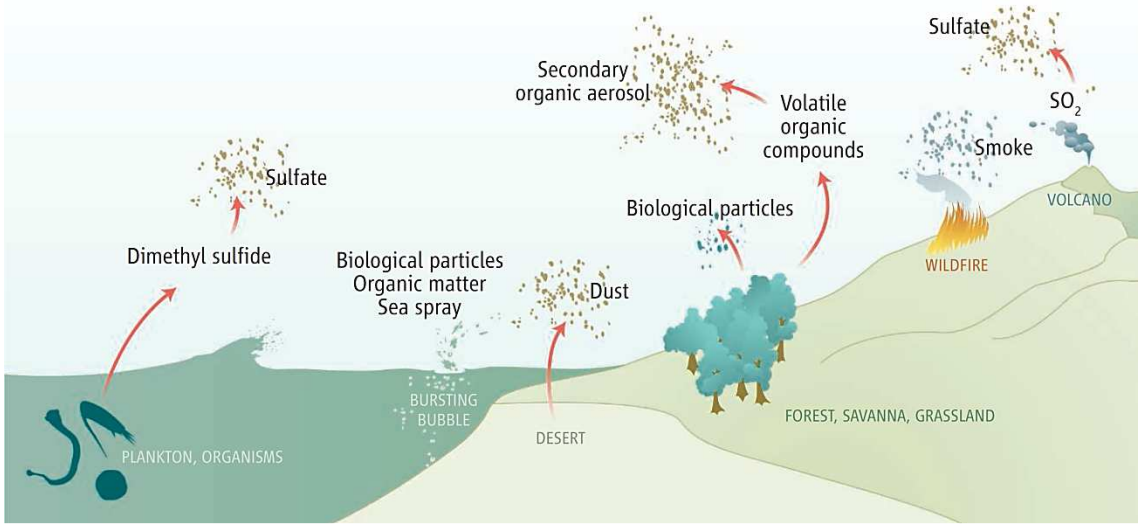

Figure 8. *Natural aerosol sources. All anthropogenic sources such as industry, aviation, road traffic, ship traffic, land use, or anthropogenic biomass burning are not shown. Adopted from Andreae (2007).*

Table 1. *Global emission estimates for major aerosol sources based on several studies. Adopted from Raes et al. (2000) and references therein.*

Source	Estimated global emission / (Tg yr^{-1})
Sea salt	
Total	5900
0–2 µm	82.1
2–20 µm	2460
Soil dust	
< 1 µm	250
1–10 µm	1000
0.2–2 µm	250
2–20 µm	4875
Organic carbon	
Total	69
Biomass burning	54.3
Fossil fuel	28.8
Terpene oxidation	18.5
Black carbon	
Total	12
Biomass burning	5.6
Fossil fuel	6.6
Sulfate (as H_2SO_4)	
Total	150
Natural	32
anthropogenic	111
Nitrate	11.3
Ammonium	33.6

Figure 9 shows images of aerosol particles of different shapes and sizes attributable to different sources. Besides the shape and size, a variety of optical and microphysical properties of the individual aerosol particles are strongly linked to the particle formation processes and are thus associated with the source.

In addition to the separation of aerosol particles based on natural or anthropogenic sources, aerosol particles are also classified by two main formation categories: *primary particles* and *secondary particles*. Primary particles are emitted directly from the respective sources, while secondary particles are formed by chemical processes, i.e. by nucleation and coagulation of aerosol precursor gases within the atmosphere. Secondary particles usually exhibit small particle diameters ($D_P < \sim 0.1$ µm), while primary particles can cover almost the entire size range from several nanometers (10^{-9} m) to several hundred micrometers (10^{-4} m). Figure 10 summarizes schematically the processes associated with aerosol particles in the atmosphere. Not shown are the size ranges and processes of cloud droplets as part of the atmospheric system but usually not defined as aerosol. The particles in the atmosphere are transformed by condensation of precursor gases on existing particles, by coagulation, i.e. growth of particles due to collisions and adherence based on Brownian motion, forces acting between particles like van der Waals and Coulomb forces, turbulent motion, or gravitational lowering (Seinfeld, 1986) and by serving as cloud condensation nuclei in supersaturated environments.

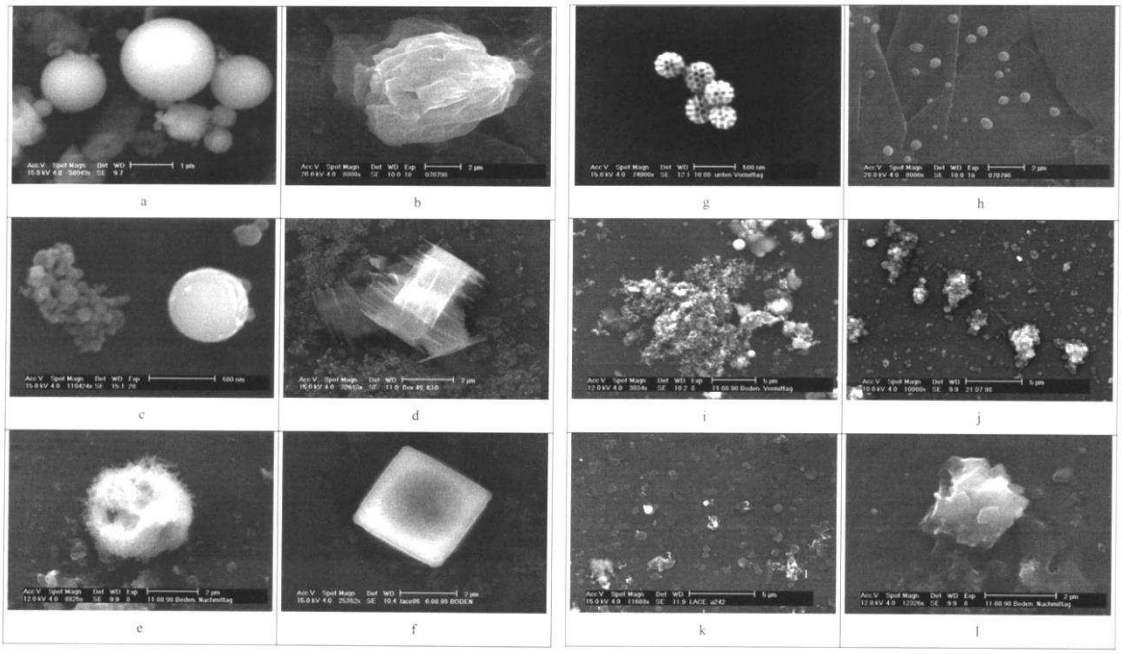

Figure 9. *Variety of aerosol particle shapes derived by secondary electron images of aerosol particles: (a) silicate spheres (fly ash); (b) silicate (presumably soil material); (c) iron oxides spheres; (d) calcium sulfate; (e) carbonate; (f) sea salt; (g) biological particle; (h) carbon/sulfate mixed particles; (i) large soot agglomerate and small silicate fly ash particles (bright spheres); (j) ammonium sulfate agglomerates; (k) soot (1), ammonium sulfate (2), and carbon/sulfate mixed particles (3); (l) carbon-rich particle. Adopted from Ebert et al. (2002).*

Effective removal processes are the coagulation for small particles, the gravitational sedimentation for large particles (*dry deposition*) and particle-cloud interactions including rainout and washout (*wet deposition*). Because for particles in the size range around $0.05 < D_P < 1$ µm no effective mechanisms for dry deposition exist (e.g. Whitby, 1978), particles accumulate in this size spectrum (Seinfeld and Pandis, 2006) and are only effectively removed by wet removal processes (Petzold and Kärcher, 2012). Taking into account all described processes, aerosol particles have lifetimes from seconds to years (Figure 11), depending on their size, the position within the vertical column of the atmosphere, the accompanied atmospheric processes and meteorological conditions. Andreae (2007) approximated that the typical averaged lifetimes of airborne particles in the troposphere is 3–10 days with about 95% of the particles being removed from the atmosphere within 30 days. As indicated in Figure 10, particles > 1 µm are less abundant compared to particles < 1 µm. Nevertheless, besides the number concentration, the mass of particles is a relevant quantity, e.g. for absorption processes. Thus, larger particles cannot be neglected in spite of their lower number concentration.

Summarizing all sources, particle transformation processes and sinks, aerosol particles are classified into four aerosol modes according to the particle diameter D_P: the *nucleation mode* ($D_P < 0.01$ µm; particles directly formed by homogeneous particle nucleation or gas-to-particle conversion from gaseous precursors), the *Aitken mode* (0.01 µm $< D_P < 0.1$ µm; particles directly emitted or formed by coagulation of particles or condensation of vapors on existing particles), the *accumulation mode* (0.1 µm $< D_P < 1$ µm; particles directly emitted or grown by particle coagulation) and the *coarse mode* ($D_P > 1$ µm; particles emitted mainly by mechanical processes like dust, sea spray, organic material or volcanic ash) (Hussein et al., 2005 and references therein).

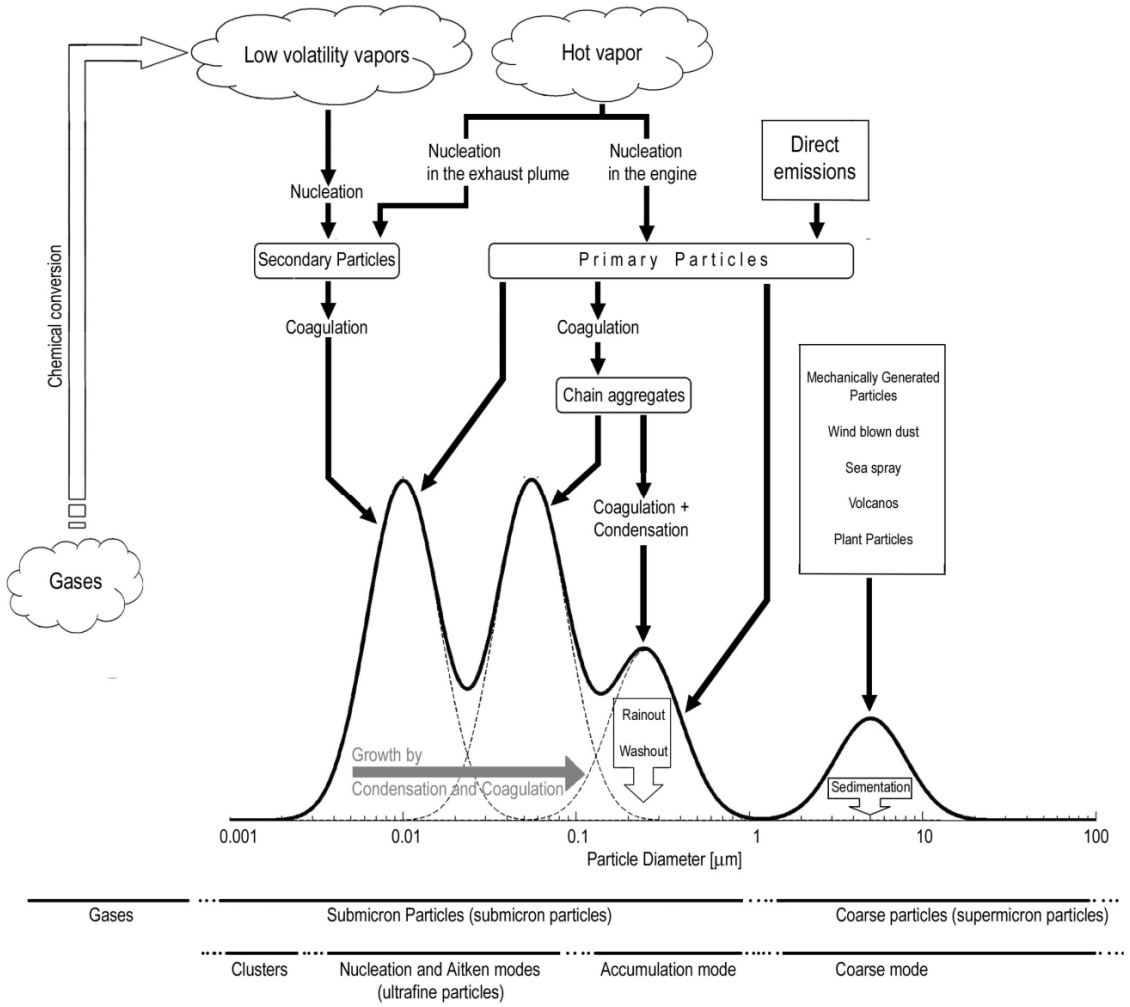

Figure 10. *Idealized scheme of an atmospheric particle number size distribution. Sources, particle formation, transformation and removal processes, and key modes are included. Adopted from Hussein et al. (2005) and references therein.*

In reality the aerosol size distribution can deviate from this idealized size distribution with distinctly defined modes and specific aerosol types are not distributed equally among these four modes due to the specific formation and transformation processes (Section 1.2). For instance, the majority of pure BC particles, usually having diameters of about 20–300 nm, is contained by the Aitken mode, while BC particles with a coating are also present in the accumulation mode and eventually in the coarse mode. Thus, transport and aging of aerosol particles in the atmosphere above the boundary layer can change the size distribution significantly, e.g. due to mixing with other aerosols (e.g. Ramanathan and Carmichael, 2008; Petzold et al., 2011; Weinzierl et al., 2011).

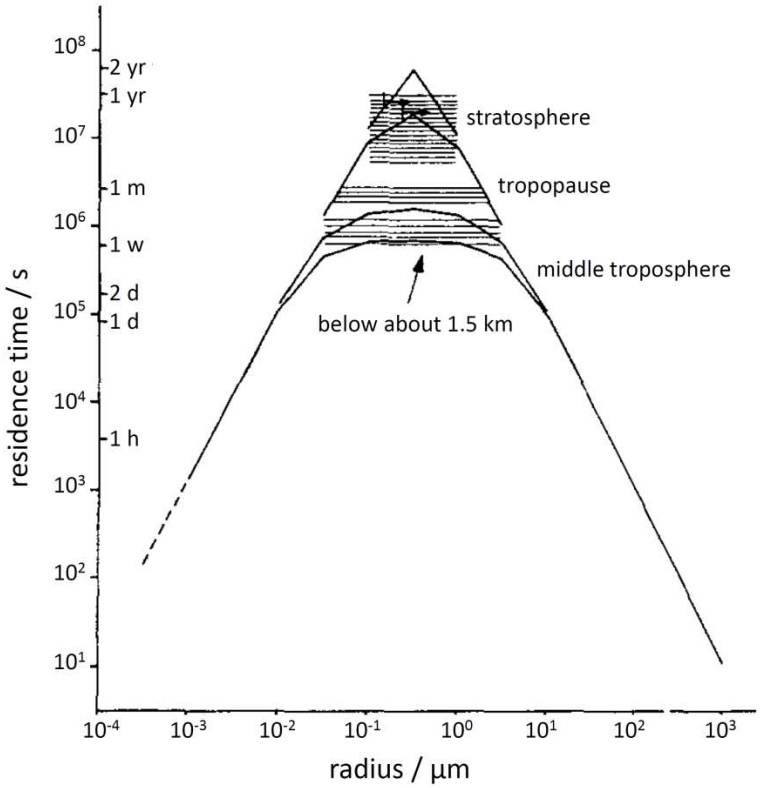

Figure 11. *Aerosol residence times of individual particles for different parts of the atmosphere. Adopted from Jaenicke (1980).*

2.2 Microphysical properties of aerosol particles

Aerosol particles are generally defined by several key properties, namely the total number and mass concentration, the particle size distributions, the particle density (~ 1.0–2.6 g cm^{-3}), the particle shape (spherical, irregularly shaped, agglomerates), the particle phase (liquid, solid), and the chemical composition (e.g. Hinds, 1999; Seinfeld and Pandis, 2006; Petzold and Kärcher, 2012). Below, the characteristics of size distributions and the particle mixing state are described in detail based on standard works like Hinds (1999) or Seinfeld and Pandis (2006).

2.2.1 Aerosol particle size distributions

Depending on the size, aerosol particles have varying effects on radiation (e.g. Horvath, 1993) and cloud processes (e.g. Twomey, 1977). To include information about the particle size, the size resolved particle number concentration $n(D_P)$ defines the particle size distribution by:

$$dN = n(D_P)dD_P, \qquad \textbf{(2.1)}$$

with the total particle number concentration N and the particle diameter D_P. Aerosol particles in the atmosphere cover a wide size range from several nanometers to larger 100 µm (Figure 10) due to the described sources, processes, and sinks (Section 2.1) and are observed in a wide concentration range from less than 10 cm^{-3} to more than 10,000 cm^{-3}. Thus, usually particle size distributions are illustrated on logarithmic scales (e.g. Hinds, 1999; Raes et al., 2000). In addition, the measured size distribution needs to be normalized for the width of the bins ΔD_P, because for optical aerosol particle measurements usually the measured particles are grouped to size bins with the borders of the bins being specific for the different instruments (e.g. Seinfeld and Pandis, 2006). Thus, to ensure comparability of measured size distributions based on different instruments with varying width of the bins, following normalization is done:

$$\frac{dN}{d\log D_P} = n(D_P)\frac{dD_P}{d\log D_P}. \qquad \textbf{(2.2)}$$

Empirically, the single modes j, emerging in an aerosol particle size distribution (Section 2.1), can be approximated as log-normal distributions. Thus, the size distribution can be approximated combining the log-normal fits for each single mode (e.g. Hussein et al., 2005). Using the log-normal fits, the particle number concentration per diameter $n(D_P)$ can be expressed as

$$n(D_P) = \frac{N_j}{\sqrt{2\pi}D_P \log GSD_j}\exp\left(-\frac{(\log D_P - \log CMD_j)^2}{2(\log GSD_j)^2}\right), \qquad \textbf{(2.3)}$$

with the number concentration N, the count median diameter CMD, and the geometric standard deviation GSD for each mode j. The CMD is the median diameter of the particle population in one mode, i.e., it defines the maximum of the specific mode, while the GSD defines the width of the mode, i.e. the spread of particle sizes in the mode. Monodisperse aerosol has a GSD of unity, while the larger the GSD gets, the wider the aerosol mode emerges. For multimodal size distributions, the sum of the single modes j gives the best possible approximation of the real (measured) aerosol particle size distribution.

Aerosol size distributions can be given as number size distribution, as shown, as surface size distribution or as volume size distribution, depending on the scientific objective. Several aerosol characteristics depend on the particle mass distributions with respect to particle size. Thus, besides number size distributions, in this study, mass size distributions are presented, defined as

$$\frac{dM}{d\log D_P} = \frac{1}{6}\pi D_P^3 \rho n(D_P)\frac{dD_P}{d\log D_P} = m(D_P)\frac{dD_P}{d\log D_P} \qquad \textbf{(2.4)}$$

with the particle mass concentration M and the size resolved particle mass concentration $m(D_P)$, assuming a constant particle density ρ. In mass size distributions the mass median diameter (MMD) is used instead of the CMD defining the maximum of the distribution.

2.2.2 Aerosol mixing state

The mixing state of aerosol particles is subdivided into two major idealized mixing states, namely *external mixing* and *internal mixing*. An aerosol population is externally mixed (Figure 12a) if the aerosol population is comprised of different types of aerosol particles, e.g. mineral dust particles mixed with soot particles. In internally mixed particle populations, the individual particles consist of several compounds based on coagulation, condensation and coalescence processes or chemical reactions on particle surfaces (e.g. Weinzierl, 2007). Depending on the solubility of the components, the internal mixing is subdivided into two subgroups: *internally homogeneously mixed particles* (Figure 12b) for soluble components and *internally heterogeneously mixed particles* (Figure 12c) for mixtures containing insoluble components. The particles of the mixing state shown in Figure 12c are also referred to as coated particles.

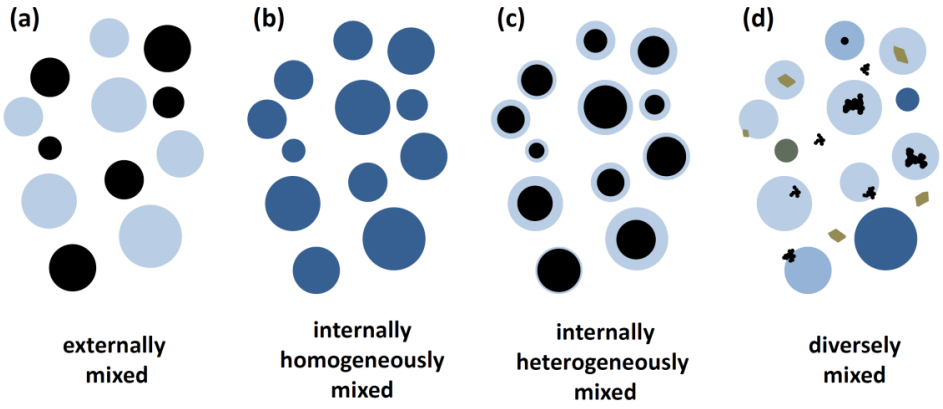

Figure 12. *Mixing states of an aerosol population composed of different chemical components. (a) externally mixed aerosol, (b) internally homogeneously mixed aerosol, (c) internally heterogeneously mixed aerosol, and (d) diversely mixed aerosol containing various different chemical components and a mixture of mixing states and internal structures. The latter depicts schematically the potential diversity of atmospheric aerosol populations. Adopted from Bond and Bergstrom (2006) (black and brown: insoluble components (e.g. BC or dust); blue: soluble components).*

The mixing state of the aerosol particles plays a significant role because the aerosol-radiation-interaction of internally mixed layers and external mixtures can differ (Jacobson, 2001). Non-absorbing coatings on absorbing particles like BC are relevant for the climate due to the enhancement of the absorption of the absorbing core based on the so-called *lensing effect* where the incident light is optically focused on the core. Thus, the heating potential of absorbing aerosol layers on the surrounding air is amplified (e.g. Bauer et al., 2010; Shiraiwa et al., 2010). Coatings can enhance the absorption of BC cores by at least 30% (Schwarz et al., 2008b) and up to 100% for thickly coated particles with a ratio of the particle diameter to the BC core diameter (D_P/D_{BC}) of 2 (Shiraiwa et al., 2010). However, Cappa et al. (2012) report a significant difference in the absorption enhancement by coatings between ambient observations and model results. Thus, the understanding of the absorption enhancement by mixed atmospheric BC is still incomplete and needs further investigations. In general, the fraction of internally mixed aerosol increases with the age of the aerosol population (e.g. Riemer et al., 2004), because condensation and coagulation processes take place during transport. Consequently, the mixing state serves as a qualitative

indicator for the atmospheric age of aerosols since emission. Figure 12a-c shows the aerosol particles schematically as spheres. However, the shape of particles might vary, especially for insoluble components in external mixtures. With increasing residence time, condensation and coagulation can transform aspherical particles into spherical particles, internally homogeneously or heterogeneously mixed. For soluble particles (Figure 12b) or soluble components condensed on insoluble particles (Figure 12c) a spherical shape can be approximately assumed. However, due to the variety of aerosol particles and mixing processes during the residence time in the atmosphere, the mixing state of an aerosol population can rarely be described by one of the ideal mixing states (Figure 12a-c), but is rather a mixture of the different mixing states (Figure 12d). As a result, particle clusters, typical for soot particles, and angular shaped particles, typical for mineral dust, exist beside spherical particles. In addition, the spherical particles exhibit various internal structures like insoluble surface-near cores or even insoluble particles attached to soluble particles consisting of various chemical components. Such semi-external mixtures, such as particles attached to each other or near-surface BC particles (Mishchenko et al., 2004; Liu and Mishchenko, 2007; Lieke et al., 2011), exist in the atmosphere. Nevertheless, most modeling studies assume ideally mixed core-shell particles as a basis for radiative transfer calculations. Thus, the implementation of information on the mixing state might improve future modeling study results. More information on particle mixing is given in e.g. Buseck and Posfai (1999), Posfai et al. (2003), and Posfai et al. (2004).

The structure of mixed particles also can have an influence on the efficiency of the particle to serve as cloud condensation or ice nucleus and is thus relevant for the indirect aerosol effect (Hoose and Möhler, 2012). Besides the effects on the atmosphere, the mixing process can even have an impact on the internal particle structure: clustered soot particles are reported to collapse partially when they are incorporated in soluble materials (e.g. Saathoff et al., 2003; Cross et al., 2010).

In summary, all these mixing processes create a complex system of particle mixing, influencing the microphysical and optical properties and thus the climate in heterogeneous ways, e.g. directly, by changing the optical properties of aerosol particles (e.g. Bauer et al., 2010; Shiraiwa et al., 2010), or indirectly, due to the modification of the efficiency to act as CCN and IN (e.g. Cruz and Pandis, 1998; Möhler et al., 2005; Möhler et al., 2008), or due to effects on the age of aerosol particles (e.g. Slowik et al., 2007a).

2.3 Optical properties of aerosol particles

The diversity of the described aerosol particles interact with the incident radiation in a variety of mechanisms (Figure 13). The mechanisms relevant for this study are the interaction of the particles with the radiation via light scattering, where the wavelength λ of the incoming and outgoing radiation remains the same, and via absorption of the radiation and the related release as thermal radiation. Some species of aerosols like sulfate aerosols mainly scatter light, whereas other species, e.g. particles from combustion processes like BC, partially scatter and partially absorb the incoming radiation energy. Furthermore, the particle mixing state is relevant for the optical properties of aerosol particles (see Section 2.2.2). In the following, the key quantities of the optical properties of aerosol particles are

described and defined following Seinfeld and Pandis (2006) and Bohren and Huffman (1983). In the equations, the dependencies of parameters are only presented the first time mentioned (in brackets in the left term of the specific formula) to improve the clarity and coherence of the equations.

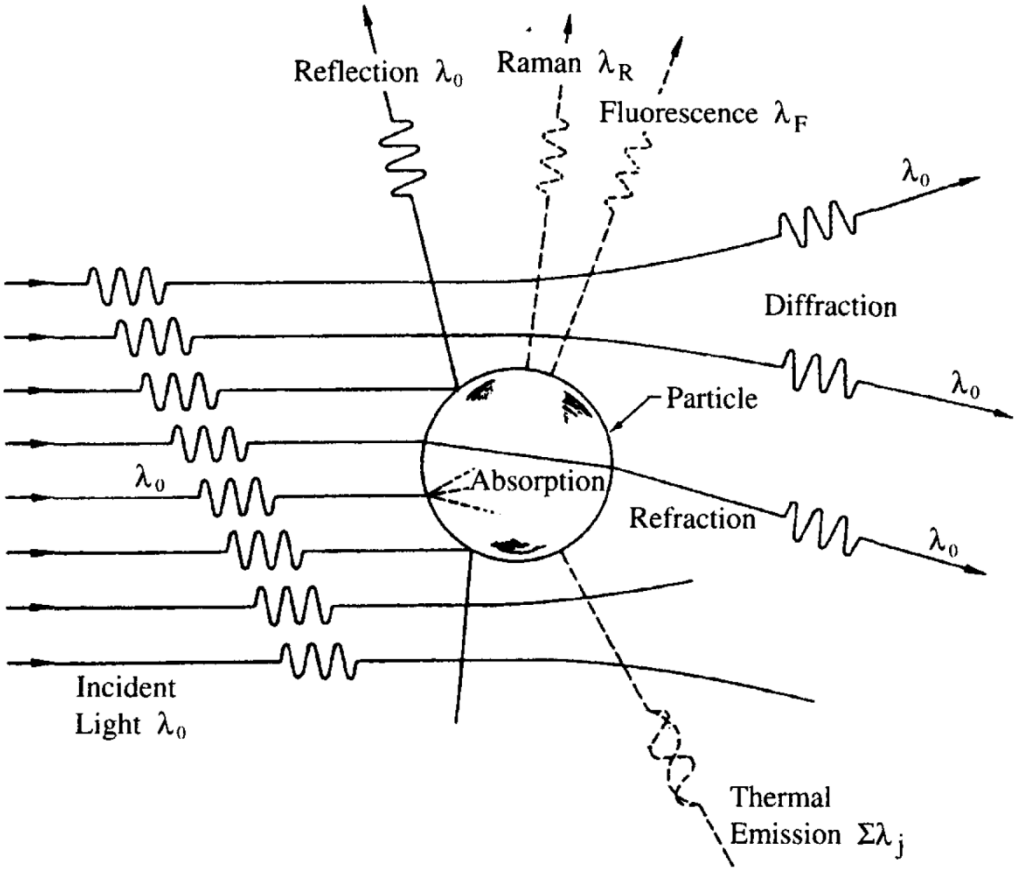

Figure 13. *Interaction mechanisms between an aerosol particle and the incident radiation. Adopted from Seinfeld and Pandis (2006).*

The optical properties of the light scattering and absorbing characteristic of aerosol particles are defined by various parameters such as the particle morphology and the wavelength-dependent normalized complex refractive index *m*

$$m(\lambda) = n + ik = \frac{N_p}{N_m} \approx n_p + ik_p. \qquad \textbf{(2.5)}$$

The complex refractive index is composed of the real part *n* and the imaginary part *k* and is the ratio of the complex refractive index of the particle N_p to the complex refractive index of the surrounding medium N_m. N_m is approximately 1 if the surrounding medium is air (Seinfeld and Pandis, 2006). Thus, the normalized complex refractive index can be approximated as the real part n_p and the imaginary part k_p of N_p. The real part defines the light scattering part, while the imaginary part defines the absorbing part of the refractive index. While every aerosol particle scatters light, only particles with $k > 0$ absorb light. Details on the refractive index of different materials and mixtures can be found in, e.g., Ackerman and Toon (1981), Ouimette and Flagan (1982), and Chýlek et al. (1988).

The ability of a particle to scatter or absorb electromagnetic radiation is quantified by its scattering cross-section C_{sca} and its absorption cross-section C_{abs}. Both are a function of the wavelength of the incident light, the complex refractive index and the particle diameter. These cross-sections have the dimension of an area and represent the fraction of the incident irradiance I_0, also referred to as intensity, which is scattered (W_{sca}) or absorbed (W_{abs}) across the surface A of a sphere:

$$C_{sca}(\lambda, m, D_P) = \frac{W_{sca}}{I_0}, \quad C_{abs}(\lambda, m, D_P) = \frac{W_{abs}}{I_0}, \quad C_{ext}(\lambda, m, D_P) = \frac{W_{ext}}{I_0}, \quad \textbf{(2.6)}$$

where the sum of C_{sca} and C_{abs} is the extinction cross-section C_{ext}:

$$C_{ext} = C_{sca} + C_{abs}. \quad \textbf{(2.7)}$$

Based on the cross-sections, the efficiencies for extinction, scattering and absorption of spherical particles can be derived as the ratio of the respective cross-section to the geometric cross-section of the particle. Thus the dimensionless scattering efficiency Q_{sca}, the absorption efficiency Q_{abs} and the extinction efficiency Q_{ext} are derived:

$$Q_{sca}(\lambda, m, D_P) = \frac{C_{sca}}{C_{geometric}} = \frac{4}{\pi D_P^2} C_{sca}, \quad \textbf{(2.8)}$$

$$Q_{abs}(\lambda, m, D_P) = \frac{C_{abs}}{C_{geometric}} = \frac{4}{\pi D_P^2} C_{abs}, \quad \textbf{(2.9)}$$

$$Q_{ext}(\lambda, m, D_P) = \frac{C_{ext}}{C_{geometric}} = \frac{4}{\pi D_P^2} C_{ext}, \quad Q_{ext} = Q_{sca} + Q_{abs}\,. \quad \textbf{(2.10)}$$

To relate scattered light to absorbed light, the ratio of scattered light to extinction can be derived. This fraction is called single-scattering albedo ω_0 and is wavelength dependent:

$$\omega_0(\lambda, m, D_P) = \frac{C_{sca}}{C_{ext}} = \frac{Q_{sca}}{Q_{ext}} = \frac{Q_{sca}}{Q_{sca} + Q_{abs}}. \quad \textbf{(2.11)}$$

Light scattering of a particle can be divided into three general regimes:

The *Rayleigh scattering regime* is valid when the optical particle diameter is much smaller than the wavelength of the incident light ($D_P \ll \lambda$). For the visible light spectrum, particles smaller than approximately 0.1 µm belong to this regime.

The *geometric scattering regime*, used for particles much larger than the wavelength of the incident light ($D_P \gg \lambda$) such as rain droplets, describes the scattering of particles mainly caused by reflection, refraction and diffraction (e.g. Seinfeld and Pandis, 2006).

The *Mie scattering regime* is valid for particles with sizes comparable to the wavelength ($D_P \approx \lambda$), which is the case for the majority of atmospheric particles irradiated by the solar

radiation spectrum. For this regime, solutions to the Maxwell equations describing electromagnetism exist: the most common solution for spherical particles, which is also used in this study, is the analytical solution of the Maxwell equations for a sphere developed by Gustav Mie (Mie, 1908). This Mie solution, also called Mie theory, allows the exact determination of optical properties such as the light scattering and absorption cross-section for spherical particles. Details on the Mie solution and on the theory of light scattering and absorption of particles are presented in Bohren and Huffman (1983), for example. In this study, optical properties of aerosol particles are derived using the Mie solution codes BHMIE and BHCOAT for spherical internally mixed particles and spherical core-shell particles, respectively, following Bohren and Huffman (1983).

Based on the determination of optical properties of single particles presented so far, for aerosol populations additional aspects have to be considered. For a monodisperse aerosol particle population composed of spherical particles, the extinction coefficient σ_{ext} is a function of the particle diameters D_P, the complex refractive index of the particles m, the wavelength λ of the incident light and the particle number concentration N:

$$\sigma_{ext}(\lambda, m, D_P) = \frac{\pi D_P^2 N}{4} Q_{ext} = N C_{ext} \,. \qquad \textbf{(2.12)}$$

In analogous ways, the absorption coefficient σ_{abs} and the scattering coefficient σ_{sca} are derived using Q_{abs} and Q_{sca} instead of Q_{ext}. The extinction coefficient is the sum of the scattering coefficient and the absorption coefficient:

$$\sigma_{ext} = \sigma_{sca} + \sigma_{abs}. \qquad \textbf{(2.13)}$$

For polydisperse aerosol populations the extinction coefficient is derived by integration over the aerosol size distribution:

$$\sigma_{ext}(\lambda, m, D_P) = \int_{D_P^{min}}^{D_P^{max}} \frac{\pi D_P^2}{4} Q_{ext} \frac{dN}{d \log D_P} d \log D_P. \qquad \textbf{(2.14)}$$

The extinction coefficient can be used to derive the attenuation of light through a medium with a geometrical extent of Δz, using the Lambert-Beer Law

$$I = I_o e^{-\sigma_{ext} \Delta z} \,, \qquad \textbf{(2.15)}$$

where I_0 is the incident intensity and I is the attenuated intensity.

Many of the described parameters are wavelength dependent. Therefore, information on the wavelength dependence is necessary. A parameter parameterizing the wavelength dependence of the light extinction, scattering, or absorption coefficient is the Ångström exponent $å$, representing the relationship by $\sigma \approx \lambda^{-å}$. The Ångström exponent of extinction $å_{ext}$ is:

$$å_{ext}(m, D_P) = -\frac{d \log \sigma_{ext}}{d \log \lambda} \cong -\frac{\log\left(\frac{\sigma_{ext_1}}{\sigma_{ext_2}}\right)}{\log\left(\frac{\lambda_1}{\lambda_2}\right)}. \quad \textbf{(2.16)}$$

In analogy, the Ångström exponent of scattering $å_{sca}$ and of absorption $å_{abs}$ can be derived:

$$å_{sca}(m, D_P) = -\frac{d \log \sigma_{sca}}{d \log \lambda} \cong -\frac{\log\left(\frac{\sigma_{sca_1}}{\sigma_{sca_2}}\right)}{\log\left(\frac{\lambda_1}{\lambda_2}\right)}, \quad \textbf{(2.17)}$$

$$å_{abs}(m, D_P) = -\frac{d \log \sigma_{abs}}{d \log \lambda} \cong -\frac{\log\left(\frac{\sigma_{abs_1}}{\sigma_{abs_2}}\right)}{\log\left(\frac{\lambda_1}{\lambda_2}\right)}. \quad \textbf{(2.18)}$$

Not knowing the chemical composition of the aerosol particle, *å* gives evidence whether the aerosol particles contain predominantly components with strong spectral dependence, like BrC with respect to absorption, or components with insignificant spectral dependence, like BC with respect to absorption.

Another parameter describing BC aerosol is presented in the following: each body with a temperature T larger than absolute zero emits thermal energy. The amount of thermal energy radiated from a body depends largely on the temperature of the body (Seinfeld and Pandis, 2006). A body emitting the maximum intensity of radiation for a certain temperature for every wavelength is called blackbody. The intensity of radiation emitted by a blackbody depends only on the wavelength and absolute temperature. According to Planck's law, the spectral radiance *B(λ,T)* (in W m^{-2} m^{-1}) emitted by a blackbody as a function of wavelength is

$$B(\lambda, T) = \frac{2\pi c^2 h \lambda^{-5}}{e^{ch/k_B \lambda T} - 1}, \quad \textbf{(2.19)}$$

where h is the Planck's constant ($6.626 \cdot 10^{-34}$ J s), c is the speed of light in a vacuum ($2.9979 \cdot 10^{8}$ m s^{-1}) and k_B is the Boltzmann constant ($1.381 \cdot 10^{-23}$ J K^{-1}).

Figure 14 shows Planck curves for different temperatures. The maximum of the curves shifts towards smaller wavelengths and the intensity increases throughout the whole spectral range with increasing temperature. Details are described in, e.g., Bohren and Huffman (1983). The blackbody theory is strongly linked to the measurement principle of the Single Particle Soot Photometer (SP2; Section 3.3.1). A more detailed explanation of the linkage between SP2 and the blackbody theory and assigned characteristics can be found in Section 3.4.3 and Stephens et al. (2003), Schwarz et al. (2006), Moteki and Kondo (2007) and Heimerl (2011), for example.

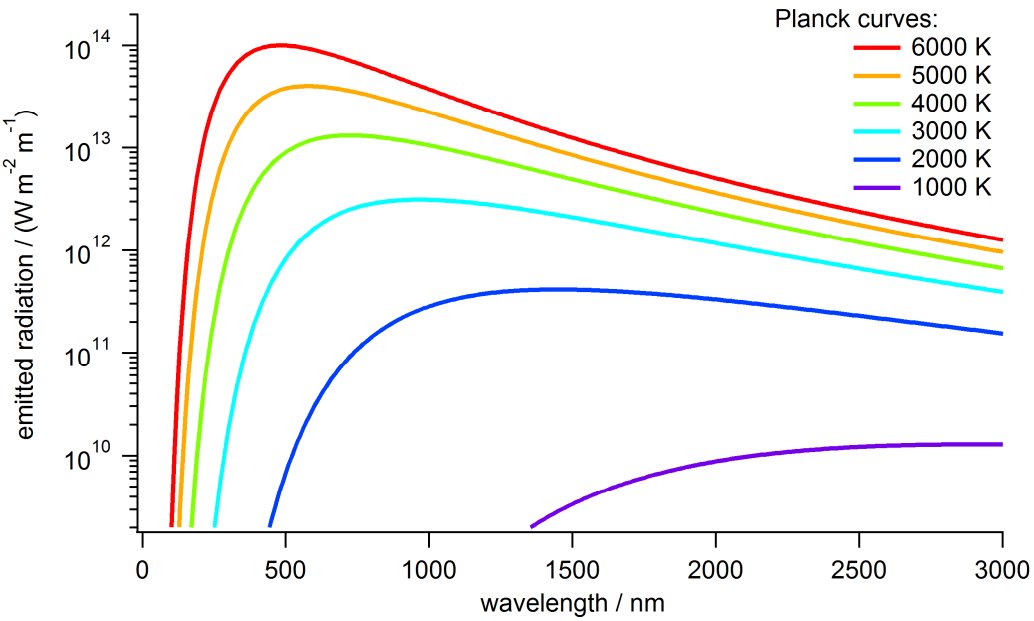

Figure 14. *Planck curves for different blackbody temperatures. The higher the temperature, the smaller the wavelength assigned to the intensity maximum.*

3 Material and methods

This chapter describes the material and methods used in this study. Measurements of microphysical and optical aerosol properties were conducted during several airborne field campaigns and a ground-based inter-comparison campaign (Section 3.1). For the airborne field campaigns the DLR research aircraft Falcon was used as measurement platform (Section 3.2), operating a variety of aerosol instruments with different measurement techniques (Section 3.3). Methods to analyze, process and interpret the data are described in Section 3.4. The quality and accuracy of the data is guaranteed by targeted instrument preparation, accurate calibrations and method validation, creating a valuable data set with a high spatial and temporal resolution, which are described in the particular sections.

3.1 Campaigns

In this study, data collected during several campaigns, summarized in Table 2, is used. In the following, the campaigns are described in detail.

Table 2. *Overview of data sets used in this study.*

Campaign	Time	Short description
AIDA SOOT-11	15 Nov. – 03 Dec. 2010	SP2 inter-comparison at AIDA facility at KIT (Karlsruhe, Germany)
SP2 test flights	06 June – 16 June 2011	3 airborne test flights for the SP2 (Oberpfaffenhofen, Germany)
CONCERT 2011	07 Sept. – 30 Sept. 2011	CONtrail and Cirrus ExpeRimenT 2011 (Oberpfaffenhofen, Germany)
ACCESS	09 July – 27 July 2012	Arctic Climate Change Economy and Society campaign (Andøya, Norway)

3.1.1 AIDA SOOT-11

The SOOT-11 campaign at the AIDA (Aerosol Interaction and Dynamics in the Atmosphere) aerosol chamber at Karlsruhe Institute of Technology (KIT) took place during 3 weeks in November/December 2010. The AIDA facility is a large (volume: 84 m^3) and unique aerosol and cloud simulation chamber used for the investigation of physical, optical and chemical aerosol properties and cloud processes as described in Möhler et al. (2001) and Wagner et al. (2009). Figure 15 shows a schematic view of the AIDA chamber, which can be operated over a wide range of atmospheric conditions, i.e. over a temperature range of 183–333 K and over a pressure range from below 1 mbar to above 1 bar, including ice and water supersaturation.

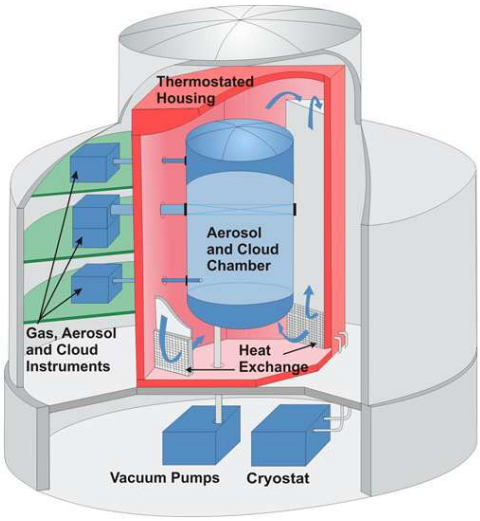

Figure 15. *Schematic view of the AIDA (Aerosol Interaction and Dynamics in the Atmosphere) chamber at KIT (source: http://www.imk-aaf.kit.edu/304.php).*

During the SOOT-11 campaign, the AIDA chamber was set up with an extensive set of instruments. Among other objectives, this campaign focused on the inter-comparison of 6 different Single Particle Soot Photometers (SP2) for different types of aerosols. Groups operating SP2s from Karlsruhe Institute of Technology (KIT), Paul Scherrer Institute (PSI), University of Manchester (UMN), German Aerospace Center (DLR), Max Planck Institute for Chemistry (MPI) and Laboratoire de Glaciologie et Géophysique de l'Environnement (LGGE) participated in the SOOT-11 campaign. More details on this specific campaign can be found in Laborde et al. (2012b). This campaign resulted in the estimations of the uncertainties of the SP2 (Section 3.4.3) and thus provides the basis for the reliability of the presented SP2 results in this study.

3.1.2 SP2 test flights

In June 2011, three test flights were performed with the Falcon. The objective of the flights was to test the SP2 (and other aerosol in-situ instruments) for airborne operation. The test flights on 7, 15, and 16 June 2011 were performed from Oberpfaffenhofen, Germany (EDMO; 48°05' N, 11°16' E, 593 m above sea level (a.s.l.)). During the flights, several issues of the SP2 were tested. On the one hand, mechanical characteristics were surveyed such as the leakproofness of the system, the handling of the instrument onboard the aircraft and the flow and pump system, but, on the other hand, also instrument-related issues such as the influence of internal pressure changes, the stability of the provided sample flow and temperatures, the stability of the laser system and particle recording issues. The instrument was compared to other aerosol instruments delivering size distributions to confirm good counting efficiency (i.e. that 100% of the particles are counted in the SP2 size range) and particle size classification. One consequence of the test flights was the change to manual settings of detection thresholds because the automatic threshold settings resulted in corrupt particle detection (see Section 3.4.3). The results of the test flights were important for the successful operation of the SP2 during the following CONCERT 2011 campaign.

3.1.3 CONCERT 2011

Within the framework of the CONtrail and Cirrus ExpeRimenT (CONCERT) two aircraft field experiments were performed. The major scope of the CONCERT missions in 2008 and 2011 (Voigt et al., 2010) was to measure microphysical and optical properties of contrail cirrus (Voigt et al., 2011; Schumann et al., 2011) and natural cirrus in order to investigate their climate impact (Kübbeler et al., 2011; Schumann et al., 2013; Jeßberger et al., 2013). In addition, volcanic aerosol layers from the stratospheric eruption of the Kasatochi in 2008 (Jurkat et al., 2010; Schmale et al., 2010) and the quiescently degassing Etna in 2011 have been probed.

The majority of data used in this study originate from CONCERT 2011 in September 2011. During CONCERT 2011, the DLR Falcon research aircraft was based in Oberpfaffenhofen, Germany, (EDMO; 48°05' N, 11°16' E, 593 m a.s.l.) and performed 11 research flights between 7 September and 30 September 2011 in Central Europe (Figure 16). Most of the flights were conducted over Germany, with additional landings in Norway and Italy. Instruments from DLR and the Universities of Mainz and Clermont-Ferrand were operated onboard the DLR Falcon. The measured parameters will be listed in Section 3.3.

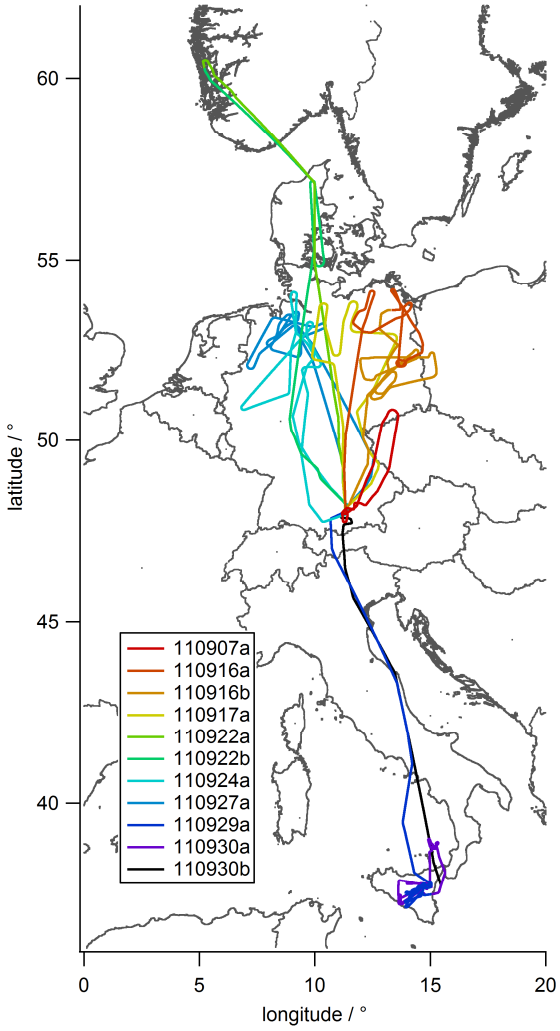

Figure 16. *Research flights during the CONCERT 2011 field experiment in Central Europe. The Falcon was based in Oberpfaffenhofen, Germany, but had further stops at airports in Germany, Italy, and Norway. The flight tracks are color-coded based on the flight ID.*

3.1.4 ACCESS

The ACCESS (Arctic Climate Change Economy and Society) project is a European project focusing on the assessment of the impacts of climatic change on marine transportation (including tourism), fisheries, marine mammals and the extraction of oil and gas in the Arctic Ocean (http://www.access-eu.org/). 27 institutions from 9 European countries and the Russian Federation participate in this project. DLR contributed to this project with airborne in-situ measurements onboard the Falcon in July 2012. The main objective of ACCESS is the experimental investigation of emission sources in the Arctic to estimate the increase of arctic pollution due to climate change. The Falcon was based at the airport of Andenes on Andøya (ENAN; 69°17' N, 16°08' E, 13 m a.s.l.), the northernmost island (489 km^2) in the Vesterålen archipelago in northern Norway. During the campaign, 13 research flights were conducted, measuring emissions and distributions of trace compounds, such as nitrogen oxides, hydrocarbons, sulfuric dioxide, and aerosol particles, including BC aerosol. One part of the measurements addressed the emissions of different vessel types (passenger ships, cargo ships and fishery ships) and the emissions of oil platforms located in the Norwegian Sea, where primarily emitted pollutants and the formation of secondary trace gases and aerosol particles in the exhaust plumes were studied. A second part of the campaign focused on the pollution originating from Russian industrial areas located in the Arctic as well as from Siberian biomass burning source regions. In this thesis, the microphysical properties of aerosol measured in biomass burning layers during the ACCESS campaign serve as evaluation of the characteristics of forest fire aerosol observed during the CONCERT 2011 campaign. Detailed information on aerosol layers observed during the entire ACCESS data set will be published in Rose (2014).

3.2 Research aircraft DLR Falcon

The airborne in-situ measurements of aerosols were conducted onboard the DLR research aircraft Falcon 20-E5 (D-CMET; Figure 17), a twin-engine jet aircraft, which was modified for atmospheric in-situ measurements and remote sensing purposes.

Figure 17. *DLR research aircraft Falcon 20-E5 (D-CMET), hereafter referred to as Falcon. On the top the bent black aerosol inlet and below the wings the red cylindrical containers for the wing-mounted instruments are visible (source: http://www.dlr.de).*

Depending on the flight altitude and weight, the Falcon has a maximum flight duration of roughly 4 h and a maximum range of 2,000–4,000 km. The maximum aircraft speed is up to 250 m s^{-1}. The maximum flight altitude of 12,800 m enables in-situ measurements throughout the whole troposphere and partly the lower stratosphere. Several modifications corroborate the Falcon as a unique measurement platform with scientific instruments inside the cabin as well as outside at four standardized, cylindrical containers under the wings. Besides the containers under the wings, the aerosol inlet, providing the cabin-mounted instruments with sample air, is an essential modification of relevance for this study. For the Falcon, an especially designed isokinetic aerosol inlet (Figure 18), as described in, e.g., Wendisch et al. (2004), is used to ensure aerosol sampling free of interference, i.e. without impact on aerosol particle properties (e.g. Hinds, 1999; Fiebig, 2001).

Isokinetic conditions exist if the flow velocities outside and inside the sampling lines are similar, i.e. if the flow is not modified due to an acceleration or deceleration caused by the aerosol inlet (Addlesee, 1980; Baumgardner et al., 2011). Large changes in the flow from ambient conditions to the sampling line conditions, i.e. anisokinetic conditions, can cause enrichment or depletion of the particle number concentrations and can change their size compared to the ambient conditions (e.g. Belyaev and Levin, 1974; Liu et al., 1989).

Due to high flow velocities outside the aircraft, the sample air needs to be decelerated before sampling. Near-isokinetic conditions are guaranteed by a diffuser cone, which reduces the flow velocity due to an increased flow cross-sectional area. However, minor effects on the aerosol particles caused by the sampling construction cannot be avoided, such as the warming of the air based on the deceleration of the sample flow and based on heat transfer through the walls of the sampling lines from the cabin. The warming reduces the relative humidity, which can affect the aerosol. In addition, the larger inertial aerosol particles cannot follow the streamline of the gas. Depending on the angle of the bending in the tubing, particles larger than several µm may impact on the walls and thus may not be sampled.

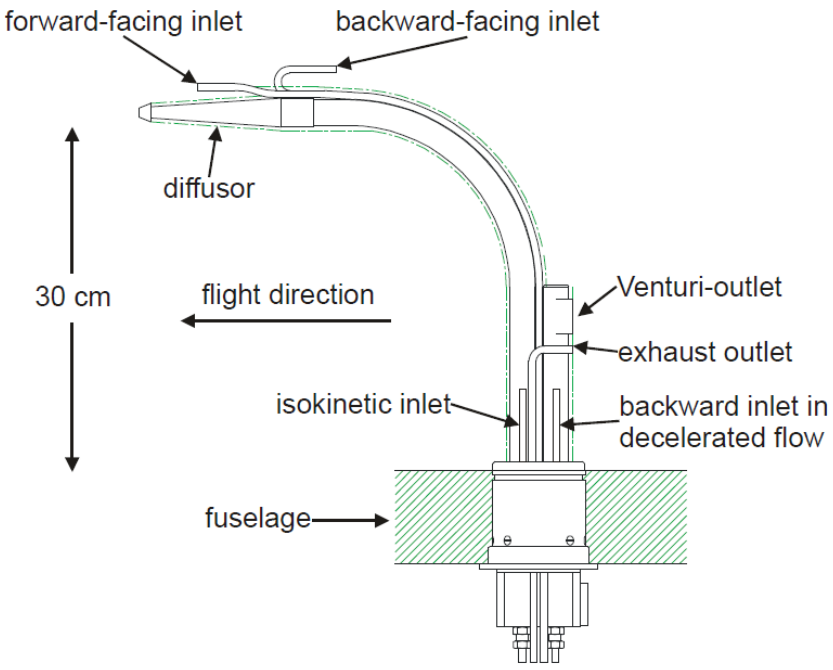

Figure 18. *Isokinetic aerosol inlet used onboard the Falcon. Adopted from Fiebig (2001).*

The aerosol inlet has to sample outside of the aircraft's boundary layer to avoid effects caused by this boundary layer. In the case of the Falcon, the aerosol inlet samples roughly 300 mm above the Falcon's top ceiling, which is provably outside the boundary layer of the aircraft. However, sampling losses in number concentrations ascribed to the aerosol inlet cannot be avoided completely. The sampling efficiency $E(D_P)$ of the isokinetic inlet system as a function of the particle diameter was characterized by Fiebig (2001), Wendisch et al. (2004) and Hamburger (2010). The median upper cutoff diameter $D_{cutoff,50}$, where the sampling efficiency $E(D_{cutoff,50})$ is 0.5, strongly depends on the ambient conditions, i.e. on the outside pressure and air speed. $D_{cutoff,50}$ decreases with altitude from approximately 2.5 µm on the ground to roughly 1.5 µm at flight altitudes above 10 km (Fiebig, 2001). Thus, depending on the flight altitude, the cabin-mounted instruments are unsuitable for the measurement of super-micron particles. Consequently, the wing-mounted instruments, free of interferences caused by the aerosol inlet or the tubing, are essential to characterize and quantify aerosol larger than $D_{cutoff,50}$ and thus to obtain comprehensive information on the entire aerosol particle size spectrum (see Section 3.3).

Generally, for all cabin-mounted instruments it is essential to ensure a leakproof operation to exclude cabin air artifacts and to guarantee a high-quality data set. This is done by installing a particle filter near the isokinetic inlet in the aerosol sample line and by performing a ground-based leak test for pressures down to about 100 mBar. For instruments counting particles as a tracer for ambient air and thus for a leak in the system, the tubing is iteratively checked and improved until no particles are counted.

3.3 Instrumentation

For each field campaign, a special-purpose set of instruments is used onboard the Falcon, depending on the scientific objectives of the particular campaign. Besides the aerosol in-situ measurements, several trace gas instruments and meteorological instruments, for example for temperature, pressure or humidity measurements, were operated during the campaigns discussed in this study (Section 3.1).

Table 3 contains a list of all instruments operated during the airborne field campaigns CONCERT 2011 and ACCESS and the measured parameters. The following detailed description of instruments, however, only includes the aerosol instruments essential for the present study. Figure 19 shows the size ranges of the operated aerosol instruments and a schematically number size distribution. The aerosol number size distribution is largely measured by different Optical Particle Counters (OPC; Section 3.3.3). The size range of the individual instruments depends on the type of the operated particle counter.

For example, for the CONCERT 2011 campaign, the aerosol number size distribution was measured in the size range 0.06–30 µm, while the total number concentrations were measured for particles > 4 nm (with a CPC; Section 3.3.4). In addition, the absorption of the bulk aerosol was measured with a Particle Soot Absorption Photometer (PSAP; Section 3.3.2). During the CONCERT 2011 campaign, for the first time the Single Particle Soot Photometer (SP2; Section 3.3.1) was operated onboard the Falcon for scientific purposes. The operation of this new instrument on the Falcon was one of the main objectives of this thesis. Comprehensive preparations and certifications, which were an essential part of this

study, were realized in advance of the scientific campaigns. The SP2 measures the rBC mass of aerosol particles as well as the size of the particles.

Table 3. *Instrumentation onboard the DLR Falcon during CONCERT 2011 and ACCESS. "x" marks operated instruments, while "---" marks not mounted instruments. Cabin-mounted aerosol in-situ instruments were operated behind an isokinetic inlet (see text for aerosol inlet characteristics). [CPC, Condensation Particle Counter; CPSA, Condensation Particle Size Analyzer; TD, thermal denuder; UHSAS-A, Ultra-High Sensitivity Aerosol Spectrometer Airborne; PCASP, Passive Cavity Aerosol Spectrometer Probe; OPC, Optical Particle Counter (SKY-OPC, Grimm); FSSP, Forward Scattering Spectrometer Probe; PSAP, Particle Soot Absorption Photometer; SP2, Single Particle Soot Photometer. [a]Aerosol in-situ instruments sampling at wing stations; [b]University of Mainz; [c]University of Clermont-Ferrand; [d]for CONCERT 2011.]*

Instrument	Property (+ nominal size ranges)	Campaign	
		CONCERT 2011	ACCESS
Aerosol in-situ instruments			
CPC/CPSA	integral number concentration (0.004 µm < D_P < $D_{cutoff,50}$)	x	x
TD (255°C) + CPC/CPSA	non-volatile integral number concentration (0.004 µm < D_P < $D_{cutoff,50}$)	x	x
UHSAS-A[a]	size distribution (0.06 < D_P < 1 µm)	x	x
PCASP-100X[a]	size distribution (0.1 < D_P < 3 µm)	---	x
OPC	size distribution (0.25 µm < D_P < $D_{cutoff,50}$)	x	x
TD (255°C) + OPC	non-volatile size distribution (0.25 µm < D_P < $D_{cutoff,50}$)	x	x
FSSP-300[a]	size distribution (0.3 < D_P < 20 µm)	x	x
FSSP-300[a,b]	size distribution (0.3 < D_P < 20 µm)	x	---
FSSP-100 [a]	size distribution (1 < D_P < 100 µm)	---	x
FSSP-100[a,b]	size distribution (1 < D_P < 100 µm)	x	---
2D-C[a,c]	size distribution (25 < D_P < 800 µm)	x	---
Polar Nephelometer (PN)[a,c]	extinction coefficient, asymmetry factor, backscatter coefficient	x	---
3λ-PSAP	absorption coefficient (λ = 467, 530, 660 nm)	x	x
SP2	single-particle optical diameter + number size distribution of rBC-free particles (0.14 < D_P < 0.29 µm) single-particle rBC mass (0.5 < m < 78.1 fg)[d] + rBC mass and number size distribution (0.08 < D_{rBC} < 0.44 µm)[d] single-particle optical diameter of rBC-free and rBC-containing particles + number size distribution (~ 0.15 < D_P < ~ 0.55 µm; cutoff dependent on rBC fraction) coating thickness of rBC-containing particles	x	x
Trace gas instruments			
UV absorption	O_3	x	x
VUV fluorescence	CO	---	x
Chemiluminescence (CL) + photolytic converter	NO, NO_2	x	x
Cavity Ring Down Spectrometry (PICARRO)	CO_2, CH_4	x	x
Ion-trap Chemical Ionization Mass Spectrometry (CIMS)	SO_2	---	x
flask samples / GC	Volatile organic compounds (VOCs)	---	x
Atmospheric chemical Ionization Mass Spectrometer (AIMS)	HNO_3, HONO, SO_2, HCl, $ClONO_2$	x	---
Atmospheric chemical Ionization Mass Spectrometer (AIMS)	BrO, H_2O	x	---
WARAN (WAter vapoR ANalyzer) tunable diode laser (TDL) hygrometer (WVSS-II)	H_2O	x	---
Meteorological instruments			
Falcon standard instrumentation	T, ρ, RH, 3D-wind velocity	x	x

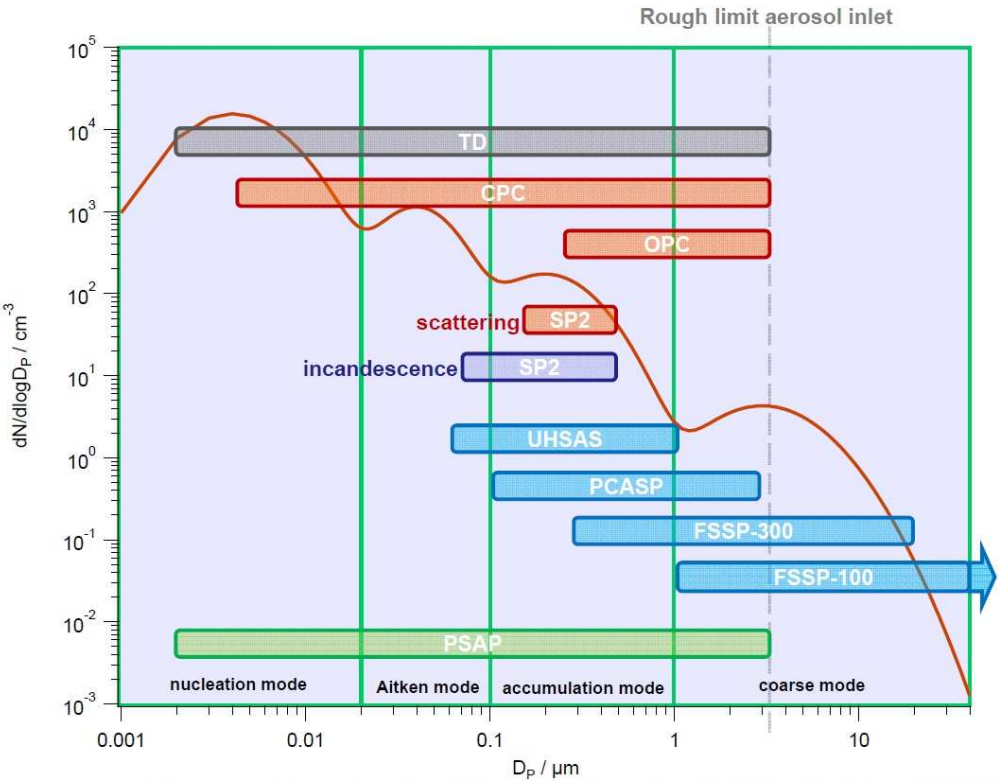

Figure 19. *Schematic view of an arbitrary aerosol size distribution (red line) and the DLR aerosol in-situ instrumentation including their detection size ranges onboard the DLR Falcon as a function of the particle diameter D_P. The dashed grey line represents the approximate cutoff diameter of the aerosol inlet while the green boxes represent the four aerosol particle modes (see Section 2.1).*

A comprehensive description of airborne in-situ instruments to measure aerosol particles, including most of the instruments described in this study, can be found in, e.g., Baumgardner et al. (2011) or Minikin et al. (2012).

3.3.1 Single Particle Soot Photometer (SP2)

SP2 overview

Within the framework of this thesis, the Single Particle Soot Photometer (SP2; Revision C), manufactured by Droplet Measurement Technologies (DMT; Boulder/Colorado, USA), was prepared for airborne in-situ measurements onboard the DLR Falcon for the first time. The advantage of the SP2 is the direct detection of the mass of strongly absorbing rBC particles. The following description of the SP2 contains parts published in Dahlkötter et al. (2014).

In the SP2, a concentric-nozzle jet system is used to direct all particles through a high-intensity continuous-wave intra-cavity Nd:YAG laser beam (λ = 1064 nm). Four different detectors are used to characterize individual particles with 100% detection efficiency within the respective detection limits (see Table 3). The SP2 detects the optical size of individual particles passing through the laser beam by light scattering and the mass of individual rBC particles based on their incandescence (e.g. Schwarz et al., 2010a), independent of particle morphology and mixing state (Cross et al., 2010). The functionality is explained in detail afterwards.

The laser beam has a maximum power of 0.4 W, which is confined to the TEM_{00} mode, i.e. a Gaussian beam shape, with a nominal diameter of roughly 230 µm at a power level of 90% (DMT, 2012). The laser is reflected by a mirror at one end of the cavity and in turn on the highly reflective side of the crystal, which allows the laser to enter the cavity but prevents it from exiting the cavity. A schematic cross-sectional view of the SP2's laser system is given in Appendix 1. The mirrors have to be carefully aligned, so that the laser beam retains the confined Gaussian beam shape. A minor amount of the 1064 nm laser light (< 0.03%) leaks through the output coupler mirror onto a photodiode, the YAG-power monitor (DMT, 2012). The YAG-power monitor detects the leaked laser intensity as a proxy of the laser intensity inside the cavity.

The particle-laden sample air enters the cavity at the top through a concentric-nozzle jet system (Figure 20). The aerosol stream is narrowed by a filtered sheath air flow to a diameter much thinner than the width of the laser beam (Gao et al., 2007). More details and the functional principles of the SP2 have been described in several papers (e.g. Stephens et al., 2003; Baumgardner et al., 2004; Schwarz et al., 2006; Gao et al., 2007; Moteki and Kondo, 2007).

Detailed information on the detectors, signal analysis and interpretation and all parameters derived from the SP2 measurements are described in Section 3.4.3, which contains also the analysis of quality and accuracy of the instrument.

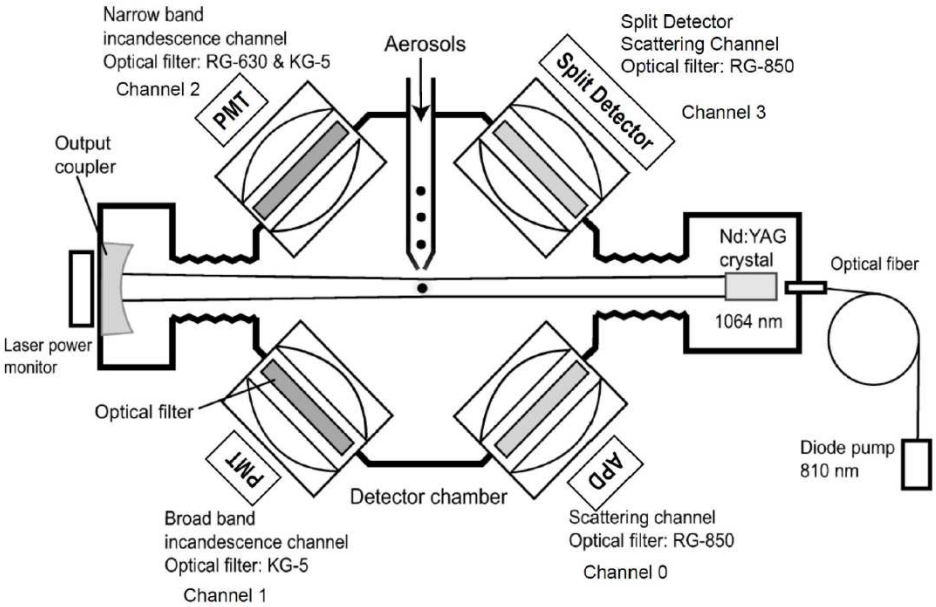

Figure 20. *Schematic diagram of the Single Particle Soot Photometer (SP2) (Heimerl, 2011; adopted from Moteki and Kondo, 2007). The aerosol jet is perpendicular to the plane containing the detectors and the laser beam.*

3.3.2 Particle Soot Absorption Photometer (PSAP)

The absorption of the bulk aerosol is measured with the Particle Soot Absorption Photometer (PSAP). The PSAP is mounted inside the cabin of the Falcon. For the described campaigns, most of the absorption is caused by soot particles, which prevail in the submicron range. Thus, for the data presented in this study, the measured absorption is less

affected by aerosol inlet efficiency effects. The PSAP was used at DLR for many studies (e.g. Fiebig et al., 2002; Petzold et al., 2009; Petzold et al., 2011). The absorption is derived by the differential transmission measurement of light through a filter (Bond et al., 1999; Virkkula et al., 2005). One part of the filter is continuously perfused with filtered air and a second part with particle-laden sample air (Figure 21). The change of the transmission is measured at three different wavelengths (λ = 467, 530, and 660 nm). This version of the PSAP is also known as 3λ-PSAP (Virkkula et al., 2005; Virkkula, 2010). To derive the absorption coefficient σ_{abs} from the measurements, the scattering coefficient σ_{sca} needs to be known to correct for scattering effects on the transmission. σ_{sca} can be estimated theoretically using Mie theory with an assumed refractive index and the measured size distribution. The detection limit of σ_{abs} measured with the PSAP is $0.1 \cdot 10^{-6}\,m^{-1}$ at standard conditions (273.15 K, 1013.25 hPa) (Petzold et al., 2002).

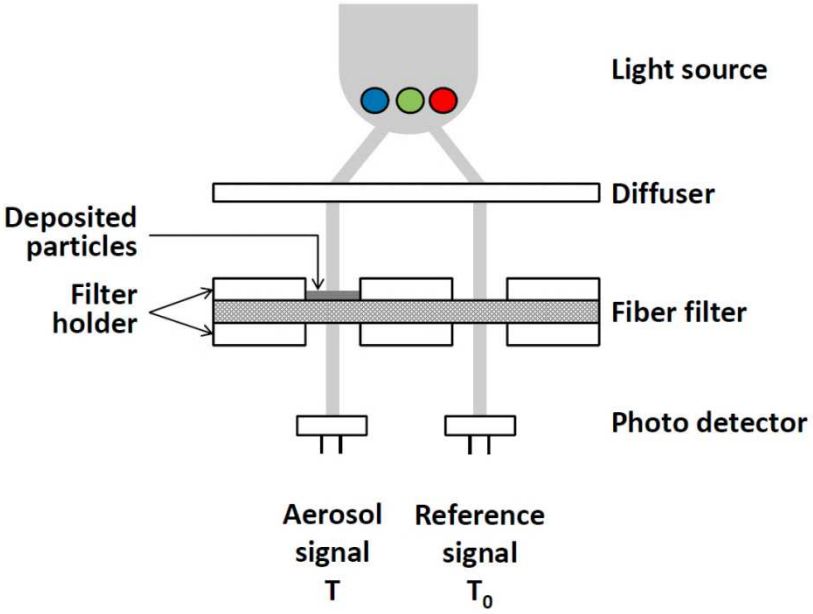

Figure 21. *Schematic of the 3-wavelength Particle Soot Absorption Photometer (3λ-PSAP). Adopted from Bond et al. (1999) and Veira (2011).*

In the following, the calculation of the absorption coefficient σ_{abs} derived from the output signal of the PSAP $\sigma_{abs,PSAP}$ is explained using the following procedures:

The PSAP has to be corrected empirically for changes in the transmission of the filter. The particle loading on the filter increases with increasing time of aerosol exposure of the filter and thus the transmission decreases, which is expressed in the transmission correction function *f(Tr)*. Furthermore, as described before, scattering particles have an impact on the transmission. This is considered with the scattering correction factor *s*. The transmission correction function (Bond et al., 1999) is part of the firmware. Thus, following the procedures suggested by Virkkula et al. (2005) and Virkkula (2010), the absorption coefficient σ_{abs} is calculated as

$$\sigma_{abs} = f(Tr)\sigma_0 - s\,\sigma_{sca} = \sigma_{abs,PSAP} - s\,\sigma_{sca} \qquad \textbf{(3.1)}$$

with σ_0 as unprocessed signal of the instrument, i.e. without internal transmission correction. The correction routine was established at DLR by Hamburger (2010). Based on Equation (3.1) and on the following equation (Virkkula et al., 2005),

$$f(Tr) = \frac{1}{1.0796\,Tr + 0.71} \quad \textbf{(3.2)}$$

with the measured transmission Tr, the unknown parameter σ_0 can be calculated from $\sigma_{abs,PSAP}$. The absorption coefficient is then calculated using the equation

$$\sigma_{abs} = (k_0 + k_1(h_0 + h_1\omega_0)\ln Tr)\sigma_0 - s\,\sigma_{sca} \quad \textbf{(3.3)}$$

with ω_0 being the single-scattering albedo. The constants k_0 (0.377; 0.358; 0.352), k_1 (-0.640; -0.640; -0.674), h_0 (1.16; 1.17; 1.14), h_1 (-0.63; -0.71; -0.72) and s (0.015; 0.017; 0.022) for each wavelength (λ = 467, 530, and 660 nm) are taken from Virkkula (2010). The information on σ_{sca} is derived from the measured size distribution and Mie theory (see Sections 2.2 and 2.3). To obtain ω_0, needed in Equation (3.3) and defined as

$$\omega_0 = \frac{\sigma_{sca}}{\sigma_{sca} + \sigma_{abs}}, \quad \textbf{(3.4)}$$

a first estimate of σ_{abs} is required to allow solving Equation (3.3):

$$\sigma_{abs} = k_0 + k_1 \ln Tr\,\sigma_0 - s\,\sigma_{sca}. \quad \textbf{(3.5)}$$

With this first estimate of σ_{abs} in Equation (3.5), and thus of ω_0 in Equation (3.4), σ_{abs} can be calculated with Equation (3.3). That, in turn, affects Equation (3.4) again. Thus, Equations (3.3) and (3.4) are iterated until σ_{abs} does not change anymore.

To account for deviations between different PSAPs in the flow rate and the spot size, on which aerosol particles are deposited, corrections need to be made (Bond et al., 1999). Due to internal errors of the PSAP flow rate up to 20%, the flow rate needs to be corrected with an externally measured flow rate:

$$f_{flow} = \frac{Q_{PSAP}}{Q_{meas}} \quad \textbf{(3.6)}$$

where Q_{PSAP} and Q_{meas} are the flows measured internally by the PSAP and measured externally with a flowmeter, respectively. The spot size is corrected as follows:

$$f_{spot} = \frac{A_{PSAP}}{A_{meas}} \quad \textbf{(3.7)}$$

where A_{PSAP} and A_{meas} are the spot sizes given by the manufacturer and the remeasured value, respectively.

Previous studies (e.g. Petzold et al., 2002) showed that the PSAP absorption measurements are only reliable at flight sequences with a near-constant altitude due to an impact of pressure changes on the measured PSAP signal during ascent and descent of the aircraft.

These measurement artifacts limit the application of the PSAP data and PSAP inversion (3.4.6). Therefore, the PSAP inversion was applied only for sequences without or with just moderate pressure changes. Furthermore, sequences with absorption coefficients σ_{abs} below the detection limit of the PSAP ($0.1 \cdot 10^{-6}$ m^{-1} at standard conditions) (Petzold et al., 2002) were not considered.

3.3.3 Optical Particle Counter (OPC)

Optical Particle Counters (OPC) provide detailed information on the aerosol number size distribution. An OPC determines the size of a single aerosol particle by measuring the intensity of light scattered by an aerosol particle passing through a laser beam. The measured scattering signal is converted into an electrical signal, which is ranged in an array of channels according to the signal amplitude (Minikin et al., 2012). The intensity of the scattered light depends on the wavelength of the emitted laser beam, on the detection angle of the instrument and on the refractive index of the aerosol particle. A complex refractive index of the bulk aerosol needs to be allocated representatively for the aerosol type to ensure a correct signal-to-diameter assignment for the OPCs. This difficulty is explained in more detail, for instance in Weinzierl et al. (2009). The refractive index is estimated in the framework of this study by use of the PSAP inversion (Section 3.4.6). The shape of the sampled particles is assumed to be spherical, causing a minor uncertainty for this approach (e.g. Fiebig et al., 2002; Minikin et al., 2012). Due to variations in the scattering angles and electronics, OPCs can cover different size ranges. To ensure high quality data, the instruments are calibrated using monodisperse aerosol particles of known refractive index to determine the instruments' channel borders.

Cabin-mounted OPCs are the Grimm SKY-OPCs (model 1.129) with a nominal size range of 0.25–30 µm (Figure 22). However, the upper cutoff is limited by the aerosol inlet system (Section 3.2).

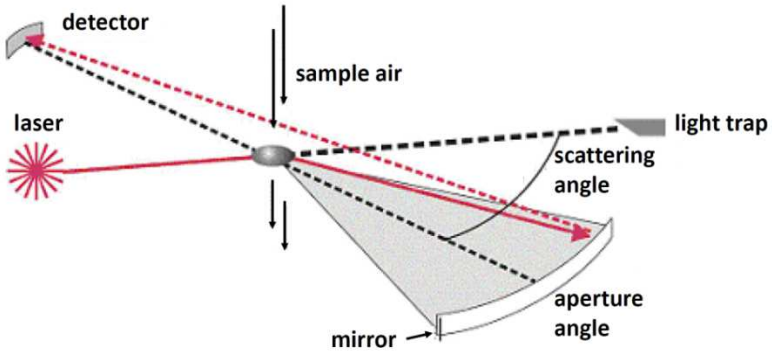

Figure 22. *Scheme of the principle of an Optical Particle Counter (OPC), in particular a Grimm 1.129 SKY-OPC. Other OPCs use different setups of the laser, angles and detectors. Adopted from Grimm (2007).*

Besides the cabin-mounted Grimm SKY-OPC, several wing-mounted OPCs were operated by DLR, including two Forward Scattering Spectrometer Probes (FSSP-100, FSSP-300), an Ultra-High Sensitivity Aerosol Spectrometer Airborne (UHSAS-A), and a Passive Cavity Aerosol Spectrometer Probe (PCASP-100X). The advantage of wing-mounted OPCs is the

independence of the described sampling issues due to aerosol inlet systems (see Section 3.2). The properties of the used OPCs are summarized in Table 4 and the listed wing-mounted OPCs are described below:

Two versions of the FSSP (e.g. Baumgardner et al., 1992; Gayet et al., 2002; Weinzierl et al., 2009) were used. The nominal size range of the FSSP-100 and the FSSP-300 is 1–100 µm and 0.3–20 µm with particles being classified into 15 and 30 size channels, respectively. The PCASP-100X measures aerosol particles in the size range of 0.1–3 µm and classifies them to 30 size channels. The fourth wing-mounted OPC, the UHSAS-A, covers the size spectrum of 0.06–1 µm. The particles are classified into up to 100 size channels. With this variety of the described wing-mounted OPCs, a size range of 0.06–100 µm can be covered. However, due to reasons of space, it is not possible to operate all those instruments simultaneously. Nevertheless, the best possible coverage of the naturally occurring size spectrum is aspired during measurements on the Falcon.

Table 4. *List of OPCs used in this study. $D_{cutoff,50}$: median upper cutoff diameter of aerosol inlet (see Section 3.2).*

OPC	Nominal size range	Number of channels	Location
Grimm SKY-OPC	0.25 µm < D_P < $D_{cutoff,50}$	31	cabin-mounted
UHSAS-A	0.06 < D_P < 1 µm	100	wing-mounted
PCASP-100X	0.1 < D_P < 3 µm	30	wing-mounted
FSSP-300	0.3 < D_P < 20 µm	30	wing-mounted
FSSP-100	1 < D_P < 100 µm	15	wing-mounted

The sizing, calibration and uncertainties of the OPCs used onboard the Falcon is described in detail in Weinzierl (2007) and Fiebig (2001). The OPCs are calibrated by use of aerosol particles of known diameter and refractive index. However, the OPCs cannot distinguish between BC-free and BC-containing particles. Thus, the particles in the considered FSSP-300 size range were assumed to be non-absorbing (zero complex part of the refractive index). This assumption increases the uncertainty of the OPC data compared to the SP2 size distribution, which distinguishes between particles containing BC and BC-free particles. However, due to a low fraction of BC-containing particles in the presented data set (< 25%; median: 9%), only minor effects of the refractive index assumption on the particle size distribution are expected.

The counting efficiency of the UHSAS-A was experimentally derived to be 98% and the error in the determination of particle diameter is derived to be < 4% for particles smaller 700 nm (Schmidt, 2009). The accuracy of the FSSPs, given by the manufacturer, for both versions is ±20% for the particle diameter and ±16% for the number concentration.

3.3.4 Condensation Particle Counter (CPC)

A Condensation Particle Counter (CPC), also referred to as Condensation Nucleus Counter (CNC), measures integral total particle number concentrations on a high temporal resolution (Hinds, 1999). The CPC uses the principle of growth of aerosol particles exposed to supersaturated conditions, necessary for particles, which are too small in their original size to be detected by optical measurements with an OPC, for instance. The sample flow is exposed to a saturated working substance in a heated saturation chamber. The working

substance used for the CPCs in this study was butanol. Due to a cooling of the sample in a condenser, the butanol condenses rapidly onto the particles and lets them grow to much larger sizes, which then can be detected optically (Figure 23). The lower cutoff diameter of the CPCs depends on the level of supersaturation, which is controlled by the temperature difference between saturation chamber and condenser. The lower cutoff diameter can be varied between 4 nm and 20 nm, with the lowest lower cutoff diameter at the highest temperature difference (Stein et al., 2001). An overview of different types of CPCs is given in Kulkarni et al. (2011). Besides CPCs, DLR-developed Condensation Particle Size Analyzers (CPSA) are used. They are based on the same measurement principle as the CPC.

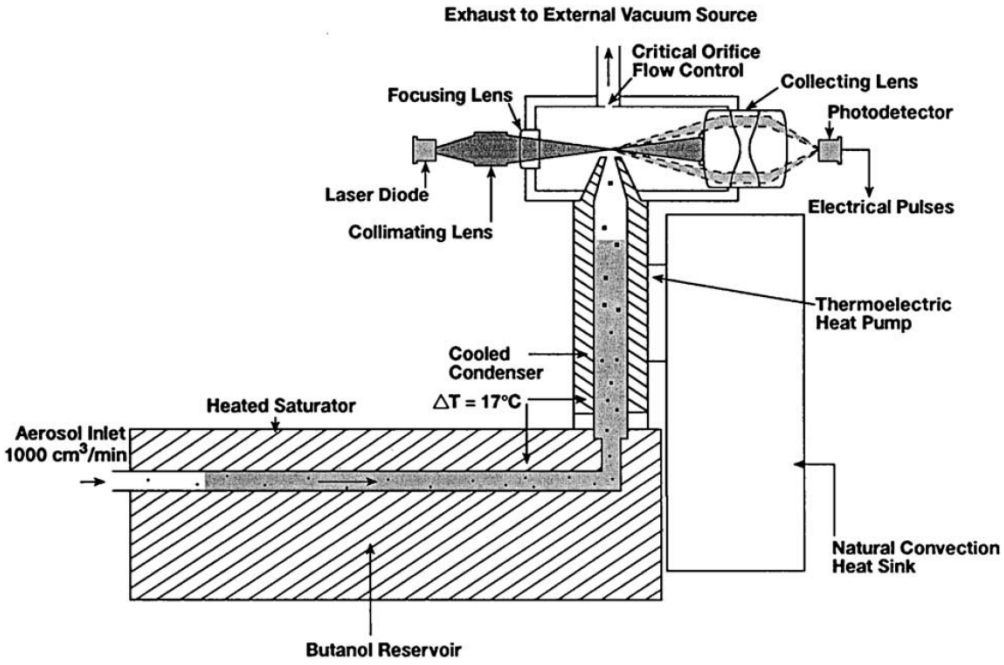

Figure 23. *Schematic view of a Condensation Particle Counter (CPC; TSI CPC 3010). Adopted from Sem (2002).*

Besides delivering total particle number concentrations, a CPC can also be used to gather information on the mixing state of aerosol particles, by heating parts of the sample air to 255°C with a thermal denuder (TD) before entering the CPC (Clarke, 1991; Fierz et al., 2007). Thereby aerosol particles or aerosol particle components, which are volatile at the set temperature or even at lower temperatures, evaporate and only non-volatile particles remain and are measured. This process can change the particle number concentration by removing purely volatile particles, or can shift the particle size distribution by removing volatile compounds from internally mixed aerosol particles and thus cause a shrinking of the individual particles (Figure 24).

To obtain the non-volatile particle fraction, the number concentration of the thermally denuded sample is compared to the number concentration derived by a CPC measuring unheated aerosol. Hereafter, the particle fraction not evaporated during the traverse of the thermal denuder is called *non-volatile*, while the evaporated fraction is called *volatile*.

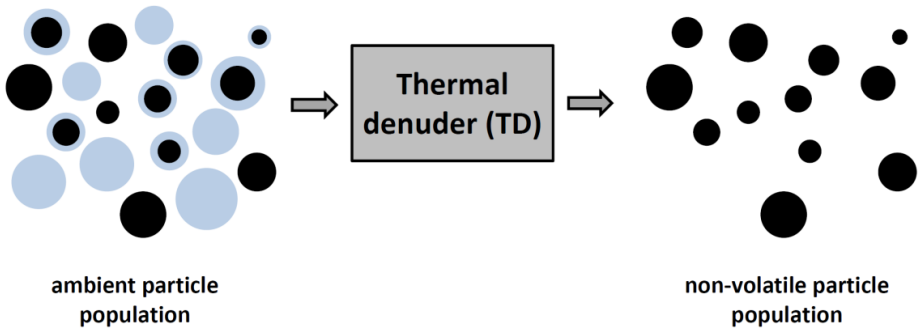

Figure 24. *Schematic of the alteration of an aerosol particle population traversing the thermal denuder (TD). Volatile particle components are light blue, while non-volatile particle components are black. The TD removes all compounds, which are volatile at the set TD temperature.*

According to the approach described in (Weinzierl, 2007), the quality and accuracy of the CPCs were determined. First of all, the flow rate was determined to ensure a correct calculation of particle concentrations. In addition, for every field campaign the CPCs were compared to each other to determine the counting efficiency of every CPC. Due to the different lower cutoffs, a diffusion screen was used, which increases (depending on the number of screens) the lower cutoff of all CPCs to the same diameter (Weinzierl, 2007), guaranteeing that all CPCs measure an aerosol with the same cutoffs. Based on these tests and approaches, the accuracy of the integral particle number concentrations is estimated to be < ±20% for the presented data sets.

3.3.5 Differential Mobility Analyzer (DMA)

A Differential Mobility Analyzer (DMA) enables the selection of specific particle sizes from a polydisperse aerosol sample, relevant for, e.g., the calibration of OPCs using a polydisperse aerosol standard. It is based on the principle of electrostatic classification, i.e. the path of charged particles through an electrical field according to their electric mobility (Figure 25). The electrical mobility is determined by the ratio of the elemental charge of the particle and the particle diameter. The DMA uses a cylindrical column with two coaxial electrodes, with the sample air flowing through the column as laminar flow. The voltage of the two electrodes defines the trajectory of the charged particles, which are bent towards one of the electrodes. Only particles of a particular electric mobility and thus with a certain trajectory reach the narrow exit of the column at a set voltage. All other particles are removed from the sample air by impacting to the walls, i.e. the electrodes of the column. To control the charge of the particles, the sample air is drawn through a neutralizer, a Kr-85 bipolar charger, which ionizes the particles to a known charge equilibrium, resulting in particles with a known charge distribution. More details on the DMA are given, for example, in Minikin et al. (2012) where parts of the description are taken from. In this study, this technique is used to select specific size ranges from polydisperse aerosol samples to calibrate instruments in the laboratory, as it is done, for example, with the polydisperse soot standard fullerene soot for the calibration of the SP2. In this study, a 3071A Electrostatic Classifier (TSI Incorporated; USA) was used.

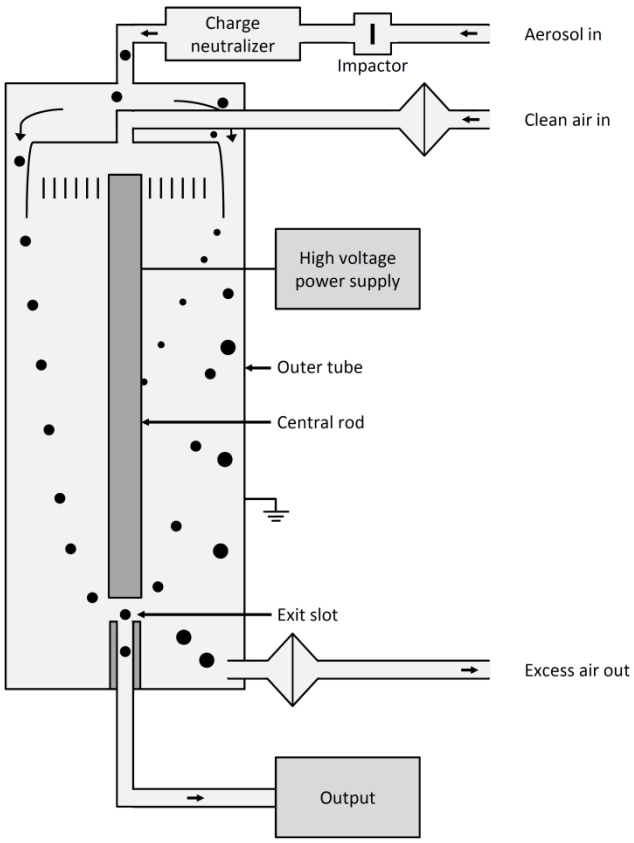

Figure 25. *Schematic of a Differential Mobility Analyzer (DMA). See text for explanation. Adopted from Hinds (1999) and Weinzierl (2007).*

3.4 Data analysis

Several tools to analyze and process the aerosol data are used in this study. In the following, the methods to identify aerosol layers (Section 3.4.1) and to allocate the aerosol layers to sources (Section 3.4.2) are described. Afterwards, the processing of the data collected with the SP2 using the SP2 toolkit (Section 3.4.3) is described. Further analysis of the data include the determination of number size distributions based on the SP2 and OPC data, (Section 3.4.4) and BC number size distribution estimates (Section 3.4.5), while optical properties are calculated using the PSAP inversion (Section 3.4.6).

3.4.1 Aerosol layer identification

In this study, aerosol layers were identified predominantly using airborne in-situ measurements with the Falcon. Furthermore, ground-based lidar measurements from the Leibniz Institute for Tropospheric Research (TROPOS) in Leipzig are used to gather additional information on specific aerosol layers.

To identify the aerosol layers, first the time series of the measured parameters is analyzed for sequences during the flights with enhanced particle number or mass concentrations and absorption coefficients measured with the presented instruments (Section 3.3). However, it is difficult to clearly separate aerosol layers based on the time series because, e.g., lofted layers often are situated on top of the PBL (Mattis et al., 2008). Thus, also the vertical profiles of the measured quantities for the flights are analyzed. An example of the identification of the vertical dimension of the aerosol layers based on vertical profiles is given in Figure 26. The combination of time series and vertical profiles for different aerosol parameters allows a temporal and vertical separation of aerosol layers, indicated by black boxes in Figure 26, even if they blend into each other.

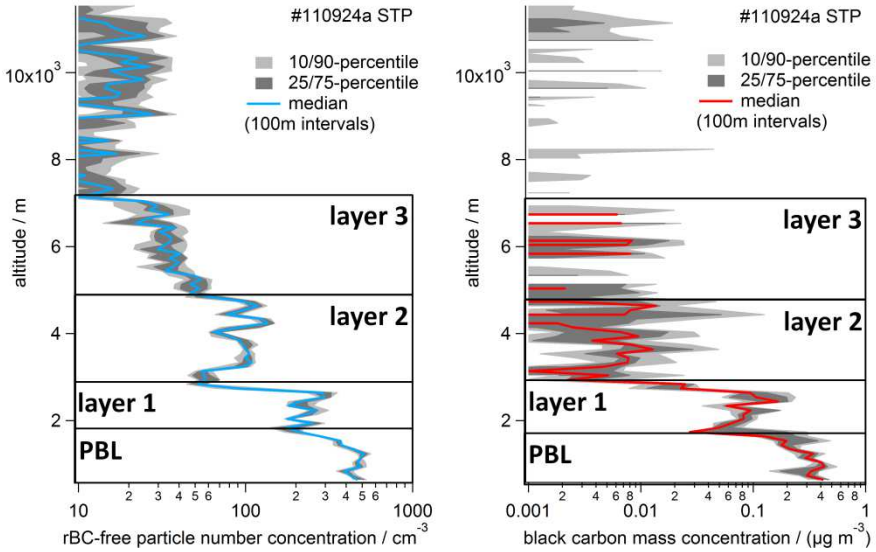

Figure 26. *Ascent of flight #110924a during CONCERT 2011, serving as example for the aerosol layer identification: left for the number concentration of rBC-free particles and right for the rBC mass concentration measured with the SP2. Black boxes show the chosen vertical aerosol layer sequences.*

The following example should clarify this complexity: in the left panel of Figure 26 enhanced number concentrations of rBC-free (≙ purely scattering) particles are observed in altitudes between 0 km and 7 km. Due to minor changes of the values of this quantity, two aerosol layers could be identified, ranging from ground to about 3 km and from 3 km to about 7 km. However, only considering additional data, like the rBC mass concentration, shows that even more aerosol layers are present: in the right panel of Figure 26 enhanced rBC mass concentrations are observed from ground to about 5 km. However, some distinct drops are present (at about 1.8 km and 3.0 km). Thus, combining the shown quantities, four altitude sequences are identified: the lowermost with enhanced rBC-free particle number concentrations and rBC mass concentrations representing the PBL[11], the second (~ 1.8–3.0 km) also with enhanced rBC-free particle number concentrations and rBC mass concentrations, the third (3–5 km) with moderately enhanced rBC-free particle number concentrations and rBC mass concentrations and the fourth (5–7 km) with moderately enhanced rBC-free particle number concentrations but just marginally enhanced rBC mass

[11] In this study, the PBL is mainly used as a comparison for the observed elevated aerosol layers and not considered as aerosol layer itself.

concentrations. Thus, the upper and lower boundaries and the start and end of the measurement sequences of the aerosol layers are determined by significant increases or decreases above defined threshold values of the quantities measured by the variety of instruments. Considering the variety of measured aerosol layer properties, the layers can be separated distinctly and the method results just in minor deviations in the determination of the borders of the aerosol layers.

3.4.2 Trajectory and dispersion calculations

To characterize the defined aerosol layers, trajectory (see bullet 1 in this section) and dispersion calculations (see bullet 2 in this section) are used to gather information on the transportation and the sources of air masses. For these source apportionment and dispersion calculations, HYSPLIT (Hybrid Single-Particle Lagrangian Integrated Trajectory Model; http://www.arl.noaa.gov/HYSPLIT_info.php), a Lagrangian trajectory and dispersion model (Draxler and Hess, 1997; Draxler and Hess, 1998), is used. The HYSPLIT model of the Air Resources Laboratory (ARL), developed by National Oceanic and Atmospheric Administration (NOAA) and Australia's Bureau of Meteorology, allows a variety of computations, from simple air parcel trajectories to complex deposition and dispersion simulations. The purpose of HYSPLIT is the support of a wide range of issues related to the atmospheric transport, dispersion, and deposition of pollutants and hazardous materials. HYSPLIT combines a Lagrangian approach, using a moving reference frame for the calculations of advection and dispersion as the air parcels move from the starting location, and an Eulerian approach, using a fixed three-dimensional grid as a reference frame to calculate the concentration of a pollutant in the air. The model uses external meteorological forecast fields from regional and global models to compute the advection and the stability. Trajectories can be computed forward or backward in time, including the output of meteorological variables along the trajectory. More details on the HYSPLIT model and the setup options can be found in the manual or on the website (http://www.arl.noaa.gov/HYSPLIT_info.php).

1. In this study, trajectories are computed backward in time to determine the path and the source region of the measured air masses, using meteorological data sets and starting from the GPS locations (longitude, latitude, altitude) of the research aircraft Falcon at the time of the observation of an aerosol layer. Additionally, several trajectories are started in the vicinity of the flight path to estimate the reliability of the calculated backward trajectories. To further verify the reliability of the backward trajectories calculated with HYSPLIT, detailed trajectory analysis is conducted using FLYTUL (FLight analYsis Tool Using LAGRANTO), comprising the calculation of air mass trajectories, the combination with meteorological fields and emission data bases (Hamburger, 2010). The consistency between HYSPLIT and FLYTUL increases the reliability of the calculated trajectories.

2. Dispersion calculations are used to calculate qualitatively the distribution of aerosol layers, originating from a known source, e.g. forest fires, as a function of time. Input for the (forward) plume dispersion calculations are the location of the source and the altitude range of the emission. For the HYSPLIT dispersion runs in this thesis following assumptions are made: the dispersion is calculated for 0.5° grid cells for 3 h time steps. To qualitatively include the effects of particle deposition, all particles are assumed to have a diameter of

1 µm, a particle density of 1 g cm^{-3}, and a deposition velocity of 0.1 mm s^{-1}. Wet deposition is not implemented, preconceiving that data on precipitation in the meteorological data set comprises major uncertainties and considering that wet deposition is of minor relevance for this qualitative approach to determine the distribution of aerosol layers. However, for quantitative approaches of the concentration and microphysical properties of aerosols assessed with HYSPLIT (not implemented for this study), wet deposition needs to be considered. The vertical resolution of the dispersion calculation is chosen to suit the specific scientific question. For example, for a pyro-convective forest fire plume (Section 4.3), the dispersion is calculated for five vertical levels ranging from 0–6 km, 6–8 km, 8–10 km, 10–12 km and 12–14 km above ground level (a.g.l.) to cover the entire troposphere with pronounced consideration of the upper troposphere.

For this study, HYSPLIT is initialized with meteorological data from the European Centre for Medium-Range Weather Forecasts (ECMWF) and the Global Forecast System (GFS). Because no relevant differences between the qualitative results for GFS and ECMWF data are observed, for the sake of consistency in this study only the results for the ECMWF data are presented.

3.4.3 SP2 analysis

SP2 detector signals and derived quantities

Four optical detectors, two measuring scattered light and two measuring thermal radiation, are used to detect and describe the aerosol particles passing through the laser. All four detectors lie in a plane with the laser perpendicular to the aerosol jet (Figure 20). The light is focused via a lens system on the detection surface of each detector. For each particle the response curve of each detector is recorded for 44 µs with a temporal resolution of 0.2 µs. The four detectors (Table 5) are described below. To support the following description of the functionality of the SP2 detectors, Figure 27 shows an example of the detector signals for a coated rBC particle passing the laser beam for the time interval 8–44 µs (see x-axis). The following description of the SP2 contains parts published in Dahlkötter et al. (2014).

Table 5. *List of SP2 detectors and measured quantity with size ranges being valid for the CONCERT 2011 field experiment.*

SP2 detector	**measured parameter**
broadband incandescence detector (BID)	mass of rBC core ($0.5 < m < 45.8$ fg) ($0.08 < D_{rBC} < 0.36$ µm at rBC density ρ = 1,800 kg m^{-3})
narrowband incandescence detector (NID)	mass of rBC core ($1.3 < m < 78.1$ fg) ($0.11 < D_{rBC} < 0.44$ µm at rBC density ρ = 1,800 kg m^{-3})
light scattering detector (LSD)	optical size of rBC-free particles ($0.14 < D_P < 0.29$ µm)
position sensitive detector (PSD)	position of the particle in the laser beam

Two photomultiplier tubes (PMT) detect thermal radiation in the visible spectrum emitted by light-absorbing and refractory particles. In Figure 20 labeled as channel 1 and channel 2, they are restricted by optical filters to the light spectrum of 300–800 nm (limited by a Schott KG5 filter) and 630–800 nm (limited by a Schott KG5 and a RG630 filter), respectively. Based on the width of the wavelength spectrum, the detectors are hereafter referred to as broadband incandescence detector (BID) and narrowband incandescence detector (NID). Due to the limited bandwidth of the NID and the resulting reduced incoming radiation, the signal of the NID is hardware-based amplified.

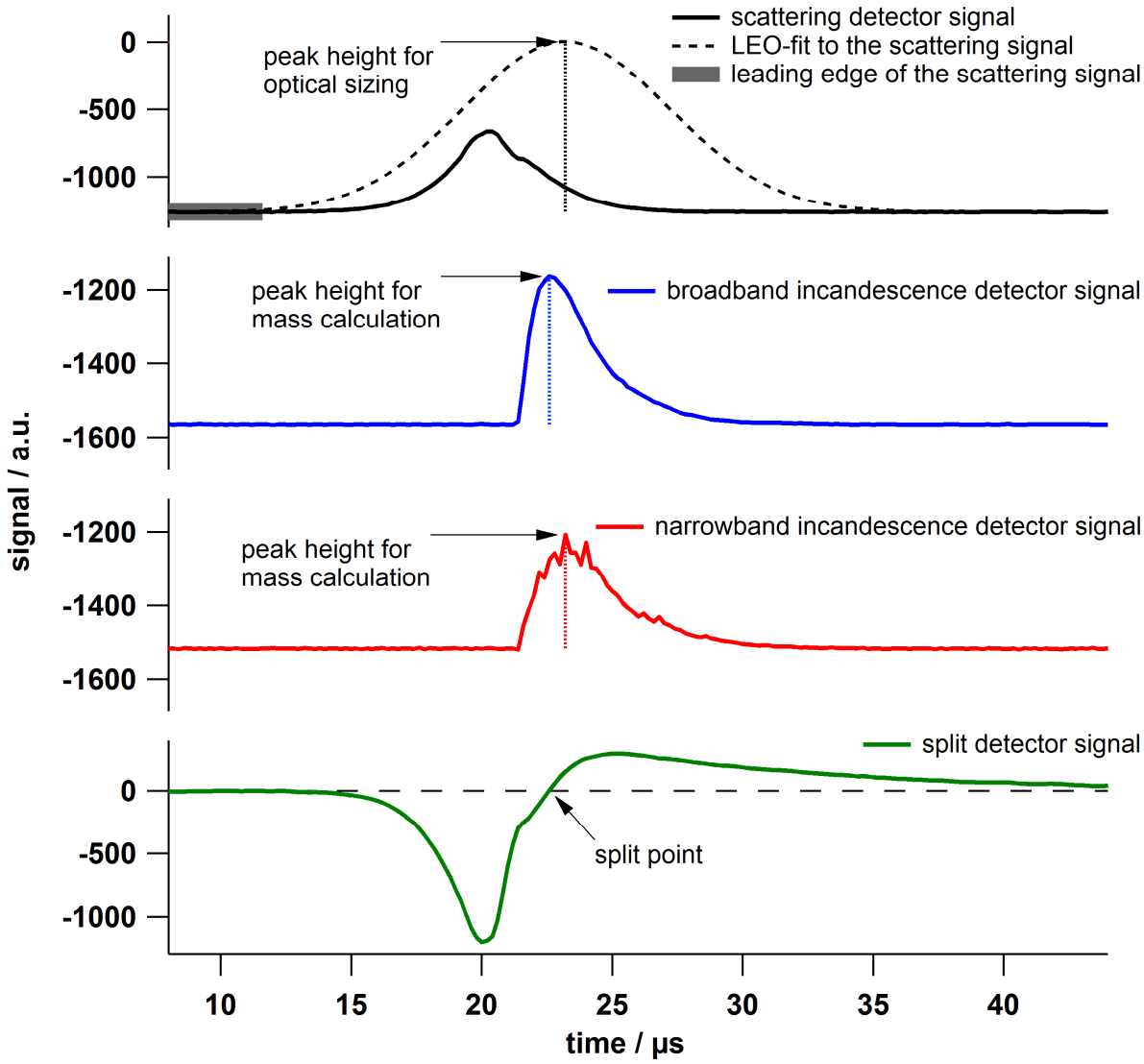

Figure 27. *Response signals of all four detectors of the SP2 for a coated rBC particle traversing the laser beam. The coated rBC particle enters the laser beam, heats up, and evaporates. The signals of the scattering detector (LSD), the broadband and narrowband incandescence detectors (BID, NID) and the split detector (PSD), are illustrated as black, blue, red, and green line, respectively. In the uppermost panel, the Gaussian trace extrapolated using the LEO-fit is added as a dashed black line. Vertical dotted lines (for LSD, BID, NID) represent the signal peak heights used to calculate the optical size D_P and the rBC core mass m_{rBC} of the coated particle. See text for explanations. Adopted from Heimerl (2011).*

An absorbing particle passing through the laser beam absorbs the intense laser light and heats up. Accordingly, the particle emits thermal radiation (red and blue lines; Figure 27). Depending on the particle material, the particle starts to evaporate at its specific boiling point temperature. The peak intensity of the thermal radiation is typically reached at the vaporization temperature of the most refractory particle component, i.e. the component with the highest vaporization temperature. These incandescence signals from atmospheric aerosol particles normally originate from rBC and the peak height is proportional to the rBC mass in the particle, independent of particle morphology or coatings with non-refractory aerosols components (Schwarz et al., 2006; Moteki and Kondo, 2007; Moteki and Kondo, 2010). Due to the subsequent evaporation, the incandescence signal decreases from this stage due to the reduction of the particle size until no signal can be detected. To derive the mass of the rBC particles, the maxima of the signals from both incandescence channels are used. The rBC mass of each rBC-containing particle is calculated by applying the signal-to-mass relationship derived from the rBC mass calibration. The mass equivalent diameter of the rBC particle D_{rBC} is calculated in this study assuming a void-free rBC material with a bulk density ρ = 1,800 kg m^{-3} (Moteki and Kondo, 2010). The applied design of the SP2 during the CONCERT 2011 campaign limits the rBC core measurements to a size range of approximately 80–440 nm (mass: 0.5 < m < 78.1 fg) and during the ACCESS campaign to a size range of approximately 85–500 nm (mass: 0.6 < m < 117.8 fg) to fulfill the specific objectives of the particular campaigns.

A light scattering detector (LSD; channel 0; see Figure 20) detects elastically scattered light (λ = 1064 nm) using an avalanche photodiode (APD) and is used for the optical sizing of the particles. Non-absorbing (rBC-free) particles cross the laser-beam unaltered, i.e. without evaporation of particle material, and the peak amplitude of the LSD signal is proportional to the scattering cross-section of the particle. These rBC-free particles produce a Gaussian shaped signal traversing the Gaussian intensity laser beam. Figure 28 shows a schematic describing the signal-detector-interaction for the scattering detectors.

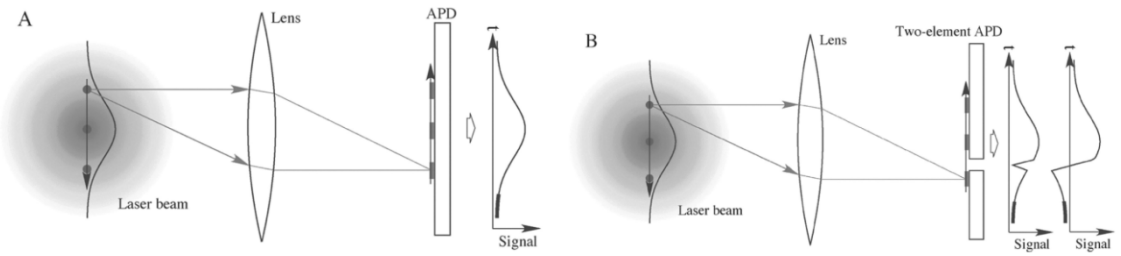

Figure 28. *Schematic view of the detection principle of the SP2 for non-absorbing (rBC-free) particles. An aerosol particle (grey dot) passes through the laser beam with Gaussian intensity. (A) The scattered light is collected onto the avalanche photodiode (APD) of the LSD producing a Gaussian signal following the Gaussian laser profile. (B) The scattered light is collected onto the two-element APD (TEAPD) of the PSD, exhibiting a gap in the signal due to the gap between the two elements of the detector. The signal from the lower part is electronically inverted. Adopted from Gao et al. (2007).*

The peak height of a non-absorbing particle depends only on the particle size and the particle's refractive index if the intensity of the continuous laser is kept constant. Assuming the particle material and thus the refractive index of the non-absorbing aerosol particle, the peak height can be converted directly into the particle size. In this study, the size of non-

absorbing particles is calculated in the SP2 toolkit by comparing the measured signal peak heights of the LSD with a look-up table, which is implemented in the toolkit, containing theoretically derived values (Mie theory) for the assumed refractive index of the measured particle. This relation is shown in Figure 29 for a refractive index of 1.60-0.00i. For this study, the LSD covers a size range of the optical diameter D_P from roughly 140–285 nm for both, the CONCERT 2011 campaign and the ACCESS campaign.

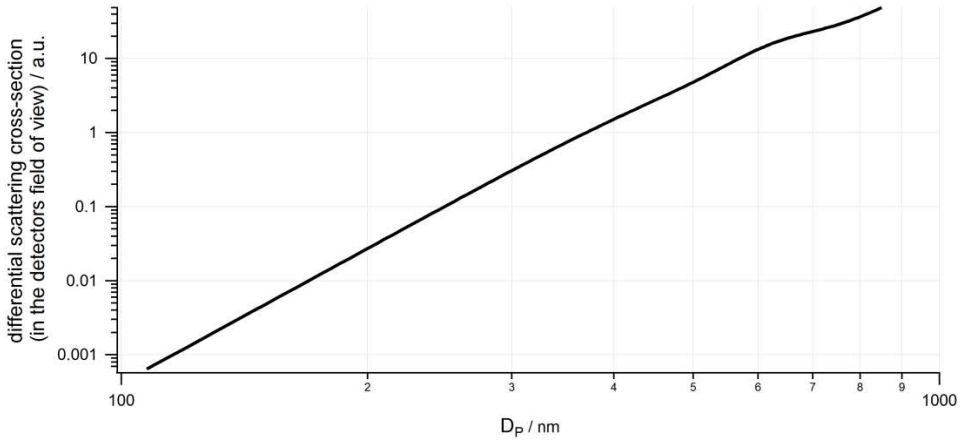

Figure 29. *Relation between optical diameter D_P of the particle and the differential scattering cross-section in the LSD field of view shown here for a refractive index of 1.60-0.00i. The data is taken from the look-up table implemented in the SP2 toolkit.*

Particles containing rBC are absorbing and heat up as they pass the laser beam, resulting in evaporation of the rBC-free coatings and eventually even the rBC core. Therefore, the peak amplitude of the LSD signal does not represent the scattering cross-section of the undisturbed particles (compare black solid and black dashed line; Figure 27). However, Gao et al. (2007) introduced the position sensitive detector (PSD; also called split detector), a two-element APD (TEAPD), which makes it possible to determine the scattering cross-section of rBC-free as well as rBC-containing[12] particles at any time (position) in the laser beam. Therefore, the position of the particle in the laser beam is needed. Based on the structure of this detector, using uses two sensor surfaces (see Figure 28)[13], the PSD signal crosses the zero line at the so-called split point (see green line in Figure 27), defining the particle position in the laser beam by assuming a constant particle velocity during the traverse of the laser beam. The approach for the time-resolved scattering cross-section analysis applied here, described in detail in Laborde et al. (2012a), is largely based on Gao's method (Gao et al., 2007) but uses the actual laser beam profile rather than assuming a perfect Gaussian beam shape. To determine the size of rBC-containing particles, the scattering cross-section of the unperturbed particle is obtained from the LSD signal in the leading edge of the laser beam (up to 3% of maximal laser intensity) before the onset of coating evaporation (grey bar in the upper panel of Figure 27). This is commonly referred to as the leading-edge-only (LEO) fit method (Gao et al., 2007). The LEO-fit extends the upper detection limit for the optical sizing of rBC-free particles to larger diameters, in this case up

[12] The term "rBC-containing" particle is used for referring to the whole combustion particles with some rBC content. A particle is classified as a "rBC-free" particle, if the Single Particle Soot Photometer (SP2) does not detect any rBC in the particle, which does not exclude the presence of a small amount of BC below the lower detection limit of the SP2 (< ~ 0.5 fg rBC in a particle).

[13] For the lower detector surface, the signal is electronically inverted.

to around 550 nm (Table 3). Similar to the standard optical sizing (see above), the optical diameter of rBC-free particles is inferred from the scattering cross-section measured with the LEO-fit approach assuming a homogeneous sphere and a refractive index of 1.60+0.00i. Inferring the optical size of rBC-containing particles[14] from their scattering cross-section is not straight forward as the particles are inhomogeneous and typically not spherical. Here the approach described in Schwarz et al. (2008b) and Laborde et al. (2012b) is used. Briefly, a concentric-spheres core-shell morphology is assumed for the Mie calculations. The core size is constrained by the rBC core mass equivalent diameter, D_{rBC}, from the incandescence measurement. To obtain the total optical diameter, D_P, of the unperturbed particle, including core and shell (before the onset of evaporation), the diameter of the total particle is varied until the calculated scattering cross-section matches the measured scattering cross-section. This is shown in Figure 30 for the refractive indices used in this study in the Mie calculations (2.26-1.26i and 1.60-0.00i for the rBC core and the coating, respectively). The particular value for the refractive index of the BC core was measured by Moteki et al. (2010) for thermally denuded ambient BC particles using an APM (Aerosol Particle Mass Analyzer) and an SP2.

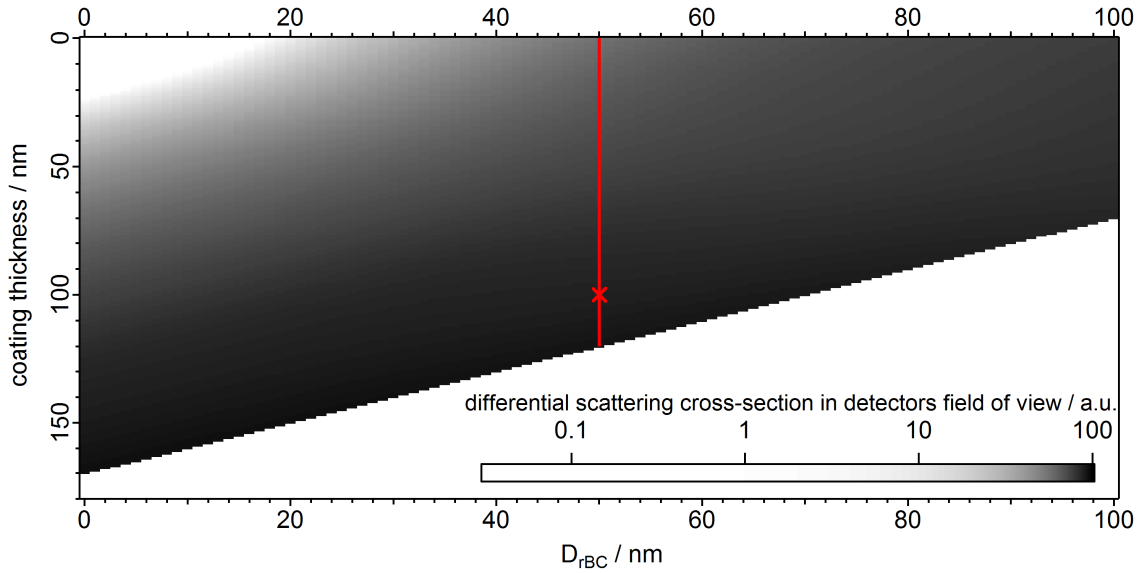

Figure 30. *Relation between rBC core size D_{rBC}* (x-axis), *coating thickness Δ_{coat}* (y-axis), *and the differential scattering cross-section in the LSD field of view (shading) shown for refractive indices of 2.26-1.26i and 1.60-0.00i for the rBC core and the coating, respectively. To determine the total diameter of an rBC-containing particle with known rBC core diameter D_{rBC} (here as example 50 nm), known measured scattering cross-section (here as example at the red cross), and assumed refractive index, the unknown coating thickness is varied (along the red line) until the measured and theoretical scattering cross-sections match. Here, the particle diameter D_P is 250 nm (D_{rBC} + 2*Δ_{coat}). The data is taken from the look-up table implemented in the SP2 toolkit with white color in the lower part of the plot indicating missing data.*

[14] To clarify the effect of the loss of particle material of rBC-containing particles in the laser beam on the scattering cross-section, the LSD signal for the particle without successive evaporation of particle material can be inverted (dashed line in the upper panel of Figure 27) based on the determined scattering cross-section in the leading edge of the laser beam and the information from the PSD, showing significant differences to the measured LSD signal (solid black line; Figure 27).

To obtain this information on the mixing state of individual BC-containing particles the coating thickness Δ_{coat} can be derived using the LEO-fit approach (Section 3.3.1), assuming a concentric-spheres core-shell structure. Here, the coating thickness of coated rBC particles is defined as the difference between the total radius of the particle r_P, derived with the LEO-fit approach, and the radius of the rBC core r_{rBC}:

$$\Delta_{coat} = r_P - r_{rBC} = 0.5(D_P - D_{rBC})\,. \qquad \textbf{(3.8)}$$

Besides the size D_{rBC} and mass m_{rBC} of the rBC core, the size of the entire particle D_P and the related measured size distributions (see Table 3), the SP2 delivers further information on the aerosol particles: for measurements with the mass median diameter (MMD) of the rBC mass size distribution lying within the measured range, the integral total rBC mass concentration can be extrapolated using a log-normal fit applied on the measured rBC mass size distribution. The method is schematically shown in Figure 31.

Additionally, as an indicator for the boiling point temperature of the rBC particle, the color (or band) ratio is derived following

$$color\ ratio = \frac{signal(BID)}{signal(NID)}. \qquad \textbf{(3.9)}$$

The color ratio is the ratio between the maximum signal heights of the two incandescence detectors changing as a function of the boiling point temperature according to the blackbody theory (Section 2.3). That allows separating different incandescing materials according to their varying boiling point temperatures (e.g. Heimerl, 2011). However, the detector settings influence the color ratio, implying a difficulty comparing color ratios when different detector settings or even different SP2 are used.

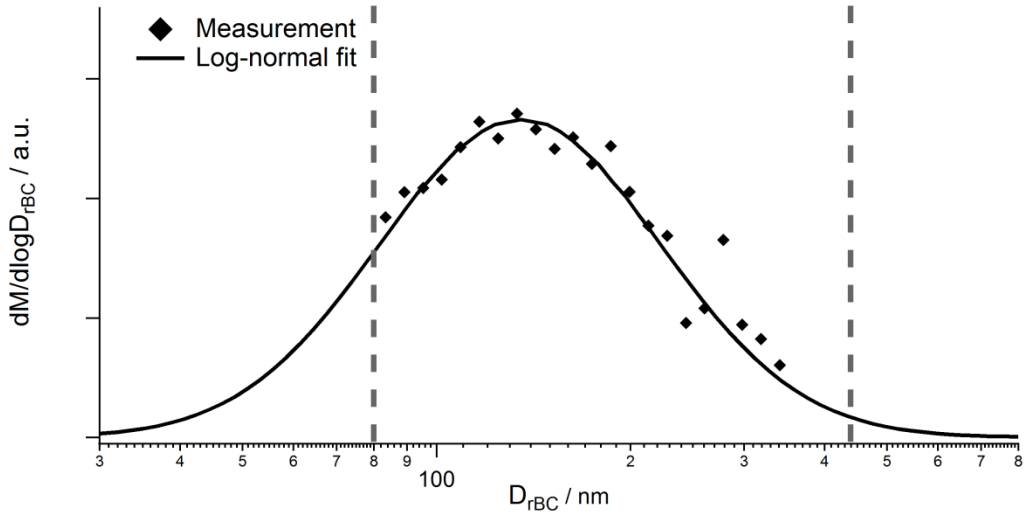

Figure 31. *Scheme of the determination of rBC mass size distributions showing the measurements (diamonds), the measurement size range (between dashed lines), and the applied log-normal fit (black line). Based on the fit, the total rBC mass concentration can be derived. For details see text. Adopted from Dahlkötter et al. (2014).*

Information on particle structures based on the SP2 signals

Corresponding to the described response curves of the respective detectors, a classification of the particle regarding their mixing structure can be achieved, which is relevant because the interaction of BC-containing particles with solar radiation depends on their morphology and mixing state with light-scattering aerosol components (Kahnert et al., 2012). This is described in the following, containing parts published in Dahlkötter et al. (2014).

The BC cores of combustion particles are fractal-like or compact aggregates and the BC can be mixed with light-scattering material in different manners, including, e.g., surface contact of the BC with the light-scattering components, full immersion of the BC in the light-scattering component or immersion of the light-scattering components in the BC aggregate (Scarnato et al., 2013). Previous laboratory and field experiments have shown that the SP2 signals of rBC-containing particles can sometimes give indirect evidence of how the rBC core is mixed with the light-scattering components beyond just quantifying the coating thickness (Sedlacek et al., 2012; Moteki and Kondo, 2007).

Figure 32 schematically shows the particle-laser interaction (left panels) of different particle types and the corresponding SP2 signals (right panels), including the time-resolved scattering cross-section C_{sca} as inferred from the raw LSD signal according to the method described in Laborde et al. (2012a).

For rBC-free particles (Figure 32a) the LSD signal usually follows an almost Gaussian shape. The LSD signal is directly proportional to the laser intensity profile along the flight path of the particle through the laser beam because the size and thus also the scattering cross-section of a non-absorbing particle remains unchanged during laser transition. The maximum of the LSD signal from rBC-free particles occurs at the center of the laser beam (here at time 26 µs; Figure 32a).

In contrast, the size of an rBC-containing particle is reduced during laser transition, first through evaporation of non-refractory coating material followed by evaporation of rBC, which has a higher boiling point. Figure 32b shows typical SP2 signals of an rBC-containing particle with a medium to thick coating. The LSD responds with an increasing signal when the particle enters the laser beam and scatters the laser light with a constant scattering cross-section. Travelling further into the laser beam, the rBC core absorbs the laser radiation and heats up. As a consequence, the coating evaporates and causes a decrease in the scattering cross-section. This often results in a first local maximum of the LSD signal (here at time 21 µs; Figure 32b). After complete evaporation of the coating, the scattering cross-section of the particle stabilizes for a short time and the LSD signal raises again, because the laser intensity still increases (time range 22–23 µs; Figure 32b). The rBC core heats up further until it reaches the boiling point of rBC. The thermal radiation, emitted by the particle and detected by the incandescence detectors, now reaches its maximum (here at time 24 µs; Figure 32b), and the rBC core evaporates, resulting in a fast decrease of the rBC mass and thus also the scattering cross-section of the residual particle, which is reflected in a fast decrease of the BID and LSD signals, respectively. Consequently, the LSD signal can have a second local maximum around the peak of the BID signal (here at time 23 µs; Figure 32b). This second local maximum is typically higher than the first local maximum of the LSD signal for rBC particles with a thin or medium coating, such that the global maximum of the LSD signal occurs about at the same time as the peak of the BID signal. For thickly coated rBC particles, the first local maximum of the LSD signal is typically higher than the second

local maximum, such that the global maximum occurs before the peak of the BID signal. Moteki and Kondo (2007) have shown that the time lag between the peaks of the LSD and the BID signals (BID peak position minus LSD peak position) gives a crude information about the mixing state of rBC-containing particles, where values > ~ 2 µs are associated with thick coatings, while values < ~ 2 µs are associated with thin to medium coatings.

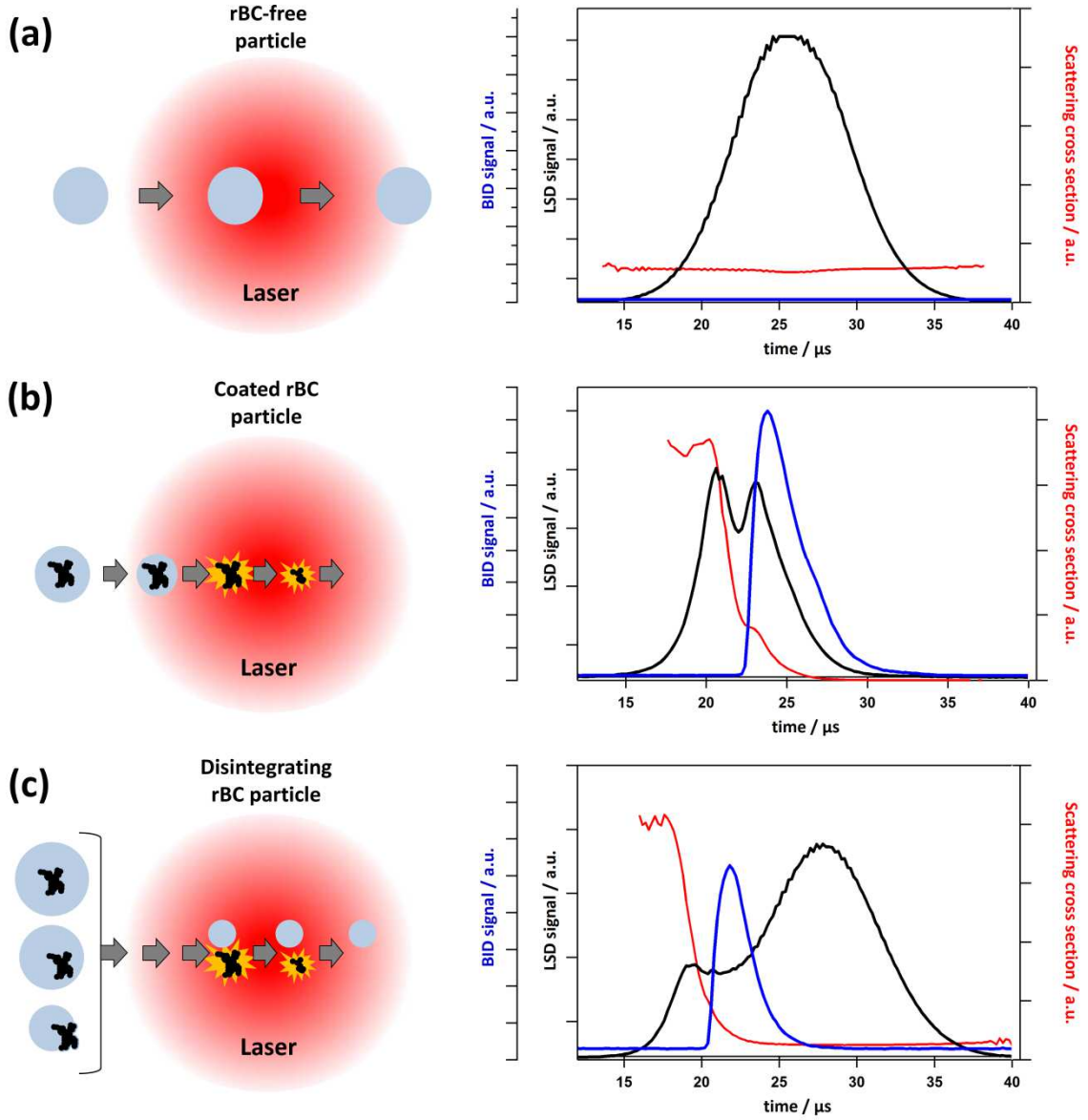

Figure 32. *SP2 raw signals for selective particles showing the light scattering detector (LSD) signal (black), the broadband incandescence detector (BID) signal (blue) and the scattering cross-section C_{sca} (red) for an rBC-free particle (a), a coated rBC particle (b), and a disintegrating rBC particle (c). Schematics for particle-laser-interaction for each raw signal plot are shown on the left. For the disintegrating rBC particle in (c) several initial structures are possible: a very thickly coated rBC particle (up); a thickly coated particle with an eccentrically located rBC core (middle); a rBC particle located at the surface of a rBC-free particle (bottom). For reasons of depiction, the size of the schematically shown particles (left) is enlarged compared to the laser diameter. The scattering cross-section was obtained by dividing the scattering signal by the laser intensity profile. The incandescence is indicated by the yellow star. Adopted from Dahlkötter et al. (2014).*

However, in the literature also particles that disintegrate in the laser beam of the SP2 have been reported (Moteki and Kondo, 2007; Sedlacek et al., 2012). Disintegration occurs before the rBC core reaches its boiling point and results in an rBC-free fragment, which remains stable after disintegration, and an rBC fragment that eventually evaporates. Figure 32c shows the SP2 signals of such a disintegrating rBC-containing particle. Disintegration can be identified by the fact that the LSD signal does not fully disappear after evaporation of the rBC core, i.e. that the scattering cross-section stabilizes again after the peak of the BID signal, as the rBC-free fragment does not evaporate any further (here at time > 24 μs; Figure 32c). Furthermore, this stabilization is a key feature that distinguishes disintegrating particles from coincidence of an rBC-containing and an rBC-free particle. The rBC-free fragment from a disintegrated particle, which behaves as an rBC-free particle after its separation, causes another local maximum of the LSD signal at the center of the laser beam (here at time 28 μs; Figure 32c). This local maximum of the LSD signal from the rBC-free fragment can be the global maximum, if the rBC-free fragment is a substantial portion of the original particle. In this case the time lag between the peaks of the LSD and the BID signals (BID peak position minus LSD peak position) becomes negative as the peak of the BID signal normally occurs before the center of the laser beam.

Sedlacek et al. (2012) have reported the identification of disintegrating particles through negative lagtimes for the first time. However, as it will be shown in Section 4.3.5, in this study only a minor fraction of all disintegrating particles could be identified via a negative lagtime, because most of the disintegrating particles either exhibited a positive lagtime or because the peak of the LSD signal and therefore also the lagtime were not defined due to LSD detector saturation. Therefore, the time-dependent (position-dependent) scattering cross-section, as inferred from the raw LSD signal, according to the method described in Laborde et al. (2012a), was used here to identify disintegrating particles. Specifically, the scattering cross-section measured with the LSD in the trailing-edge of the laser beam (at the position with 3% of the maximum laser power) was used to determine for all rBC-containing particles whether a detectable rBC-free fragment, producing an LSD signal above background noise, remained left in the trailing-edge of the laser beam. The scattering cross-section measured in the leading-edge of the laser beam (at the position with 3% of the maximum laser power) was used to determine the size of the undisturbed particles, in order to further investigate the influence of particle size on disintegration.

SP2 toolkit

The SP2 data presented in this study were predominantly analyzed with the SP2 toolkit, a software package developed and maintained by Gysel and Laborde (2012). This package is based on IGOR, a commercial and scientific graphing and data analysis program, and contains subroutines for loading the saved raw data, the input and analysis of calibration data, the main data analysis and advanced analysis methods (Gysel and Laborde, 2012).

To derive the relevant quantities from the raw data recorded with the SP2, several analysis steps are required. After loading the raw data, the detected signal traces of the four detectors are analyzed regarding the peak heights and peak positions. In the following, the particle by particle data are post-processed, i.e. the output variables are derived by applying the particular calibration data and routines. This contains, for example, the determination of rBC mass and number concentrations, rBC mass and number size distributions and total

particle number size distribution in the specific size ranges, as well as advanced calculations, e.g. calculation of time series of specific quantities or the application of the LEO-fit, as described before.

SP2 airborne preparation

In order to operate the SP2 onboard an aircraft like the Falcon, the instrument had to be prepared and certified for airborne measurements. The certification of the SP2 as part of a Falcon standard rack (Appendix 2) was realized in collaboration with Enviscope (Enviscope GmbH; Germany), Gomolzig (Gomolzig Flugzeug- und Maschinenbau GmbH; Germany) and IABG (Industrieanlagen-Betriebsgesellschaft mbH; Germany). At IAGB, the SP2 rack was tested with regard to its Electromagnetic Compatibility (EMC) to ensure an interference-proof operation onboard an aircraft avoiding impacts on the internal Falcon system. Furthermore, the instrument had to be certified regarding fire retardancy, stability, the relation of the height of the center of gravity to the total weight, the direction of mounting inside the aircraft, materials of the mountings (e.g. the breaking stress of screws), electrical safety and flow system.

SP2 accuracy and quality of the data

In this study, the SP2 was used for the first time for airborne measurements at DLR. Thus, a special focus was laid on the preparation and characterization of the SP2 beforehand and during the airborne measurements to guarantee qualitative and reproducible results. The following description contains parts published in Dahlkötter et al. (2014).

The reliability of the SP2 has been studied extensively by inter-comparisons of six different SP2s at the AIDA chamber in November 2011. Laborde et al. (2012b) report a reproducibility of 10% for rBC mass and 17% for coating thicknesses for this inter-comparison study. However, due to calibration uncertainties the absolute uncertainty may be higher. Kondo et al. (2011b) compared BC mass concentrations measured with the SP2 and a filter-based absorption photometer continuous soot monitoring system (COSMOS) and found that the methods agree to within about 10% on average. Besides, Laborde et al. (2013) made a comparison of the rBC measurements by the SP2 with a collocated thermal-optical EC measurement using a Sunset ECOC analyzer, revealing agreement well within the uncertainty of either method. For this study an uncertainty of 15% for the rBC mass is assumed, which includes the described reproducibility, calibration uncertainties and uncertainties due to airborne in-situ measurements.

Table 6 summarizes the repeatability of the SP2 derived by Laborde et al. (2012b) for the inter-comparison study at the AIDA chamber (SOOT-11; see Section 3.1.1) where, among others, the DLR SP2 participated as part of this study. To ensure uncertainties not larger than the presented values, the SP2 needs to be aligned and calibrated carefully. An overview of adjustments and calibrations recommended to ensure a good data quality is given by Laborde et al. (2012b). These recommendations, summarized in Table 7 and described in detail below, were effectuated carefully in the preparation of the SP2 for the particular airborne measurements to ensure the quality of the derived data.

Table 6. *Summary of the SP2 repeatability obtained during the SOOT-11 campaign. "Repeatability" refers to the range between minimum and maximum values observed by 6 SP2 instruments for a certain quantity, Adopted from Laborde et al. (2012b).*

Parameter description	Repeatability (% of the average)	Applicable range
Number size distribution	±5%	rBC core mass ≥ 1 fg (D_{rBC} ≈ 100 nm)
Mass size distribution	±10%	rBC core mass ≥ 1 fg (D_{rBC} ≈ 100 nm)
Optical number size distribution for rBC-free particles	±15%	D_P ≥ 140 nm
Coating thickness	±17%	150 nm ≤ D_{rBC} ≤ 400 nm

Table 7. *Recommended SP2 adjustments and implications following Laborde et al. (2012b). The procedures are described in detail in the text and indicated by the included numbering.*

Procedure	Implication
(1) Laser alignment	Generation of a Gaussian laser profile
(2) Mode aperture alignment	Spatial limitation of the Gaussian laser profile
(3) Detector block horizontal alignment	Alignment of the laser-to-aerosol jet assembly
(4) Scattering detector alignment	Focusing of the LSD
(5) Two-element APD detector alignment	Focusing of the PSD
(6) Laser power adjustment	Optimization of the laser power
(7) Flow measurement	Validation of flow system
(8) Calibration	Calibration of detector signals regarding particle property

(1) Laser alignment: The laser has to be aligned to a TEM_{00} mode, i.e. a Gaussian laser profile, following the manufacturer's procedure (DMT, 2009). This guarantees sufficient laser power in well characterized conditions. Furthermore, higher-order TEM modes will have multiple minor laser beams, which may not only not trigger the incandescence of rBC particles, but will also limit the measurement and interpretation of scattering signals (DMT, 2009). Figure 33 shows a well aligned laser beam of the DLR SP2, recorded during the preparation for the airborne operation, and a misaligned laser shape adopted from DMT (2009).

(2) Mode aperture alignment: To prevent interactions of the mode aperture with the laser beam, resulting in reduced laser intensity, the mode aperture (see Appendix 1) needs to be aligned properly (see also DMT, 2009).

(3) Detector block horizontal alignment: In the following, the correct alignment of the aerosol jet and the laser beam needs to be ensured. Therefore, the aerosol jet (integrated in the detector block) is moved horizontally with respect to the laser beam (Figure 34). The optimal position, i.e. when the aerosol jet traverses the laser intensity maximum, is determined by sampling non-absorbing particles. In this study standard polystyrene Latex (PSL; refractive index = 1.59) spheres (Duke Standards, Thermo Scientific, USA) are used. The maximum response signal for the monodisperse PSL particles measured with the LSD

indicates the optimal alignment of the aerosol jet and the laser beam (DMT, 2009), in this study at position 182. For detector block positions where the aerosol jet does not cross the laser intensity maximum, even a decrease of the counting efficiency is possible due to increased lower detection limits (Figure 34).

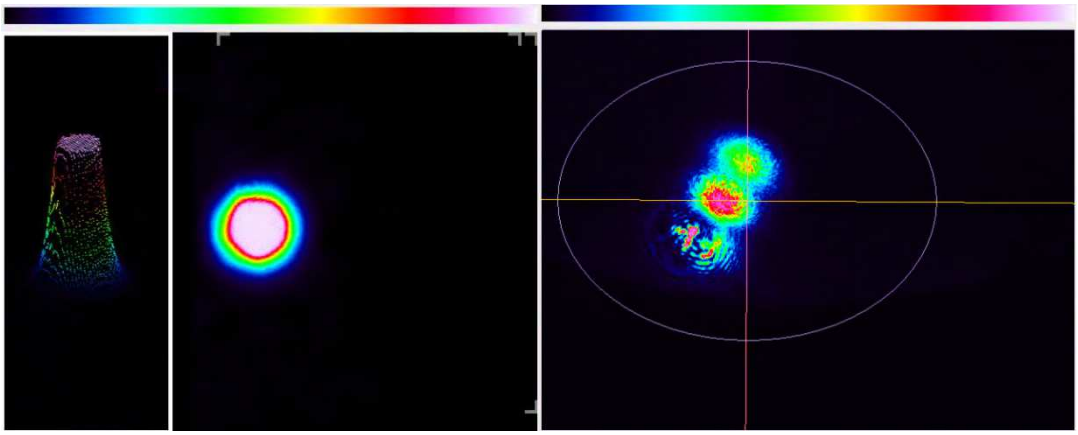

Figure 33. *Laser beam shapes recorded for the DLR instrument after alignment (TEM_{00}; left) and misaligned laser (higher order TEM mode; right) with color-coded laser intensity. The right plot is adopted from DMT (2009).*

(4) Scattering detector alignment: After the alignment of the detector block and the aerosol jet, the LSD needs to be aligned. By changing the position of the detector with respect to the detector block, i.e. the point of particle-laser-interaction, the focal point is determined. At this point, the LSD signal should exhibit high and stable amplitudes with minimal noise.

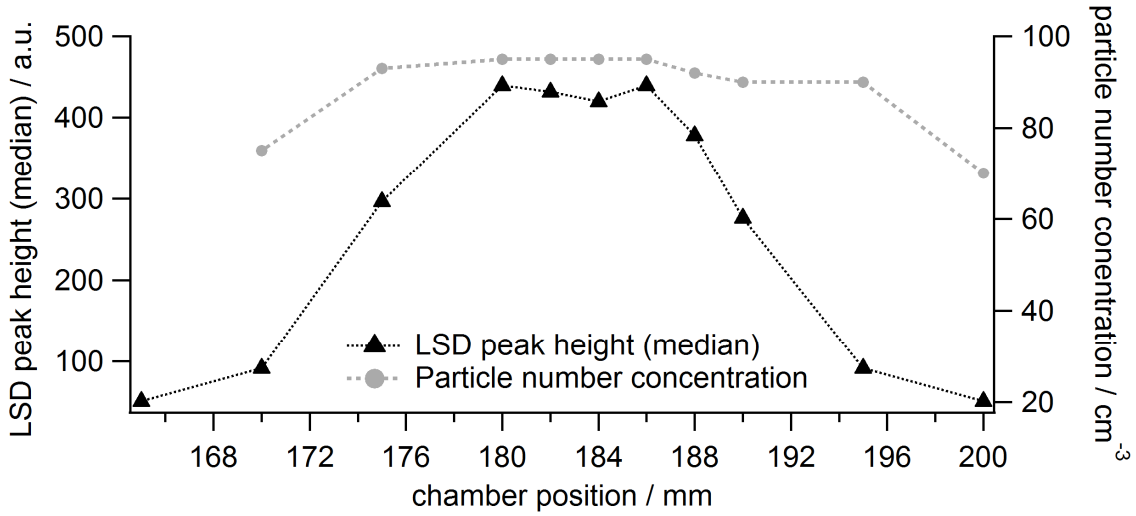

Figure 34. *Results of horizontal alignment of the detector block on 8 August 2011. The peak height (median) of the LSD (black triangles) indicates if the aerosol jet crosses the laser beam maximum (here for chamber positions 180–186 nm). If the aerosol jet crosses regions of lower laser intensity, also the counting efficiency decreases (grey dots).*

(5) Two-element APD detector alignment: According to the LSD, the PSD needs to be aligned for sufficiently high signal amplitudes. Furthermore, the purpose of the PSD alignment is to ensure the application of the LEO-fit for small rBC particles, which is achieved by moving the split point to a sufficiently early point with respect to the laser intensity maximum (Laborde et al., 2012b). The PSD alignment is done with non-absorbing particle standards (PSL) to

adjust the signal amplitude and with absorbing particle standards, in this case fullerene soot, to determine whether the split point can be derived for small pure rBC particles evaporating fast in the laser beam, which is shown in Figure 35. There, even for an 85 nm rBC particle the split point is defined by an increase of the PSD signal sufficiently above the noise (green line in Figure 35 at 16–19 µs). A well-aligned PSD response signal is also seen in Figure 27 with a split point position before the maximum laser intensity. If the split point is set to a non-recommended position, e.g. after the maximum of the laser intensity, the particles might already have evaporated before reaching the split position, resulting in an undefined split position caused by a not increasing PSD signal at the split point. In such case D_P of rBC-containing particles cannot be determined.

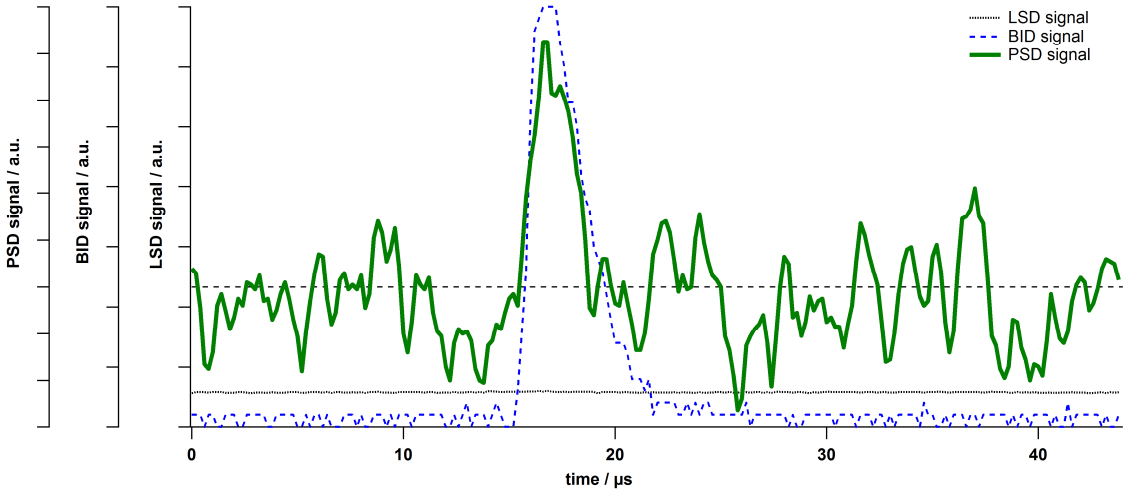

Figure 35. *Example of an (uncoated) 85 nm rBC particle detected by the SP2. Even for very small pure rBC particles the signal of a well aligned PSD (green line) increases sufficiently above the noise after reaching the split point (here at 16 µs on the x-axis), ensuring the application of the LEO-fit.*

(6) Laser power adjustment: The laser power can be adjusted by varying the power of the pump laser. This ensures the independence of the color ratio from the laser intensity (Schwarz et al., 2010a). Additionally, the laser power can be maximized to a certain extent to achieve sufficiently low rBC detection limits (Laborde et al., 2012b). This is also shown and explained in, e.g., Heimerl (2011). However, larger insufficiencies have to be adjusted by adjustment steps (1)–(3).

(7) Flow measurement: To ensure a correct flow measured by the SP2's internal flow measurement devices and thus the correct calculation of number and mass concentrations, the flow should be checked using an external flow meter.

(8) Calibration: The LSD has to be calibrated using a non-absorbing particle standard. The common material is certified PSL, commercially available for different particle diameters, e.g. 150 nm, 220 nm, 269 nm, to calibrate the scattering cross-section measurement of the LSD as described in Laborde et al. (2012b). An aqueous suspension mixed from the PSL standard and distilled water is nebulized using a commercial aerosol generator (Aerosol Generator Portable AG-100; Droplet Measurement Technologies). The monodisperse PSL particles can directly be sampled by the SP2. The incandescence detectors (BID and NID) should be calibrated using fullerene soot (Alfa Aesar, USA) or Aquadag (Aquadag®, Aqueous Deflocculated Acheson Graphite; Acheson Inc., USA) (Baumgardner et al., 2012) to derive

the sensitivity of the SP2's incandescence detectors to rBC mass. In this study, the two incandescence detectors are empirically calibrated using the fullerene soot (stock #40971, lot #FS12S011), which has been shown to provide equal incandescence detector response per mass as atmospheric rBC (Moteki and Kondo, 2010; Laborde et al., 2012a), and which is recommended as the most suitable SP2 calibration material for atmospheric rBC applications (e.g. Gysel et al., 2012 and references therein). For the AIDA SOOT-11 campaign (Section 3.1.1), besides fullerene soot, additionally Aquadag was used. These two particle standards are polydisperse. Thus, after nebulization, for calibration purposes they have to be size-segregated using a Differential Mobility Analyzer (DMA) as described in Section 3.3.4. The effective density and stability of fullerene soot and Aquadag samples was previously investigated and characterized by Gysel et al. (2011). Thus, the rBC particle mass is linked to the mass equivalent diameter D_{rBC}[15].

Figure 36 shows the results of a fullerene soot calibration performed on 12 October 2011. The fullerene soot particles of known size are related to the measured incandescence peak height, here shown for the BID. Because the DMA processing of the aerosol results in particles, which are singly, doubly and triply charged, the plot shows data separated for the charge of the particles. Based on the data points, a fit is deduced, giving the relation between the incandescence peak height and the mass of the rBC particle. The low variability of the data points represents the reliability and stability of the calibration approach. Besides the shown calibration curve, numerous calibrations are performed, especially before and after field campaigns to check the stability of the calibration as an indicator for the stability of the laser alignment, the laser power, the detector alignment, etc. (Figure 37). These sophisticated repetitions of the calibration are necessary to ensure that, e.g., unwanted shocks during the mounting to the aircraft or during the operation onboard, for example at touchdown of the aircraft, do not change mechanically the alignment steps (1)–(5) (Table 7) and thus the relation between the detector signal and particle mass.

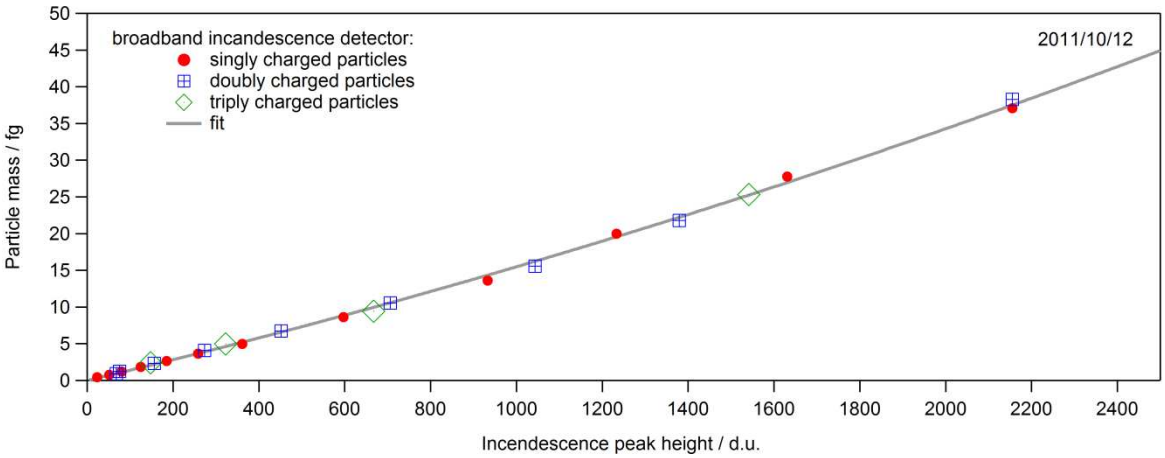

Figure 36. *Calibration curve for the fullerene soot calibration of the broadband incandescence detector (BID) on 12 October 2011.*

In addition to the recommended SP2 adjustments (Table 7), the following adjustments and tests were done and pitfalls investigated in the framework of this thesis:

[15] For fractal-like particles with very small primary particles, the detection efficiency of the SP2 is linked to the size of the primary particles, which is the case for e.g. PALAS soot (Gysel et al. 2012).

(a) Low pressure tests are conducted in the laboratory to simulate and characterize the instrument's behavior at airborne measurement conditions, ensuring the applicability of the SP2 onboard the Falcon in advance.

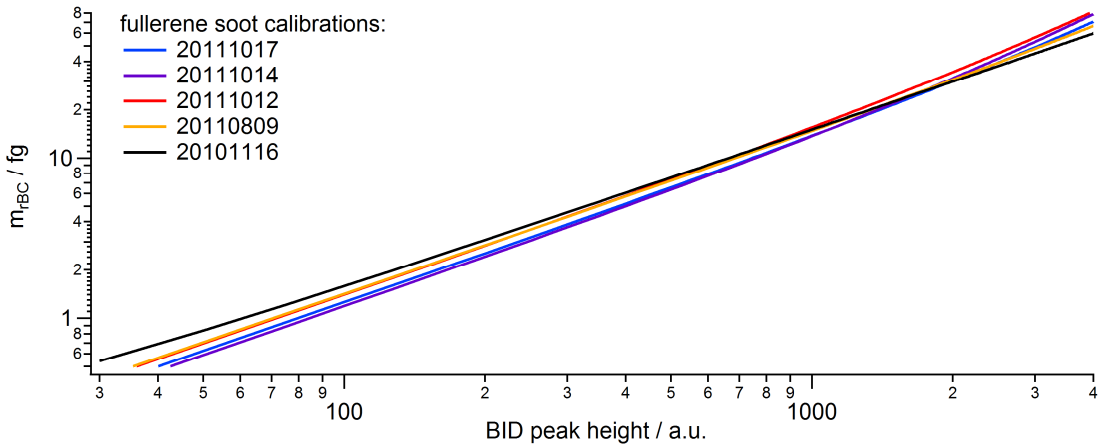

Figure 37. *Fullerene soot calibration curves for the BID from 2010 and 2011 showing the stability of the calibrations. The figure includes calibrations for the BID signal height to the mass of the rBC particle m_{rBC} before and after the field campaign CONCERT 2011.*

(b) In addition, to derive the size- and mass-resolved counting statistics of the SP2, a CPC (Section 3.3.4) was operated parallel to the SP2 as a reference instrument during laboratory studies and calibrations. Two counting statistics, derived during laboratory studies before and after the CONCERT 2011 field campaign using fullerene soot and a DMA, are presented in Figure 38. Obviously, the counting efficiency is around unity for particles > 100 nm. For particles < 100 nm the counting efficiency decreases due to the lower detection limit depending on the SP2 setup for the particular field campaigns. The variations around unity arise from the fact that the SP2 and the CPC are operated in parallel and thus sample aerosol of the same origin but not the same aerosol particles. Based on the counting efficiency tests for the field campaigns (not only the ones shown here), an uncertainty in the SP2 counting of < 10% is estimated for the size ranges given in Table 5 for the CONCERT 2011 field experiment. Additionally, the comparison of the derived number size distributions of the SP2 and various OPCs can be used to confirm the counting efficiency. This method is described in Section 3.4.4.

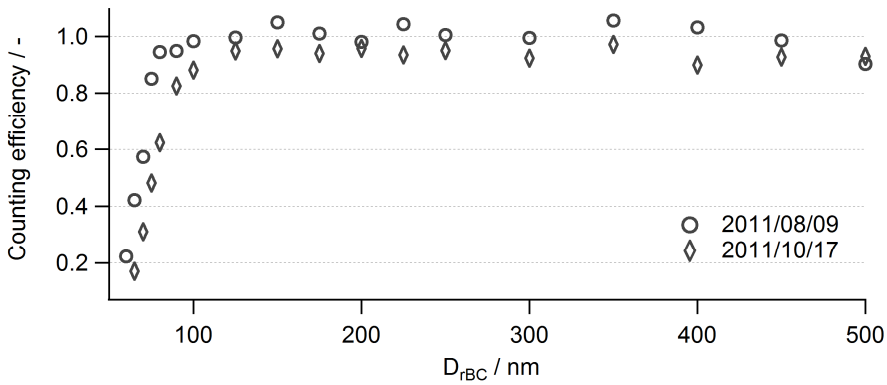

Figure 38. *Counting efficiency of the SP2 for fullerene soot compared to a reference CPC for 9 August 2011 and 17 October 2011.*

(c) As can be seen in Figure 35, the signals of the detectors always show some electronic noise[16], reflected in a jagged baseline instead of an ideally flat line. To avoid recording the noise with the SP2, internal baselines and thresholds need to be set accurately. The baseline represents the idealized stable value of the detector signal, when no particle is measured (about 0 for the PSD in Figure 35; dashed horizontal line). The threshold defines the value, which needs to be reached and exceeded by the detector signal so that the particle is recorded by the instrument. In Figure 35 a threshold of about 50 (around the baseline) would be needed for the PSD, to avoid recording noise but to ensure recording the particle's signal. Depending on the specific noise of the detector, the signals of very small particles might not significantly raise above noise level. Signals not exceeding the threshold, i.e. noise and very small particles remaining in the noise, are skipped. Thus, careful adjustments of the baseline and threshold values for the scattering and the incandescence channels guarantee both, the suppression of noise signals and the detection of small particles. By experience, misadjusted baselines and thresholds can either suppress the valid signals or include noise and thus corrupt the measurements significantly. This can be caused by thresholds set too low so that the baselines of particles are partly above the threshold, blocking the detection based on the missing reset of the particle detection trigger, i.e. based on the signal not decreasing below the threshold (red signal in Figure 39).

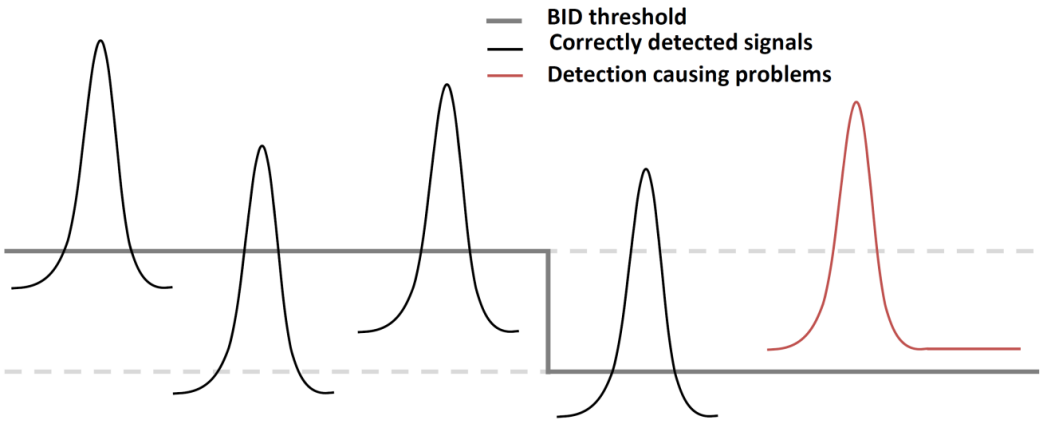

Figure 39. *Schematic view of the signal-threshold interaction, here shown for the BID detector. For particles with baselines below the threshold (grey line) the detection of the particles is reasonable (black Gaussians). For a particle with the baseline remaining above the threshold (red Gaussian) the detection is blocked because the particle detection trigger (≙ signal exceeding the threshold value) is not reset by a decrease of the signal below the threshold. Signals are simplistically shown as Gaussian traces.*

This prevents other particles to be recorded and all particles are counted erroneously as one particle as long as the baseline stays above the threshold. Figure 40 shows a measurement sequence of the flight on 16 June 2011 within the framework of the SP2 test flight campaign. During the test flights, the thresholds were set automatically by the SP2 software. However, this auto-threshold setting changed the thresholds in a way that it resulted in an influence on the particle detection. The sequence in Figure 40 shows the threshold of the BID (grey dotted line), the rBC-free and rBC-containing particle number concentration measured with the SP2 (blue and black line) and the number concentration measured with a CPC as

[16] This noise is only seen, when the signals are zoomed in. For signals for larger particles (e.g. in Figure 27), the noise is hardly visible.

reference (red line). At 12:47 UTC, a jump in the threshold caused the SP2 concentration to increase, while the CPC reference concentration stayed constant. Such erratic jumps were observed frequently during the test flights. Based on that and on further detailed analysis of this behavior, the auto-threshold option was deactivated and the thresholds were set manually for the subsequent airborne field campaigns to guarantee reasonable and replicable results based on stable settings.

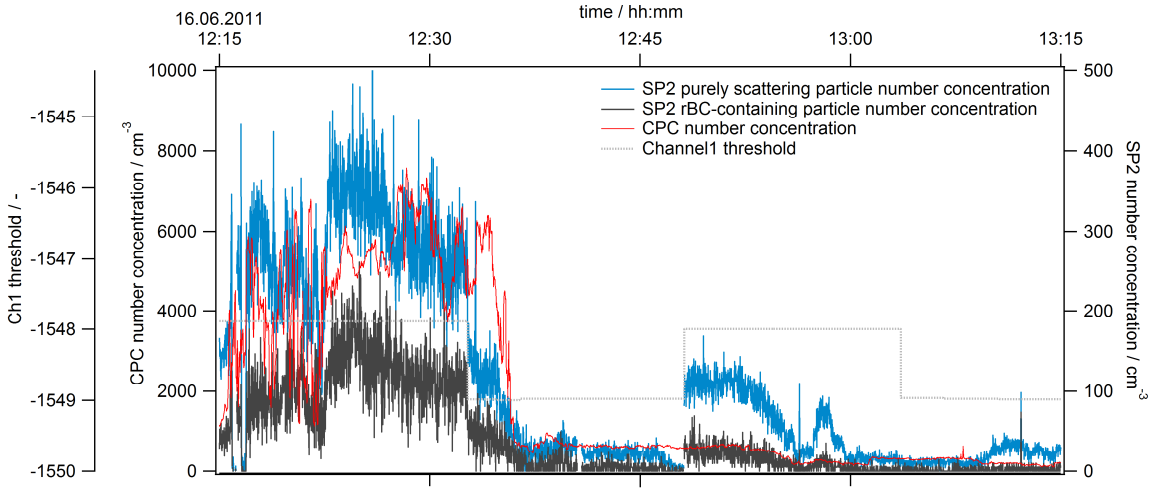

Figure 40. *Auto-threshold problem during the SP2 test flight (16 June 2011). The dotted grey line represents the SP2 auto-threshold settings of channel 1 (BID). The blue and dark grey lines represent the rBC-free and the rBC-containing particle number concentrations, respectively, measured with the SP2, while the red line represents the CPC number concentration.*

(d) Due to the temperature dependency of the YAG-power monitor (Figure 41), a not exactly known leakage of the mirrors and a possible change of the leakage caused by contamination on the reflective surfaces, the YAG-power monitor signal represents a relative, but not absolute, measurement of the laser intensity inside the cavity. The manufacturer characterizes the intensity of the intra-cavity laser beam as roughly $3 \cdot 10^6$ W cm^{-2} (DMT, 2012). Thus, the YAG-power monitor cannot be used for quantitative analyses of the stability of the laser power. Due to this issue, for the correct determination of the optical particle diameter the YAG-power measured during the PSL calibration has to be used in the toolkit for the analysis of data, even if the power drifts due to the described dependency.

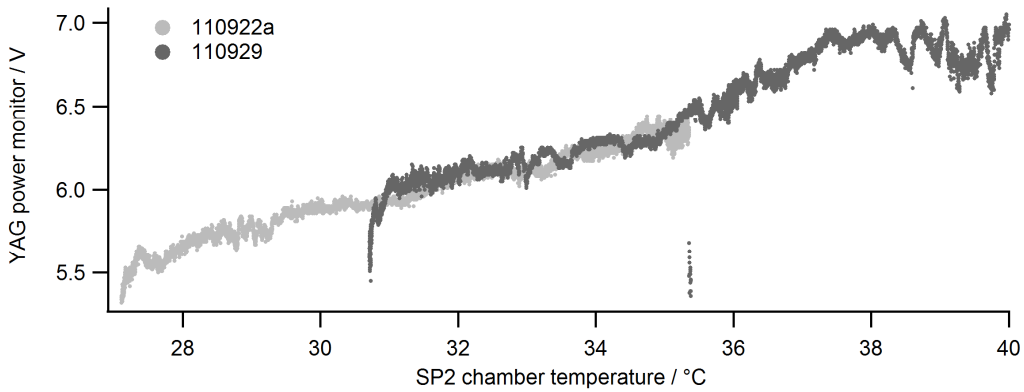

Figure 41. *Temperature dependence of the YAG-power monitor shown for two data sets (flights during CONCERT 2011) of 22 September and 29 September 2011.*

(e) Besides the presented quality checks, the quality of the determination of the size of coated rBC particles using the LEO-fit approach is tested by applying the LEO-fit to rBC-free particles. The size of rBC-free particles computed with the LEO-fit is compared automatically for every considered sequence in the SP2 toolkit to the size directly obtained from the LSD, agreeing well for the data from this study and assuring a stable quality of the LEO-fit approach. This is shown in Figure 42. The x-axis shows the peak height for rBC-free particles measured with the LSD, while the y-axis shows the scattering peak height derived by the LEO-fit approach (for the leading edge being up to 10% of the maximum laser power). The approach is valid if the dots are near the 1:1 line (orange dotted line).

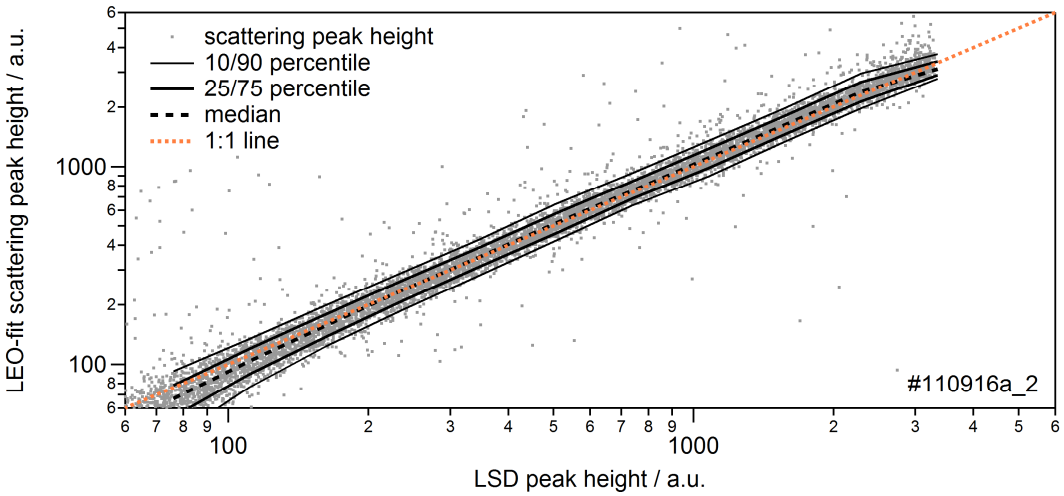

Figure 42. *Accuracy of the LEO-fit shown for the (forest fire) aerosol layer sequence #110916a_2. The x-axis represents the peak height for rBC-free particles measured with the LSD, while the y-axis represents the peak heights derived by the LEO-fit. The dotted orange line is the 1:1 line. Grey dots are the singular detected particles, while the black lines represent the 10-/90-percentiles, the 25-/75-percentiles, and the median. The LEO-fit has a lower limit of about 150 nm (≙ LSD peak height = 60 arbitrary units; a.u.) and extends the upper detection limit for the optical sizing of particles to diameters > 550 nm, depending on the fraction of rBC.*

The black lines show the median and percentile distribution of the results (grey dots). A spread of the results around the 1:1 line is discernible. However, if the results are equally distributed around the 1:1 line, i.e. the median is close to it, the errors made by the calculation of the particle size compensate themselves. A transition towards an underestimation of the particle sizes derived by the LEO-fit approach is discernible only for small particle sizes. This underestimation increases slightly for small particles if the LEO-fit approach is done for 3% of the maximum laser power (as it is used in this study), causing the main uncertainty for the determination of coating thicknesses for particles with small scattering cross-section. The underestimation is caused by the small signal heights in the leading edge of the laser beam for small particles compared to larger particles affecting the quality of the LEO-fit.

Additionally, to further validate the quality of the SP2 data, the comparison of the deduced LEO-fit number size distribution is compared to the size distributions of various OPCs as described in the next section.

3.4.4 Total particle number size distributions

The combination of the operated OPCs and the SP2, each with different limited size ranges (see Table 3), allows deriving the total particle number size distribution. The single instruments' aerosol number size distributions are merged in an aggregated aerosol number size distribution representing the largest possible size range. In this study, aggregated number size distributions are derived for standard temperature and pressure (stp; 273.15 K, 1013.25 hPa). This section contains parts published in Dahlkötter et al. (2014).

For this study, the measurements of the OPCs and the SP2 do not cover the entire Aitken mode (see Figure 10 and Section 2.2.1 for size distribution theory). To obtain information on the size distribution in the Aitken mode ($D_P < \sim 0.14$ µm), the number concentration of particles is determined for the size range between 0.01 µm (lower CPC cutoff) and the lower cutoff of the measured number size distribution of OPCs and SP2 (D_{cutoff}), by using the integral concentration of particles in the accumulation (and coarse) mode $\int N_{(size\ dist)}$, i.e. measured with the SP2 and the OPCs, and the integral CPC number concentration N_{CPC}. The number concentration $N_{(D<cutoff)}$ of Aitken mode particles in the described size range ($< D_{cutoff}$) is:

$$N_{(D<cutoff)} = N_{CPC} - \int N_{(size\ dist)}. \qquad \textbf{(3.10)}$$

This method is only valid if nucleation mode particles can be excluded. This is ensured by the measurement for particles in the size range 4–10 nm, based on measurements of CPCs with different lower cutoffs, showing low particle number concentrations in that size range. The shape of the particle number size distribution in the Aitken mode range is approximated by applying a log-normal fit, assuming that a single log-normal mode represents all particles in the Aitken mode (Weinzierl et al., 2011) with $N_1 = N_{(D<cutoff)}$ and with the particular minimum between Aitken and accumulation mode being operationally defined as 0.14 µm. Figure 43 sketches the procedure for fitting the number size distribution. The *CMD* for the Aitken mode, CMD_1, has to be assumed based on literature values for the Aitken mode and GSD_1 is estimated to provide the best fit to the residual between the measured accumulation mode and the lognormal fit to the accumulation mode in the lower end of the measurement range (of SP2/OPCs) and to match values regularly found for the specific observed aerosol type. In addition to one log-normal distribution used to describe the size distribution in the Aitken mode, one or two log-normal distributions are applied to parameterize the particle size distribution in the accumulation mode and the coarse mode, i.e. the measured size range of the SP2 and OPCs.

For the different campaigns, different sets of instruments are used (see Section 3.3 and Table 3). Thus, the size distribution is assembled based on the availability of data from the individual instruments. For the CONCERT 2011 campaign, for instance, the size distribution is assembled for most of the cases from data of the UHSAS-A, the SP2 and the FSSP-300. Based on their availability, the use of different instruments causes a change in D_{cutoff}[17] of the assembled size distribution though the widest possible range of the measurements is intended to ensure that the extrapolation towards particles $< D_{cutoff}$ is reasonable.

[17] Due to different sets of operated instruments D_{cutoff} varies between 0.06 µm and 0.14 µm.

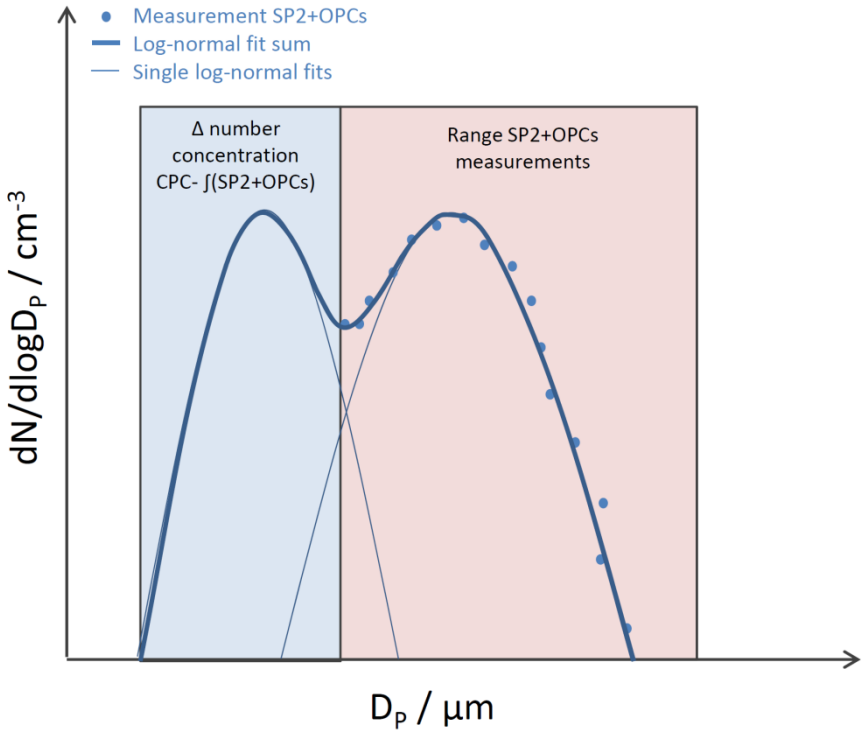

Figure 43. *Scheme for the determination of number size distributions: dots represent the combined measurement of the SP2 and the OPCs (red box; right). The integral number concentration of particles < D_{cutoff} (blue box; left) is derived from the difference of the CPC number concentration to the integral number concentration of the SP2/OPCs, presented in Equation (3.10). Log-normal fits are approximated to the measured size distribution and extrapolated towards smaller sizes. For details see text. Adopted from Dahlkötter et al. (2014).*

The accuracy and quality of the number size distribution relies on the accuracy of the individual instruments (see Sections 3.3.1 and 3.3.3). Figure 44 presents the size distribution of an (forest fire) aerosol layer sequence during CONCERT 2011 measured with different OPCs and the SP2.

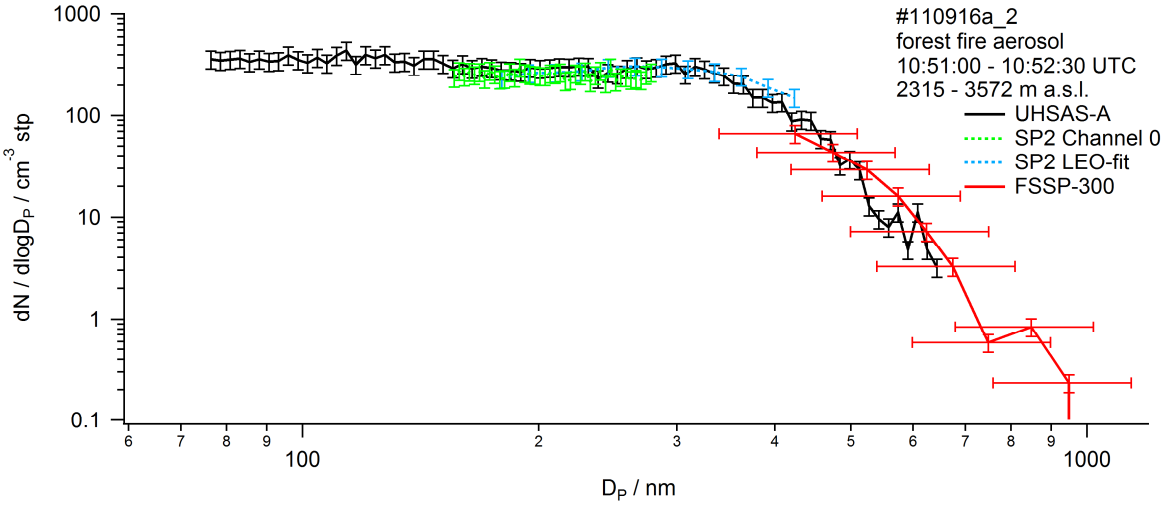

Figure 44. *Accuracy of the specific OPCs and the SP2 at standard conditions shown for the aerosol layer sequence #110916a_2 measured within a forest fire aerosol layer. Error bars represent 20% uncertainty.*

The error bars represent 20% deviations from the averages of the considered sequence. For particles < 500 nm, the size distributions agree very well with deviations < 10%. For larger particles the deviation between the UHSAS-A and the FSSP-300 is more distinct, though not far off. The increased uncertainty is caused by less good counting statistics for the larger particles, by uncertainties in the exact sensitive area of the FSSP-300 and by the use of the manufacturer calibration for the FSSP-300. The use of the manufacturer calibration implies 20% uncertainty for the number concentration in the size channels and also for the assigned diameter of the particular channels. Based on this approach, the accuracy of the derived size distributions is estimated to be ±20% for the data presented in this thesis.

3.4.5 BC particle number size distributions and BC mass concentration estimates

To determine the BC number size distribution a similar approach as used to determine the total particle number size distribution (see Figure 43) is used because the rBC number size distribution measurements using the SP2 cover a limited size range (80–440 nm for the CONCERT 2011 campaign; Table 3). To obtain information on BC particles < 80 nm, the integral rBC number concentration measured with the SP2 (*SP2 rBC*), is subtracted from the integral number concentration of non-volatile particles measured with a CPC ($N_{CPC\_non\text{-}vol}$), assuming all non-volatile particles are rBC particles. This approach can be used for well-defined combustion processes with high fractions of BC particles contributing to the emitted non-volatile particles (in terms of number concentrations), e.g. in combustion processes related to traffic or aviation.

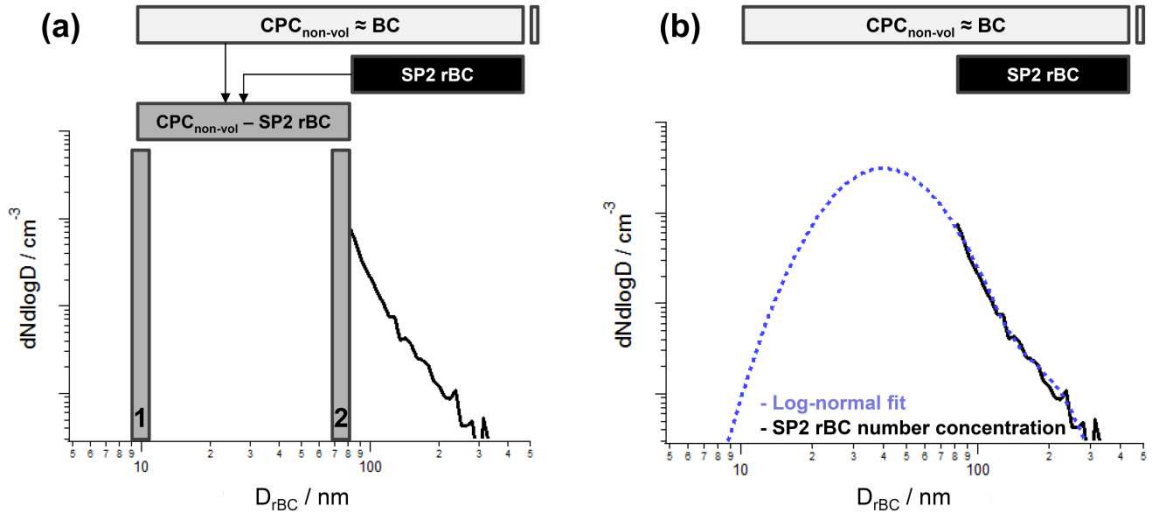

Figure 45. *Scheme for the determination of the BC number size distribution and the BC total mass concentration using the rBC number size distribution measured with the SP2 (SP2 rBC; size range: 80–440 nm; black line and black bar) and the integral number concentration of non-volatile particles $N_{CPC\_non\text{-}vol}$ (D_P > 10 nm; light grey bar). (a) The number concentration for particles < 80 nm (grey bars) is the difference between $N_{CPC\_non\text{-}vol}$ and the number concentration of SP2 rBC and is set to 10 nm and 75 nm diameter as minimum (1) and maximum (2) BC total mass concentration estimate, respectively. The best estimate (b) is derived by applying a log-normal fit (blue dashed line; N = $N_{CPC\_non\text{-}vol}$) on the measured rBC number size distribution (black line). The mass concentration is calculated using the number concentrations from (a) and (b) and 1,800 kg m^{-3} for BC density.*

The total rBC mass concentration determination described in Section 3.4.3 is possible if the *MMD* lies within the SP2 rBC size range, which allows fitting the distribution with a log-normal fit. In contrast, by this approach the total BC mass concentration can be estimated without having a *MMD* within the SP2 rBC size range (Figure 45). As minimum and maximum BC mass concentration estimate, the number concentration for particles < 80 nm are set to the minimum diameter measured with the CPC (10 nm; marked in Figure 45a as "1") and the maximum diameter measured with the CPC but not measured with the SP2 (75 nm; marked in Figure 45a as "2"). Using a BC particle density (1,800 kg m^{-3}), the measured rBC number size distribution and the particle number concentration of particles set to 10 nm or 75 nm, the BC mass concentration can be derived. Thus, the minimum and maximum conceivable BC mass concentration can be derived. To define best estimates, the BC number size distribution is extrapolated by applying log-normal fits approximated to the measured rBC number size distribution (Figure 45b) with $N = N_{CPC\_non\text{-}vol}$ followed by the calculation of BC mass concentrations using the same BC density (see above).

3.4.6 PSAP inversion

To derive relevant optical and microphysical parameters, which are not covered by the measurements of the SP2 and the OPCs (such as the refractive index or the absorption coefficient) the PSAP inversion is used (Petzold et al., 2009; Veira, 2011). This method uses the measured size distribution, an assumed refractive index and Mie theory to invert σ_{abs}. The inverted absorption coefficient σ_{abs} is then compared to the absorption coefficient measured with the PSAP (Section 3.3.2). The PSAP inversion is limited by the detection limit of the PSAP to absorption coefficients of $0.1 \cdot 10^{-6}\,m^{-1}$ at standard conditions (273.15 K, 1013.25 hPa) (e.g. Petzold et al., 2002). This study uses the PSAP inversion version (Figure 46) described in Veira (2011).

The input for the PSAP inversion is the measured PSAP raw signal, averaged to 5 s values, and the particle number size distribution assembled from different aerosol in-situ instruments measuring in different size ranges. For the CONCERT 2011 campaign, the SP2, the FSSP-300 and partly the UHSAS-A were used to determine the number size distribution (see Section 3.4.4). The measured size distribution was internally corrected with an inlet efficiency transfer function within the PSAP inversion for aerosol inlet losses, allowing for the combination of the size distribution values, measured with the loss-free wing-mounted instruments, and the aerosol inlet-biased measurement of the cabin-mounted PSAP. To derive the theoretical values for the absorption and scattering of the bulk aerosol with the PSAP inversion, a refractive index needs to be iteratively approached. The calculation of the parameters, done for all three wavelengths (467 nm, 530 nm, 660 nm) of the 3λ-PSAP, follows the scheme presented in Appendix 3. A detailed description is supplied in Veira (2011). σ_{sca}, needed to correct $\sigma_{abs,PSAP}$ (see Section 3.3.2), and σ_{abs} are calculated from the measured size distribution using the Mie theory code BHMIE of Bohren and Huffman (1983) for spherical particles for the given refractive index. Simplified, if the measured (PSAP) and the theoretically derived σ_{abs} coincide, the assumed refractive index is representative for the bulk aerosol. Finally, based on the determination of the correct bulk refractive index, the PSAP inversion delivers several optical and microphysical parameters: σ_{abs}, σ_{sca}, $å_{abs}$, ω_0, the refractive index parameters *n* and *k*, and the number size distribution.

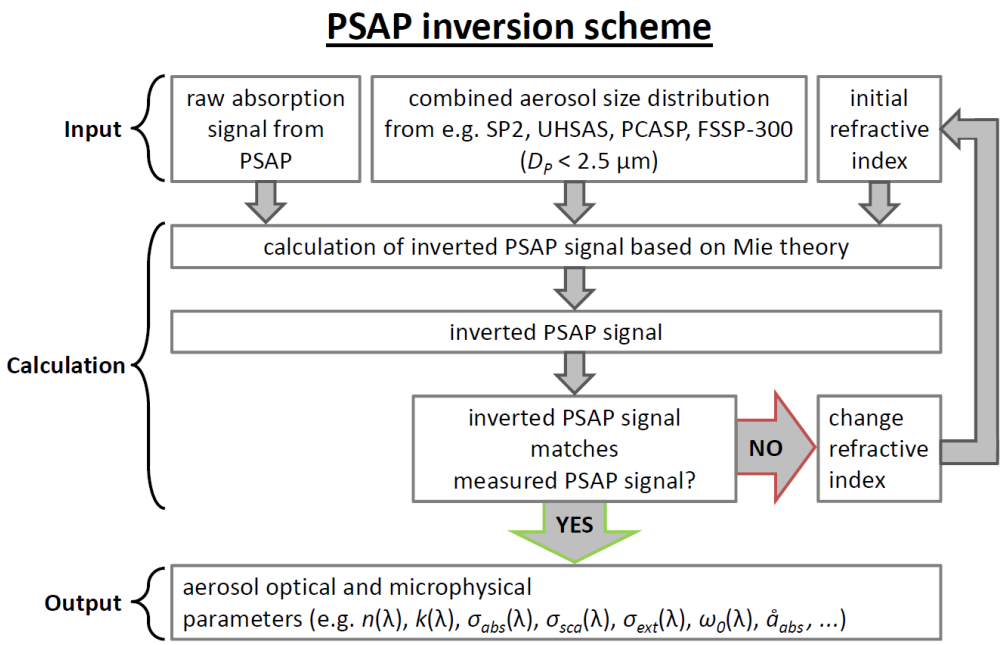

Figure 46. *Overview of the iterative PSAP inversion scheme used for the determination of optical and microphysical aerosol properties. Adopted from Petzold et al. (2009).*

The computation of the described parameters underlies several uncertainties due to measurement uncertainties or methodological assumptions. A detailed list is described in Veira (2011). This short overview addresses the most relevant uncertainties arising from this method:

On the one hand, the uncertainties attributable to the measurements have to be taken into account: the natural variability of the sampled aerosol can be represented by the calculation of percentiles for a specific measurement sequence. In addition, the limitations and accuracies of the PSAP and the OPCs need to be taken into account. Therefore, the PSAP needs to be calibrated carefully for the sample flow. Otherwise, a misaligned flow could act as a relevant source of uncertainty. This was done before every specific campaign. The required corrections (see Section 3.3.2) limit the accuracy of the measured absorption to between 20–30% (e.g. Bond et al., 1999; Virkkula et al., 2005; Lack et al., 2008). The uncertainty of the measured size distribution was addressed before.

On the other hand, uncertainties allocated to the method need to be considered. These uncertainties arise mainly from the remaining deviation between measured and theoretically derived σ_{abs} (a), the assumption of particle sphericity (b) and the non-consideration of particles smaller than the cutoff size (c).

(a) The remaining deviation can be controlled by adjusting the intervals of the chosen refractive indices, Δn and Δk, so that the intervals are small enough to ensure reasonably small deviations. Proper settings of the intervals make it possible to minimize the uncertainty due to the refractive index intervals to smaller than 1%.

(b) The uncertainty due to the assumption of spherical particles (i.e. Mie theory) is assumed by Petzold et al. (2009) and Veira (2011) to be small because in the aerosol, which is collected on a filter, randomly oriented non-spherical aerosol particles neutralize their single-particle characteristics on average.

(c) The uncertainty due to the non-consideration of particles smaller than the cutoff size is described and estimated in the following: the lower cutoff D_{cutoff} of the size distribution is determined by the lower cutoff size of the instrument delivering measurements for the smallest aerosol particle sizes. As described in Section 3.3, the UHSAS-A has a lower cutoff at 60 nm. This lower cutoff is simultaneously the lower cutoff size of the assembled size distribution. Unfortunately, at some flights the UHSAS-A had internal problems so that it has to be excluded from the combined size distribution. For those cases, the lower detection limit of the SP2 (140 nm) was used. The non-consideration of particles smaller than the lower cutoff size of the number size distribution was accepted because the contribution of sub-100 nm particles to the absorption of visible light is assumed to be negligibly small. To determine this uncertainty produced due to the non-consideration of the smaller particles, tests were done where the smaller particle sizes were estimated based on the difference of the integral number concentration of a CPC (N_{CPC}) and the integrated number concentration of the assembled size distribution $\int N_{(size\ dist)}$, as already used in Section 3.4.4. The difference represents the integral number concentration $N_{(D<cutoff)}$ of particles smaller than the lower cutoff of the assembled size distribution D_{cutoff}, according to Equation (3.10). The uncertainties introduced by the non-consideration are presented for a chosen sequence measuring a forest fire plume on 16 September 2011. The integrated number concentration $\int N_{(size\ dist)}$ for this sequence is 106 cm^{-3}, while $N_{(D<cutoff)}$ is 750 cm^{-3} with the cutoff diameter D_{cutoff} at 140 nm. Thus, the majority of the particles are smaller than D_{cutoff}. To test the response of the PSAP inversion on the non-consideration of particles smaller than D_{cutoff}, $N_{(D<cutoff)}$ is set to 20 nm, 50 nm, and 100 nm and the differences in the calculated parameters are derived and compared to the results for the same sequence neglecting particles < D_{cutoff} (Table 8).

Table 8. *Error estimates for the negligence of particles smaller than D_{cutoff} of the number size distribution in the PSAP inversion. The estimate is calculated for a forest fire aerosol layer sequence on 16 September 2011 (41740–41900 s after midnight). The number size distribution is merged from the SP2 and the FSSP-300 data with a lower cutoff of 140 nm. σ_{absRef}: calculated absorption coefficient for the sequence neglecting particles < D_{cutoff}; σ_{abs}: calculated absorption coefficient for the sequence with particles < D_{cutoff} set to 20 nm, 50 nm or 100 nm.*

	λ = 467 nm	**λ = 530 nm**	**λ = 660 nm**
σ_{absRef} / σ_{abs} with $N_{(D<cutoff)}$ at 20 nm	1.000	1.000	1.000
σ_{absRef} / σ_{abs} with $N_{(D<cutoff)}$ at 50 nm	0.999	0.999	0.999
σ_{absRef} / σ_{abs} with $N_{(D<cutoff)}$ at 100 nm	0.995	0.995	0.995

For the calculated absorption coefficient (Table 8) and for the Ångström exponent of absorption (not shown) the effect is insignificant. However, for other parameters like the bulk imaginary part of the refractive index or the theoretically derived scattering coefficient, the deviations for this error estimate example are up to 13% and 4%, respectively (not shown).

Considering the different sources of uncertainty for the PSAP inversion, the most relevant uncertainties arise from the measurement. Thus, a careful setup and analysis of the in-situ measurements reduce the uncertainty allocated to the PSAP inversion substantially. Petzold et al. (2009) use a conservative error estimate of 25%. In this study a maximum total uncertainty of 20% is assumed.

4 Results and discussion

In this chapter, characteristics of microphysical and optical properties of the observed aerosol layers are presented and discussed by using airborne in-situ data from the CONCERT 2011 campaign. First (Section 4.1), the vertical distribution of aerosol particles and aerosol layers, with special focus on BC at mid-latitudes in September 2011, is addressed as a scientific basis for e.g. the validation of global aerosol models. Second, in Section 4.2, the aerosol layers observed during the CONCERT 2011 campaign, including their attribution to different sources, are presented and discussed as a comprehensive approach, assessing general aerosol layer characteristics at mid-latitudes. In Section 4.3, a case study approaches long-range transport of forest fire aerosol from northern America, relevant due to their abundance, high BC burdens and heterogeneous aerosol characteristics. Finally, sources contributing to the BC burden in the upper troposphere, including forest fires and aviation, are approached and an estimate of their contribution is given (Section 4.4).

4.1 Atmospheric aerosol distribution at mid-latitudes in September 2011

4.1.1 Vertical profiles during CONCERT 2011

Based on the 11 research flights conducted during CONCERT 2011 (see Figure 16), the aerosol burden within the vertical column of the troposphere and the UTLS region is derived. Figure 47 shows several vertical profiles a.s.l. at stp conditions, averaged for all 11 research flights during the CONCERT 2011 field experiment. The median and percentiles are calculated for various aerosol quantities with 500 m vertical resolution and a temporal resolution of 10 s. This temporal resolution is used on the one hand to exclude noise from insufficient integration time and on the other hand to retain the horizontal resolution, which is about 2 km for a typical Falcon speed at a temporal resolution of 10 s. The median vertical distributions represent an approximation of the typical vertical profile of the aerosol quantities above Central Europe during fall 2011.

The total number concentration (Figure 47b) derived by CPC measurements shows a narrow distribution whose highest values, up to 10,000 cm^{-3}, are below 2 km altitude, indicating the enrichment of particles within the PBL. A transition range between the PBL and the free troposphere is visible between roughly 1 km and 2 km a.s.l. Above 2 km, the particle number concentration slightly increases towards higher altitudes (Figure 47b). Volatile particle formation processes taking place in the free troposphere can cause an increase in the free troposphere (e.g. Weigel et al., 2011)[18]. The lowest 10-percentile values were observed in the free troposphere (~ 300 cm^{-3}).

[18] This is supported by the low fraction of non-volatile particles explained later (Figure 47f).

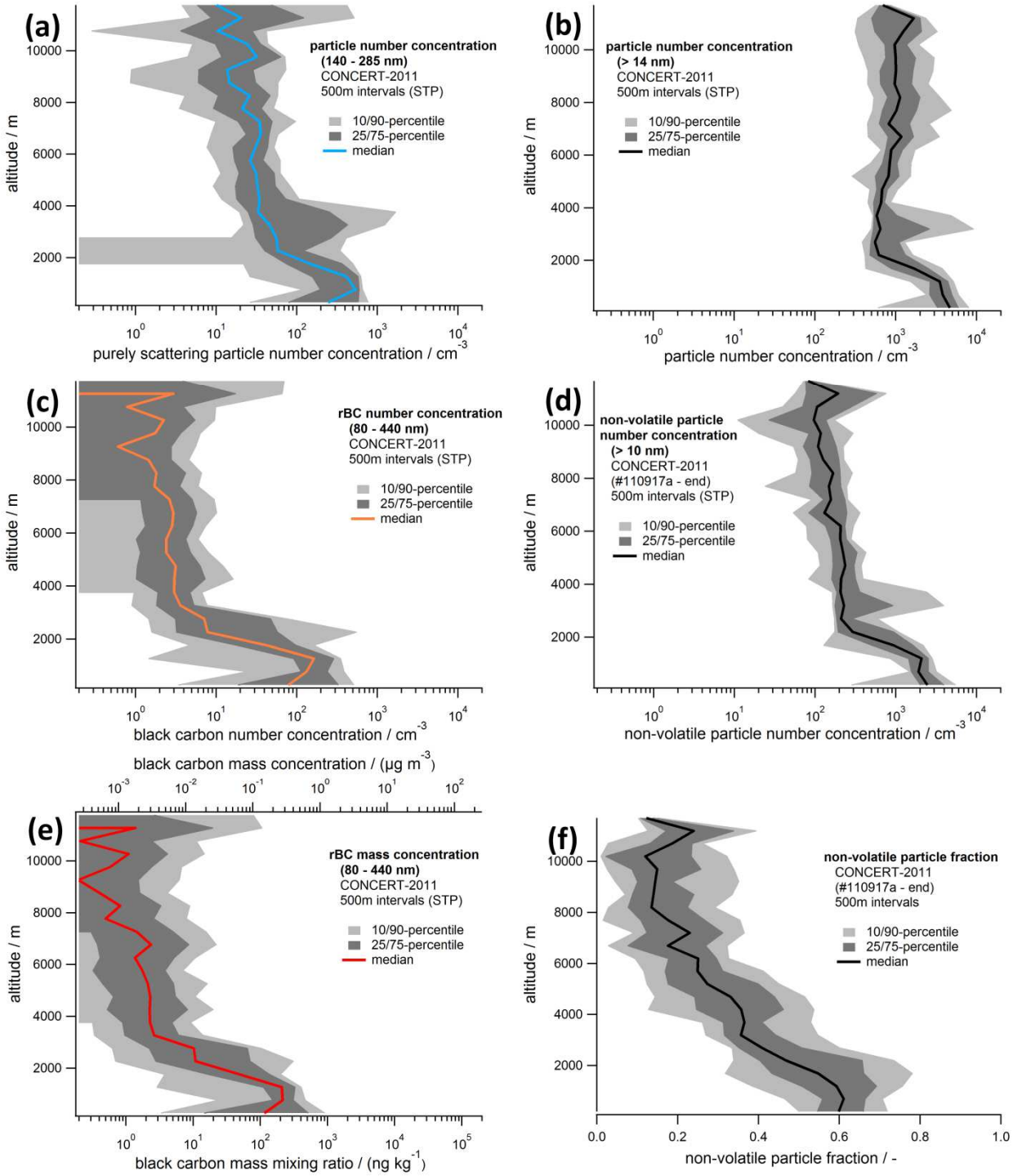

Figure 47. *Vertical profiles (stp; a.s.l.) during the CONCERT 2011 campaign as median (line), 25-/75-percentiles (dark grey shading), and 10-/90-percentiles (light grey shading) for 500 m vertical intervals and a temporal resolution of 10 seconds: (a) SP2 rBC-free particle number concentration (size range: ~ 140 < D_P < 285 nm), (b) total particle number concentration (size range: 14 nm < D_P < $D_{cutoff,50}$), (c) SP2 rBC particle number concentration (size range: ~ 80 < D_{rBC} < 440 nm), (d) total non-volatile particle number concentration (size range: 10 nm < D_P < $D_{cutoff,50}$), (e) SP2 rBC mass mixing ratio and rBC mass concentration (size range: ~ 80 < D_{rBC} < 440 nm), and (f) non-volatile particle fraction. The mass mixing ratio (MMR) in (e) was calculated from the mass concentration M (MMR = M/ρ_0). For the non-volatile particle number concentration and fraction in (d) and (f), respectively, data from the first three flights were ignored due to missing data (see text for explanation).*

Similar vertical distributions of the total particle number concentration were reported by Hamburger et al. (2011), for instance, for the EUCAARI-LONGREX field campaign in Europe.

In comparison to the total particle number concentration, the vertical distribution of the number concentration of rBC-free particles in (a) as measured with the SP2 ($\sim 140 < D_P < 285$ nm) shows consistently lower concentrations, ranging from < 1 cm^{-3} to about 2,000 cm^{-3}. Thus, the majority of the particles are < 140 nm, assuming that particles > 285 nm are less relevant in terms of number concentrations contributing negligibly to the difference between (a) and (b). In contrast to the particle number concentration shown in Figure 47b, in Figure 47a the concentrations decrease towards higher altitudes, underlining the absence of major particle sources for the considered size range in the free troposphere. The rBC particle number concentration ($\sim 80 < D_{rBC} < 440$ nm) in (c), shows a similar decrease with higher altitude, though the concentrations are far lower compared to the rBC-free particles. The highest values for the rBC particle number concentration are roughly 500 cm^{-3}.

The rBC particles shown in (c) contribute to the non-volatile particle concentration in (d) measured with a CPC after heating to 255°C (see Section 3.3.4). Related to the majority of sources emitting non-volatile and rBC particles into the PBL, the PBL shows the highest non-volatile particle number concentrations (~ 5,000 cm^{-3}), with a slight decrease of the concentration within the free troposphere and UTLS region as also visible in (a) and (c). The non-volatile number concentration reaches its minimum in the upper troposphere, with the median at roughly 100 cm^{-3}. Based on these low concentrations, long-range aerosol layer transport might influence and increase the non-volatile particle concentrations in the free troposphere compared to the background situation, contributing significantly to the aerosol burden (e.g. Brock et al., 2011). Similar profiles for total particle number concentrations and non-volatile particle number concentrations were observed by, e.g., Hamburger (2010) during the EUCAARI-LONGREX campaign in May 2008 or Minikin et al. (2003) during the INCA project in 2000.

In (f) the non-volatile particle fraction[19] is shown, defined as non-volatile particle number concentration, shown in (d), divided by the total particle number concentration, shown in (b). A ratio of unity means all particles being non-volatile or having non-volatile components, while with decreasing ratio the number of purely volatile particles increases. At ground level, the median non-volatile particle fraction is about 0.6 and decreases towards higher altitudes to about 0.2 in the UTLS region. This is caused by the sources of non-volatile particles, which are mainly located at ground-level, increasing the ratio at low altitudes, especially in the PBL. In addition, processes like the formation processes of volatile particles based on nucleation and accumulation taking place in the free troposphere, as described above, can affect the observed decrease of the non-volatile particle fraction with altitude.

However, at high altitudes still more than 10% of the particles contain non-volatile particle components, with a major part of these particles absorbing solar radiation. The absorption of aerosol particles is approximately proportional to their volume and thus to their mass (e.g. Seinfeld and Pandis, 2006). Thus, not only the number of particles has to be considered but also the volume and mass distribution. Figure 47e shows rBC mass concentration *M*

[19] For the presented non-volatile particle number concentration and fraction, data from the first three flights are ignored because for these flights none of the CPCs was operated in combination with the TD to determine the non-volatile particle number concentration.

(size range: ~ 80 < D_{rBC} < 440 nm) measured with the SP2 and the rBC mass mixing ratio (*MMR*) [ng kg^{-1}], calculated from *M* [ng m^{-3}] at standard conditions and the density of dry air at standard conditions (ρ_0 = 1.29 kg m^{-3}):

$$MMR = \frac{M}{\rho_0}. \qquad \textbf{(4.1)}$$

The rBC mass concentration spreads over three orders of magnitude, showing larger variability within the free troposphere, with the highest concentrations (~ 1 µg m^{-3}) found in the PBL and slightly above. The large variability implies that BC, in terms of mass concentrations, is emitted or transported irregularly, partly in aerosol layers, to the free troposphere or erratically removed (e.g. Stith et al., 2011).

4.1.2 Comparison of free-tropospheric BC over Europe and the remote Pacific

To support that BC aerosol layer transport contributes to the BC burden in the free troposphere, the vertical distribution during CONCERT 2011 is compared to the situation of background BC in the remote Pacific Ocean between 60° N and 20° N measured during the HIPPO campaign in January 2009. The vertical profile in the remote Pacific in Figure 48 shows a more uniform distribution in terms of BC mass mixing ratio (*MMR*) throughout the troposphere and UTLS region (Schwarz et al., 2010b). The observations show maximum values < 20 ng kg^{-1} and a steep decrease at altitudes above 10 km towards < 1 ng kg^{-1}.

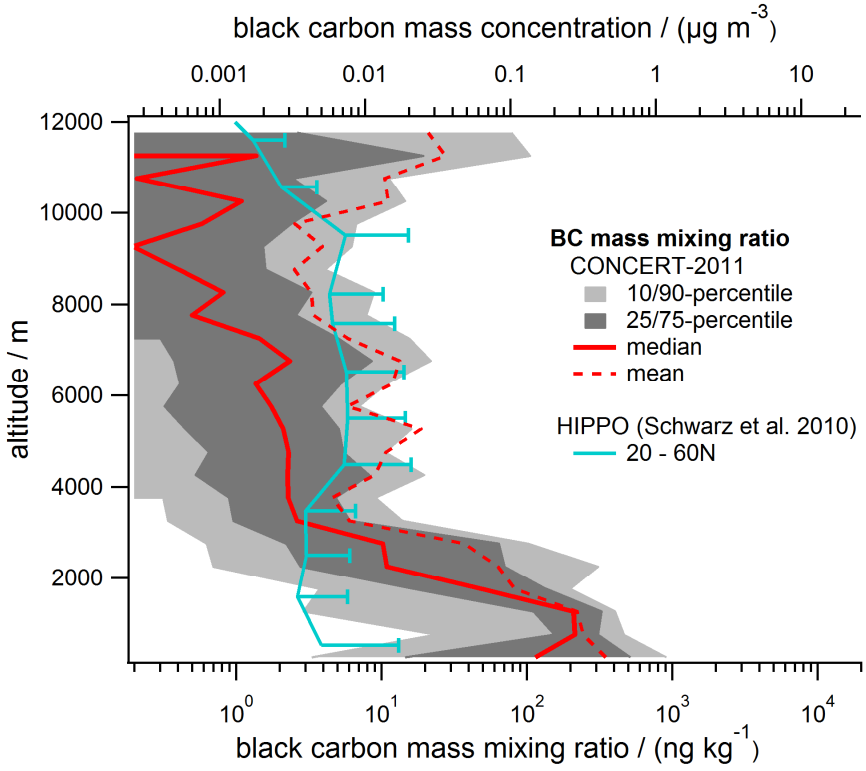

Figure 48. *Comparison of the observed rBC vertical distribution during CONCERT 2011 to average airborne in-situ SP2 measurements of BC in the remote Pacific Ocean between 20°N and 60°N during the HIPPO campaign in January 2009 (Schwarz et al., 2010b). Horizontal bars represent standard deviations (only shown on the right side due to the logarithmic scale).*

The most prominent difference to the results from this study is the rBC *MMR* at lower altitudes: below 3 km, the rBC *MMR* above Europe is significantly increased, caused by the BC sources abundantly present in Europe, while BC sources in the remote Pacific are sparse. On the other hand, the distributions of rBC *MMR*s above 3 km, observed above Europe and the remote Pacific, overlap with the free-tropospheric concentrations in the remote Pacific being even higher compared to the MBL. This overlap and the increase of the rBC *MMR* from the MBL to free troposphere observed in the remote Pacific gives evidence that the distribution of BC in the free troposphere is, in addition to the presence or absence of BC sources in the region on the ground, driven by advection and transport from remote sources and long residence times causing a zonal mixing (e.g. Schwarz et al., 2010b), which in turn is strongly dependent on wet removal processes (e.g. Oshima et al., 2012).

Findings of Aquila (2009), presenting modeled global distribution of BC at 300 hPa, support the correlation between BC in the free troposphere and transport, with the BC concentrations being more homogeneously in the free troposphere, due to (long-range) transport and zonal mixing of BC particles, compared to the source related BC mass concentrations in the PBL. The results (of this study and the mentioned publications) underline the relevance of long-range transport and elevated BC layers in the northern hemisphere.

4.1.3 Comparison of observations and model results

Comparison studies between existing model studies and measurements help to improve the current understanding of BC in the atmosphere. In order to enhance the reliability of the presented vertical profiles, the presented data is compared to model results. In Figure 49, a vertical profile of the BC concentrations is shown, which was extracted from long-term simulation results obtained by Righi et al. (2013) with the EMAC/MADE global aerosol model for the specific region (37–61° N, 5–16° E; Figure 16) and the period (7–30 September), in which the measurements were conducted during CONCERT 2011.

The comparison of model results and measurements shows a good agreement for the BC mass concentration (left panel) and for the particle number concentration (D_P > 14 nm; including BC-containing and BC-free particles; right panel) up to about 7 km altitude. The agreement gives evidence that, on the one hand, the observed vertical profiles are representative for September (for altitudes < 7 km) and that, on the other hand, the model is able to reproduce reality.

Though different size ranges for the BC mass concentrations are plotted in Figure 49 with the model showing total BC mass concentrations, while the measurements are limited to the SP2 size range, this methodological difference should not account for a deviation more than a factor of about 2 (based on BC total mass determination explained in Section 3.4.3). However, above 7 km, the results from the measurements and the model diverge significantly with the model predicting higher concentrations for both, the BC mass concentration and the particle number concentration. Aquila et al. (2011) compare the vertical profiles of simulated aerosol mass concentrations with SP2 measurements for different campaigns. For the CIRRUS campaign (over Europe), they modeled increasing BC mass concentrations as function of the altitude, while the measured concentrations decrease, which is comparable to the results shown in Figure 49. In agreement to that,

Petzold et al. (2007) show a vertical BC profile (for Central Europe in summer 2000), which decreases with the altitude. Aquila et al. (2011) speculate that meteorological conditions and specific transport patterns of the air masses during the campaign could be the reason for the difference at high altitudes. That could be a reason for the deviations found in the vertical profiles in Figure 49, as well.

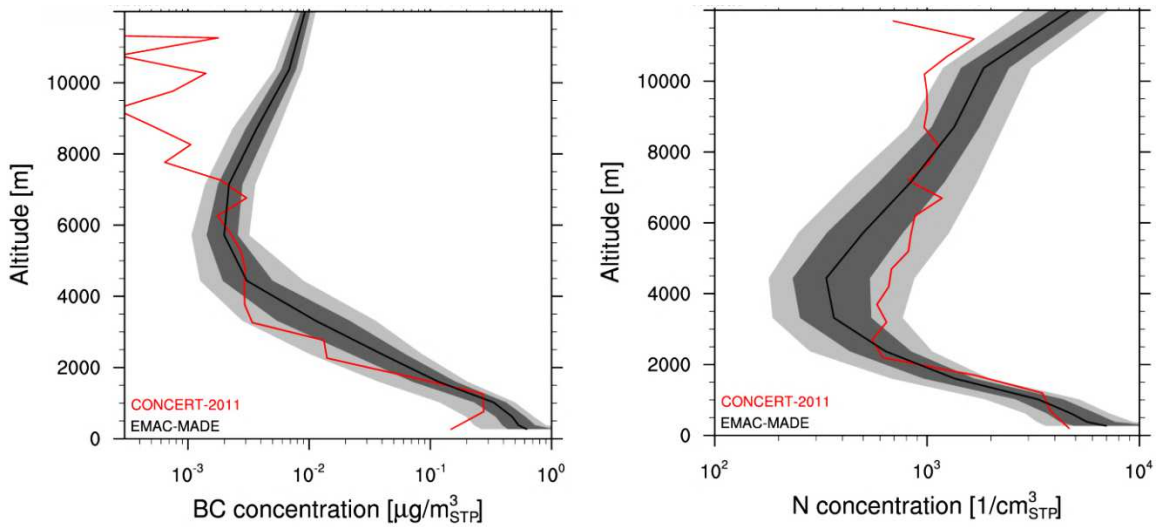

Figure 49. *Comparison of the vertical distribution of (a) the BC mass concentration and (b) the particle number concentration (D_P > 14 nm) modeled with EMAC-MADE (black line and grey shaded area) vs. the median of the measurements during CONCERT 2011 (red line). In the model the total BC mass concentration is shown, while the measurements show rBC mass concentrations for the size range 0.08 < D_{rBC} < 0.44 µm.*

This gap in understanding shows the necessity of further in-situ measurements to clarify if the presented comparison is representative or if the mismatch at higher altitudes results from an exceptional measurement situation during CONCERT 2011. Further in-situ measurements of vertical BC profiles in remote regions and source regions will also build up a global-scale data base, which allows an adequate evaluation of global models (e.g. Vignati et al., 2010) and supports the understanding of BC in the atmosphere.

4.1.4 Vertical distribution of aerosol layers in the atmosphere at mid-latitudes in fall 2011

In the previous sections, the average vertical aerosol particle distributions during CONCERT 2011 were discussed. However, singular aerosol layers can diverge significantly from the average situation (e.g. Raes et al., 2000). In the following, the vertical distribution of the elevated aerosol layers observed at mid-latitudes during CONCERT 2011 is discussed.

A high variability in particle number concentrations is visible in Figure 47a–d at roughly 2–4 km altitude with 90-percentiles reaching concentrations similar to or even higher than the highest values within the PBL. These peaks in the percentile values indicate the presence of spatially and temporally highly variable but frequently occurring aerosol layers. Although it was not a scientific objective of CONCERT 2011 (see Section 3.1.3) to localize and observe elevated aerosol layers, in all of the 11 flights, elevated aerosol layers were observed. From roughly 32.3 hours total flight time, the Falcon flew by chance roughly 3.2 hours (~ 10% of

the flight time) in elevated aerosol layers (not counting the volcanic ash layers, which were measured intentionally). Table 9 gives an overview of all CONCERT 2011 flights (Figure 16), including the approximate route, time and scope of the flight and the altitude of the detected aerosol layers.

Table 9. *List of research flights during CONCERT 2011. For each flight the lower and upper boundary and the minimal vertical depth (see text) of the detected aerosol layer a.s.l. are given. The Pagami Creek fire and Canada forest fire aerosol layers (Section 4.3) are marked with bold and italic type, respectively. OP: Oberpfaffenhofen; NB: Neubrandenburg-Trollenhagen; TRA: Temporary Restricted Area.*

Flight ID	**Route**	**Take-off time UTC / hh:mm**	**Landing time UTC / hh:mm**	**Objective**	**Presence of Elevated Layers**		
					Lower boundary / km	**Upper boundary / km**	**Vertical depth / km**
#110907a	OP – Leipzig – OP	06:21	07:53	test flight			
					2.6	3.0	0.4
					3.7	5.3	1.6
					3.4	3.9	0.5
					2.0	3.2	1.2
					10.1	10.7	0.6
#110916a	OP – Mecklenburg – NB	10:48	13:20	contrail chasing			
					1.8	2.0	0.2
					2.2	*3.4*	*1.2*
					3.4	4.5	1.1
					10.1	**11.6**	**1.5**
#110916b	NB – Leipzig – OP	14:54	17:48	contrail chasing			
					2.0	3.3	1.3
					8.7	**9.5**	**0.8**
					10.9	**11.3**	**0.4**
#110917a	OP – Hamburg – Brandenburg – OP	11:05	13:54	contrails in cirrus clouds			
					2.2	3.0	0.8
					3.0	4.3	1.3
					4.6	5.7	1.1
					2.1	3.6	1.5
#110922a	OP – Frankfurt – Bergen	07:03	09:18	stratospheric intrusion			
					4.7	5.4	0.7
#110922b	Bergen – OP	10:20	13:20	strat./trop. Layer			
					6.5	6.9	0.4
#110924a	OP – TRA Weser – OP	09:44	13:12	aged contrails			
					1.7	2.7	1.0
					3.1	4.6	1.5
					1.8	4.9	3.1
#110927a	OP – TRA Weser – OP	06:57	10:27	persistent contrails			
					1.5	2.7	1.2
					2.7	4.6	1.9
#110929a	OP – Catania	08:52	12:19	Etna volcanic ash			
					3.3	3.3	< 0.1
#110930a	Catania – Stromboli – Etna – Catania	06:34	09:34	Etna/Stromboli volcanic ash			
					0.4	2.2	1.8
					0.9	0.9	< 0.1
					3.5	3.5	< 0.1
					3.0	3.0	< 0.1
#110930b	Catania – OP	10:55	14:45	Etna/Stromboli volcanic ash			
					2.0	3.3	1.3

[20] Figure 50 shows the vertical distribution of the observed aerosol layers. Most of the measurements should approximately represent the true vertical depth in the measurement region, because the Falcon traversed most of the layers vertically during ascent or descent. However, for some cases, in which the Falcon flew at constant altitude and did not traverse the entire aerosol layer in the vertical, the given altitude ranges represent the minimal vertical depth of the aerosol layer.

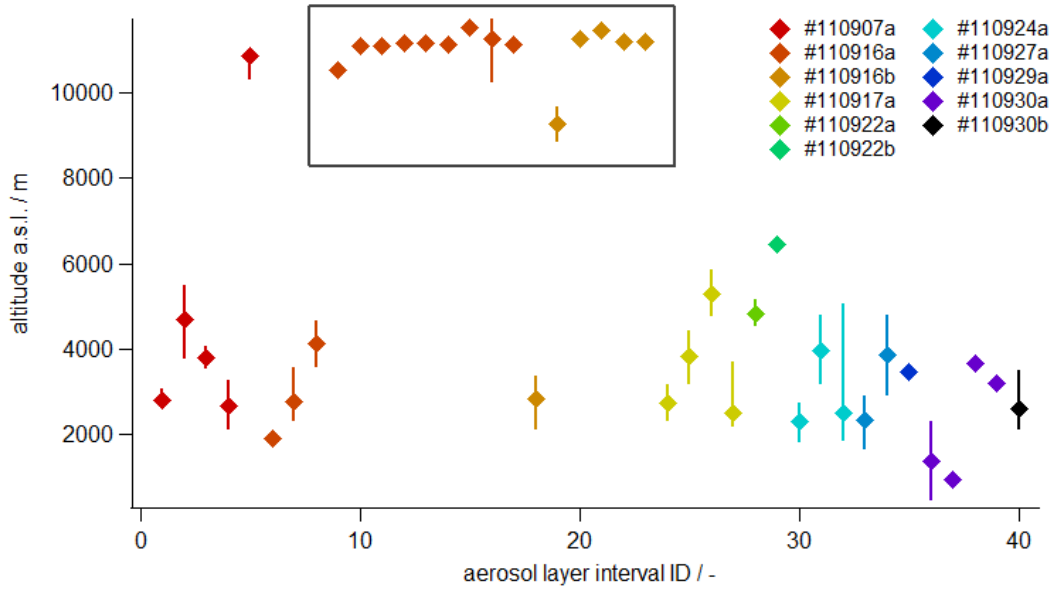

Figure 50. *Altitudes (a.s.l.) of aerosol layer observations during the CONCERT 2011 campaign. The different flights are color-coded. Diamonds represent the median values. The grey box represents the considered sequences within the Pagami Creek fire plume (see Section 4.3). The altitude ranges of the observations do not necessarily coincide with the true aerosol layer depth due to the specific Falcon flight pattern (see text). The aerosol layer sequences were numbered consecutively according to the date and time of observation.*

As can be seen from Table 9 and Figure 50, most aerosol layers were observed between 2 km and 6 km altitude a.s.l. Below about 2 km no aerosol layers (except for the volcanic ash layers) are shown because the PBL is not considered as an elevated aerosol layer in this study. Above 6 km, just a few aerosol layers were observed. This might be caused by the main process of mixing from the PBL (e.g. Cohn and Angevine, 2000), resulting in aerosol layers below 6 km, while intense vertical transport mechanisms such as thunderstorms (e.g. Yin et al., 2012) and pyro-convection, resulting in aerosol layers in the UTLS region, occur less frequent. However, aerosol layers in the UTLS region are less affected by wet removal processes and thus potentially exhibit longer lifetimes (e.g. Jaenicke, 1980)[21].

In comparison to the presented frequency and distribution of aerosol layers, Mattis et al. (2008) report pollution above the European continental boundary layer in 43% of their lidar measurements, with a maximum in June to August. 19% of their measurements are

[20] In Figure 47, the highest variability of the rBC *MMR* is present in 10–12 km altitude. It will be shown in Section 4.3 that the strongly enhanced 75- and 90-percentile values at this altitude are related to the high loadings detected in the Pagami Creek forest fire smoke plume that was crossed during two flights on 16 September 2011 (marked with a grey box in Figure 50).

[21] Particular processes affecting the vertical distribution of aerosol layers are approached later in Sections 4.2 and 4.3.

attributable to forest fire smoke advected from Canada and anthropogenic pollution advected from urban areas of the USA and Canada. The comparison of the probability of occurrence of aerosol layer observations between Mattis et al. (2008) and this study give further evidence that aerosol layers occur frequently above Europe and that observations in 10–20% can be expected.

The vertical distribution of aerosol layers from this study and from Mattis et al. (2008) are similar (Figure 7 and Figure 50): most of the layers are present at altitudes < 7 km (for CONCERT 2011 > 80% (see Table 9); for Mattis et al. (2008) > 90%) and the vertical depth of the individual aerosol layers is predominantly < 4 km (for CONCERT 2011 in all cases; for Mattis et al. (2008) about 75%). The measurement method can influence the frequency and distribution of aerosol layer observations: The observations from this study are punctual airborne in-situ measurements within the atmosphere, while Mattis et al. (2008) probed the entire vertical column of the troposphere with a lidar, implying a higher chance of aerosol layer detection with the chance of several layers theoretically being detected at the same time. Thus, lidar measurements are more suitable to determine the aerosol layer frequency and distribution at a specific location. However, airborne in-situ measurements are suitable to also deliver, besides the frequency and distribution of aerosol layers, detailed microphysical and optical parameters, relevant quantities to characterize aerosol layers in the atmosphere, which will be assessed in the next section.

4.2 Aerosol layer characteristics at mid-latitudes in September 2011

In this section, the sources of the aerosol layers observed during CONCERT 2011 are determined to allocate specific aerosol layers to specific sources. The main part of this section approaches the microphysical properties of the observed aerosol layers (forest fire aerosol layers are described in detail in Section 4.3) with respect to their sources and discusses the implications resulting from the presented observations.

4.2.1 Source attribution

To determine the source of the aerosol layers observed during CONCERT 2011, backward air parcel trajectories were calculated for all aerosol layers using HYSPLIT (see Section 3.4.2). For each aerosol layer sequence, several trajectories were calculated to define the variability of the calculated trajectories with the number of calculated trajectories depending on the duration of the measurement in the respective aerosol layer. Based on the trajectories and the microphysical properties, the aerosol layers were allocated to main source regions, namely the marine boundary layer (MBL), the European and partly the African PBL, volcanic emissions, long-range transport of air masses from northern America, forest fires, and not clearly attributable sources hereafter termed as unknown source (Figure 51)[22]. For reasons of clarity, in Figure 51 just one backward trajectory, namely the trajectory for the median location and time during the observation, is shown for each observed aerosol layer sequence.

[22] Aviation as a source of confined aerosol layers will be treated later in this study (Section 4.4.2).

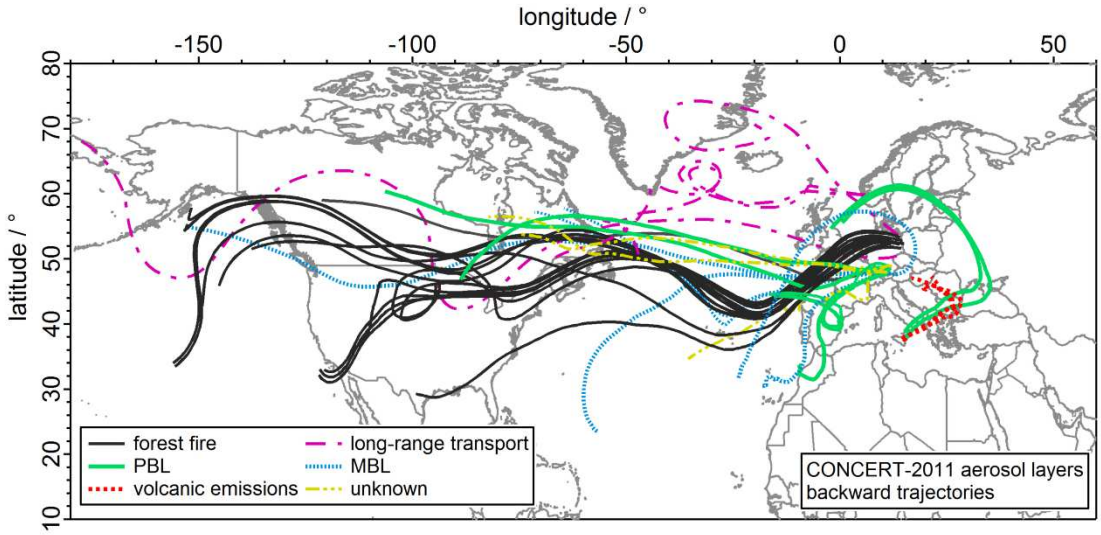

Figure 51. *Backward trajectories (6 days) for the different aerosol layers observed during CONCERT 2011 with color-coded attributed source regions.*

Some aerosol layer sequences could be assigned precisely to specific sources: the volcanic emissions originated from the Etna volcano and the Stromboli volcano in Italy and were the only aerosol layers, which were probed intentionally during CONCERT 2011. The attribution of the sparse aerosol layers implies larger uncertainties:

A layer was attributed to the PBL or MBL when the backward trajectory reached typical PBL or MBL altitudes (threshold: < 1.5 km a.g.l.), generally possible for aerosol layers originating from the MBL or PBL of Europe and Africa. It is crucial that PBL and MBL represent hereafter the source regions (not the measurement regions). For example, an aged and lofted air mass, originating from a specific source region like the PBL or MBL, is labeled PBL (or MBL) aerosol layer though it is observed in the free troposphere or UTLS region and is not measured within the boundary layer. Thus, in the following, fresh, recent PBL aerosol is distinguished from (aged lofted) PBL aerosol.

In contrast, some aerosol layers, originating from northern America, could not directly be attributed to specific sources like, e.g., the North American PBL due to increasing uncertainties of the trajectories with the duration of the transport. Thus, the source is generalized to be northern American (long-range transport) aerosol.

Not all aerosol layer sequences could be attributed to specific sources by showing long-range transport characteristics or reaching typical PBL or MBL heights. These remaining aerosol layer sequences are attributed in the following to unknown sources. It cannot be excluded that these aerosol layers originate from one of the described sources. However, due to uncertainties and limitations of the source attribution method used here, for example, due to insufficiently spatial, and temporal, resolved meteorological data sets they could not be related to the described source regions.

Similar difficulties of the source attribution are reported in Mattis et al. (2008). Although minor uncertainties remain in the attribution of the sources of the aerosol layers, the presented source attribution helps to differentiate the properties of the aerosol layers and to obtain general information on the age and transportation of these layers. The main objective of this thesis, the microphysical and optical properties of aerosol layers, is not affected by these uncertainties.

To connect the findings on the sources of the layers with the altitude of the observation, Figure 52 shows the altitude range of the observed aerosol layers, color-coded by the attributed source region. The observed volcanic ash plumes are very confined in the vertical depth and observed at low altitudes due to the proximity of the measurements to the particular source. Apart from this specific issue, no significant trends in the relation between the aerosol layer type and the altitude can be determined based on this data set. Similar insignificant distributions of aerosol layers attributed to specific source regions are reported by Mattis et al. (2008). Thus, the vertical aerosol layer distribution is primarily a function of age and meteorological conditions during the transport.

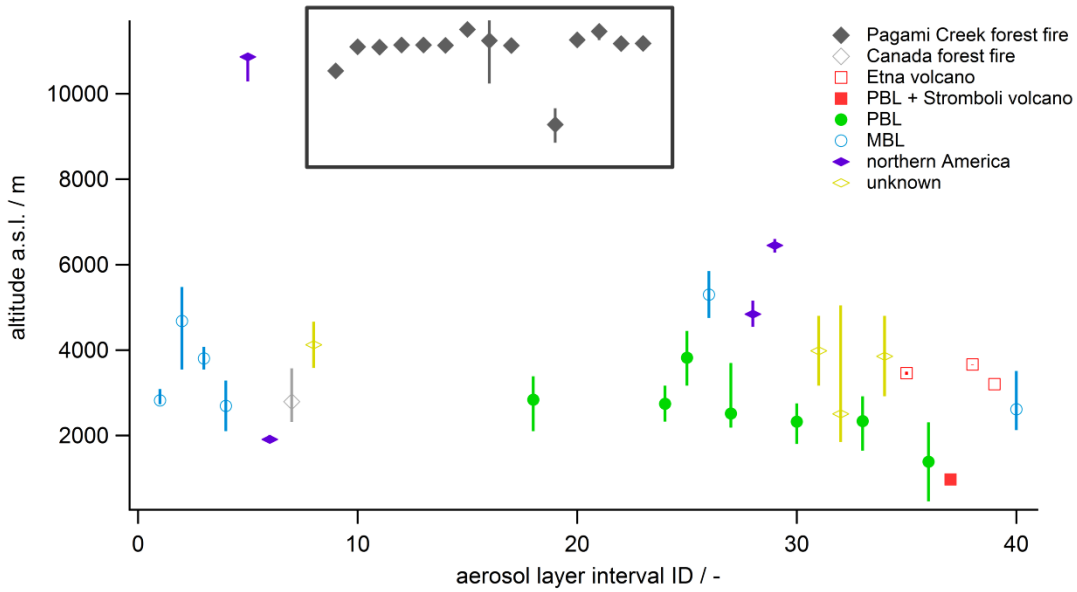

Figure 52. *Altitudes (a.s.l.) of aerosol layer observations during the CONCERT 2011 campaign. The attributed sources are color-coded. Markers represent the median values. The lines show the measured vertical depth of the layer, i.e. the minimal vertical depth of the respective aerosol layer, as the altitude ranges of the observations do not necessarily coincide with the total aerosol layer depth due to the specific Falcon flight pattern (see Section 4.1.4). The grey box represents the sequences within the Pagami Creek fire plume (see Section 4.3).*

4.2.2 Variations of BC in elevated aerosol layers

BC mass concentrations (SP2 size range)

The BC mass concentration is crucial for the potential of aerosol layers in the atmosphere to absorb the incoming radiation. Figure 53 shows the rBC mass concentrations of the considered aerosol layer sequences, measured during the CONCERT 2011 campaign for the SP2 size range $80 < D_{rBC} < 440$ nm, separated for the attributed source regions. The rBC mass concentrations range from about 2 ng m^{-3} to 400 ng m^{-3}, exhibiting a factor of 200 as the variation between highest and lowest measured rBC mass concentrations in the described size range. Aerosol layers attributed to the MBL show the lowest rBC mass concentrations (< 10 ng m^{-3}), followed by the measured Etna volcanic ash plumes (< 20 ng m^{-3}). In comparison, a volcanic ash plume from the Stromboli volcano mixed with fresh PBL aerosol contains high rBC burdens above 260 ng m^{-3}. Aerosol layers not attributed to source regions (described as *unknown)* feature intermediate rBC mass concentrations of

roughly 6–30 ng m^{-3}. Aged lofted PBL aerosol air masses, both, from the PBL in Europe and North Africa, have rBC mass concentrations between 50 ng m^{-3} to above 130 ng m^{-3}, on average lower than the rBC mass concentrations of the forest fire layer sequences ranging between roughly 25 ng m^{-3} and 300 ng m^{-3}. The highest rBC mass concentrations in the SP2 size range were found in long-range transport aerosol layers (> 10–400 ng m^{-3}). In three of the long-range transport layers a large fraction of the rBC particles has diameters at the upper size limit of the SP2, contributing to the major part of the high rBC mass concentration up to > 400 ng m^{-3}.

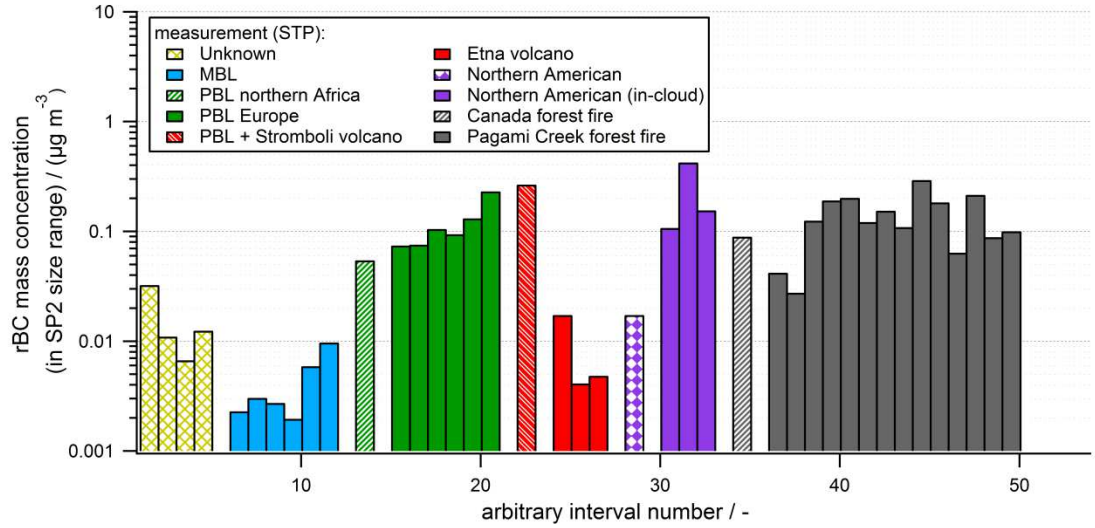

Figure 53. *rBC mass concentrations in the SP2 size range (~ 80 < D_{rBC} < 440 nm) for the different aerosol layer sequences observed during CONCERT 2011, separated with respect to their attributed source regions (unknown: yellow; aged lofted MBL aerosol: blue; aged lofted PBL aerosol from northern Africa and Europe: green; volcanic emissions mixed with fresh PBL aerosol and pure volcanic emissions: red; long-range transport from northern America: purple; forest fire aerosol from the Canada forest fire and from the Pagami Creek fire: grey).*

BC mass concentrations (total)

Based on the method described in Section 3.3.1 and Figure 31, the measured rBC mass size distribution was extrapolated for the cases where the *MMD* lies in the size range of the SP2 rBC measurements. In this study, the total rBC mass concentration was derived for 70% of the observed aerosol layer sequences (Figure 54). For these sequences, the SP2 measured 55–89% (median: 80%) of the total rBC mass concentration, implying that the remaining fraction of the rBC mass concentration (11–45%; median 20%) is outside of the SP2 size range (D_{rBC} < 80 nm or D_{rBC} > 440 nm). Larger particles have high particular rBC masses, while smaller rBC particles affect the mass due to their large abundance.

For the remaining 30% of the sequences and typically for fresh combustion aerosol layers, the majority of the rBC particles and thus the *MMD*s are smaller than the lower detection limit of the SP2 (< 80 nm), inhibiting the determination of the total rBC mass concentration.

The total rBC mass concentrations vary by more than a factor of 100 between the aerosol layers with the lowest and with the highest rBC load (3–348 ng m^{-3}). The aerosol layer with the lowest rBC load is, however, defined by the aerosol layer identification method used in this study (Section 3.4.1). Aerosol layers with even lower rBC mass concentrations are present in the atmosphere, but they are not considered in this study. The qualitative

difference between the rBC mass concentrations of layers attributed to specific source regions remains similar to the differences shown in Figure 53.

For comparison, two additional sequences showing fresh PBL aerosol, measured on 16 September 2011, averaged from ground level up to about 500 m a.g.l. and from ground level up to about 1,000 m a.g.l., are added to Figure 54. These two fresh PBL aerosol sequences represent the fresh polluted boundary layer in the vicinity of the metropolitan area of Munich, Germany. The observed aged, lofted aerosol layers (from the European and African PBL and from forest fires) show similarly high rBC mass concentrations as the fresh polluted boundary layer, highlighting the high burdens of BC in those aerosol layers.

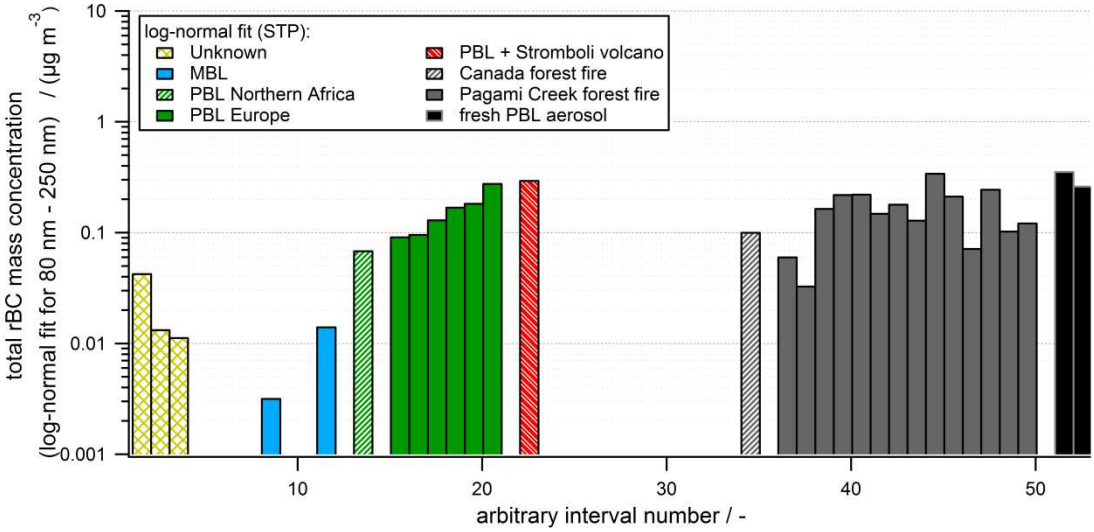

Figure 54. *Same plot as Figure 53 but here as total rBC mass concentration deduced from the log-normal fit applied to the measured rBC mass size distribution as explained in Section 3.3.1 and Figure 31. Only the sequences with viable application of the log-normal fit are shown. Additionally, two sequences showing fresh PBL aerosol measured on 16 September 2011 averaged from ground level up to about 500m a.g.l. (left black bar) and from ground level up to about 1,000 m a.g.l. (right black bar) are shown for comparison.*

BC mass size distributions

Figure 55 shows the log-normal fits of the rBC mass size distribution at stp conditions for the sequences shown in Figure 54[23].

Aged lofted PBL aerosol layers (green) and the volcanic ash layer within the present PBL (red) are presented in Figure 55a. The *MMD* ranges between 88 nm and 150 nm with two layers exhibiting rather large *MMD*s and high rBC mass concentrations, while all other layers shown in Figure 55a are less concentrated with smaller *MMD*s. Figure 55b shows the rBC mass size distributions for the aerosol layer sequences attributed to forest fires, described in detail in Section 4.3. Less concentrated aerosol layer sequences attributed to MBL aerosol and aerosol layer sequences with unknown source region are presented in Figure 55c and Figure 55d, respectively (note the factor 10 between the scaling of the y-axis of the respective panels).

[23] The measured rBC mass size distribution and, if applicable, the associated fit for each aerosol layer sequence, are presented in Appendix 4, color-coded corresponding to the attributed source region with the errors bars representing 15% uncertainty as described in Section 3.4.3.

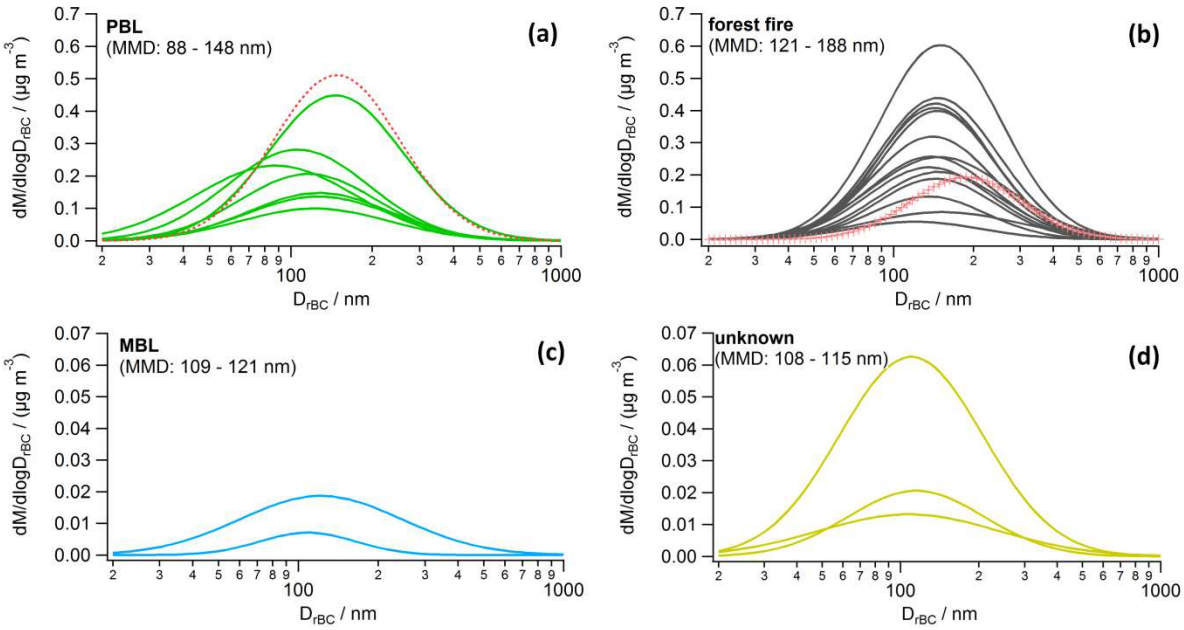

Figure 55. *Log-normal fits of the rBC mass size distribution at stp conditions for the sequences shown in Figure 54. Observed aerosol layer sequences of aged lofted PBL aerosol (green lines) and fresh PBL aerosol mixed with volcanic emissions (red dashed line) in (a), forest fire aerosol layer sequences measured inside the Pagami Creek fire plume (dark grey lines) and the Canadian forest fire plume (light red markers) in (b), aerosol layer sequences originating from the MBL in (c) and aerosol layers originating from unknown sources in (d). The y-axis in (a) and (b) ranges up to 0.7 and in (c) and (d) up to 0.07.*

Table 10 summarizes the results for rBC mass parameters determined for the considered aerosol layer sequences during CONCERT 2011. The presented lower and upper boundaries have to be considered as the boundaries of the aerosol layer observations (see Figure 52), but not necessarily as the real upper and lower boundary of the aerosol layer, based on to the flight track of the Falcon. In addition to the attributed source, the rBC mass concentration in the size range $80 < D_{rBC} < 440$ nm is listed. For those layers where the log-normal fit approach was applicable to determine the total rBC mass concentration, the parameters of the log-normal fit, the *MMD*, the *GSD*, and the total rBC mass concentration at stp conditions are given. The stp factors are added as conversion factors to ambient conditions.

For the sequences with applied log-normal fit, the total rBC mass concentrations vary between < 5 ng m^{-3} and 350 ng m^{-3}, while the *MMD*s and the *GSD*s are 88–188 nm and 1.52–2.22, respectively. Due to an internal heterogeneity within BC-containing aerosol layers, locally higher BC mass concentrations can be expected.

The highest rBC mass concentrations (> 420 ng m^{-3}) were observed in an aerosol layer for which the total rBC mass concentration could not be determined by applying a log-normal fit. Thus, even higher total BC mass concentrations for the aerosol layer showing the maximum rBC load have to be assumed. However, this aerosol layer was observed in an in-cloud sequence, which underwent distinctly different microphysical and chemical processes, transforming the properties of the aerosol particles. For example, parts of the rBC can be embedded in ice crystals or cloud droplets larger than the cutoff of the aerosol inlet and consequently cannot be measured by the SP2.

Table 10. *Overview of the observed aerosol layers during CONCERT 2011. For each observation sequence the flight ID, the vertical boundaries of the observation, the attributed source, the rBC mass concentration in the size range 80 < D_{rBC} < 440 nm, the parameters of the log-normal fit (if applicable) and the stp factors are given. The fit parameter defining the area of the curve is simultaneously the total rBC mass concentration. Blue italics mark in-cloud sequences (see text). LRT-NA: long-range transport from northern America; FF forest fire; PC: Pagami Creek; EVE: Etna volcanic emissions; SVE: Stromboli volcanic emission; fPBL: fresh PBL aerosol.*

Flight ID	Observed aerosol layer sequences		Attributed source	rBC mass concentration 80 < D_{rBC} < 440 nm	Log-normal fit parameters			stp factor
	Lower boundary / km	Upper boundary / km	/ -	(stp) / ng m^{-3}	*MMD* / nm	*GSD* / -	Total rBC mass concentration (stp) / ng m^{-3}	/ -
#110907a	2.6	3.0	MBL	2.3	-	-	-	1.48
	3.7	*5.3*	*MBL*	*3.1*	*-*	*-*	*-*	*1.81*
	3.4	*3.9*	*MBL*	*2.7*	*109*	*1.52*	*3.2*	*1.62*
	2.0	3.2	MBL	2.0	-	-	-	1.43
	10.1	*10.7*	*LRT-NA*	*107.6*	*-*	*-*	*-*	*3.66*
#110916a	*1.8*	*2.0*	*LRT-NA*	*17.3*	*-*	*-*	*-*	*1.27*
	2.2	3.4	FF Canada	89.6	188	1.62	101.7	1.47
	3.4	4.5	Unknown	32.4	110	1.89	43.2	1.68
	10.4	10.4	FF PC	125.4	149	1.83	167.4	3.64
	10.8	11.0	FF PC	191.8	143	1.65	223.7	3.90
	10.9	11.0	FF PC	202.1	144	1.63	224.9	3.94
	10.9	11.0	FF PC	121.6	138	1.72	151.1	3.93
	10.9	11.0	FF PC	154.6	140	1.69	182.5	3.93
	10.9	11.0	FF PC	109.7	136	1.71	131.2	3.93
	11.2	11.5	FF PC	294.2	150	1.70	348.0	4.15
	10.1	11.6	FF PC	184.3	146	1.64	216.2	3.94
	10.9	11.0	FF PC	27.6	121	1.75	33.3	3.92
#110916b	2.0	3.3	PBL	74.3	127	1.87	92.6	1.47
	11.0	11.2	FF PC	64.1	135	1.65	72.8	3.94
	11.1	11.3	FF PC	214.9	147	1.68	249.0	4.07
	11.0	11.1	FF PC	88.8	144	1.66	104.4	3.90
	10.9	11.0	FF PC	100.4	148	1.72	123.7	3.90
	8.7	9.5	FF PC	42.1	153	1.94	61.1	3.04
#110917a	2.2	3.0	PBL	75.8	127	1.83	97.5	1.45
	3.0	4.3	PBL	54.6	122	1.90	69.5	1.62
	4.6	5.7	MBL	5.9	-	-	-	1.90
	2.1	3.6	PBL	105.3	116	1.80	131.9	1.44
#110922a	*4.7*	*5.4*	*LRT-NA*	*424.8*	*-*	*-*	*-*	*1.80*
#110922b	*6.5*	*6.9*	*LRT-NA*	*155.4*	*-*	*-*	*-*	*2.15*
#110924a	1.7	2.7	PBL	94.3	88	1.98	171.8	1.39
	3.1	4.6	Unknown	11.0	115	1.82	13.5	1.67
	1.8	4.9	Unknown	6.7	108	2.22	11.4	1.46
#110927a	1.5	2.7	PBL	131.4	106	1.84	185.8	1.37
	2.7	4.6	Unknown	12.5	-	-	-	1.61
#110929a	3.3	3.3	EVE	17.3	-	-	-	1.56
#110930a	0.4	2.2	PBL	231.3	146	1.78	280.8	1.25
	0.9	0.9	SVE + fPBL	267.2	148	1.71	299.6	1.21
	3.5	3.5	EVE	4.1	-	-	-	1.59
	3.0	3.0	EVE	4.8	-	-	-	1.51
#110930b	2.0	3.3	MBL	9.7	122	2.02	14.3	1.44

In-cloud sequences are aerosol layer sequences 2, 3, and 5 on flight #110907a, sequence 1 on flight #110916a, and the aerosol layer sequences on flights #110922a and #110922b (Table 10). Apart from sequence 3 on flight #110907a, the log-normal fit was not applicable

for any of these sequences. Thus and because of general challenges for in-cloud aerosol measurements (e.g. Baumgardner et al., 2011), these sequences were not considered in major parts of the further discussions. Consequently, Figure 54 and Table 10 give a valuable overview of BC mass concentrations expected in different types of aerosol layers observed over Europe, though distributions with *MMD*s < 80 nm are missing. The wide variation between the rBC mass concentrations and the distribution (e.g. with *MMD*s from < 80 nm up to 188 nm) shows the heterogeneous characteristics of BC in aerosol layers and implies a wide range of interactions with the other aerosols, trace gases, clouds and the radiation.

Figure 56 shows the relation of the *MMD* as a function of the *GSD* for the size range 80 < *MMD* < 440 nm. An indication of a negative correlation is visible for aged lofted PBL aerosol layers, potentially attributable to an increasing *MMD* and a decreasing *GSD* with increasing age. However, for the remaining sources the correlation is less distinct, partly caused by the low sample quantity. For the Pagami Creek fire, the sequences show large variations in the *GSD* (1.63–1.94), while the *MMD* is more stable, which will be discussed in detail in Section 4.3.

Considering all observed sequences, a range is determined (grey dashed lines in Figure 56), to which the relations of *GSD* to *MMD* of all sequences are allocated (except for one in-cloud sequence). This range indicates that an aging of the rBC mass size distribution is observed, by e.g. the aged forest fire plumes showing small *GSD*s and large *MMD*s. However, in this study, the exact source and thus the age of the aerosol layers could just be determined for the minority of the aerosol layers. Consequently, a detailed investigation of the relation between *MMD* and *GSD* remains a feature to be studied in the near future. To characterize this behavior in detail, a comprehensive analysis of the age of aerosols and their interactions with the atmosphere during the transport, like washout, needs to be realized.

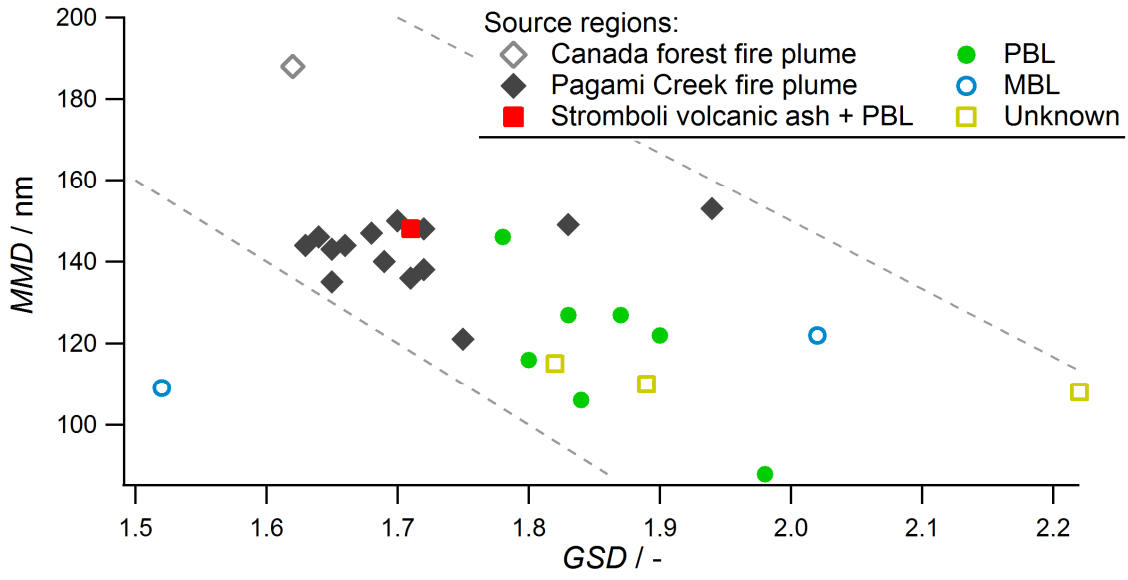

Figure 56. *Relation of MMD to GSD of the rBC mass size distributions of the aerosol layers observed during CONCERT 2011 for 80 < MMD < 440 nm. Dashed grey lines represent approximated boundaries of the relation.*

Color ratios

Aerosol layers can contain different types of BC (e.g. Laborde et al., 2012a; Laborde et al., 2013), characterized by, e.g., different boiling point temperatures. As an indicator for the boiling point temperatures of different BC types, the color ratio (Section 3.4.3), derived from the SP2 data, can be used. Figure 57 shows the median color ratios as functions of the peak height, measured with the BID of the SP2 as a proxy for the BC mass of individual rBC particles. For all types of aerosol layers, a decrease of the color ratio towards higher BC masses, i.e. towards higher BID peak heights, can be observed.

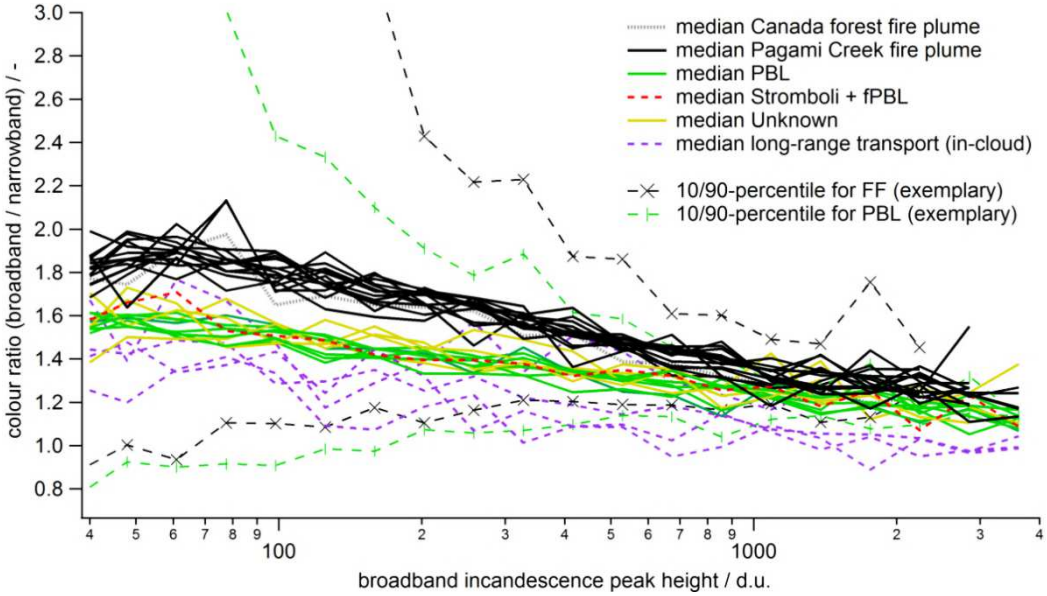

Figure 57. *Median color ratios for the observed aerosol layers presented as a function of the peak height of the BID, i.e. the mass of the BC particle. To show the range of the observed color ratios, the 10- and 90-percentiles are shown generically for one sequence measured in the Pagami Creek fire plume and one in an aged lofted PBL aerosol layer (dashed lines with markers). Due to insufficient counting statistics, data for aerosol layers attributed to volcanic emissions and to the MBL are not shown. (FF: forest fire aerosol; fPBL: fresh PBL aerosol).*

However, in comparison, the color ratios observed in the forest fire aerosol layers are distinctly larger compared to the color ratios observed for the remaining aerosol layers, indicating a higher boiling point temperature of BC particles in forest fire plumes.

The color ratios for the observed sequences, excluding in-cloud sequences and forest fire plume sequences, are similar and show only little variation in this study. This indicates that similar BC material is found in those aerosol layers, which can very likely be ascribed to anthropogenic sources. Those color ratios can be differentiated from color ratios found for BC from boreal forest fire aerosol layers.

In Figure 57 the 10-/90-percentiles are shown as examples for one forest fire plume sequence and one aged lofted PBL aerosol layer. The generically shown ranges are representative for all other sequences. Corresponding to the shown medians, the 10-/90-percentiles for forest fire aerosols are slightly higher compared to the sparse aerosol layers. However, large variations of the color ratios are present, even within an aerosol layer population originating from one specific source like PBL aerosol. This range between the 10-percentile and the 90-percentile clarifies the heterogeneity of BC particles in aerosol layers covering a wide range of color ratios, especially for particles with smaller BC masses.

Even so, the presented values suggest that forest fire BC has, on average, a higher boiling point[24] compared to BC from the sparse sources. Schwarz et al. (2006) speculate that structure of the BC particle or impurities play some role in measured color ratio. Differences in the structure of BC, very likely associated with the combustion conditions, modify the potential of the particle to interact with the radiation or with atmospheric components (e.g. Martins et al., 1998). Thus, the color ratio is a useful quantity to investigate the boiling point of BC particles, a proxy for BC types and eventually BC structures.

Diverging from the described sources, in-cloud sequences show the lowest color ratios. Those low values might be an indication for several features:

1) The structure of the BC particle influences the color ratio (Schwarz et al., 2006). Thus, a transformation of the BC particle when being embedded in cloud droplets might cause a change in its structure, e.g. a collapse of the fractal-like aggregates (e.g. Saathoff et al., 2003; Cross et al., 2010), and thus in its boiling point.

2) Due to the low statistics of aerosol layer sequences, generally it has to be taken into account that the in-cloud sequences contained by chance a different BC type.

3) It is also possible that measurement artifacts during cloud sequences cause the change of the color ratio by, e.g., measuring a different type of refractory material. It is conceivable that e.g. metal from the aerosol inlet or the sampling line is released when measuring in clouds.

However, which feature causes the difference of the color ratio of BC from in-cloud measurements needs to be investigated in further detail, e.g. with cloud chamber experiments.

4.2.3 Characteristics of the total particle number size distributions of elevated aerosol layers

In the observed aerosol layers less than 25% (median: 9%) of the particles in the SP2 size ranges are BC-containing particles. Thus, to account for BC-free particles, total particle number size distributions, including BC-containing and BC-free aerosol particles, were derived for the observed aerosol layers based on measurements with the OPCs, the SP2 and the CPCs (see Section 3.4.4)[25].

Figure 58 shows the size distributions for the available sequences with measured number size distributions (diamonds) and the applied log-normal fits (line), separated for the attributed sources. The parameters of the fits are shown in Table 11. The total number concentration, i.e. the sum of the number concentrations N_j of the three modes, is taken from the CPC measurements, delivering the integral particle number concentrations for particles 10 nm < D_P < $D_{cutoff,50}$ with $D_{cutoff,50}$ being ~ 1.5 µm at high altitudes. The fit represents the number size distribution of the Aitken mode, the accumulation mode, and, if existing, the coarse mode.

[24] For data sets using different SP2 setups, different amplifications of the incandescence detectors will result in not comparable color ratios.

[25] In-cloud sequences and time-sequences with a lack of size distribution information, caused by defective measurements or not mounted instruments for specific flights, were excluded.

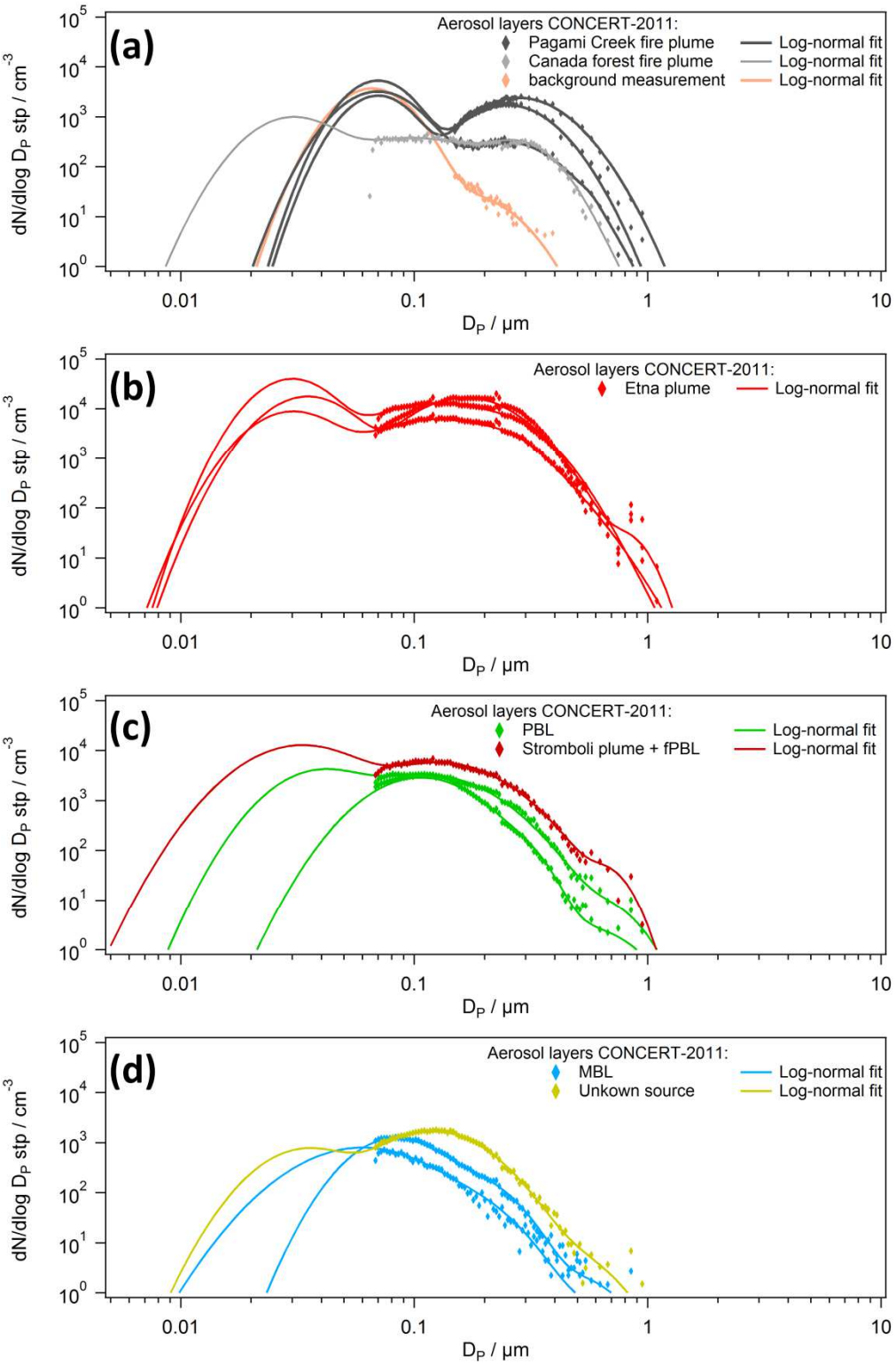

Figure 58. *Number size distributions (stp) of aerosol layer sequences during CONCERT 2011. In-cloud sequences were excluded. Number size distributions are extrapolated by log-normal fits (lines) for the respective measurements (markers) for forest fire sequences showing the maximum, median and minimum sequence for the Pagami Creek fire plume (dark grey), the Canada forest fire plume (light grey) and the background aerosol sequence (related to Section 4.3 and Figure 77) in (a), volcanic ash plumes of the Etna volcano in (b), aged lofted PBL aerosol layers (green) and the Stromboli volcano plume mixed with fresh PBL (fPBL) aerosol (red) in (c), and aerosol layers attributed to the MBL (blue) and attributed to unknown sources (yellow) in (d). The parameters of the fits are presented in Table 11.*

To ensure that the omission of the nucleation mode for the aerosol layer sequences during CONCERT 2011 is reasonable, the number concentration of CPCs with varying lower cutoffs, e.g. 4 nm and 10 nm, are compared as an indicator for nucleation events. The small differences between the measured number concentrations (not shown) indicate low particle number concentrations in the nucleation mode for the aerosol layer sequences during CONCERT 2011 and confirmed the assumption of a negligible nucleation mode.

Table 11. *Parameters of the log-normal fits of the number size distributions presented in Figure 58 at stp conditions. For each sequence the flight ID, the attributed source, and the parameters of the log-normal fits are given (FF: forest fire; PC: Pagami Creek; EVE: Etna volcano emissions; SVE: Stromboli volcano emission; fPBL: fresh PBL aerosol).*

Aerosol layer sequence	Source	N_1 / cm^{-3}	GSD_1 / -	CMD_1 / nm	N_2 / cm^{-3}	GSD_2 / -	CMD_2 / nm	N_3 / cm^{-3}	GSD_3 / -	CMD_3 / nm
#110907a_1	MBL	428	1.640	60	15	1.390	175	0.2	1.350	450
#110916a_2	FF Canada	350	1.400	30	230	1.750	100	80	1.320	280
#110916a_3	Unknown	308	1.450	35	745	1.500	120	2	1.400	440
#110916b_1	PBL	1273	1.500	107	13	1.225	282	1	1.430	550
#110916 PC max	FF PC	760	1.300	70	957	1.440	281	-	-	-
#110916 PC median	FF PC	1517	1.300	70	641	1.406	251	-	-	-
#110916 PC min	FF PC	1077	1.360	70	130	1.455	243	1	1.100	550
#110916 background		1131	1.325	66	9	1.400	175	-	-	-
#110929a_1	EVE	13000	1.350	30	7000	1.650	120	1000	1.380	250
#110930a_1	PBL	1600	1.450	40	1662	1.610	115	2	1.300	650
#110930a_2	SVE + fPBL	6100	1.550	33	2900	1.600	130	7	1.200	660
#110930a_3	EVE	6495	1.400	35	7500	1.500	165	5	1.200	800
#110930a_4	EVE	3200	1.400	30	3600	1.700	125	200	1.260	250
#110930b_1	MBL	450	1.400	83	60	1.370	175	0.6	1.350	500

Figure 58a shows predominantly bimodal number size distributions of the observed forest fire aerosol layers. The comparison to the background aerosol sequences shows that the accumulation mode is mainly caused by the forest fires (discussed in detail in Section 4.3.4). The young volcanic ash layers from the Etna volcano (Figure 58b) show a similar bimodal structure, though with far higher concentrations and *CMD*s shifted towards smaller particle sizes compared to the forest fire aerosol from the Pagami Creek fire. The volcanic ash results are internally consistent, exhibiting similar number size distributions as expected for a plume of one specific volcano without changing eruptive characteristics, in this case the degasing Etna volcano. Figure 58c shows the number size distributions for aged lofted PBL aerosol layer sequences (green) and a sequence representing the Stromboli volcano plume mixed with fresh, current PBL aerosol (dark red). While the mixed (Stromboli plume + fresh PBL aerosol) aerosol layer shows characteristics of a bimodal structure, for the aged lofted PBL aerosol layers, the bimodal structure is just slightly discernible or not present. For these sequences the separation between Aitken and accumulation mode becomes indistinct and smaller particles are far less abundant compared to the fresh PBL aerosol mixed with the Stromboli plume. However, for both, the Etna volcano and the Stromboli volcano, low particle number concentrations were observed in the coarse mode (D_P > 1 µm) related to

the low activities of the volcanoes during the measurements. The presented number size distribution of the aerosol layer not attributable to a known source (*unknown*; Figure 58d) shows a less pronounced bimodal structure with higher concentrations in the accumulation mode. In comparison, the aerosol layers attributed to MBL aerosol (Figure 58d) show a predominantly monomodal size distribution covering the Aitken and accumulation mode, with only low concentrations being observed for larger particle sizes. These aerosol number size distributions attributed to the MBL are similar to the aged lofted PBL aerosol layers, though exhibiting number concentration almost one magnitude lower.

The observed aerosol layers vary with almost two orders of magnitude in their total number concentrations. Besides widely varying total concentrations, the variable shapes of the Aitken and the accumulation mode, ranging from distinctly separated modes to merging modes, represent the most prominent difference between the aerosol layers attributed to the specific source regions. The specific appearance of the size distributions, partly showing a fusion of the modes for some of the aerosol layers, is caused by a) the source defining the original size distribution and b) the transportation including dilution, transformation, mixing, and removal processes.

To test for the significance of the variations between the number size distributions of aerosols of different origin, the ranges of the size distributions from specific sources are determined based the distributions shown in Figure 58 including uncertainties for the number concentrations. For the size range measured with the OPCs and the SP2 20% uncertainty are added. For the extrapolated size range, i.e. < D_{cutoff} of the measured size distribution, 50% uncertainty in the number concentrations are added. Thus, Figure 59 shows the ranges of the total number size distributions for the specific aerosol layer types. Abrupt changes for the shown ranges are caused by the described difference in the considered uncertainties (50% for the size range < D_{cutoff} of the measured size distribution and 20% for the measured size distribution) and by the determination of the minimum and maximum values based on different measurement sequences (see Figure 58).

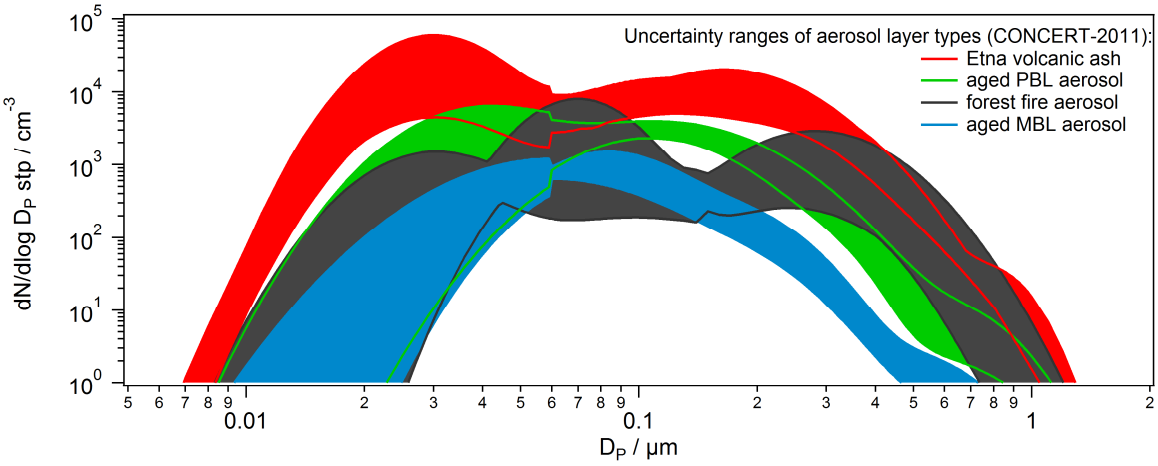

Figure 59. *Uncertainty ranges of the total number size distributions shown in Figure 58: Etna volcanic ash (red), aged PBL aerosol (green), aged forest fire aerosol (black) and aged MBL aerosol (blue) observed during CONCERT 2011. The area between upper and lower lines of the same color represents the range for the observed number size distributions of the specific aerosol types. See text for methodological details.*

Figure 59 shows significant differences of size distributions of fresh volcanic ash aerosol (here from the Etna volcano) and aged MBL aerosol. In addition, the ranges of size distributions of fresh volcanic ash aerosol and aged PBL aerosol only overlap in a minor size range (about 300–700 nm). In the measured size range even aged MBL and aged PBL aerosol can significantly be distinguished. However, due to higher uncertainties in the extrapolated size range the differences between aged PBL aerosol and aged MBL aerosol are insignificant. The size distributions of the forest fire aerosol layer observations overlap with the ranges of the number size distributions of all other aerosol types.

Figure 60 shows number size distributions of fresh MBL aerosol and the number size distribution for the volcanic ash plume of the Eyjafjalla volcanic eruption in 2010 for comparison to the observed number size distributions of MBL aerosol and volcanic ash layers, respectively.

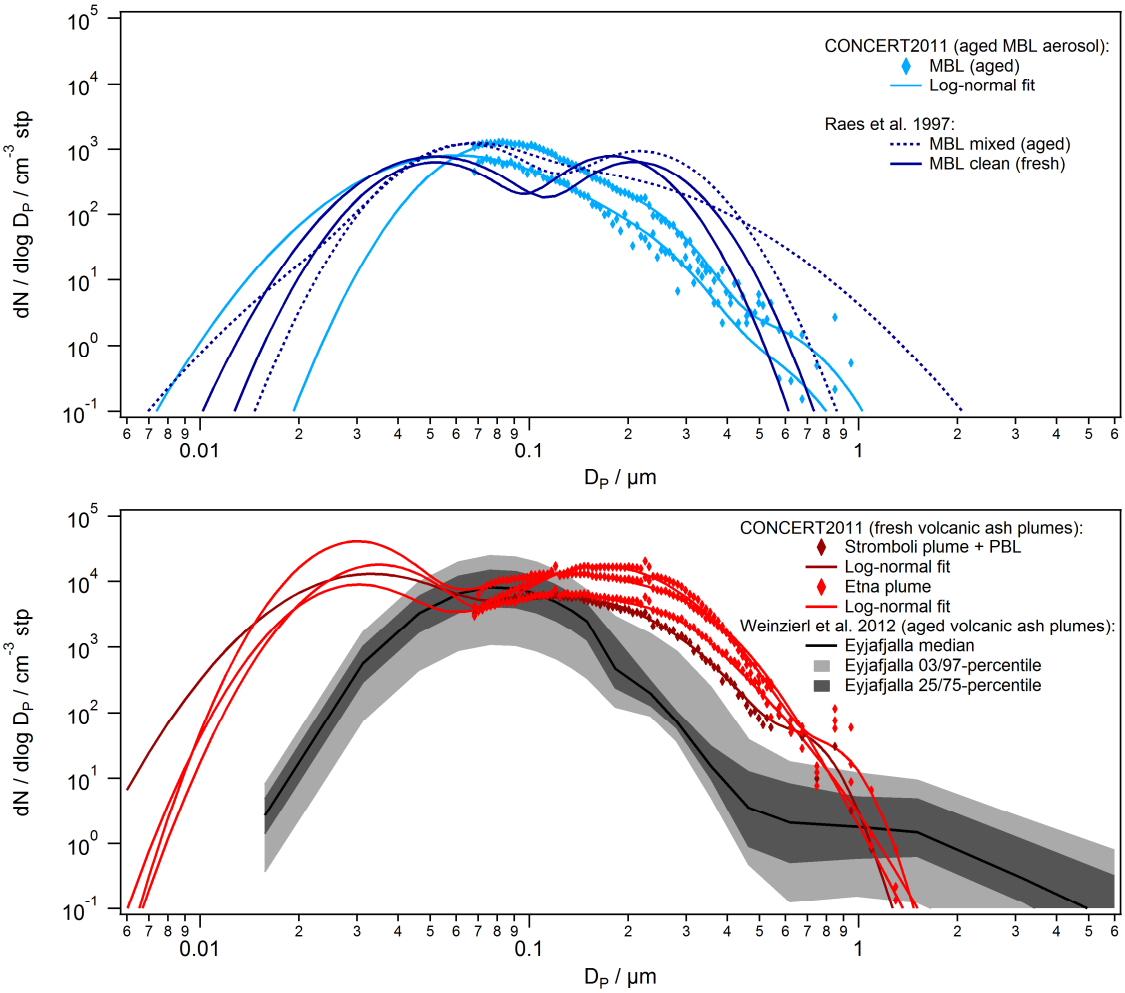

Figure 60. *Comparison of the number size distributions of observed aged MBL aerosol layers aerosol and number size distributions for mixed and clean MBL aerosol from Raes et al. (1997) (upper panel, and comparison of the number size distributions of observed volcanic emissions and the Eyjafjalla volcanic ash plume (ambient values) (Weinzierl et al., 2012) (bottom panel).*

In comparison to the results from this study, mixed and clean MBL aerosols (Raes et al., 1997) show a bimodal number size distribution, with the more distinct structure for the clean MBL aerosols (Figure 60; upper panel). In contrast, the rather monomodal distributions from this study do not contain high number concentrations in the

accumulation mode. This difference might be caused by the transformation and processing of the aerosol during the transport, which will influence the aged aerosol layer from CONCERT 2011 considerably more in comparison to the fresh MBL aerosol. The similarity of the aged MBL aerosol to the mixed MBL aerosol (Raes et al., 1997) suggests that the aged MBL aerosol layers observed during CONCERT 2011 show characteristics of mixed aerosol and thus probably underwent mixing with other aerosol types during the transport. Compared to BC sources in the PBL, in fresh MBL aerosol, a very low fraction of BC is expected because of sparse BC sources like shipping in the MBL (Bond et al., 2013). However, in Section 4.2.2 it was shown that the measured sequences contained a considerable amount of BC (rBC-containing particle number fraction in the SP2 size ranges: 4–8%). Thus, it is likely that the airmass initially contained BC before the transport through the MBL or that the initially pure MBL aerosol mixed during transport to the measurement location with BC-rich airmasses.

In contrast to the number size distribution of volcanic ash layers observer during CONCERT 2011, the number size distribution of the Eyjafjalla volcanic ash plume (Weinzierl et al., 2012) exhibits a pronounced mode between about 30 nm and 200 nm and a distinct coarse mode (Figure 60; bottom panel). These differences might be caused for the following reasons:

1) The Eyjafjalla volcanic ash plume arose from an intensive eruption event, while the plumes from the Etna and the Stromboli were emitted during low activity periods of the volcanoes. Thus, the emitted size distributions were already distinctly different, e.g. no coarse mode particles were emitted via explosive eruptions by the Etna and the Stromboli volcanoes.

2) The Eyjafjalla volcanic ash plume was measured after 7 hours to 5 days after the emission. In contrast, the Etna and Stromboli plumes were measured shortly after emission. Thus, aging and transformation as a function of plume age have influenced the distribution, e.g. by shifting the *CMD*s towards larger particle sizes. Note that the results for the Eyjafjalla volcano are given as ambient values, implying that the concentrations cannot be compared directly. Nevertheless, this does not influence the described difference in the shapes of the distributions.

The presented comparisons clarify the variations of the number size distributions present in aerosol layers attributed to the same source. In summary, the processing of the aerosol during the transport significantly influences the distributions, partially controlled by the atmospheric conditions during transport, and whether interactions with clouds or other aerosol species occur. However, the number size distributions might already vary widely based on the emission conditions at the source, e.g. for volcanic emissions based on the volcanic activity or the source material, and for MBL aerosol based on the atmospheric conditions during the emissions, e.g. wind velocity or wave characteristics. This complexity creates a high uncertainty for the parameterization of aerosol layers attributed to different source regions. However, this study presents a generic range of size distributions, which can be expected for different aerosol types for September in Central Europe.

4.2.4 Mixing state of BC-containing particles

As already shown in Section 2.2.2, the internal mixing state of individual particles plays a significant role on the impact of aerosol particles on the atmosphere. In this context, the coating thickness of individual particles measured by the SP2 delivers information on the mixing state of individual particles (Section 3.4.3). Figure 61 presents coating thickness histograms for the presented aerosol layer sequences separated by their attributed source.

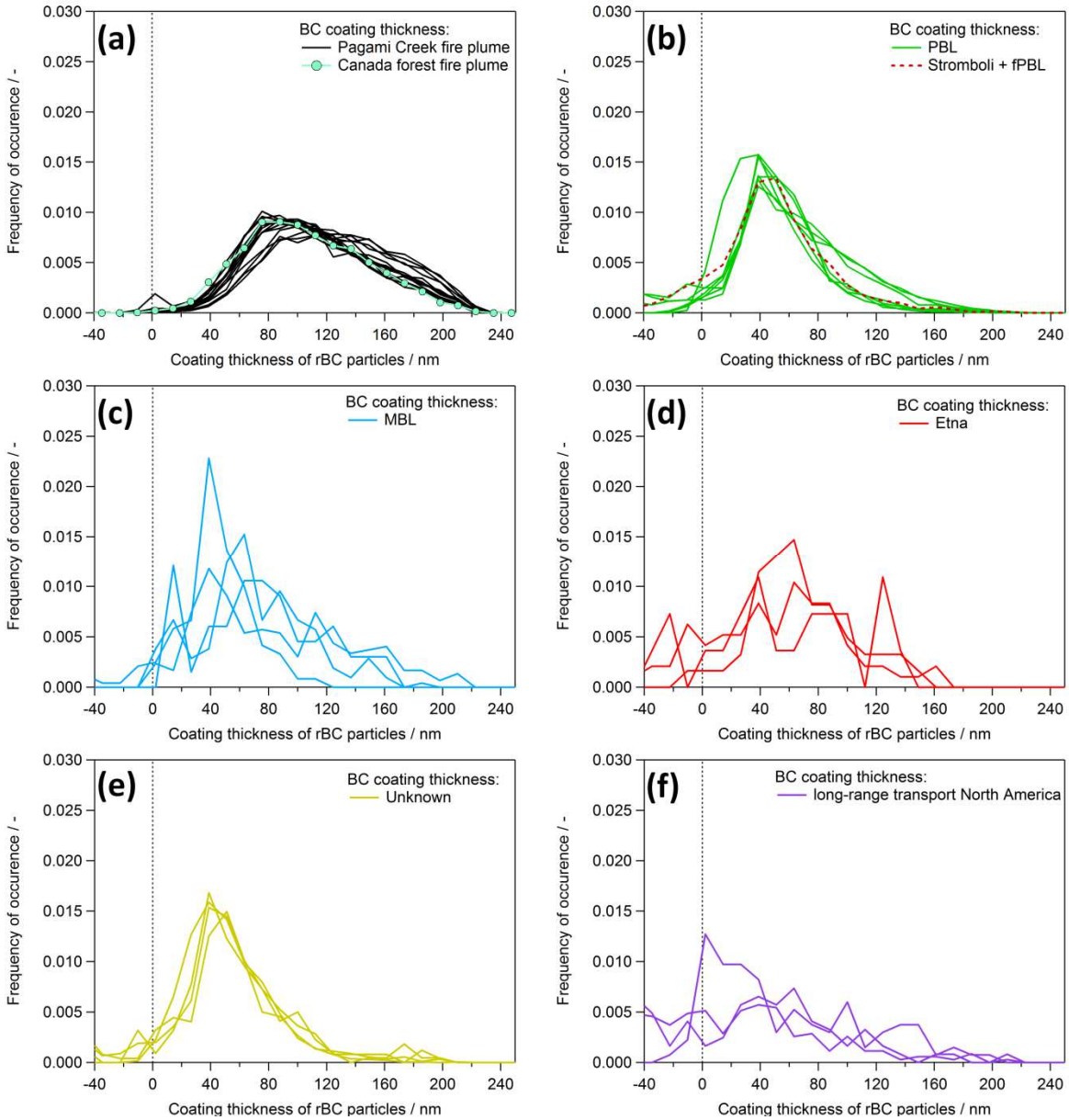

Figure 61. *Coating thickness histograms for aerosol layer sequences attributed to forest fires (a), aged lofted PBL aerosol (b), MBL aerosol (c), volcanic ash layers from the Etna volcano (d), unknown sources (e) and long-range transport from North America (f). In (b) a differentiation is made for aged lofted PBL aerosol layers (green solid line) and Stromboli volcano emissions mixed with fresh PBL (fPBL) aerosol (red dashed line). The histograms contain data from all rBC-containing particles detected by the SP2.*

Figure 61a shows coating thickness histograms for forest fire aerosol layer sequences (discussed in detail in Section 4.3.5), ranging between 40 nm and 220 nm with a maximum

at about 80 nm. In contrast to that, the coating thickness histograms for aged lofted PBL aerosol layers and current PBL aerosol mixed with Stromboli volcano emissions (Figure 61b) show a maximum at roughly 40 nm with a maximum coating thicknesses of roughly 180 nm. It is notable that the current PBL aerosol shows the same structure as the aged lofted PBL aerosol. The coating thickness histograms for aerosol layers of unknown source (Figure 61e), have similar structures as the aged lofted PBL aerosol layers with the majority of the coating thicknesses between 0 nm and 120 nm. On the other hand, due to less abundant rBC-containing particles[26] in the aged lofted MBL aerosol layers (Figure 61c), volcanic ash plumes of the Etna volcano (Figure 61d) and long-range transport aerosol layers (Figure 61f), the histograms show noisier and less clear structures with the bulk of the coating thicknesses ranging between 0 nm and 160 nm.

Coating thicknesses < 0 nm are caused by uncertainties based on the assumptions made in the coating thickness approach, e.g. the assumption of particle sphericity, a specific rBC density and refractive indices. In addition, the histograms only summarize information for those rBC particles in the SP2 size range for which the coating thickness method was applicable. The data is limited by lower detection limits and saturation effects of the detectors as a function of the rBC diameter and the coating thickness. The maxima of the coating thickness histograms at 40 nm (e.g. in Figure 61b and e) are caused by these methodological limits.

In reality (without these methodological limits) it is possible that the maximum of the coating thickness histogram is lower, i.e. that the majority of the particles are coated with coatings < 40 nm. This issue will be explained in the following:

Figure 62 shows the relation between the rBC core diameter and the coating thickness for fresh PBL aerosol (a), for aged lofted PBL aerosol layers (b), and for sequences in the Pagami Creek fire plume (c) as color-coded 2D-histograms. The color represents the number of occurrence of the combination of the rBC core size and the coating thickness in the respective size bins. The edged shape, which is indicated with grey lines in Figure 62c, represents the boundaries of the method due to the lower particle detection limits and saturation issues. Due to this edged shape, the combination of small rBC particles and small coating thicknesses cannot be assessed by this method, creating a gradual bias for coating thicknesses < 40 nm if combined with rBC particles < 120 nm. If the majority of the rBC particles are small with a thin coating, the lack of information for this combination leads to a decrease in the coating thickness histogram at roughly 40 nm towards smaller coating thicknesses as visible, for example, in Figure 61b and e.

As discernible in Figure 62c, this issue plays no role for the majority of observed particles of the considered forest fire aerosol layer sequences, due to large coating thicknesses (described in Section 4.3.5).

For aged lofted PBL aerosol layers, this limitation can be identified in Figure 62b: the majority of the rBC particles are small (< 130 nm) with a thin coating (< 100 nm). Thus, the real maxima of the coating thickness histograms (Figure 61b) probably lie at even smaller coating thicknesses.

[26] In the SP2 size ranges, the rBC-containing particle number fraction is for volcanic ash plumes of the Etna volcano < 1% and for the MBL aerosol layers < 8%, while for PBL aerosol layers fractions > 20% are observed.

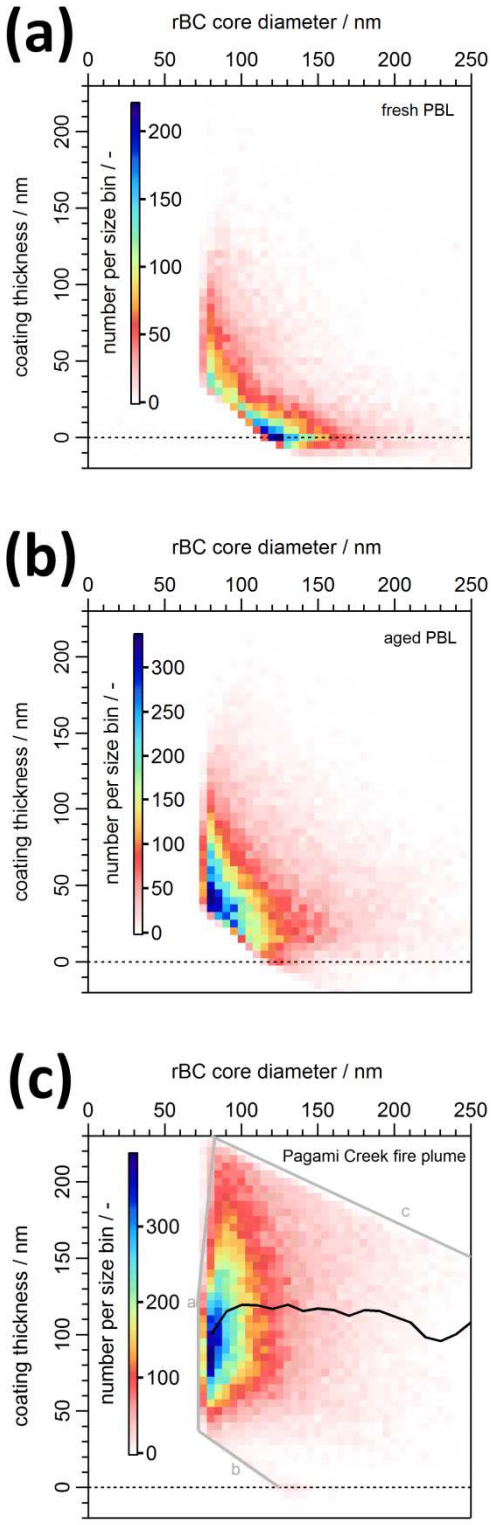

Figure 62. *The relation between rBC core diameter D_{rBC} and coating thickness Δ_{coat} for fresh PBL aerosol (a), for aged lofted (European and African) PBL aerosol layers (b) and for sequences in the Pagami Creek fire plume including the median coating thickness (black line) (c) as 2D-histograms with color-coded frequency of occurrence of the combination of D_{rBC} and Δ_{coat} in the respective size bins. The methodological boundaries are indicated by grey lines (a: BID and NID signal below lower detection limit; b: LSD signal below lower detection limit; c: LSD signal above higher detection limit). The age of the aerosol increases from (a) towards (c).*

The same behavior is discernible in Figure 62a, showing the relation of rBC core size and coating thickness for fresh PBL aerosol observed on 16 September 2011. In comparison to aged lofted PBL aerosol, the fresh PBL aerosol indicates a larger range of rBC core sizes up to roughly 150 nm, while the coatings are thin (< 70 nm).

Besides for the fresh PBL aerosol and the aged PBL aerosol (Figure 62a and b), for the aerosol layers originating from the MBL, volcanoes, long-range transport and unknown sources (Figure 61b–f), this methodological issue causes the maximum at 40 nm, similar to Figure 62b.

Except for the forest fire plumes, the coating thickness histograms (Figure 61) show similar structures for all sources, however, for aerosol from specific sources, e.g. aged lofted PBL aerosol and aerosol from unknown sources, with a higher statistical significance and thus less noise on the histogram due to higher number concentrations of rBC-containing particles. This similarity suggests source independent coating processes taking place for rBC particles of all described sources observed during CONCERT 2011. Based on these results, for Central Europe a typical coating thickness distribution can be assumed for lofted, aged aerosol layers. However, this aged aerosol coating thickness distributions differ significantly from the coating thickness histograms of fresh PBL aerosol observed in Neubrandenburg and Oberpfaffenhofen, both in Germany, as proxy for typical fresh PBL aerosol (Figure 62a).

The wide variations of coating thicknesses observed for the different types of aerosol layers clarifies the relevance of the mixing state of individual particles in the atmosphere, because coatings with shell-core diameter ratios (D_P/D_{BC}) of 2 can already enhance the absorption by 100% (Schwarz et al., 2008b; Shiraiwa et al., 2010). Therefore it is possible that larger coatings might even enhance the absorption of the absorbing core of particles by more than 100%, depending on the coating material. However, Cappa et al. (2012) report a significant difference in the absorption enhancement by coatings between ambient observations and model results with the ambient absorption enhancement observations being lower. Thus, the understanding of the absorption enhancement of mixed atmospheric BC is still incomplete and needs further investigation.

The results of this study suggest 3 specific distributions of coating thicknesses for September 2011, distinguishable for fresh PBL aerosol, aged (elevated) aerosol layers, and the special case of forest fire aerosol layers, indicating specific potentials on the interaction with solar radiation due to the lensing effect (Section 2.2.2). The presented findings allow parameterizing coating thicknesses of BC-containing particles from specific sources, which then can be implemented in models. However, deviations from these particular findings, based on a limited data set, and intermediate coating thickness distributions need to be taken into account, due to different ages of aerosol layers and atmospheric processes. In this context, detailed information on the transportation and mixing help to understand the contributions of the particular effects affecting the coating thickness.

Besides condensed on BC particles, coatings can also enhance the absorption of other absorbing aerosols. The lensing effect of the coating should be investigated for slightly absorbing materials like dust likewise. In addition, the coatings can modify the IN and CCN efficiency significantly. Thus, coatings on aerosol particles are of major relevance in the atmosphere by modifying different particle properties and further studies approaching the coating thickness (on BC, dust, etc.) will help to improve the understanding of the relevance of the mixing state of absorbing particles.

4.3 Characteristics of absorbing forest fire aerosol layers

From the aerosol layers observed during CONCERT 2011 (see Section 4.2), forest fire aerosol layers are investigated in detail in this study, due to significant differences to microphysical properties of other aerosol types, the high burden of BC and the resulting relevance for the absorption of solar radiation. The most interesting aerosol layer was found during CONCERT 2011 on 16 September, when a highly concentrated and more than 3 km thick forest fire aerosol layer was measured in the UTLS region. In addition, a second forest fire aerosol layer was observed in the lower troposphere on the same day. In the following, the observations for these two layers, with the main focus on the forest fire aerosol layer observed in the UTLS region, will be described in detail and the findings will be discussed. This section contains large parts published in Dahlkötter et al. (2014).

4.3.1 Horizontal and vertical dimension of the observed forest fire plumes

On 16 September 2011, two flights were performed with the Falcon. In the first flight (#110916a, 10:48–13:20 UTC), the Falcon flew from Oberpfaffenhofen (EDMO; 48°05' N, 11°16' E, 593 m a.s.l.) in southern Germany to Neubrandenburg-Trollenhagen (ETNU; 53°36' N, 13°18' E, 69 m a.s.l.) in northern Germany. The second flight (#110916b, 14:54–17:48 UTC) was from Neubrandenburg-Trollenhagen back to Oberpfaffenhofen. The scope of these two flights was to sample aged contrails of commercial aircraft. However, more by chance, extended forest fire aerosol layers were also observed.

For the contrail measurements, the aircraft climbed up to more than 10 km altitude and stayed at altitudes between 10 km and 11.8 km for roughly 105 min and 95 min in flights #110916a and #110916b, respectively. As can be seen from Figure 63, showing the time series of rBC mass concentration for both flights, extended levels of rBC mass concentration, not related to thin contrails or aircraft exhaust plumes, were present at high altitudes (> 10 km a.s.l.), indicated as dark grey bars. During these time sequences, the observers in the aircraft noticed broad, greyish-brownish plumes, captured in Figure 64 (photographer: Florian Dahlkötter). Besides this extended high altitude aerosol layer in the UTLS region, a second (low altitude) forest fire aerosol layer was observed at 2.2–3.4 km a.s.l., indicated as a light grey bar in the upper left of Figure 63. As will be shown later, these two extended rBC levels at high and low altitudes are the result of long-range transport of forest fire plumes from the Pagami Creek fire in the USA and from a forest fire in Canada, respectively.

Figure 65 gives an impression of the horizontal distribution of the high altitude forest fire aerosol: the distribution of the observed aerosol layer is indicated by color-coded rBC mass concentrations (size range: $80 < D_{rBC} < 440$ nm) along the flight track. To emphasize upper tropospheric BC during the two flights on 16 September, only values for rBC mass concentrations above 9 km a.s.l. are shown. Observed rBC mass concentrations were as high as 0.67 µg m^{-3} (background: < 0.01 µg m^{-3}) and covered large parts of the measurement area above northeast Germany. For comparison, maximum rBC mass concentrations in the polluted boundary layer over Munich, averaged for 10 s, had similar values (about 0.70 µg m^{-3}) on that day. The sequence of measurement of the low altitude forest fire aerosol layer is indicated in Figure 65 as a blue circle. Due to the ascent of the Falcon during this part of the flight, this aerosol layer sequence is traversed vertically, and thus the aerosol layer was sampled just for a short time.

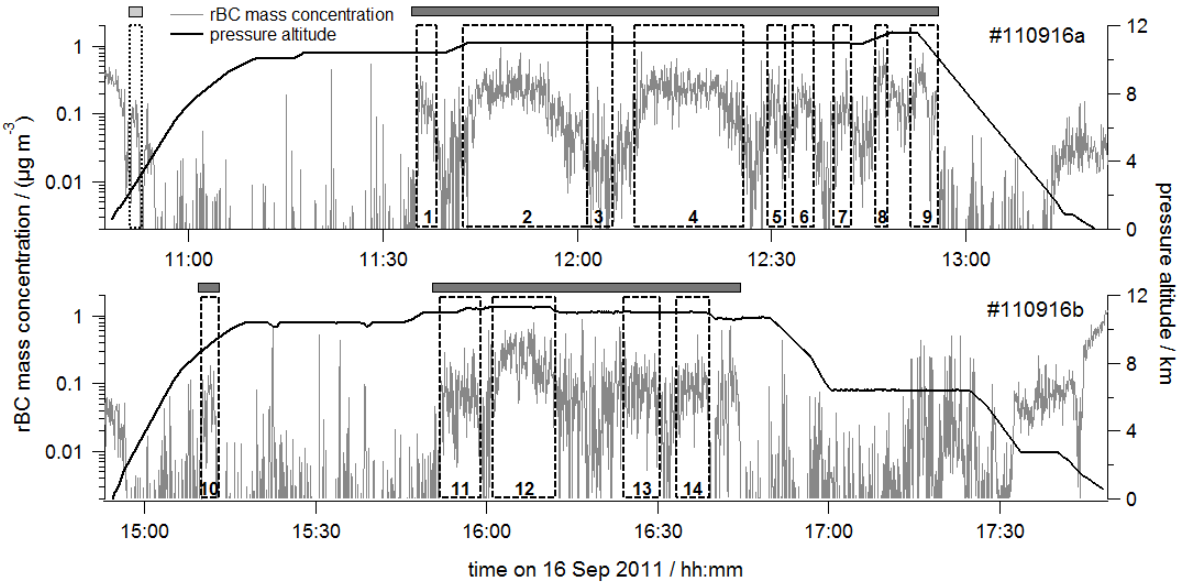

Figure 63. *Time series of the rBC mass concentration (stp) in the SP2 size range (grey lines) for flight #110916a (upper panel) and flight #110916b (bottom panel). The flight altitude is shown in black lines. The dark grey horizontal bars represent the sequences of continuous Pagami Creek fire aerosol layer sampling, i.e. the flight time in the area where the aerosol layer was situated. The dashed boxes represent sequences, which are used for the detailed analysis. These 14 sequences were chosen to represent parts of the aerosol layer with a high burden, as well as parts with a low burden without interference of other aerosol sources like aircraft emissions. The light grey bar and the dotted box at flight #110916a represent the sequence where the Canada forest fire plume was observed. Adopted from Dahlkötter et al. (2014).*

Under the assumption that the Pagami Creek fire plume was located consequently at Falcon cruise altitude, i.e. at 10–12 km, from Figure 63 and Figure 65 it can be concluded that the aerosol layer was limited at the time of the research flights southward roughly to 52° N. It is not possible to determine the northern boundary of the Pagami Creek fire plume, because obviously the Falcon did not reach far enough, so that the layer was still observed at the most northerly location of the flights (~ 54° N). According to the measurements, the layer had a horizontal extension of at least 200 km. The observed and simulated distribution of the plume is supported by data of the GOME-2 Absorbing Aerosol Index (not shown; http://www.temis.nl) (de Graaf et al., 2005), revealing the overall distribution of the plume.

Figure 64. *Photograph of the Pagami Creek fire plume taken from the DLR Falcon research aircraft over Germany on 16 September 2011. Adopted from Dahlkötter et al. (2014).*

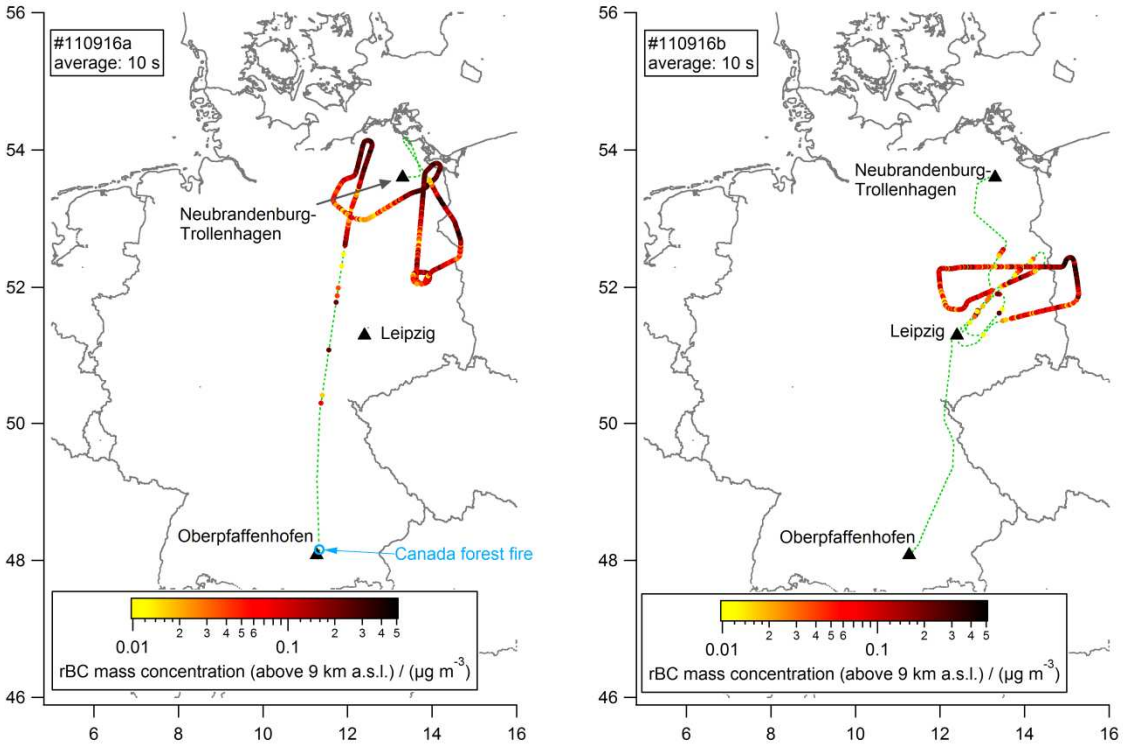

Figure 65. *Flight tracks for flight #110916a (left) and #110916b (right) on 16 September 2011 with averaged (10 s) stp rBC mass concentrations in the size range 80 < D_{rBC} < 440 nm, color-coded along the flight track. For clarity, only rBC mass concentrations for altitudes larger than 9 km a.s.l. are shown. The blue circle and the arrow in the left panel indicate the measurement location of the Canada forest fire plume. Adopted from Dahlkötter et al. (2014).*

Figure 66 shows median vertical profiles of number concentrations of rBC-free (blue line, top panels), rBC-containing particles (black line, middle panels) and rBC mass concentration (black line, bottom panels) for both flights with 100 m vertical resolution. The 25-/75-percentile values are shaded in dark grey, whereas the 10-/90-percentiles are shaded in light grey. The vertical profiles are averaged over the entire flight for altitudes > 2 km (solid line). For altitudes < 2 km in the vertical profiles, two lines indicate the measurements in the PBL over Oberpfaffenhofen (593 m a.s.l.) as a dashed line, always showing larger concentrations, and Neubrandenburg-Trollenhagen (69 m a.s.l.) as a dotted line.

The low altitude forest fire aerosol layer from Canada produces a discernible signal during flight #110916a in the range of 2.2–3.4 km a.s.l. However, the most prominent feature in both vertical profiles is the presence of enhanced aerosol concentrations at altitudes above 10 km a.s.l. associated with the Pagami Creek fire. According to Figure 66, the Falcon did not reach the top of this high altitude aerosol layer.

Nevertheless, not only the Falcon, but also the ground-based lidar at Leipzig observed this aerosol layer on 16 September 2011 in the UTLS. Figure 67 presents lidar observations between 8:36 UTC and 10:30 UTC on 16 September 2011, performed in Leipzig, Germany (51.3° N, 12.4° E), by the Leibniz Institute for Tropospheric Research (TROPOS). In the time series of the 532 nm range-corrected backscatter signal (Figure 67a), extended aerosol concentrations were present between 8 km and 12 km height a.s.l.

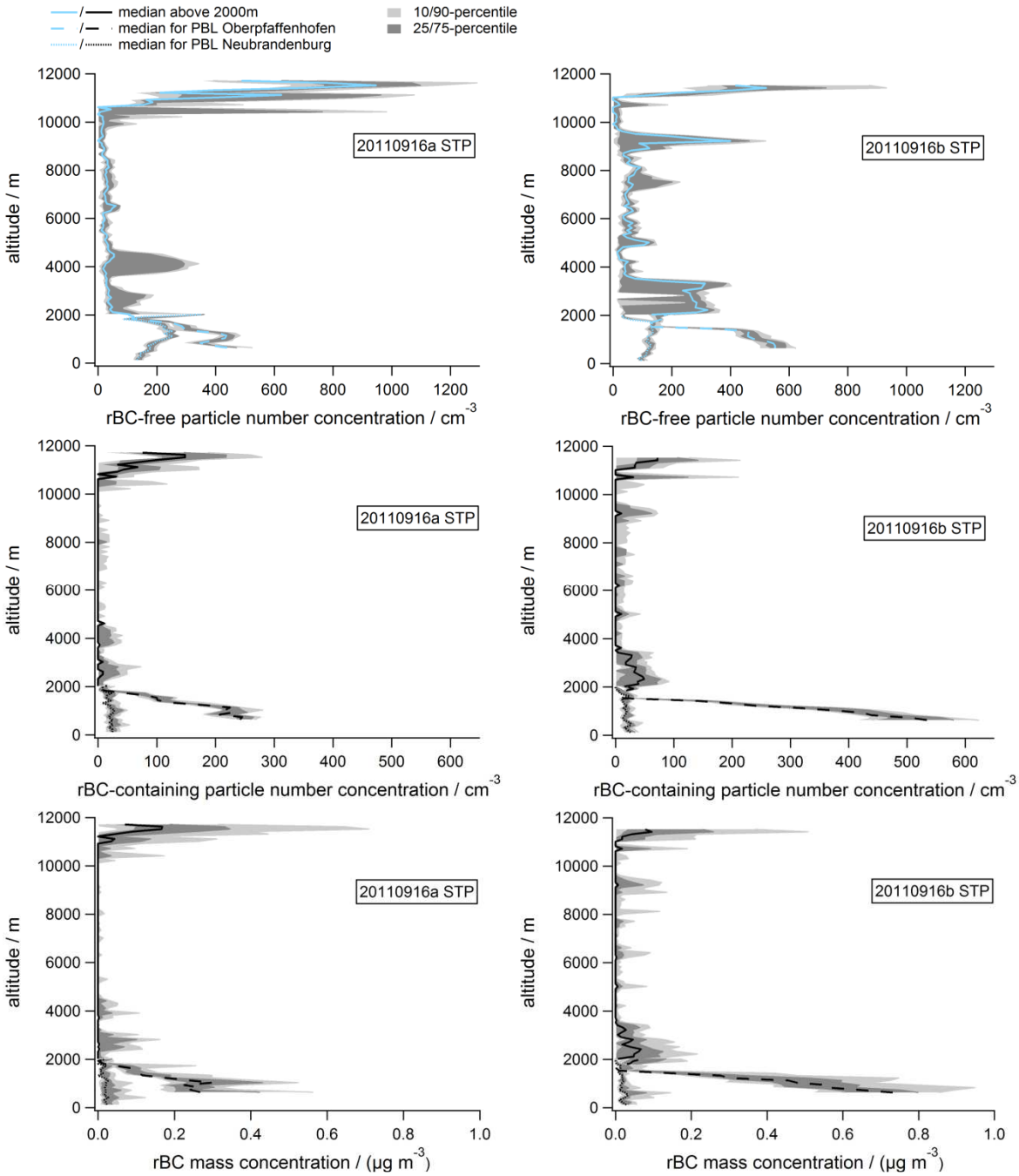

Figure 66. *Vertical profiles (stp) of flight #110916a (left) and #110616b (right) on 16 September 2011 for rBC-free particle number concentration (upper panels), rBC-containing particle number concentration (middle panels) and rBC mass concentration (bottom panels) measured with the SP2 as median (lines), 25-/75-percentile (dark grey), and 10-/90-percentile (light grey) for 100 m vertical intervals. Below 2 km altitude the data set is split into the PBL of Oberpfaffenhofen (593 m a.s.l.; dashed line), showing always higher concentrations, and Neubrandenburg (69 m a.s.l.; dotted line). Values are valid for the approximate size range of 140–285 nm and 80–440 nm for rBC-free particles (upper panels) and rBC-containing particles (middle and bottom panels), respectively. Adopted from Dahlkötter et al. (2014).*

The lidar time-height cross-section confirms the in-situ measurements, showing the maximum of the forest fire layer between 10.0 km and 11.5 km a.s.l. A humid aerosol layer was observed in the boundary layer below 1.5 km altitude, which caused the vertically striped pattern in the signal of the forest fire plume in the UTLS due to partial attenuation of

the laser light. Nevertheless, it is discernible that the base of the aerosol layer slowly descended with time and diminished in the course of the late morning. In addition, a heterogeneous and layered structure of the plume is discernible. At the time of the Falcon flyover (15:43 UTC), neither the Falcon nor the lidar in Leipzig observed signatures of the aerosol layer, supporting that the plume was limited to about 52 °N during the in-situ measurements, as described before.

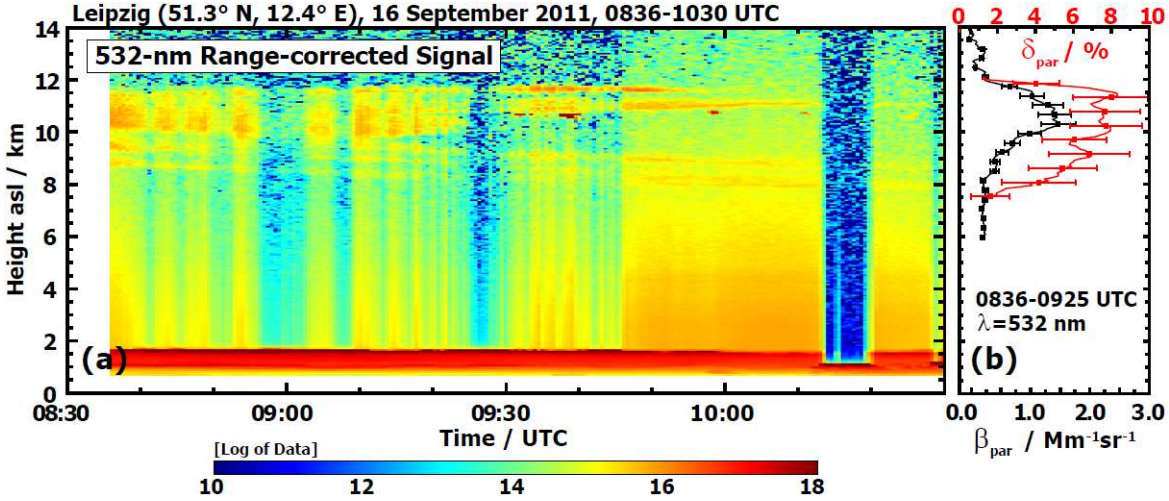

Figure 67. *Time-height cross-section of the 532 nm range-corrected backscatter signal of the lidar system in Leipzig (a) and the vertical profiles of particle backscatter coefficient β_{par} (black curve) and particle depolarization ratio δ_{par} (red curve) with error bars for the time sequence 08:36–09:25 UTC (b). Adopted from Dahlkötter et al. (2014).*

4.3.2 Estimates on the sources and classification of the observed forest fire aerosol layers

The comparison of the rBC-containing particle number concentrations up to 300 cm^{-3} (stp) and rBC-free particle number concentrations up to 1,300 cm^{-3} (stp) in the Pagami Creek fire plume (Figure 66) to the respective concentrations observed in the strongly polluted boundary layer illustrates the unexpectedly high concentrations of the plume at high altitudes. Especially the high amount of rBC-containing particles is unusual for the UTLS region. The rBC-free particle number concentration is consistently higher than in the polluted PBL, and the rBC number concentration is higher than the cleaner PBL of Neubrandenburg and all other observed aerosol layers on that day, but not as high as in the area of Oberpfaffenhofen and Munich. For the Canada forest fire plume (2.2–3.4 km a.s.l.), rBC-containing particle number concentrations up to roughly 70 cm^{-3} (stp) and rBC-free particle number concentrations up to 200 cm^{-3} (stp) are derived for the respective SP2 size ranges from the vertical profiles (Figure 66). Thus, in comparison to the Pagami Creek fire plume and the PBL, the Canada forest fire plume is less concentrated in terms of number concentrations.

To determine the source of the aerosol layer sequences within the Pagami Creek fire plume and the Canada fire plume, backward trajectories were calculated with HYSPLIT as described in Section 3.4.2. The measurements in the Pagami Creek fire aerosol layer were subdivided into sequences with rather homogeneous rBC mass concentrations. Altogether, 14 time sequences were chosen, as can be seen from Figure 63 (the 14 sequences are

indicated by the dashed boxes). The 14 sequences include sequences with maximum concentrations as well as less concentrated sequences within this heterogeneous aerosol layer. Due to the short measurement duration for the Canada forest fire aerosol layer, the sequence was not subdivided but analyzed as one sequence, indicated by the light grey bar and the dotted box in Figure 63. Figure 68 and Figure 69 show backward trajectories for the 14 sequences in the Pagami Creek fire plume and for the Canada forest fire plume, respectively. Additional trajectory analysis was conducted using FLYTUL[27] (Hamburger, 2010) (see Section 3.4.2) to verify the reliability of the trajectories calculated with HYSPLIT shown in Figure 68 and Figure 69. For the forest fire plume sequences the results agree well.

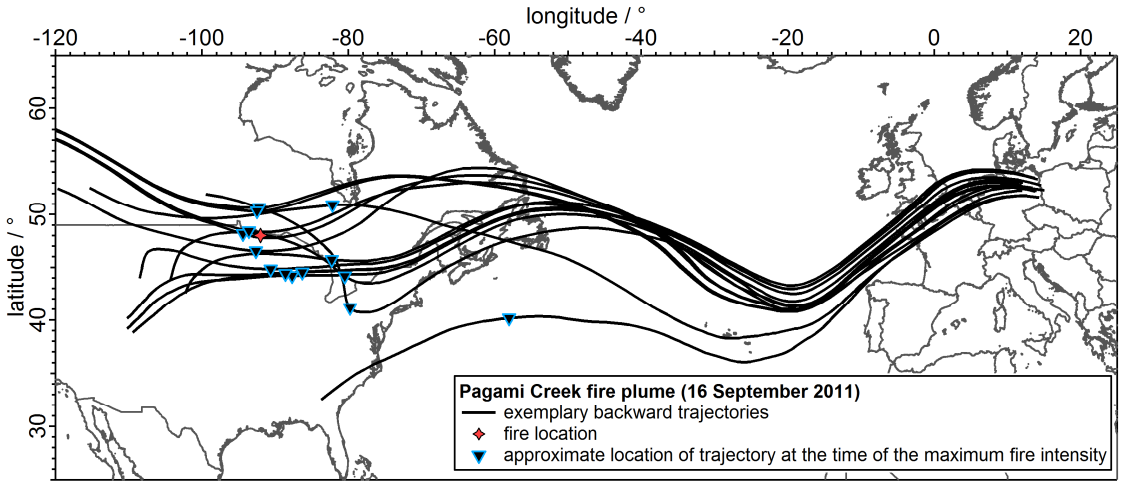

Figure 68. *Backward trajectories of the observed Pagami Creek fire aerosol layer calculated with HYSPLIT. The air mass was transported from North America via the Atlantic to Europe. The measurement took place over Germany. The location of the Pagami Creek fire is marked as a red star. Blue framed black triangles represent the location of the trajectories at 17 UTC on 12 September 2011, the approximate time of the maximum fire intensity.*

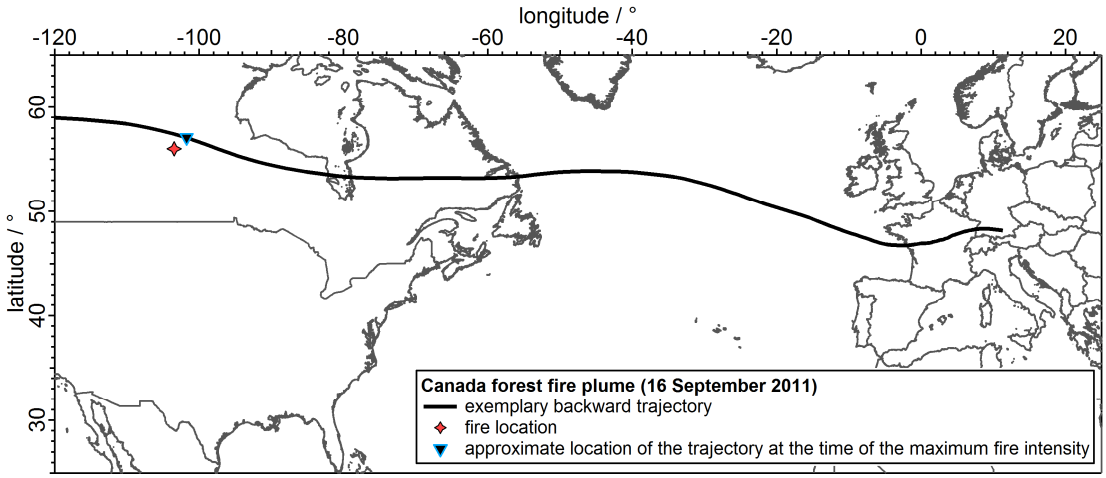

Figure 69. *Backward trajectory of the observed Canada forest fire aerosol layer calculated with HYSPLIT. The air mass was transported from North America via the Atlantic to Europe. The measurement took place over Germany. The location of the fire is marked as a red star. The blue framed black triangle represents the location of the trajectory at 00 UTC on 11 September 2011, the approximate time of the maximum fire intensity.*

[27] An example (for sequence 3 of the Pagami Creek fire plume; see Figure 63) is shown in Appendix 5.

The trajectories start at the location of observation and go backward in time for 120 h for the Pagami Creek fire plume and for 200 h for the Canada forest fire plume. The trajectories show that both, the Pagami Creek fire and the Canada forest fire air masses, were transported from North America across the Atlantic Ocean towards Europe. The Pagami Creek fire air mass passed the region of the Great Lakes, USA, at high altitudes on 12 September 2011, while the Canada forest fire air mass was transported at lower altitudes (Figure 70) farther north.

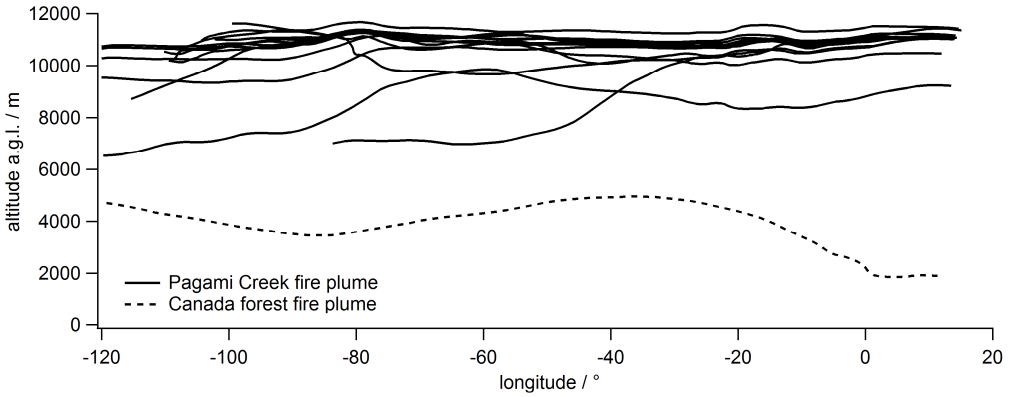

Figure 70. *Altitudes a.g.l. of the calculated backward trajectories for the Pagami Creek fire plume (solid lines) and the Canada forest fire plume (dashed line). The measurement took place over Germany at about 11–15° E.*

During the considered calculation times, none of the backward trajectories reached ground level or typical PBL heights, indicating that mixing of PBL aerosol into the free troposphere as source for these layers can be excluded. As a result, the emissions must have taken place in the free troposphere or were lifted by an intense convection event, which is not resolved by the HYSPLIT model. The red stars in Figure 68 and Figure 69 represent the locations of two major forest fires, while the black triangles with a blue frame represent the location of the trajectories at the approximate time of the maximum fire intensity of both considered forest fires. Both major forest fires are clearly recognizable in the global fire distribution for the period 8–17 September 2011 shown in Figure 5. The attribution of the observed aerosol layers to the forest fires is described in the following, first for the Pagami Creek fire and later for the Canada forest fire.

Figure 71 shows a true-color image of the Pagami Creek fire located in Minnesota, USA (approximate location 47°52' N, 91°30' W; U.S. Forest Service), taken by MODIS on 12 September 2011 at 18:50 UTC. This fire was caused by lightning on 18 August 2011. Derived from a collection of MODIS images, the fire did not evolve significantly before 12 September and thus caused only minor pollution. On 12 September 2011, the fire grew rapidly exhibiting a thick plume, which was transported eastwards (Figure 71). The Pagami Creek fire burned in total roughly 375 km^2. A cloud top brightness temperature (11.0 µm) of roughly -60 °C, corresponding to altitudes > 11 km, was observed from MODIS, which is comparable to high reaching thunderstorm clouds and is indeed colder than at any level up to 16 km in the radiosonde observation (RAOB) at International Falls, Minnesota, that day. Thus, this brightness temperature minimum indicates cloud top altitudes up to the cold point, which is even above 12 km altitude with radar echotops on the cloud anvil reaching about 13.6 km at 19:54 UTC caused by pyro-convection (e.g. Fromm et al., 2010), forming this pyro-cumulonimbus (PyroCb) cloud as a result of the extensive forest fire. Similar

observations of brightness temperatures for pyro-convective clouds, i.e. pyro-cumulonimbus clouds, are discussed in Damoah et al. (2006) and further pyro-convection events were observed and are described in e.g. Andreae et al. (2004) and Fromm et al. (2005).

MODIS imagery suggests that the bulk emission and pyro-convection event was limited from roughly 17:00 UTC on 12 September to 04:15 UTC on 13 September. In fact, AVHRR imagery suggests that pyro-convective lofting shut down sometime between 20:41 UTC and 22:41 UTC on 12 September.

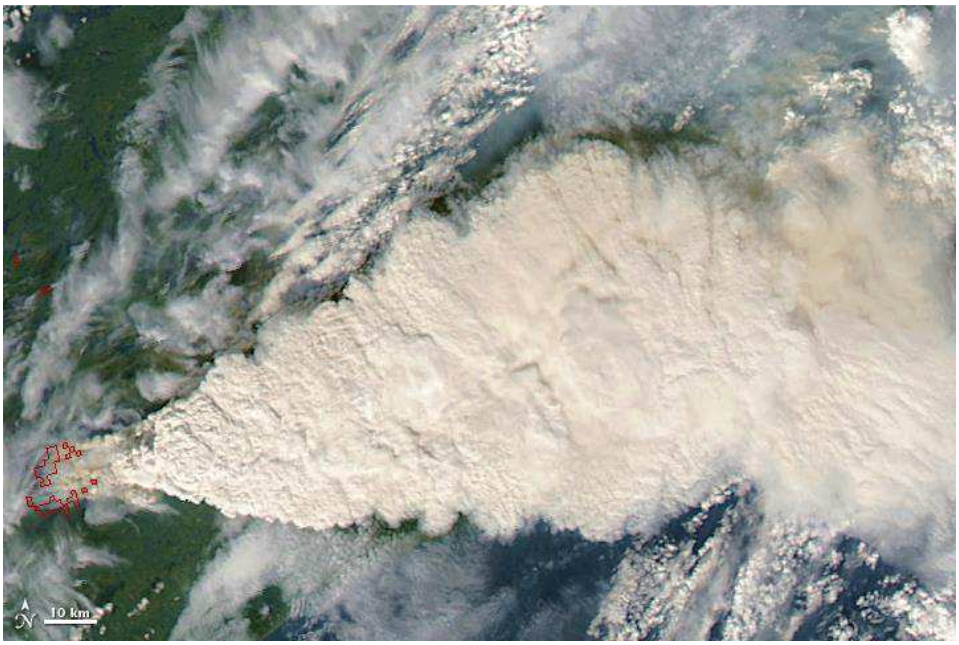

Figure 71. *MODIS picture of the Pagami Creek fire in Minnesota (USA) on 12 September 2011 18:50 UTC (source: NASA images courtesy Jeff Schmaltz, MODIS Rapid Response Team at NASA GSFC; Caption by Michon Scott). The small bar in the left lower corner represents 10 km.*

To evaluate whether the high altitude aerosol plume observed by the Falcon on 16 September over Germany originated from the Pagami Creek fire, HYSPLIT dispersion calculations were conducted, starting at the location of the Pagami Creek fire (47°52' N, 91°30' W). Based on the MODIS images, it was assumed that the Pagami Creek fire released emissions for 12 hours between 17:00 UTC on 12 September 2011 and 5 UTC on 13 September 2011 as maximum estimate. The release location was retrieved by satellite images and the release altitude was set from 10–11,000 m a.g.l., assuming pyro-convection (e.g. Fromm et al., 2005; Damoah et al., 2006) and a homogeneous vertical distribution.

The results are presented in Figure 72, which show the column-integrated (6–14 km a.s.l.) particle number concentration (a.u.) in the time span of 20:00–23:00 UTC between 12 September and 16 September 2011. The calculations underline the fact that the Pagami Creek smoke plume was transported through the area and in the altitude where the aerosol layer was measured by the Falcon and by the lidar in Leipzig. According to these simulations, the Pagami Creek plume should have reached Germany on 15 September 2011 (Figure 72). A detailed analysis of the simulation results suggests that the smoke layer was north of Leipzig on 15 September, in agreement with the lidar measurements, which did not detect the Pagami Creek plume on 15 September 2011.

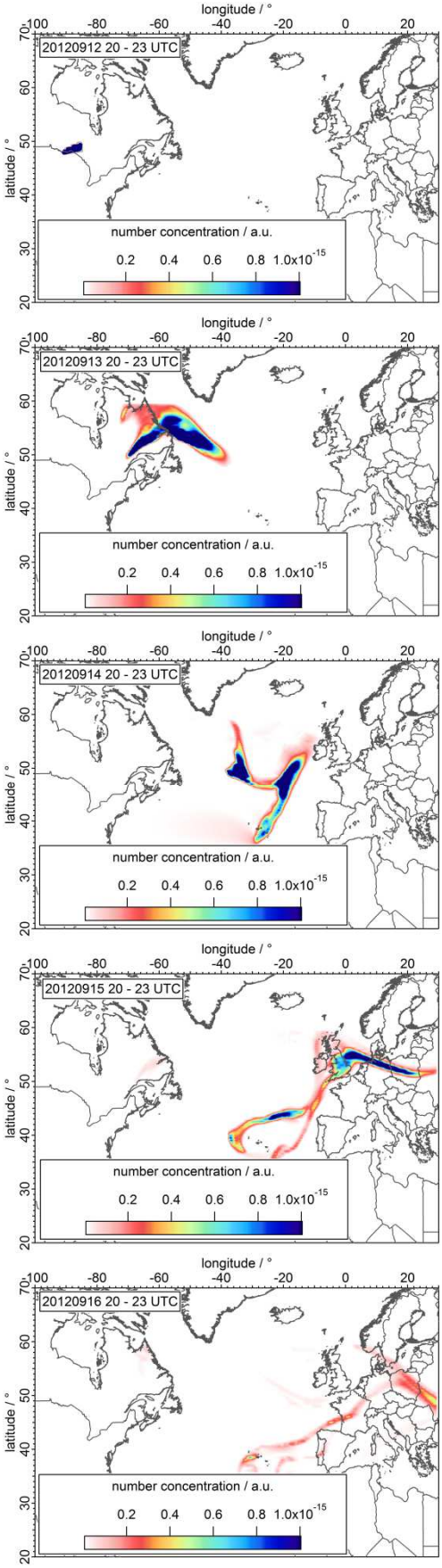

Figure 72. *Evolution and dispersion of the Pagami Creek fire plume vertically integrated from 6–14 km for the time period 20–23 UTC on each day from 12 September 2011 through to 16 September 2011 day calculated with HYSPLIT.*

Figure 73 shows zoomed in dispersion calculations of column-integrated (10–12 km a.s.l.) particle number concentrations (a.u.) on 16 September 2011 for Central Europe for the time between 8–11 UTC, 11–14 UTC and 14–17 UTC. The middle and the bottom panel in Figure 73 additionally include the Falcon flight tracks of flight #110916a (10:48–13:20 UTC) and #110916b (14:54–17:48 UTC), respectively.

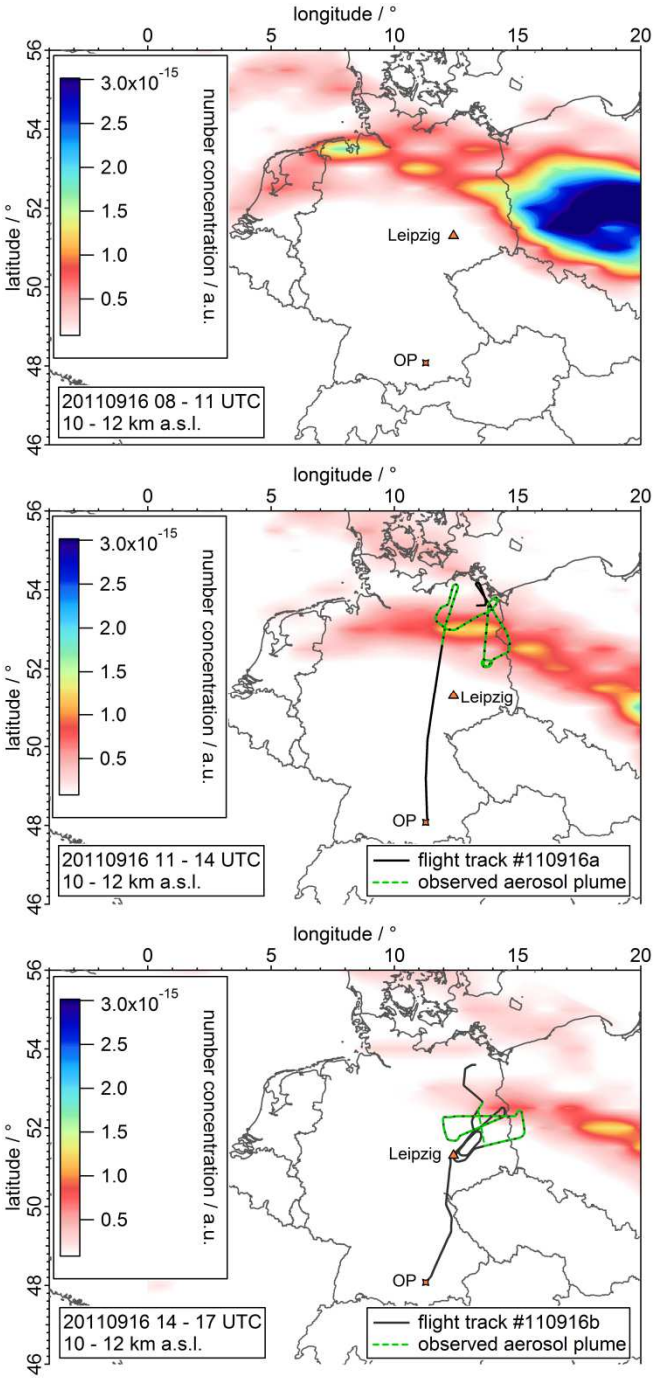

Figure 73. *Evolution and dispersion of the Pagami Creek fire plume over Germany vertically integrated (10–12 km) for the 16 September 08–11 UTC (upper panel), 11–14 UTC (middle panel) and 14–17 UTC (bottom panel) calculated with HYSPLIT, including locations of Oberpfaffenhofen (OP; star) and Leipzig (triangle). Black lines in the middle and bottom panel represent the flight tracks of flights #110916a and #110916b, while the green dashed lines represent the sequences where the Pagami Creek fire plume was measured.*

The comparison of the location of the measured plume and the plume location simulated by the dispersion calculations confirms that the Pagami Creek fire is most likely the source of the observed aerosol layer, which is, in addition, supported by observations of carbon monoxide (CO) by the Infrared Atmospheric Sounding Interferometer (IASI; provided by Ether CNES/CNRS-INSU Ether web site http://www.pole-ether.fr), a tracer for biomass burning, showing the same transportation pattern of the plume as the dispersion calculations.

According to the simulations shown in Figure 72 and Figure 73, it seems that the measurements were conducted in the tail of the plume when the maximum had already passed Germany. Thus, only the edges of the Pagami Creek plume passed over the Leipzig. This is in agreement with the lidar measurements in Leipzig, which show that the forest fire aerosol layer was no longer observed by the lidar system later than 10:30 UTC (Figure 67).

Particle linear depolarization ratios of the Pagami Creek fire plume, derived by the lidar observations of around 6–8%, are comparable to findings by Groß et al. (2013) who presented particle linear depolarization ratios of 7±2% for aged biomass burning aerosol from their own measurements and summarized that values between 2% and 8% are reported in the literature for aged biomass burning aerosol. Müller et al. (2007) report that particle linear depolarization ratios < 5% can be expected for biomass burning aerosol, probably due to their spherical shape. However, in agreement with the results for the Pagami Creek fire plume, they observed during LACE 98 particle linear depolarization ratios of up to 10% at 532 nm wavelength, which they explained by soil dust particles possibly lifted together with the smoke particles at the source of the fire. Weinzierl et al. (2011) report particle linear depolarization ratios of 6.3–16.4% (median: 13.1%) at 532 nm wavelength for biomass burning mixtures (biomass burning aerosol mixed with mineral dust from the Sahara) measured during the SAMUM-2 campaign in the Cape Verde region.

Other aerosol types can be excluded as source of the layer with ice clouds and mineral dust having higher and sea salt and sulphates having lower particle linear depolarization ratios (Groß et al., 2013). A mixture of ash and sulphate of volcanic origin might be the only explanation for the observed depolarization ratios besides biomass burning aerosol. However, volcanic eruptions did not occur in an appropriate spatio-temporal window to explain the observations above Germany. Thus, the observed particle linear depolarization ratios emphasize that a forest fire is the source of the observed aerosol layer.

In analogy to the source attribution of the Pagami Creek fire, the source of the Canada forest fire plume was determined. From 7 September 2011 to 11 September 2011 a forest fire (56°00' N, 103°27' W) near Reindeer Lake in Saskatchewan, Canada, was reported by the Canadian Forest Service (CFS; http://cfs.nrcan.gc.ca) and observed by MODIS on 10 September 2011 at 19:00 UTC (Figure 74a). This fire burned roughly 100 km^2, i.e. almost 4 times less than the Pagami Creek fire. Figure 74b shows the fire location on 11 September 2011 with yellow stars showing the active fire on that day, while red stars and purple crosses show the fire activity of the previous day and the day before that, respectively. Based on the MODIS images and the information of CFS, it was assumed that the forest fire released major emissions for 48 hours between 00:00 UTC on 10 September 2011 and 23 UTC on 11 September 2011. In contrast to the Pagami Creek fire, based on the MODIS images, no major pyro-convective conditions were assumed, resulting in lower emission heights (10–100 m a.g.l.).

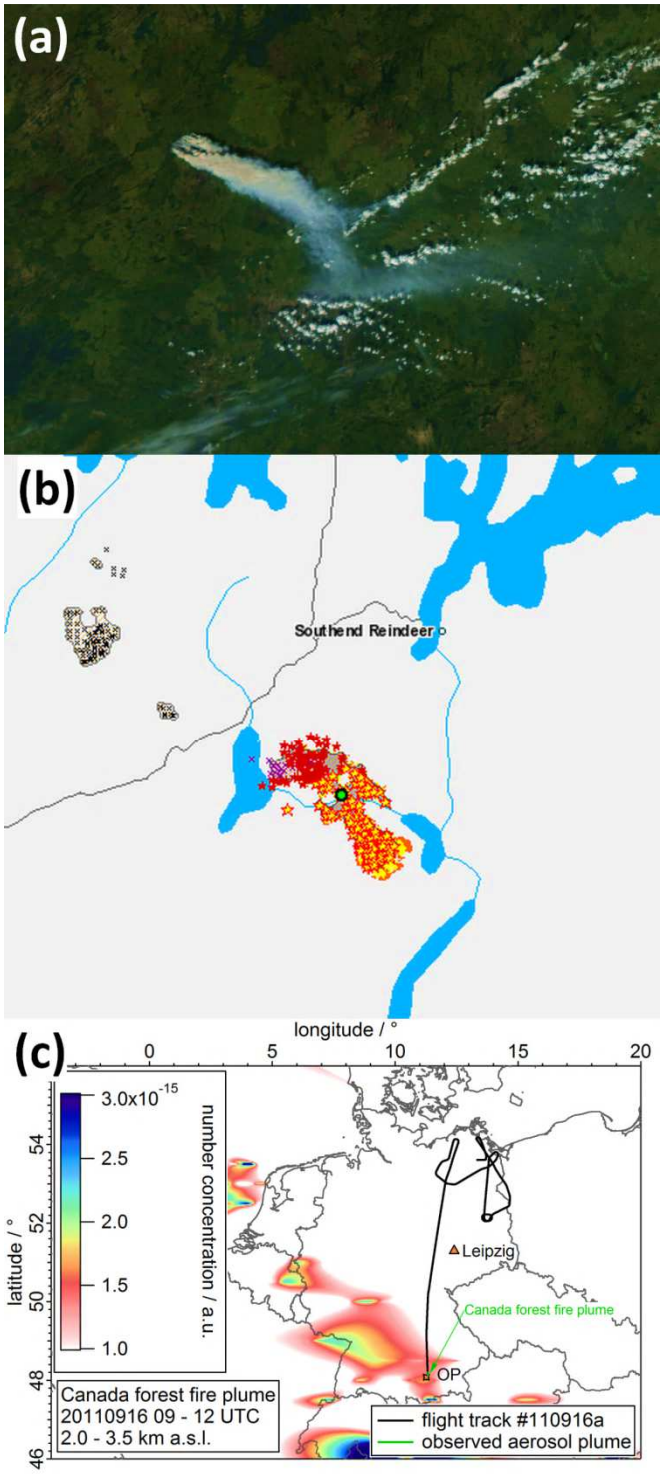

Figure 74. *Source attribution of the Canada forest fire plume. (a) MODIS picture of the forest fire near the Reindeer Lake in Saskatchewan (Canada) on 10 September 2011 at 09:00 UTC (source: http://activefiremaps.fs.fed.us/imagery.php?op=fire&passID=154396NASA; images by MODIS Rapid Response Team at NASA GSFC); (b) fire map on 11 September 2011 showing the considered forest fire south of Reindeer Lake in Saskatchewan, Canada, which burned roughly 100 km² (source: http://cwfis.cfs.nrcan.gc.ca); (c) calculated dispersion of the forest fire plume over Germany conducted with HYSPLIT vertically integrated from 2.0– 3.5 km a.s.l. for the 16 September 09–12 UTC, including locations of Oberpfaffenhofen (OP; star) and Leipzig (triangle). The black line in (c) represents the flight track of flight #110916a, while the short green line and the arrow indicate the sequences where the Canada forest fire plume was measured directly after take-off in OP.*

Detailed plume distribution calculations show that the plume of the Canada forest fire was transported from Canada to the south-western part of Germany within the assumed time scales at lower altitudes compared to the Pagami Creek fire plume (see also Figure 70). The distribution of the calculated plume at 9–12 UTC on 16 September 2011 over Germany is shown in Figure 74c as an integral particle number concentration (a.u.) for the altitude of 2.0–3.5 km a.s.l., i.e. the altitude where the aerosol layer was measured with the Falcon (Table 10). The short green line near Oberpfaffenhofen (OP) in Figure 74c represents the sequences where the Canada forest fire plume was measured by the Falcon, which traversed the Canada forest fire plume in the vertical within 90 s due to the ascent during that part of the flight. Consequently, the dispersion calculation coincides with the observations of the plume at 2.2–3.4 km a.s.l. Thus, the Canada forest fire is very likely the source of the aerosol layer observed on flight #110916a.

For the Canada forest fire plume, estimations on the dimension of the Canada forest fire plume are more complex compared to the Pagami Creek fire plume, due to less information about the fire. Furthermore, the Canada forest fire plume was measured by traversing it vertically (2.2–3.4 km a.s.l.) on flight #110916a without longer residence times within the plume. Thus, no information on the horizontal distribution of the plume is accessible based on the airborne measurements. The dispersion calculations give an indication that this plume was distributed in a more patchy way and on smaller scales (Figure 74) compared to the Pagami Creek fire plume (Figure 72; Figure 73), possibly caused by the transportation near the PBL. The heterogeneous, small-scale distribution is supported by the missing observation of the plume during descent of the Falcon 6–7 hours later on flight #110916b.

4.3.3 BC mass concentrations and size distributions in forest fire plumes

Figure 75 shows the rBC mass size distribution derived for each of the 14 Pagami Creek fire plume sequences (see Figure 63). The maximum and the minimum measured rBC mass size distribution are plotted (red and orange). Error bars represent 15% errors according to the uncertainties derived for the rBC mass measurements using a SP2 (see Section 3.4.3).

Each measured rBC mass size distribution of the Pagami Creek fire plume (dots) contains roughly 85% of the total BC mass, which is derived by an extrapolation by a log-normal fit (solid line; see Section 3.4.3 for details). The total rBC mass concentrations M for the 14 sequences of the Pagami Creek fire plume (0.033–0.348 µg m^{-3}; stp) reveal a difference of a factor of almost 10 between the lowest and highest rBC mass concentration (grey shaded area), showing large variations inside the aerosol layer, indicating a very heterogeneous structure, which was already discernible in Figure 63 and Figure 67. Aside from the emissions of the Pagami Creek fire, preexisting BC particles originating from other sources such as traffic and other anthropogenic sources contribute to the BC load in the Pagami Creek fire plume. However, due to the intensity of the fire and the remote location of the fire, this fraction is assumed to be small such that the described characteristics can be considered to be representative for forest fire particles.

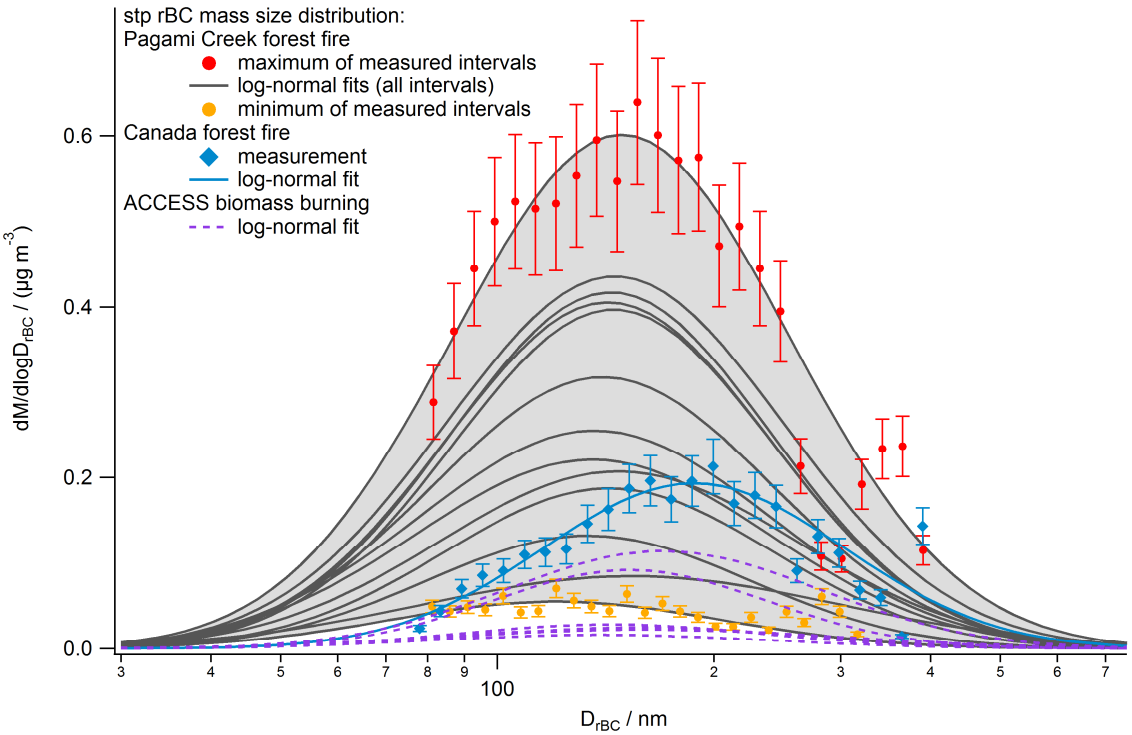

Figure 75. *Maximal (red dots) and minimal (orange dots) rBC mass size distribution out of the 14 measurement sequences in the Pagami Creek fire plume. Log-normal fits (solid lines) for the measured size range of 80–250 nm are shown for all 14 sequences. The grey shaded area represents the range between maximum and minimum log-normal fit. The mean total rBC mass concentration M is 0.033–0.348 µg m^{-3} (stp) for the Pagami Creek fire plume. The mass size distribution of the Canada forest fire plume is presented in blue. Bars represent 15% errors (see Section 3.4.3). For comparison, log-normal fits of the rBC mass size distributions of biomass burning aerosol layers observed during ACCESS (see Section 3.1.4) are shown (purple dashed lines).*

The Pagami Creek fire plume rBC mass concentration are comparable with the rBC mass concentration in the PBL over Neubrandenburg-Trollenhagen (0.107 µg m^{-3} and 0.046 µg m^{-3}) and Oberpfaffenhofen (0.376 µg m^{-3} and 0.957 µg m^{-3}) on that day. Because Oberpfaffenhofen is located near the metropolitan area of Munich, these values are representative for the polluted PBL. In the case of the Canada forest fire plume, an rBC mass concentration *M* of 0.101 µg m^{-3} was observed.

To put the results of the observed forest fire plumes in context to results for other forest fire aerosols and for other typically expected rBC-containing aerosol types, several publications were chosen (see Table 12).

Table 12. *List of publications chosen for the following comparison of BC mass concentrations and BC mass size distribution parameters.*

Publication	Content
Pratt et al., 2011	biomass burning plumes from Wyoming
Kondo et al., 2011a	biomass burning from North America and Asia
Sahu et al., 2012	biomass burning and anthropogenic emissions from California
Schwarz et al., 2008a	biomass burning and urban emissions from Texas
Metcalf et al., 2012	urban emissions from California

Kondo et al. (2011a) measured in 12–24 h old biomass burning plumes at altitudes from ground to roughly 5 km higher total rBC mass concentrations compared to the observations in this study (Figure 75; 0.033–0.348 µg m^{-3}), with the highest values in smoldering burning events (0.27–1.24 µg m^{-3}). Sahu et al. (2012) observed rBC mass concentrations of 0.5±0.17 µg m^{-3}, while Pratt et al. (2011) reported total rBC mass concentrations in fresh biomass burning plumes (~ 2–120 min old) in altitudes of 0–3.5 km a.g.l. up to 2 µg m^{-3}, which are also far larger than the Pagami Creek fire results. The dilution of the plume will affect the concentrations and possibly contribute to the difference between this study describing a very aged plume (3–4 days old) and the fresh plume not older than 1.5 h (Pratt et al., 2011).

The heterogeneity of forest fire plumes described above, aside from being reflected in variations of BC mass concentrations, is also reflected in variations of the BC fractions in forest fire aerosol. Pratt et al. (2011) observed with their SP2 average rBC mass fractions of 0.3–34% in fresh biomass burning plumes. The largest part of the mass was non-refractory organic material (60–90%). Similar high mass fractions of organic material, i.e. 56–92%, are reported by Kondo et al. (2011a), while the BC mass fraction is 1.7–4.9% in that study comparable to findings from Sahu et al. (2012) presenting < 5% rBC mass fractions. The higher amount of OC compared to BC can be explained by emission factors, which are, for instance, for boreal needle-leaf forests 7.8 g and 0.2 g per kg burned mass for OC and BC, respectively (McMeeking, 2008). In the SP2 size range, the median volume fractions of rBC-containing particles are 2.5–3.9% and 4.8% for the 14 considered sequences in the Pagami Creek fire plume and the Canada forest fire plume, respectively, which is in agreement with the findings of the studies discussed above. Nonetheless, despite of the small mass fractions, BC is of significant relevance in those forest fire plumes due to the large mass absorption cross-section. No measurements of organic material were performed, but it has to be assumed that in the forest fire cases in this study, OC, a potentially weak absorber, is also a major part in terms of mass fraction. As a result, this lack of information causes a significant uncertainty for the determination of the absorbing properties of the Pagami Creek fire plume[28].

Besides the BC mass concentration and fraction, the mass size distribution is an important aspect for BC in the atmosphere. Parameters of the log-normal fit to the measured rBC mass size distribution (stp) and the total rBC mass concentrations derived from the log-normal fit (stp) are shown in Table 13. The mass median diameter (*MMD*) of all mass size distributions of the Pagami Creek forest fire plume is in the size range between 121 nm and 153 nm (see Table 10). In comparison to the Pagami Creek fire plume, the Canada forest fire plume (blue; Figure 75) exhibits slightly different parameters: the mass size distribution is shifted with a *MMD* of 188 nm towards larger particle sizes. The geometric standard deviation (*GSD*) of the log-normal fit is smaller for the Canada forest fire plume (1.62) compared to the Pagami Creek fire plume (1.63–1.94; median: 1.70), influenced by differences in the burning conditions or different aerosol processing during the transport. Schwarz et al. (2008a) observed *MMD*s of roughly 160–180 nm for urban emission and roughly 200–220 nm for biomass burning aerosol, while Metcalf et al. (2012) observed modes of roughly 120–140 nm for boundary layer aerosol and roughly 160 nm for free tropospheric aerosol during airborne measurements in the Los Angeles Basin. The *MMD*s of the Pagami Creek fire plume

[28] The contribution of OC to the absorption will be approached in more detail in Section 4.3.6.

are smaller than those observed by Kondo et al. (2011a), who found MMDs between 177 nm and 197 nm in fresh biomass burning plumes (age: 1–2 h, origin: North America) and values between 176 nm and 238 nm in aged biomass burning plumes (age: 2–3 days, origin: Asia). MMDs in biomass burning plumes in altitudes 0–3.5 km a.g.l. in California observed by Sahu et al. (2012) are 193±16 nm. In contrast to the Pagami Creek fire plume, the MMD of the Canada forest fire plume fits well to the referenced values for biomass burning aerosol.

Table 13. *Values for the parameters of the log-normal fit to the rBC mass size distribution and stp factors for the minimum, median and maximum of 14 sequences during the Pagami Creek fire aerosol layer measurements and for the Canada forest fire plume measurements. In comparison to the rBC mass concentration within the SP2 size range in the Pagami Creek fire plume (0.028–0.294 µg m^{-3}; stp) a free tropospheric background sequence at that altitude on that day had a mean rBC mass concentration of < 0.004 µg m^{-3} (stp).*

Parameter		**Pagami Creek fire**			**Canada forest fire**
		Minimum	**Median**	**Maximum**	
Parameters of log-normal fit of rBC mass size distribution (stp)					
M	(µg m^{-3})	0.033	0.159	0.348	0.102
GSD	-	1.75	1.70	1.70	1.62
MMD	nm	121	144	150	188
stp factor	-	3.92	3.93	4.15	1.47

To explain the variations of forest fire plumes, Petzold et al. (2007), Weinzierl (2007) and references therein, describe an increase in the *CMD* and a decrease of the *GSD* of the accumulation mode of total particle number size distributions, including BC-containing and BC-free particles, with increasing plume age for boreal forest fire aerosol due to coagulation processes and the absence of nucleation processes. This is tested in this study also for the aging of rBC mass size distribution (Figure 76). In comparison to the Pagami Creek fire plume, the Canada forest fire plume has a larger *MMD,* while the *GSD* is smaller, which is in agreement with the plume ages of 3–4 days and 4–7 days for the Pagami Creek fire plume and the Canada forest fire plume, respectively. While the *MMD*-*GSD*-relations presented by Kondo et al. (2011a) agree with the results from this study, at least for the biomass burning aerosol from Asia, the *MMD*-*GSD*-age-relation is significantly different.

Thus, besides the plume age, other processes need to be considered with respect to their effect on the BC mass size distributions of forest fire aerosol plumes, such as burning conditions or wet removal. (Size dependent) wet removal (Moteki et al., 2012; Oshima et al., 2012) can shift the *MMD* of aged BC layers towards smaller particle sizes and might cause differences in observed *MMD*s for BC particle populations with varying exposure to wet removal conditions during the transport.

Meteorological analysis of the precipitation rate along the calculated backward trajectories (FLYTUL) shows that in all cases, i.e. for all considered forest fire sequences, wet removal occurred[29]. The precipitation rate varies by about a factor of 10 between the particular sequences. In addition to varying burning conditions, this variability in the wet removal might be a reason for the heterogeneous BC particle number and BC mass concentrations

[29] An example (for sequence 3 of the Pagami Creek fire plume in Figure 63) is presented in Appendix 6.

observed in the plumes and the presence or absence of wet removal processes might dominate the parameters of the BC mass distribution and thus the *MMD* and the *GSD*.

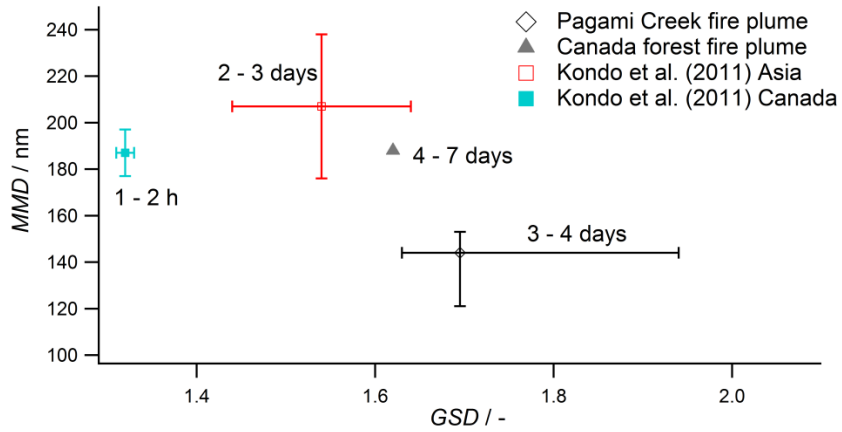

Figure 76. *Relation of the MMD to the GSD of the rBC mass size distributions of biomass burning aerosol layers of different ages. For comparison, values given in Kondo et al. (2011a) are included.*

The presented comparison of BC mass size distribution characteristics of forest fire aerosol layers reveals a wide spread of the describing parameters, which are influenced by a number of mechanisms, such as the burning conditions during the emission, the washout and the transportation time. However, the exact determination of the influence of these processes on the BC mass needs additional information on the exact particle emissions at the source, the age of the air mass and the exact amount of precipitation modifying the aerosol. Consequently, additional data is required to extend the data base and to identify the main controlling processes of the aging in BC-containing aerosol layers in detail.

4.3.4 Characteristics of forest fire plume total particle number size distributions

As discussed in the previous section, BC accounts for only small fractions in forest fire aerosols. Thus, it is not sufficient to investigate BC in forest fire plumes but also the entirety of aerosols, including BC and other aerosol particles, needs to be considered. Figure 77a shows the total particle number size distribution of the forest fire plumes and a background aerosol sequence. The background sequence, a sequence south of the observed Pagami creek fire aerosol layer during flight #110916a, was chosen to be representative for the altitude, at which the plume was measured. The presented minimum (orange), median (red) and maximum (dark red) size distributions represent the range of observations for the 14 considered sequences (Figure 63) in the Pagami Creek fire plume. The Canada forest fire plume is shown in blue.

The values of the parameterized number size distributions (Figure 77a; solid lines) and factors to convert stp to ambient conditions are shown in Table 14. The values for the Aitken mode are printed in italics in Table 14, because here only the concentration (N_1) is available, according to the extrapolation for particles smaller than the lower cutoff of the measurements (see Section 3.4.4), while the *GSD* and the *CMD* had to be assumed. The minimum and the maximum values of N_1 for all 14 sequences within the Pagami Creek fire plume are 760 cm^{-3} and 2,228 cm^{-3}, respectively. The number concentrations in the

measured accumulation and coarse mode size range vary roughly with a factor of 7 within the 14 sequences as an indication of heterogeneous concentrations and distributions within the vertical column of the plume. The Canada forest fire plume shows consistently lower concentrations in the measured size range, while the deviation of the distributions for particles below the lower cutoff is more uncertain due to the assumptions described before.

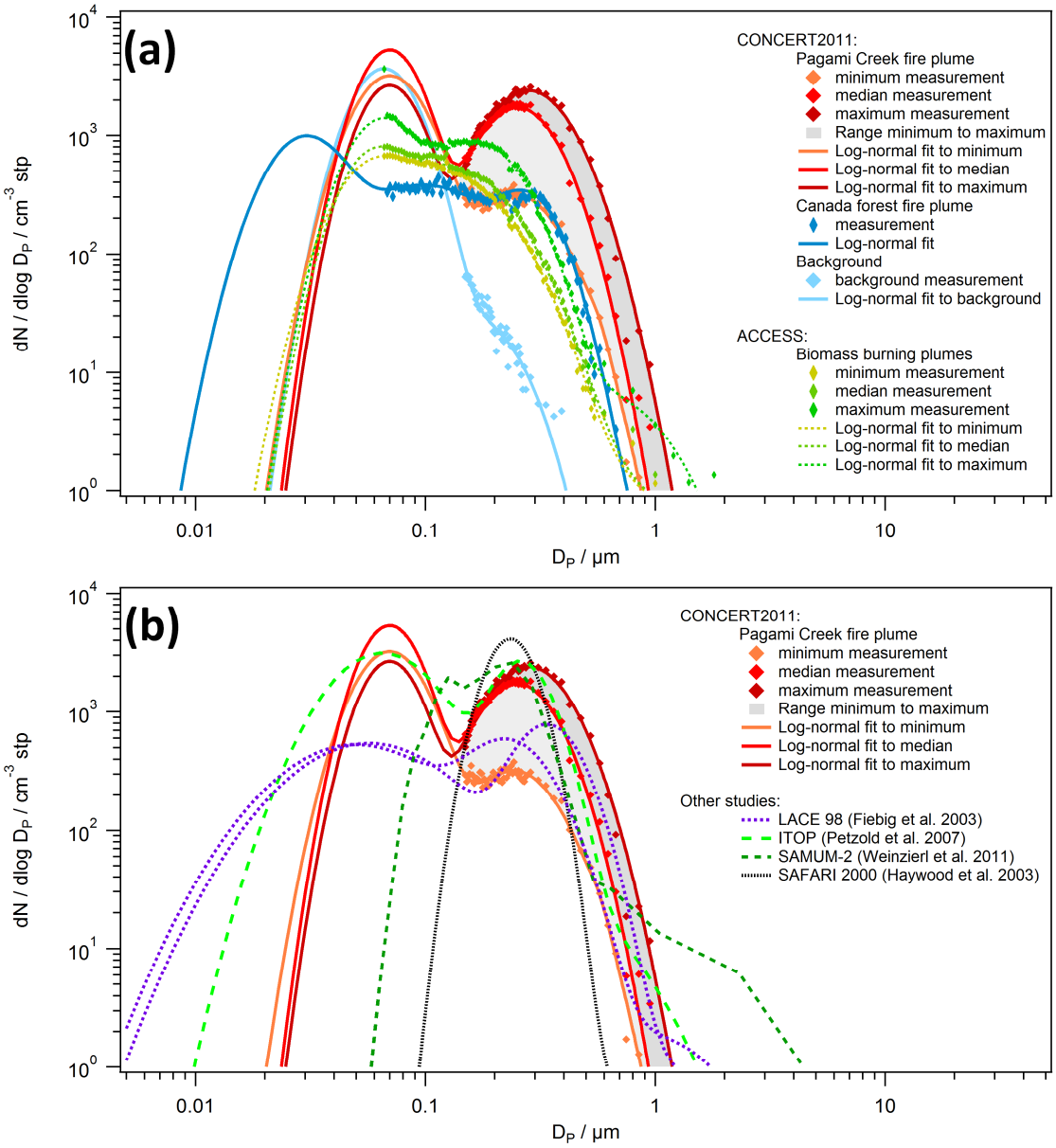

Figure 77. *(a) Number size distributions (stp) for the background aerosol (light blue markers), for the Canada forest fire plume (blue markers), for the minimum, median and maximum (reddish markers) and the range (light grey area) of measurements in the Pagami Creek fire plume, and for biomass burning aerosol plumes measured during ACCESS (greenish markers). Number size distributions are extrapolated by log-normal fits for the minimum, median and maximum of the Pagami Creek fire plume (reddish solid lines), the Canada forest fire plume (blue solid line), background measurements (light blue solid line) and the ACCESS biomass burning plumes (greenish dashed lines) and compared to biomass burning plumes (dotted and dashed lines) from LACE 98 (purple; ambient), ICARTT-ITOP (light green), SAMUM-2 (dark green) and SAFARI 2000 (black) in (b). Normalized values from SAFARI 2000, showing only the accumulation mode due to a lack of measurements for particle sizes < 100 nm, are scaled to similar magnitudes.*

Table 14. *Values for the parameters of log-normal fits to the total number size distribution and stp factors for the minimum, median and maximum of 14 sequences during the Pagami Creek fire aerosol layer measurements and for the Canada forest fire plume measurements. Values in italics are extrapolated from total number concentration values (see Section 3.4.4).*

Parameter		Pagami Creek fire			Canada forest fire
		Minimum	Median	Maximum	
Parameters of log-normal fit of total particle number size distribution (stp)					
N_1	cm^{-3}	*1077*	*1517*	*760*	*350*
GSD_1	-	*1.360*	*1.300*	*1.300*	*1.400*
CMD_1	nm	*70*	*70*	*70*	*30*
N_2	cm^{-3}	130	641	957	230
GSD_2	-	1.455	1.406	1.440	1.750
CMD_2	nm	243	251	281	100
N_3	cm^{-3}	1	-	-	80
GSD_3	-	1.100	-	-	1.320
CMD_3	nm	550	-	-	280
stp factor	-	3.92	3.93	4.15	1.47

The Pagami Creek fire plume shows a distinct bimodal structure. In comparison, the Canada forest fire plume shows a similar size distribution, but with increased merging modes and shifted towards smaller particle sizes. The comparison of the biomass burning size distributions with measurements in clean tropospheric "background" air on 16 September 2011 (light blue; Figure 77a) shows one striking feature: no particles larger than 400 nm were present in the monomodal background air, while particles up to larger 1 µm were detected in the Pagami Creek plume. In all Pagami Creek fire plume cases, the Aitken and accumulation modes give roughly comparable contributions to the particle number, while the accumulation mode only gives a very minor contribution in the background case. Thus, particles larger than 140 nm can be attributed to the forest fire. This is likewise the case for the Canada forest fire plume, though the accumulation mode is less pronounced. Biomass burning aerosol layers observed during the ACCESS field campaign (see Section 3.1.4) show also characteristics of a bimodal distribution, however with blurred modes, a less pronounced accumulation mode and lower concentrations compared to the Pagami Creek fire plume.

In comparison to number size distributions of biomass burning plumes at 3–5 km altitude from the LACE 98 campaign (Fiebig et al., 2003), the ICARTT-ITOP campaign at 3–9 km altitude (Petzold et al., 2007), the SAMUM-2 campaign at 0.8–4.2 km altitude (Weinzierl et al., 2011) and SAFARI 2000 at about 2–5 km altitude (Haywood et al., 2003), especially the ICARTT-ITOP case (6–9 days old) is similar to the Pagami Creek fire results with a predominantly bimodal structure and similar *CMD*s (Figure 77b). Results from LACE 98 (6–7 days old) exhibit a bimodal structure with similar *CMD*s as well with total number concentration about 2–9 times higher than in the Pagami Creek fire plume by approximating stp conditions, however with similar blurred modes like the Canada forest fire plume. The SAMUM-2 case (3–6 days old) shows a similar *CMD* for particles in the accumulation mode, but the particle concentrations in the Aitken mode are not as extended compared to the Pagami Creek fire results. This difference might be caused by different burning conditions, plume ages, or environmental conditions during the transport or simply by the presence or

absence of a background aerosol. Weinzierl et al. (2011) reported a significant coarse mode for data collected during the SAMUM-2 campaign, attributable to mineral dust, whereas in this study no significant amount of aerosol particles larger 1 µm was observed. Results from SAFARI 2000 show only the accumulation mode, because no measurements or extrapolations for particles < 100 nm were performed. Furthermore, the SAFARI 2000 size distribution was scaled to quantities found in this study and the compared studies, because in Haywood et al. (2003) the size distribution is given as normalized distribution.

In addition, number size distributions for forest fires of different age, calculated by Dentener et al. (2006), feature similar *CMD*s of roughly 150–300 nm. For aged forest fire aerosol from Canada they observed a mode in the size range smaller than 100 nm, comparable to the findings of this study. In contrast, Quennehen et al. (2011) and Quennehen et al. (2012) measured aerosol particle properties for diameters > 20 nm and observed predominantly monomodal or not well-pronounced bimodal biomass burning aerosol number size distributions with lower *CMD*s for aged (5–14 days old) aerosols during the POLARCAT campaign.

In summary, biomass burning number size distributions, especially for ICARTT-ITOP and LACE 98, fit well to the observations made for the Pagami Creek fire and the Canada forest fire plume, indicating similar source material, environmental and burning conditions or transportation. The layers often show similar modes in the accumulation mode size range, while the Aitken mode is observed less frequently in some cases possibly representing an aerosol, where the background aerosol might still dominate over the biomass burning influence. Thus, a dominant accumulation mode and a relatively large modal diameter (~ 200–400 nm) seem to be common features of forest fire aerosols.

Petzold et al. (2007), Weinzierl (2007) and references therein describe an increase in the *CMD* and a decrease of the *GSD* of the accumulation mode of number size distributions with increasing plume age for boreal forest fire aerosol due to coagulation processes and the absence of nucleation processes. Figure 78 shows this relationship, including the data from this study for the Pagami Creek fire plume (minimum, median and maximum) size distributions and the Canada forest fire plume size distribution (Table 14). The findings for the Pagami Creek fire plume (3–4 days old) and for the Canada forest fire plume (4–7 days old) underline this general relationship. In comparison to the plumes from the literature, there is an indication for a faster transformation towards smaller *GSD*s and larger *CMD*s for the forest fire aerosol layers from this study. Reason for this difference might be different particle size distributions at the source or differences in atmospheric conditions and components influencing the rate of particle modification. Nevertheless, the relation of *CMD* to *GSD* from this study is in the range of the observations reported in the literature (approximately on the dashed line in Figure 78) though the associated ages of the plumes (Pagami Creek fire plume: 3–4 days old; Canada forest fire plume: 4–7 days old) deviate slightly from dependency of *CMD*, *GSD* and age shown in Weinzierl (2007) and references therein.

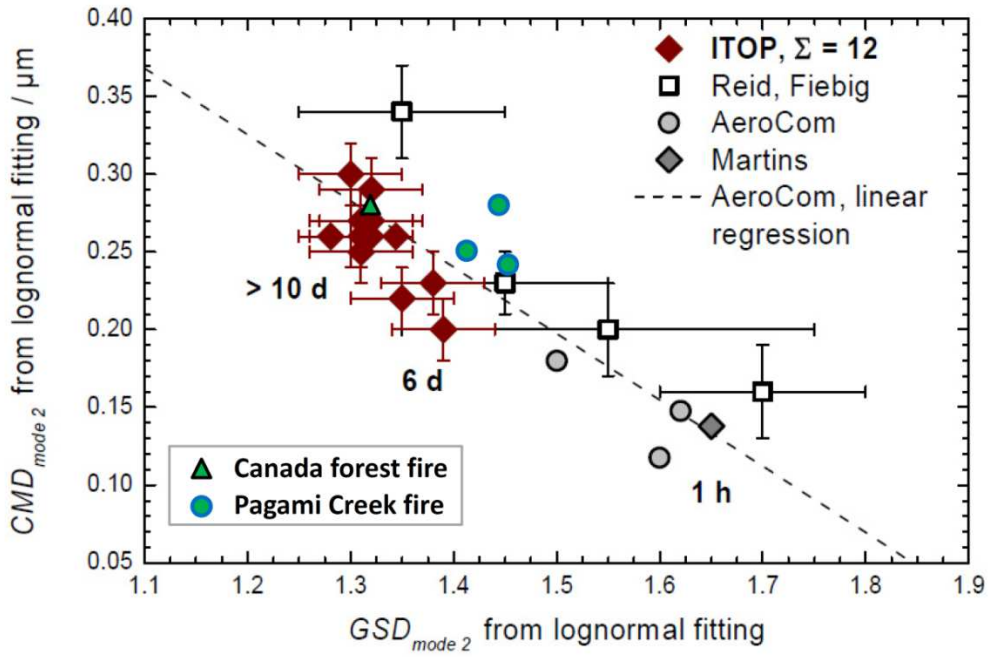

Figure 78. *Count median diameter (CMD) of forest fire plume number size distributions as a function of the geometric standard deviation (GSD) for the accumulation mode , including results for the Pagami Creek fire plume (3–4 days old) and for the Canada forest fire plume (4–7 days old). Comparison data are published in Martins et al. (1996), Fiebig et al. (2003), Reid et al. (2005b), Dentener et al. (2006) and Weinzierl (2007). Adopted from Weinzierl (2007).*

4.3.5 Particle mixing states and structures within forest fire plumes

Coating thickness

In both forest fire plumes the majority of the BC cores are smaller than 150 nm. However, BC is not only present in the Aitken mode (Figure 77), but can be found also in the accumulation mode and even the coarse mode if they are mixed with other aerosol components (see Figure 12). Thus, besides the size distribution information of aerosol layers, the internal mixing state of individual particles plays an important role in their impact on the atmosphere and in the characterization of aerosol layers. As described in Sections 3.3.1 and 3.4.3, the coating thickness of individual particles inferred from the SP2 measurements delivers relevant information on the mixing state of individual particles. Figure 79 shows normalized histograms of the observed coating thickness of all BC-containing particles with BC cores in the size range of rBC mass equivalent diameters between D_{rBC} = 140–160 nm and D_{rBC} = 180–220 nm for the 14 different sequences of measurements in the Pagami Creek fire plume and for the Canada forest fire plume measurement. These two size ranges are chosen exemplarily to test if the coating thickness (Δ_{coat}) varies with changing BC core size. As it can be seen from Figure 79a, the coating thickness of individual aerosol particles from the Pagami Creek aerosol layer ranges from Δ_{coat} = 20 nm up to > 180 nm, in both BC core size ranges shown, with a flat maximum between ~ 80 nm and 160 nm (median coating thickness: 105–136 nm). The small number of BC cores with coatings below 20 nm observed within the forest fire plume are likely from UTLS background particles and/or aircraft emissions. The observed coating thickness

distributions are very similar for all 14 sequences in the Pagami Creek fire plume, indicating very homogeneous BC particle properties across the different plume areas. Though the Pagami Creek fire plume and the Canada forest fire plume show similar histograms for coating thicknesses, the histogram for the Canada forest fire plume is shifted slightly towards smaller coating thicknesses (median: 110 nm), implying that less coating material was condensed on the BC particles.

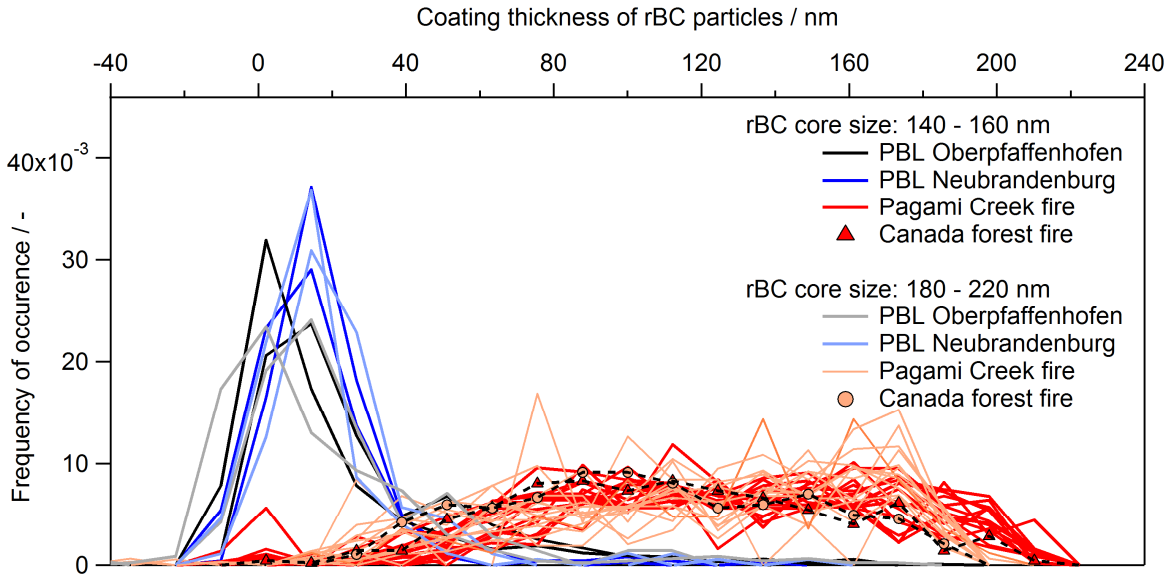

Figure 79. *Histograms of the coating thickness Δ_{coat} for 14 sequences inside the Pagami Creek fire aerosol layer (red lines), the Canada forest fire aerosol layer (red markers), and for fresh boundary layer aerosols in Oberpfaffenhofen, near Munich, and Neubrandenburg in black and blue, respectively. Bright colors show the results for rBC core sizes of 140–160 nm, while light colors show the results for rBC core sizes of 180–200 nm. Adopted from Dahlkötter et al. (2014).*

For comparison, histograms of coating thicknesses from frequently observed, freshly emitted boundary layer aerosol are presented. The boundary layer aerosol particles in the region of Neubrandenburg (blue lines) and Munich (black lines), as an example of typical continental boundary layer aerosol, are thinly coated, showing coating thicknesses of roughly -20–120 nm (median: < 40 nm). For the majority of the coated particles observed in the PBL (75-percentile), coating thicknesses of less than 65 nm were measured. Thus the particles in the observed forest fire aerosol layers exhibit much larger coating thicknesses than younger aerosol particle populations such as the PBL aerosol.

Negative coating thickness values determined for some particles are caused by random noise and potential systematic biases resulting from the assumptions made about the refractive indices and particle shape. Based on the presented results the systematic uncertainty for the coating thickness is assessed to be < ±20 nm.

The raster graphics in Figure 80 illustrate the relationship between the size of the rBC core and the coating thickness integrated over all Pagami Creek fire plume sequences (a), equal to Figure 62c, and for the Canada forest fire plume sequence (b). The color-coding represent the number of particles in each pixel and the grey lines represent the detection limits of this method, which was described in detail in Section 4.2.4. Coating thickness values up to the

detection limit, which is as high as $\Delta_{coat} \approx 240$ nm for core sizes $D_{rBC} \leq 100$ nm, are observed for all core sizes. The distribution of coating thickness values is similarly broad for all BC core sizes with particles with thin coatings ($\Delta_{coat} \leq 40$ nm) being always a negligible fraction.

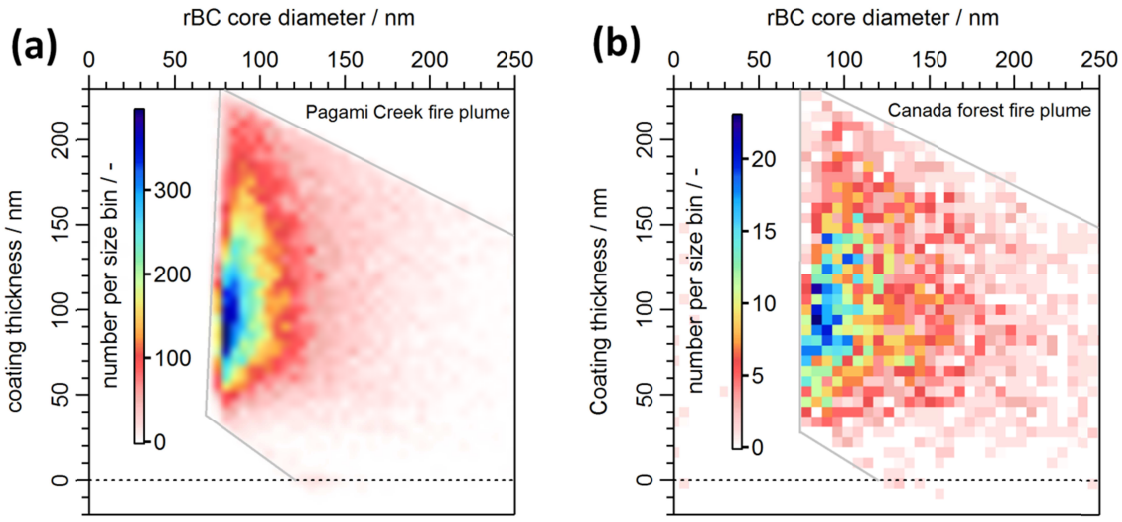

Figure 80. *The relation between rBC core diameter D_{rBC} and coating thickness Δ_{coat} for all 14 sequences in the Pagami Creek fire aerosol layer (a) and the Canada forest fire aerosol layer (b) as color-coded 2D-histogram. The detection limits are indicated by grey lines.*

The median coating thickness is $\Delta_{coat} \approx 105–136$ nm for the 14 flight sequences in the Pagami Creek fire plume independent of BC core size (note, the median coating thickness values for BC core sizes $D_{rBC} < 90$ nm and > 170 nm are likely biased by detection limit effects). This translates to median shell/core diameter ratios of $D_P/D_{rBC} = 3.7$, 2.8 and 2.4 at $D_{rBC} = 90$ nm, 130 nm and 170 nm, respectively, while the highest observed values are as high as $D_P/D_{rBC} = 7.4$ (Figure 81). For the Canada forest fire plume, slightly smaller D_P/D_{rBC} ratios (maximum: 7.2; median: 2.9; 10- and 90-percentiles: 1.8 and 4.4) were derived. Due to the short sampling sequence in the Canada forest fire plume and the smaller amount of sampled rBC-containing particles (see color-scale in Figure 80b) the distribution appears to be noisier.

Besides the accumulation of coating material during the almost four-day transport, most likely, major parts of the coating were condensed on the rBC particles during or shortly after the burning event. This hypothesis is in agreement with the discussed coating thicknesses observed for aerosol layers attributed to other source regions (Section 4.2.4), which show uniform coating thickness histograms almost independently of source, age and atmospheric processing with smaller coating thicknesses compared to the coating thicknesses derived for the observed forest fire plumes.

Akagi et al. (2012) found for a chaparral fire that 4 h after biomass burning emission, 85% of the BC cores may have been thickly coated, i.e. with shell-core diameter ratios (D_P/D_{BC}) larger than approximately 2, as an indication for coating processes during or shortly after the burning event. Kondo et al. (2011a) observed thickly coated BC particles after 1–2 h in biomass burning plumes with shell-core ratios (D_P/D_{rBC}) of 1.3–1.6. These values are somewhat lower than the observations in this study, which may be related to differences in the properties of the freshly emitted particles or continued mass acquisition of the BC

particles during the long-range transport in the forest fire plumes. Anyway, the coatings reported for the BC particles from forest fires in all three studies discussed here are substantial. This is in contrast to BC particles emitted from diesel engines and wood burning for residential heating, which emit particles with very little and moderate coatings, respectively, and also the median coating thickness observed in aged aerosols typically remains clearly below 100 nm (Laborde et al., 2013 and references therein).

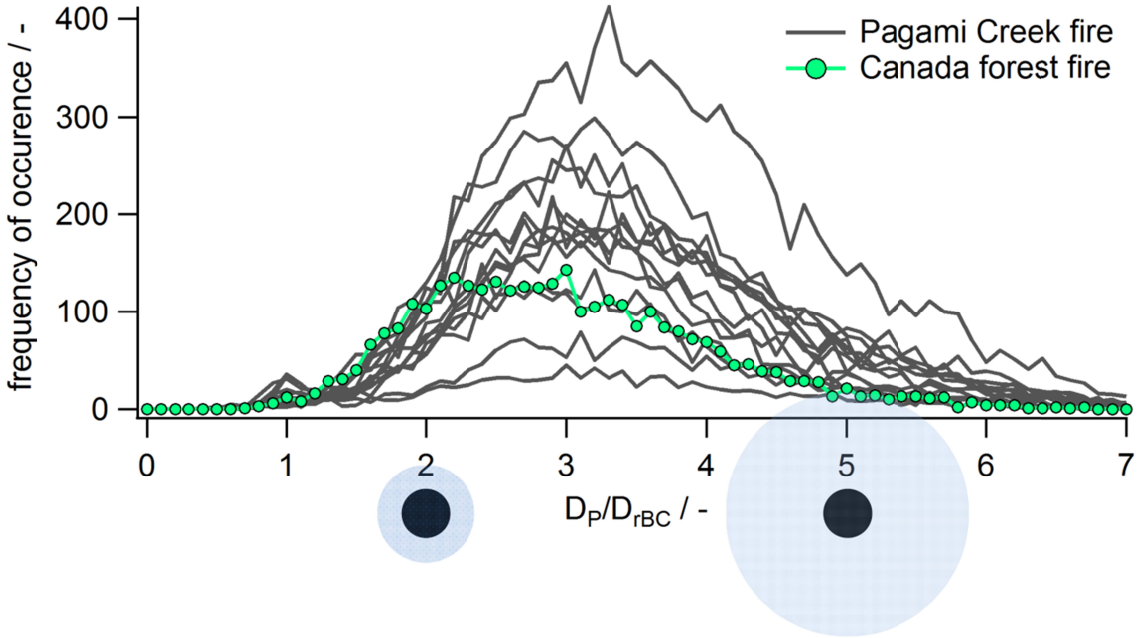

Figure 81. *Frequency distribution of the ratio of total particle diameter D_P to rBC core diameter D_{rBC} for the sequences of observations in the Pagami Creek fire plume (grey lines) and the Canada forest fire plume (green line). The ratios are schematically illustrated for $D_P/D_{rBC} = 2$ and $D_P/D_{rBC} = 5$ with the rBC core in black and the coating in light blue. The histograms are valid for the methodological size ranges (see Section 3.4.3 and Figure 80).*

The very thick coatings of the BC particles in the forest fire plume, most likely consisting of a mix of organic and inorganic species, will influence their light absorption properties. Coatings with D_P/D_{BC} ratios of 2 can already enhance the absorption by 100% (Schwarz et al., 2008b; Shiraiwa et al., 2010). Therefore it is possible that these high D_P/D_{rBC} ratios enhance the absorption by even more than 100%, depending on the coating material even though the relation of the absorption enhancement and the coating thickness is not linear and saturates for a sufficiently thick coating and large uncertainties of this effect remain (e.g. Cappa et al., 2012). The high D_P/D_{rBC}-ratios observed in the Pagami Creek forest fire plume and the Canada forest fire plume imply that substantial light-absorption enhancement effects are expected. Furthermore, coatings will also influence the interaction of BC particles with clouds. They are expected to be good cloud condensation nuclei through the mere size effect as well as the additional hygroscopic water uptake by the coating (e.g. McMeeking et al., 2011; Laborde et al., 2013; Liu et al., 2013). Furthermore, the mixing state of the BC with organic and inorganic matter might have an influence on the ice nucleation efficiency of the particles and is thus relevant for the indirect aerosol effect (Hoose and Möhler, 2012).

In summary, very thick coatings on forest fire BC particles were observed in this study, which is in qualitative agreement with previous literature, while the variability between

individual forest fire plumes is considerable. This variability is strongly linked to the condensation and coagulation processes modifying the individual forest fire particles during and shortly after the burning event and during transport. In addition, the highly variable particle material, mixing state and concentrations create heterogeneous appearances of biomass burning plumes, which consequently have manifold impacts on the interactions of particles within the atmosphere and are not yet fully understood and need further in-situ investigations.

Morphology and mixing state of BC particles

The interaction of BC-containing particles with solar radiation depends on their morphology and mixing state with light-scattering aerosol components (Kahnert et al., 2012). The coating thickness values reported before were inferred assuming a concentric-spheres core-shell morphology for the BC core and a light-scattering coating (see Section 3.4.3). However, the BC cores of combustion particles are fractal-like or compact aggregates and can be mixed with light-scattering material in different manners, including, e.g., surface contact of the BC with the light-scattering component, full immersion of the BC in the light-scattering component or immersion of the light-scattering components in the BC aggregate (Scarnato et al., 2013). Previous laboratory and field experiments have shown that the SP2 signals of rBC-containing particles (Figure 32; Section 3.4.3) can sometimes give indirect evidence of how the rBC core is mixed with light-scattering components beyond just quantifying the coating thickness (Sedlacek et al., 2012; Moteki and Kondo, 2007).

Based on the method described in Laborde et al. (2012a) (see Section 3.4.3), the mixing structure of the rBC-containing particles is assessed. The trailing-edge LSD signal indicates that in the Pagami Creek forest fire plume about 50% of the rBC-containing particles with particle sizes of about D_P = 300 nm disintegrated in the laser beam, leaving a detectable rBC-free fragment (Figure 82). The fraction of disintegrating particles increased with increasing particle size, so that > 90% of the rBC particles disintegrated at large sizes (D_P > ~ 480 nm). Conversely, the majority of the smaller particles (D_P < ~ 300 nm) showed no disintegration characteristics. However it cannot be distinguished if they really evaporate completely or if potential rBC-free fragments just remain below the detection limit of the LSD (Figure 82). Overall ~ 40–50% of all detected rBC-containing particles in the Pagami Creek fire plume were identified as disintegrating particles with the trailing-edge LSD signal method. In agreement to the Pagami Creek fire plume, for the Canada forest fire plume a similarly high fraction of disintegrating particles was observed.

Only 3.5–6.8% (median: 4.6%) of all rBC particles, corresponding to roughly 5–20% of all identified disintegrating rBC particles, exhibited a negative lagtime in this study. This shows that the lagtime method presented in Sedlacek et al. (2012) (see Section 3.4.3) only provides a lower limit for the total fraction of disintegrating particles. The success rate of the lagtime method for the identification of disintegrating particles depends on particle and instrument properties such as, e.g., the particle size and the saturation level of the LSD.

Sedlacek et al. (2012) observed disintegrating particles during a ground-based field campaign in summer 2011. More than 60% of rBC-containing particles in the forest fire aerosol plume from several wildfires east of Lake Winnipeg and into western Ontario on July 30 were disintegrating rBC particles, exhibiting negative lagtimes in the SP2. The observations of this study show for the first time the occurrence of disintegrating rBC

particles in high-altitude BC layers (40–50% of all detected rBC-containing particles, according to the trailing-edge LSD signal method).

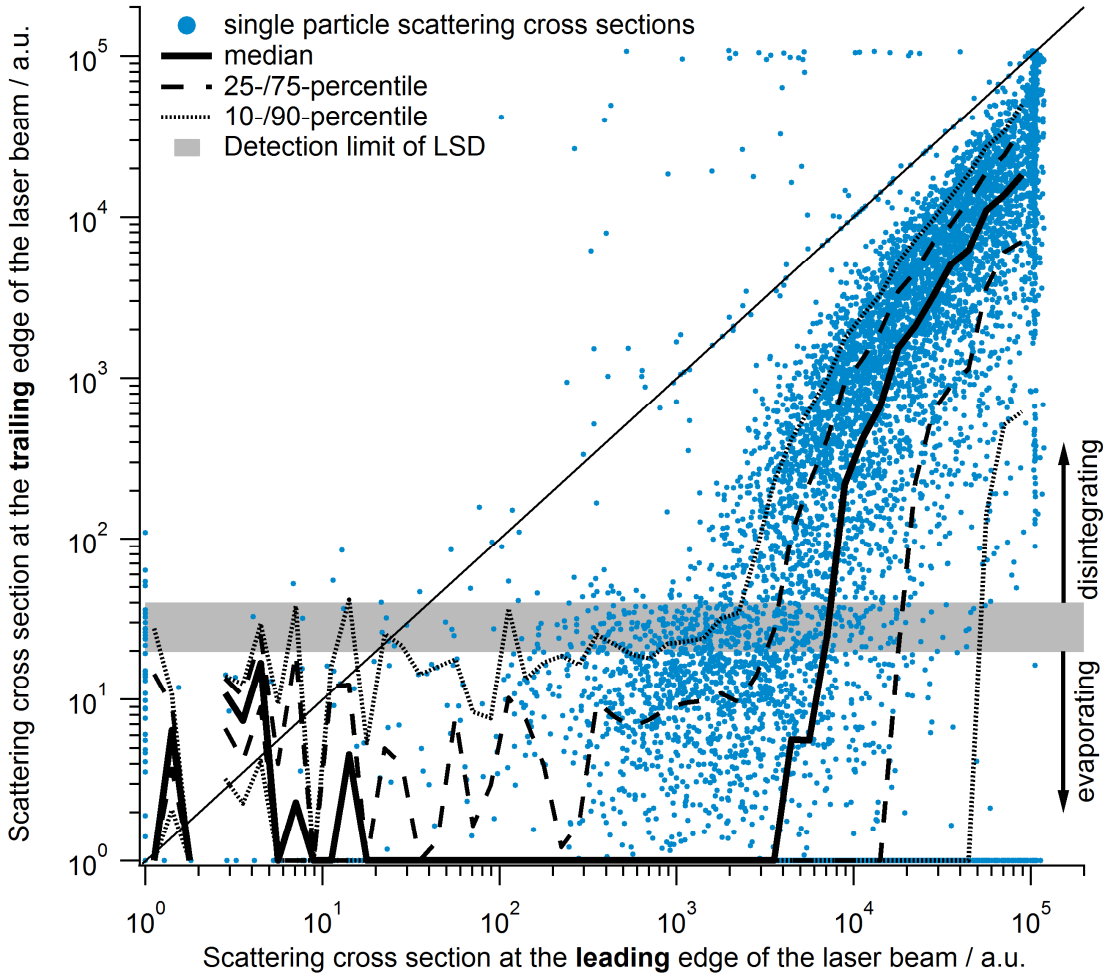

Figure 82. *Relation of the scattering cross-section C_{sca} at the leading edge and at the trailing edge of the laser beam for BC-containing particles (blue dots) with median (solid black line), 25-/75-percentiles (dashed black lines) and 10-/90-percentiles (dotted black lines) shown for a sequence measured in the Pagami Creek fire plume (11:36–11:46 UTC, 16 September 2011). The grey bar represents the detection limit of the LSD. Particles with scattering cross-section at the trailing edge of the laser beam remaining above the detection limit of the LSD indicate the disintegration of BC-containing particles.*

Sedlacek et al. (2012) suggested that disintegrating particles are associated with a particular particle morphology, where the BC is located near or at the surface of the BC-containing particles. Moteki and Kondo (2007) also reported the occurrence of disintegrating particles in laboratory experiments with graphic cores that were coated with glycerol or oleic acid. In that study, the number fraction of disintegrating particles was mainly a function of overall particle diameter. No disintegration was observed for small sizes, while almost all larger particles disintegrated. The threshold particle diameter for the occurrence of disintegration was 450–600 nm depending on the coating type. Moteki and Kondo (2007) speculated that disintegration might be associated with eccentrically positioned BC cores in their case, while near-surface BC morphology was not expected based on the process applied to coat the BC cores.

The specific BC particle morphology, i.e. core-shell versus near-surface BC, is relevant because the light-absorption efficiency enhancement effect by light-scattering coatings internally mixed with BC depends on the coating volume fraction as well as the particle morphology. Besides, disintegrating particles might also complicate the analysis of SP-AMS (Soot-Particle Aerosol Mass Spectrometer; Onasch et al., 2012) measurements, because the BC-free fragment would not be evaporated by the laser. This should be further investigated with specific laboratory experiments involving biomass burning aerosol and the SP-AMS.

Sketches of three conceivable morphologies of disintegrating BC-containing particles are shown in Figure 32c (on the very left): concentric core-shell, eccentric core-shell or near-surface BC/attached BC morphology. Light-scattering matter that is simply attached to a BC core causes very little enhancement of the light-absorption efficiency (Liu and Mishchenko, 2007; Scarnato et al., 2013). In contrast, a substantial light-absorption efficiency enhancement can be expected for coated BC-containing particles with a concentrically or eccentrically positioned core.

A process that can produce near-surface BC morphologies is coagulation of almost bare BC aggregates with BC-free particles. Condensation of secondary organic or inorganic aerosol components on BC particles can either result in particles with core-shell morphology (concentric or eccentric) or with near-surface BC morphology. Adachi et al. (2010) proposed a mechanism producing near-surface BC particles via condensation processes, which involves condensation of organic material onto nascent BC that effectively preserves the aggregate of primary BC particles in an un-collapsed form, followed by further mass acquisition via condensation preferentially onto the more organic portion of the particle.

Based on the observations in the aged Pagami Creek smoke plume and the Canada forest fire plume, disintegration was associated with large rBC-containing particles (overall optical diameter $\gtrsim 300$ nm; see above). These large particles generally had a very low BC mass fraction because the majority of the rBC cores were < 130 nm in diameter. These particles can be the result of extensive condensation of secondary aerosol components onto the nascent BC aggregates or of coagulation of BC-particles with large BC-free particles during transport. Indeed, the initial plume was highly concentrated such that both processes are likely to occur during aging of the BC particles in the plume. Thus, it is in principle possible that both BC particle types with near-surface BC or core-shell morphology are present in the aged plume. However, the observed number fraction of disintegrating particles is for the most part a function of overall particle size, indicating that disintegration was possibly just the result of very thick coatings, as reported in the laboratory study by Moteki and Kondo (2007). Specific evidence neither to corroborate nor to discard the assumption of near-surface BC morphology is available.

The particular features of the particles in the aged Pagami Creek fire and Canada forest fire plume observed in this study are the enhanced size of all particles and the enhanced coating thickness of BC-containing particles compared to the observations outside the plume. Both can be attributed to extensive coagulation and/or condensation in the forest fire plume. It is important to consider the large particle size when assessing direct light-scattering of solar radiation of such plumes. When assessing the absorption of solar radiation, it is recommended, based on above discussion about the morphology of BC particles, to consider the light-absorption enhancement effect that is expected to occur for thickly coated BC particles with core-shell morphology.

The first two reports of disintegrating BC particles in ambient aerosols are from forest fire plumes (Sedlacek et al., 2012; this study). The question if disintegrating particles are uniquely or predominantly associated with biomass burning aerosol remains to be addressed. The fact, that biomass burning BC-particles often exhibit thicker coatings compared to BC particles from, e.g., diesel engines, even with allowance for coating acquisition during atmospheric aging (e.g. Laborde et al., 2013), might be a reason for preferential occurrence of disintegrating particles in biomass burning aerosol.

4.3.6 Optical properties of forest fire aerosol layers

Besides the single-particle mixing state, bulk optical properties are derived using the PSAP measurements, number size distributions and Mie theory, as described in Section 3.4.6. The bulk absorption coefficient of the Pagami Creek fire plume, determined for the 14 sequences within the plume, ranges between 0.6 Mm^{-1} and 15.0 Mm^{-1} (including 20% uncertainty; see Section 3.4.6; median: 4.9 Mm^{-1}) at stp conditions at 530 nm wavelength (Table 15). In comparison, the Canada forest fire plume exhibits bulk absorption coefficients (530 nm) of 3.0 Mm^{-1} at stp conditions on an average. Weinzierl et al. (2011) observed, for biomass burning (3–6 days old) from the western part of Africa, absorption coefficients of 0.8–40.1 Mm^{-1} (median: 13.1 Mm^{-1}) at 530 nm wavelength, higher compared to the results for the Pagami Creek fire plume.

Table 15. *Absorption coefficients for the forest fire aerosol layer sequences, i.e. the Pagami Creek fire plume and the Canada forest fire plume, including the measured bulk absorption coefficient σ_{abs} (530 nm; 20% uncertainty; see Section 3.4.6), the estimated BC core absorption coefficient $\sigma_{abs,rBC}$ (550 nm) as minimum, best estimate and maximum, and the resulting contribution of uncoated rBC particles to the bulk absorption (PC: Pagami Creek).*

FF aerosol layer sequence	**σ_{abs} (530nm) PSAP measurements /Mm^{-1}**	**$\sigma_{abs,rBC}$ (550nm) calculation /Mm^{-1}**			**Contribution of BC cores to bulk absorption / %**
		minimum	**best estimate**	**maximum**	
PC_1	4.6±0.9	1.1	1.3	1.5	20–41
PC_2	7.8±1.6	1.4	1.7	2.0	15–32
PC_3	0.8±0.2	0.2	0.3	0.3	21–47
PC_4	8.4±1.7	1.4	1.7	2.0	14–30
PC_5	5.2±1.0	1.0	1.1	1.3	16–31
PC_6	5.8±1.2	1.2	1.4	1.6	17–34
PC_7	4.1±0.8	0.8	1.0	1.1	16–34
PC_8	12.5±2.5	2.2	2.6	3.0	15–30
PC_9	8.2±1.6	1.4	1.6	1.9	14–29
PC_10	1.8±0.4	0.4	0.5	0.5	19–35
PC_11	2.7±0.5	0.5	0.6	0.6	15–28
PC_12	10.0±2.0	1.6	1.9	2.2	13–28
PC_13	3.5±0.7	0.7	0.8	0.9	17–32
PC_14	4.2±0.8	0.8	0.9	1.1	16–33
PC_median (range)	*4.9 (0.6–15.0)*		*1.2 (0.2–3.0)*		*22 (13–47)*
Canada	3.0±0.6	0.6	0.8	0.9	17-38

The described absorption parameter reflects the bulk absorption of all absorbing particles included in the aerosol population, e.g. BC particles, coated BC particles, absorbing dust particles or absorbing BrC, schematically shown in Figure 83 on the left. Compared to the absorption of an aerosol population containing only the uncoated BC particles (Figure 83, right), the mixed population has a larger absorption, as indicated by the arrows illustrating the outgoing light.

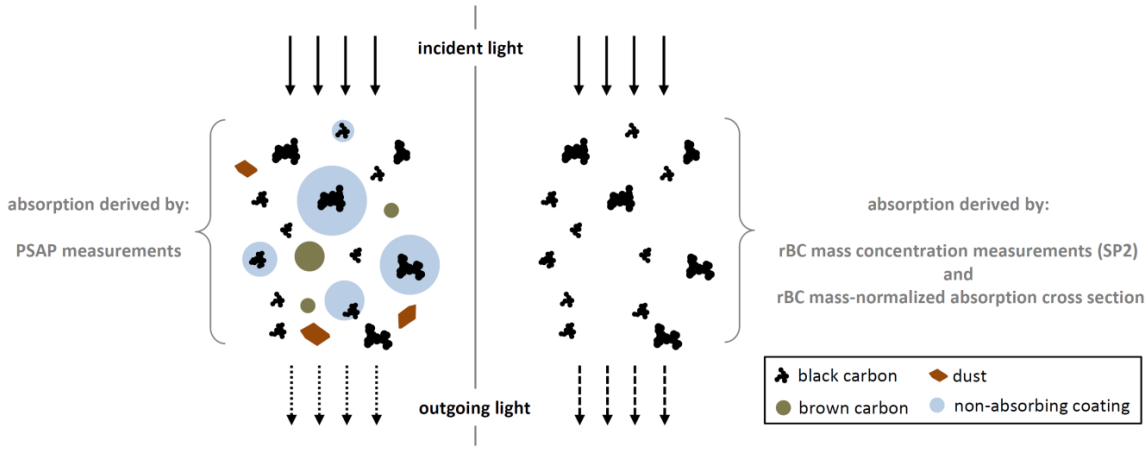

Figure 83. *Schematic showing the absorption of an aerosol population containing a mixture of dust particles, brown carbon particles, BC particles and coated BC particles (left) and containing only uncoated BC particles (right). The mixture (left) absorbs more of the incident light compared to the aerosol population only containing the BC cores.*

The absorption of the uncoated BC particles $\sigma_{abs,rBC}$ (see Figure 83, right) can be derived using the measured rBC mass concentration and mass-normalized absorption cross-section for uncoated BC particles at a specific wavelength. In this study, 7.5±1.2 $m^2\ g^{-1}$ are used for the mass-normalized absorption cross-section of uncoated, light absorbing carbon for a wavelength of incident light of 550 nm (Bond and Bergstrom, 2006). Sheridan et al. (2005) determined for pure kerosene soot at 530 nm wavelength the same value (7.5±1.2 $m^2\ g^{-1}$) as an indication for the representativeness of that value for atmospheric BC. Multiplying the rBC mass concentration and the mass-normalized absorption cross-section for light absorbing carbon particles, i.e. BC particles, absorption coefficients related to uncoated BC ($\sigma_{abs,rBC}$) of 0.2–3.0 Mm^{-1} (median: 1.2 Mm^{-1}) are derived (Table 15). The estimate for the absorption coefficient for uncoated BC particles $\sigma_{abs,rBC}$ (550 nm) in the Canada forest fire plume ranges from 0.6 Mm^{-1} to 0.9 Mm^{-1}.

Compared to the absorption coefficient derived from the PSAP measurements (see Figure 83, left), uncoated BC particles contribute 13–47% to the bulk absorption of the Pagami Creek fire plume and 17–38% to the bulk absorption of the Canada forest fire plume (Table 15), neglecting the wavelength difference between 530 nm and 550 nm.

These findings can be explained by several mechanisms:

1) Reid et al. (2005b) and references therein, present BC/OC ratios of 3–15% for biomass burning in temperate and boreal forests. Thus, a large fraction of OC might contribute significantly to the absorption though it is less absorbing. An absorbing OC is, for example, BrC, formed as the result of smoldering combustion of biomass (Moosmüller et al., 2009). Kirchstetter and Thatcher (2012) calculated that, integrated over the solar spectrum from

300–2,500 nm, OC would account for 14% and BC would account for 86% of solar radiation absorbed by wood smoke in the atmosphere, implying that BC is the dominant light-absorbing component in wood smoke, though absorbing OC contributes significantly. This is in agreement with the results of Kirchstetter et al. (2004) who stated that a fraction of the light absorption of biomass burning aerosol is attributable to OC produced by low-temperature and incomplete combustion processes.

2) Coatings on the BC particles can enhance their absorption significantly (compare with Sections 2.2.2, 4.2.4 and 4.3.5). Because large coatings were observed in the Pagami Creek fire plume and the Canada forest fire plume, this lensing effect contributes to the presented difference between the measured total absorption coefficients and the theoretically derived absorption coefficient for uncoated BC particles.

3) By observations of the particle linear depolarization ratios, Müller et al. (2007) found that soil dust particles are possibly lifted together with the smoke particles during intense forest fire events. The particle linear depolarization ratios observed in the Pagami Creek fire plume indicate that dust was lifted by the Pagami Creek fire as well (compare with Section 4.3.2). Hence, absorbing dust might also contribute to the difference in the presented absorption coefficients.

It is highly probable that a combination of these three effects causes the difference of 53–87% between the bulk absorption coefficients and the absorption coefficients of the BC cores. Lack et al. (2012) estimated the contributions of BC, BrC and the lensing effect to the absorption of fresh biomass burning aerosol showing highly variable fractions, though dominated by the absorption of BC. This is in agreement with the findings of this study. Considering variations in the burning conditions and the source material and the alteration of the aerosol during the transport, large uncertainties concerning the contribution of the particular absorbing components for biomass burning aerosol remain. Further studies, including chemical analyses of the aerosol particles, are needed to be able to characterize the contributions of the particular effects on absorption.

To gather information on the wavelength dependence of the absorptive properties of the aerosol, the bulk Ångström exponent of absorption $å_{abs}$ can be derived (e.g. Russell et al., 2010). Therefore, the absorption coefficient at three different wavelengths (λ = 467 nm, 530 nm, 660 nm; Section 3.3.2) is used (see Section 2.3). For pure BC, an Ångström exponent of absorption of around 1 is expected due to its wavelength-independent absorption. However, $å_{abs}$ observed for the Pagami Creek fire plume (1.7–3.4; median: 2.7; Table 16) and the Canada forest fire plume (1.2–1.8; best estimate: 1.5; Table 16) is significantly larger than 1. Weinzierl et al. (2011) observed for the biomass burning from Africa $å_{abs}$ of 1.2–1.9 (median: 1.3). The difference to the expected $å_{abs}$ for pure BC indicates that also wavelength dependent absorbing components contribute to the bulk absorption. This is in agreement with the findings of the absorption coefficients for the bulk aerosol and for uncoated BC particles discussed above, where absorbing OC and dust are assumed to contribute significantly to the bulk absorption. Both materials have a wavelength dependent absorption illustrated, e.g., for Saharan dust by $2.5 < å_{abs} < 5.9$ (Weinzierl et al., 2011). Thus, the results for $å_{abs}$ are further indicators for absorbing OC and dust contributing significantly to the absorption, though they are far less absorbing than BC.

The imaginary part of the refractive index k (Section 3.4.6) at 530 nm wavelength derived for the bulk aerosol underlines the presented findings: for the Pagami Creek fire plume, k is

0.010–0.023 (including 20% uncertainty; median: 0.015), while for the Canada forest fire plume a value of 0.039–0.059 (including 20% uncertainty; best estimate: 0.049) was derived. In comparison, Reid et al. (2005a and references therein) report values for k of 0.0094±0.003 for boreal forest fires in the USA and Canada, comparable to the lower end of observations for the Pagami Creek fire plume but far lower than the observations for the Canada forest fire plume. Weinzierl et al. (2011) observed for the biomass burning from Africa imaginary parts of the refractive index of 0.025–0.071 (median: 0.042). These are higher values than observed for the Pagami Creek fire plume, but similar to the Canada forest fire plume. This might be caused by different compositions of the bulk aerosols, e.g. possibly lower BC fractions for the Pagami Creek fire plume (see Section 4.3.3).

Table 16. *Optical parameters of the forest fire plumes observed during CONCERT 2011. For the Pagami Creek fire plume, median values are presented and the range of observations including 20% uncertainty is given in parentheses. σ_{abs}: absorption coefficient (530 nm); $å_{abs}$: Ångström exponent of absorption (467/660 nm); k: imaginary part of refractive index.*

Parameter	Pagami Creek fire plume	Canada forest fire plume
σ_{abs} / Mm^{-1}	4.9 (0.6–15.0)	3.0 (2.4–3.6)
$å_{abs}$ / -	2.7 (1.7–3.4)	1.5 (1.2–1.8)
k / -	0.015 (0.010–0.023)	0.049 (0.039–0.059)

Recent studies report a bias of organic aerosols (OA) on the absorption measurements of the PSAP: Cappa et al. (2008) found for laboratory measurements a possible bias of up to 100% and Lack et al. (2008) report 50–80% bias at ambient measurements for aerosols with a high OA burden with respect to BC due to a redistribution of liquid-like organic aerosol around the fibers of the filter modifying light scattering and due to a possible coating and absorption enhancement of pre-existing absorbing aerosol particles as OA is deposed (Lack et al., 2008). Thus a higher uncertainty than presented in Section 3.4.6 needs to be considered as OA is expected to be abundant in biomass burning aerosol layers. That leads to a possible overestimation of σ_{abs} and k. Based on that, the presented values for σ_{abs} and k in Table 16 should be considered with caution as maximum estimates.

To assess the vertical distribution of the optical properties of the Pagami Creek forest fire aerosol layer, the vertical profiles of particle backscatter coefficient β_{par} (black curve) and particle linear depolarization ratio δ_{par} (red curve) are presented in Figure 67b, based on the average 532 nm elastic backscatter signal of the time period from 08:36–09:25 UTC, determined by Leibniz Institute for Tropospheric Research (TROPOS). Sequences strongly affected by the low-level clouds were removed from the analysis. As no Raman scattering information was available, the lidar data analysis was performed using the Klett-Fernald-method (Klett, 1981; Fernald, 1984). This requires the assumption of the extinction-to-backscatter ratio (lidar ratio). From earlier studies (e.g. Groß et al., 2013 and references therein) it is known that a lidar ratio of 70 sr is reasonable for biomass burning aerosol. Thus, this value is used for the analysis of the lidar data. Particle linear depolarization ratios of around 6–8% are observed throughout the layer between 8 km and 12 km altitude. As a result of the distribution of the plume (Figure 65; Figure 73), the values for the particle backscatter coefficient β_{par} are only to a limited extent representative for the entire biomass burning aerosol layer, because the lidar in Leipzig only measured in the lateral end of the plume. This might have a big influence on β_{par}, which, in this case, is up to 1.5 Mm^{-1} sr^{-1}, but

probably larger for the central part of the plume. Uncertainties shown for the retrieved optical properties are due to signal noise and the assumption of a reference value and a lidar ratio (Rocadenbosch et al., 2010).

In summary, in this section detailed information on microphysical and optical properties of forest fire aerosol layers are presented. In comparison to the findings for the variety of observed aerosol layers during CONCERT 2011 (Section 4.2), forest fires aerosol is a major source for the BC burden in the atmosphere[30] and due to possibly large coatings on the BC of major relevance for the absorption of solar radiation.

4.4 Sources contributing to the BC load in the UTLS region

BC in the UTLS region has a longer lifetime compared to lower altitudes due to less frequent removal caused by washout (e.g. Bond et al., 2013). Based on the data gathered during CONCERT 2011, estimates on the BC mass import to the atmosphere can be made to evaluate the relevance of different sources for the BC load in the UTLS region. Section 4.4.1 approaches the BC mass import for the special case of the Pagami Creek fire, containing results from Dahlkötter et al. (2014). In contrast to such ground-based sources, aviation directly emits BC to the UTLS region. For several aircraft exhaust sequences the rBC mass concentrations are derived and discussed with respect to the contribution to the UTLS BC (Section 4.4.2).

4.4.1 BC mass import of the Pagami Creek fire to the atmosphere

In this section three estimates are presented to determine the primary emissions from the Pagami Creek fire (first approach), to determine the import of BC from the Pagami Creek fire to the UTLS region (second approach) and to determine the import of BC from the pyro-convective forest fires in the USA and Canada in 2002 to the UTLS region (third approach).

The first approach applied here estimates the total OC and BC emissions based on the burnt area, wood mass per area and emission factor for boreal needle-leaf forests. For this rough estimate of the BC and OC mass directly emitted by the Pagami Creek fire (Figure 84a) values presented in Wiedinmyer et al. (2011) are used: BC and OC emission factors for boreal needle-leaf forests (0.2 g per kg biomass burned and 7.8 g per kg biomass burned, respectively) (McMeeking, 2008) and fuel loadings for North American boreal forests (25,000 g m^{-2}) (Akagi et al., 2011 and references therein) are combined with the burned area (~ 350 km^2; U.S. Forest Service), resulting in roughly $2 \cdot 10^3$ Mg (i.e. tons; t) BC and $68 \cdot 10^3$ Mg OC emitted from the Pagami Creek fire. This estimate is strongly linked to the information on the burned area and to the applied emission factors and needs to be considered with caution as empirical estimate, implying large uncertainties. However, large parts of these primary emissions will fall out quickly, by e.g. wet deposition, or will be transported at altitudes below 8 km (Mattis et al., 2008; Weinzierl et al., 2011) or will not

[30] Bond et al. (2013) estimates the contribution of open burning to the global total BC emissions to be about 37%.

enter the free troposphere. The fraction of the emissions entering the upper troposphere is more relevant in terms of its impact on the radiation budget due to lower washout rates associated with longer life times and the possibility of long-range transport.

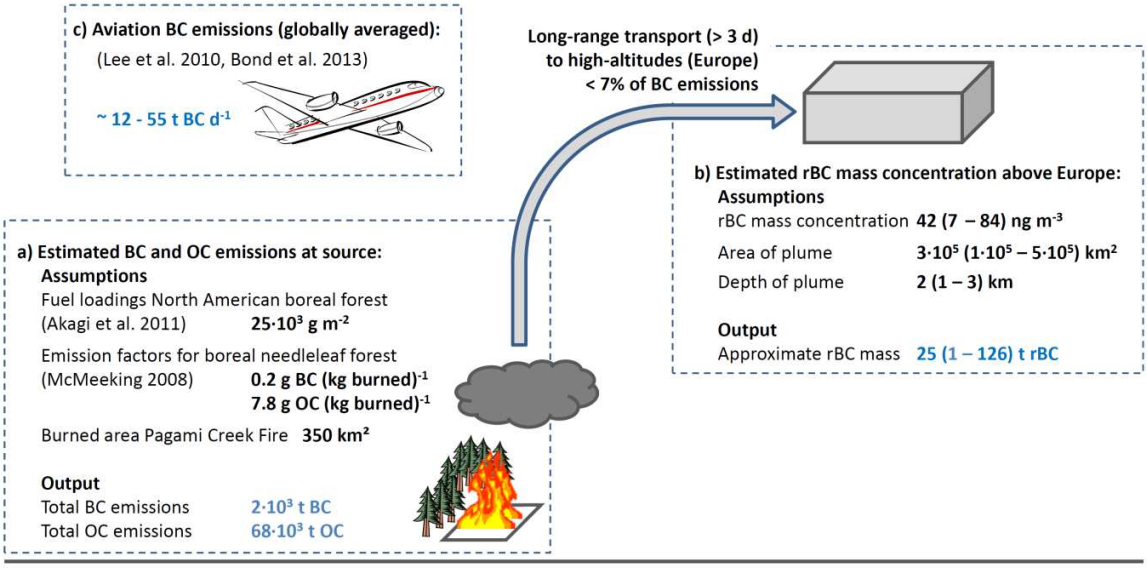

Figure 84. *Schematic for BC mass import of the Pagami Creek fire: a) Calculation of total BC and OC emission from the fire, based on fuel loadings, emission factors and burned area; b) rBC mass import to the UTLS region above Europe, based on the dispersion of the plume and measured rBC mass concentrations as best guess (and total range); c) comparison to daily soot emissions of global aviation. Adopted from Dahlkötter et al. (2014).*

In order to assess the BC import of the Pagami Creek fire to the UTLS, the second approach uses the measurements in the plume and the plume dispersion modeling (HYSPLIT) to estimate the BC import of the Pagami Creek fire plume to the UTLS region above Europe. Assuming a homogeneously distributed aerosol layer, the BC mass import of the Pagami Creek fire event to the UTLS region above Europe can be derived (Figure 84b) from the measurements and dispersion model simulations. The area of the aerosol layer is deduced from the HYSPLIT dispersion calculation by sizing the plume area for 15 September 2011 (20:00–23:00 UTC) representative for the plume observed 12 h later above Europe by assuming a plume concentration threshold (0.1 a.u.; see Figure 72) and a rational uncertainty (area: $(3\pm2) \cdot 10^5$ km^2; Section 4.3.2), based on the similarity of the dispersion calculation and observations from IASI (Section 4.3.2) and GOME (Section 4.3.1). The height of the aerosol layer is deduced from the lidar observations (height: 2±1 km; Section 4.3.1). Thus, the volume of the aerosol layer is ($1 \cdot 10^5$–$15 \cdot 10^5$ km^3; best estimate: $6 \cdot 10^5$ km^3). As BC mass concentration, the median rBC mass concentration from the SP2 measurements in the edge of the plume is used (7–84 ng m^{-3}; median of measurement sequences: 42 ng m^{-3}; at ambient conditions). Values in brackets in Figure 84b show the range of uncertainty. From these data a best estimate for the rBC total mass import to the high altitude aerosol layer above Europe of 25 Mg (i.e. tons; t) rBC is obtained, ranging from 1–126 Mg rBC. This estimate depends strongly on the assumed duration of the emission, because, e.g., a shorter duration would decrease the area covered by the plume of the dispersion calculations at the time of measurements. Nevertheless, it was shown (Section 4.3.2) that the chosen duration of the emissions is in good agreement with observations of the duration of the fire. The local

inhomogeneities observed both in simulation (Figure 72) as well as in measurement (Figure 63) cause a large uncertainty in both the plume area as well as the average concentration. However, the uncertainties of this estimate are smaller compared to the theoretical estimate on the direct total emissions of the Pagami Creek fire described above, because the input parameters are based on direct measurements and calculations related to the specific event compared to generalized emission factors used in the first approach. Because the dispersion calculation suggests that the measurements took place in the less-concentrated tail of the plume, the maximum value of 126 Mg rBC might still be an underestimation of the imported BC mass. However, it is highly probable that the real BC mass of the Pagami Creek fire plume ranges within in the presented span of 1–126 Mg BC.

Comparing the direct emissions at the source with the plume observed above Europe and taking into account the given uncertainties due to the assumptions, e.g. for plume distribution calculation and emission factors, and that only the plume transported to Europe in altitudes above 10 km was considered, the extended aerosol layer above Europe on 16 September 2011 contains < 7% of the BC mass emitted from the fire. This is reasonable agreement, keeping in mind that both estimates contain considerable uncertainties and that the second approach only estimates the portion of the emissions that remains in the atmosphere after 4 days of long-range transport at high altitudes whereas the estimate based on the first approach is for the total direct BC emissions. However, the reasonable agreement between the two independent estimates gives better trust in these numbers.

These estimates show that singular forest fire events can be a relevant source for the BC loadings in the UTLS region on the time scale of at least days. Besides forest fires, another (permanent) source for BC in the UTLS region are emissions from aircraft (Figure 84c). Aviation emissions are estimated by Lee et al. (2010) to be 16 Mg d^{-1} soot (defined as BC + OC). The BC/OC ratio for aviation-induced soot emissions is roughly 3.5 (Bond et al., 2004, and references therein). Thus, the aviation-induced soot emission value of Lee et al. (2010) can be converted to about 12 Mg d^{-1} BC. Bond et al. (2013) estimate the aviation-induced BC to be about 55 Mg d^{-1} BC. The BC emissions from aviation to the UTLS region are even smaller, taking into account that the total aviation-induced emissions contain also emissions to lower altitudes during take-off and landing. Nevertheless, the best guess of the BC mass imported from the Pagami Creek fire to the UTLS region over Europe after several days of transport is the same magnitude as the daily globally averaged BC mass emission of aviation. The comparison of 1–126 Mg BC in the Pagami Creek fire plume in the UTLS region over Europe to 12–55 Mg d^{-1} BC related to aviation shows the relevance of such singular forest fire events as a source for the import of black carbon into the atmosphere.

For biomass burning and forest fires comprehensive data sets of emission factors for different ecozones (e.g. Turquety et al., 2007), land cover types (e.g. Wiedinmyer et al., 2011) or global regions (e.g. van der Werf et al., 2006) are available. In addition, pyro-convective plumes, such as the Pagami Creek fire plume, are observed frequently and reported in various case studies (e.g. Jost et al., 2004; Fromm et al., 2005; Rosenfeld et al., 2007; Fromm et al., 2008; Gatebe et al., 2012; Trickl et al., 2013) with the vertical distribution of the plume being modeled for some singular pyro-convective events (e.g. Trentmann et al., 2006; Luderer et al., 2007), providing information on the emissions heights of the respective plumes. However, due to varying meteorological conditions and burning conditions, a generalization and parameterization of the vertical distribution of

pyro-convective plumes is not available in literature. In addition, though pyro-convection is frequently described, the abundance and global distribution of pyro-convective events is insufficiently investigated. Thus, the extrapolation of the results found for the Pagami Creek forest fire plume to the import of BC to the UTLS region is not realizable on global scale. To set the Pagami Creek forest fire pyro-convective event described above into broader context, in the following an approach assessing the contribution of pyro-convective forest fires to the BC burden in the UTLS region on a regional scale is described:

Fromm et al. (2010) report 17 pyro-convective events in the USA and Canada for the year 2002. For this data set the BC emissions can be calculated (third approach), using the same strategy as described in the first approach, though a combination of emission factors and fuel loading for boreal needle-leaf forests and temperate broad-leaf forests (emission factor: 0.2–0.6 g BC per kg biomass burned; fuel loading: 10,500–25,000 g m^{-2}) from Wiedinmyer et al. (2011) is used. Thus, the pyro-convective forest fires, reported by Fromm et al. (2010), emitted in total roughly $2 \cdot 10^4$–$13 \cdot 10^4$ Mg (i.e. tons; t) BC. Again, this estimate is strongly linked to the assumptions made for the burned area and the applied emission factors and needs to be considered with caution as empirical estimate, implying large uncertainties. In this study it is assumed that roughly 20–80% of the total burned area of the fires, belonging to the described 17 pyro-convective events, burned during the pyro-convective event, and thus that 20–80% of the total emissions potentially are transported to the free troposphere during the pyro-convective event, and that about 10%[31] of these emissions are transported by the pyro-convection to the UTLS region. That results in $4 \cdot 10^2$–$1 \cdot 10^4$ Mg BC transported to the UTLS region. However, modeling studies for the Chisholm fire plume in Alberta, Canada (Trentmann et al., 2006; Luderer et al., 2007), suggest that a larger fraction (> 50% of the emitted aerosol mass) is transported to altitudes above 8 km. Using this fraction (50–90%), the pyro-convective forest fires from the USA and Canada in 2002 emitted roughly $2 \cdot 10^3$–$9 \cdot 10^4$ Mg BC to the UTLS region. These values, considering only pyro-convective forest fires in the USA and Canada, are of the same magnitude as the annual emissions of BC from aviation ($6 \cdot 10^3$–$2 \cdot 10^4$ Mg BC) (Lee et al., 2010; Bond et al., 2013). It is important, that the data for pyro-convective forest fires in 2002 should be considered as a maximum estimate due to a drought in 2002 in North America and due to parts of the BC particles probably being washed out quickly due to precipitation during the pyro-convective transport. Nevertheless, considering the contribution of pyro-convective forest fires from all other regions (not only North America), the global import of BC from pyro-convection to the UTLS region plays a significant role for the BC burden in the UTLS region. This result is based on several assumptions. Therefore the given values should be considered with caution as rough estimated values but can illustrate the potential relevance of forest fires as a source for BC in the UTLS region.

[31] This value is based on the fraction of particles (< 7% of the BC mass) contained in the Pagami Creek fire plume above Europe, reported earlier in the section.

4.4.2 BC mass import of aviation to atmosphere

As already mentioned in the previous section, besides the BC mass import due to forest fires, aviation is a relevant minor but continuous source for BC in the UTLS region (e.g. Bond et al., 2013). However, the current estimations of BC emissions by aviation are uncertain and deviate by up to an order of magnitude or more (e.g. Stettler et al., 2013a and references therein) and BC number emission indices are probably higher than used in most modeling studies (e.g. Schumann et al., 2013). Detailed in-situ measurements of aviation-related BC emissions can help to reduce the described uncertainties.

The BC import by aviation can be determined by probing aircraft exhaust plumes and contrails (short for condensation trails, i.e. with a significant amount of ice crystals). To determine BC mass concentrations in aircraft exhaust plumes, 5 sequences were analyzed from flights #110916b and #110924a (CONCERT 2011) representing different conditions and different aircraft types including A346, A343, B77W and A321. Figure 85 shows the non-volatile particle number concentration (10 nm < D_P < $D_{cutoff,50}$), the integral number concentration measured with the FSSP-300 (0.45 < D_P < 30 µm) and the flight altitude. The blue dotted boxes represent the 5 considered sequences. For all 5 sequences, probed at typical cruise altitudes of commercial aircrafts, the non-volatile particle number concentration shows fluctuating enhancements, while the FSSP-300 number concentration only changed significantly for sequences 3 to 5 as an indicator for large particles, e.g. ice particles, and thus for contrail formation.

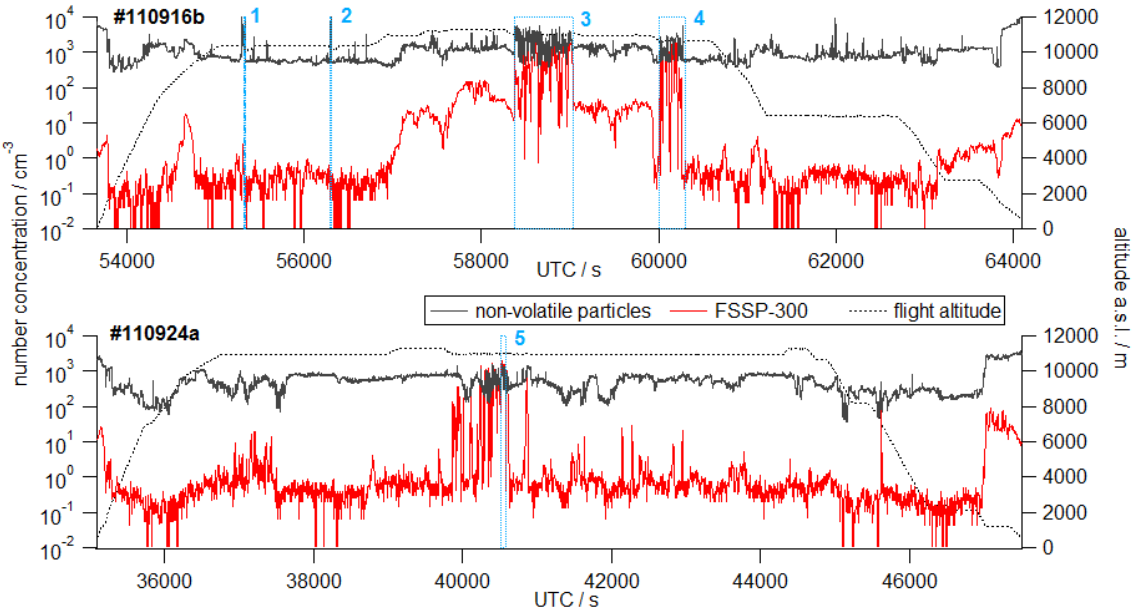

Figure 85. *Time series of the non-volatile particle number concentration (grey solid line; 10 nm < D_P < $D_{cutoff,50}$), the integral FSSP-300 number concentration (red solid line; 0.45 < D_P < 30 µm) at stp conditions and the flight altitude a.s.l. (black dashed line) for the flights #110916b (upper panel) and #110924a (bottom panel). Sequences chosen for contrail and aircraft exhaust analysis are marked with blue dotted boxes and are numbered.*

Table 17 gives the minimum, mean and maximum values for the considered sequences for CO_2, NO, NO_Y and *RHi*, which are parameters relevant for the contrail classification and age determination. The values for *RHi* show that the sequences 3 to 5 were around saturation with respect to ice, while *RHi* in sequence 2 was significantly lower, agreeing with the

number concentration measured by the FSSP-300 (Figure 85). Due to an uncertain sensitive area of the FSSP-300, the total quantities are undefined. However, the qualitative objective of contrail and cirrus detection is unaffected by this issue.

To determine the BC mass concentrations of the exhaust plumes, the approach described in Section 3.4.5 was applied, assuming that all non-volatile particles are BC particles and that BC particles in internally mixed particles > $D_{cutoff,50}$ are negligible regarding their number and mass concentration. The first assumption is based on Bond et al. (2004) and references therein, presenting fractions of 0.7 for BC (and 0.2 for OC) contributing to the total particulate matter emitted by aircrafts (0.14 g kg^{-1}), and Petzold et al. (1999), reporting even higher fractions of BC for thrust levels > 60%. The probed aircrafts all flew at high thrust levels. The latter assumption is irrelevant for the sequences 1 and 2, where no significant amount of particles > $D_{cutoff,50}$ was observed, representing exhaust plumes without developed contrail. Using this approach, a range of the BC mass concentration, labeled as minimum and maximum estimates, is derived for an assumed BC density ρ of 1,800 kg m^{-3} (Table 18). The best estimate is derived from the BC number size distributions for the 5 considered sequences shown in Figure 86, with diamonds representing the rBC number size distribution measured with the SP2 and the related log-normal fits (dashed lines) assuming the same BC density (ρ = 1,800 kg m^{-3}).

Table 17. *Microphysical and chemical characteristics of the 5 considered contrail and aircraft exhaust plume sequences as mean values and the range (in brackets). The non-volatile particle number concentration (stp) was measured with a CPC (D_P > 10 nm), while the SP2 measured the rBC number concentration (stp) in the size range 80 < D_{rBC} < 440 nm. Δ CO_2 represents the difference in CO_2 between the exhaust plume and the related background.*

Contrail/ exhaust sequence	**-**	**1 (#110916b)**	**2 (#110916b)**	**3 (#110916b)**	**4 (#110916b)**	**5 (#110924a)**
start time	s	55320	56290	58370	60000	40520
end time	s	55340	56310	59030	60300	40580
Non-vol. number conc.	cm^{-3}	3273 (741–15415)	7011 (502–21312)	2072 (345–5624)	1375 (521–5449)	853 (306–1502)
SP2 rBC number conc.	cm^{-3}	325 (59–598)	80 (13–186)	26 (5–68)	79 (2–247)	12 (3–20)
CO_2	µmol mol^{-1}	390.2 (389.9–390.7)	387.8 (387.7–387.9)	388.4 (387.3–389.9)	388.7 (387.4–390.4)	388.9 (388.1–389.6)
Δ CO_2	µmol mol^{-1}	3.1	0.1	1.9	2.5	1.3
NO	nmol mol^{-1}	12.3 (3.2–57.1)	-	3.6 (0.1–11.7)	3.2 (0.0–14.2)	5.6 (0.4–11.2)
NO_Y	nmol mol^{-1}	13.3 (5.5–39.2)	-	6.3 (1.3–16.3)	5.6 (1.2–19.9)	9.4 (2.0–16.4)
RHi	%	-	71 (66–77)	95 (80–112)	101 (82–129)	97 (91–107)
error *RHi*	%	-	10 (10–11)	14 (12–17)	15 (12–21)	13 (12–14)

The minimum estimates for the BC mass concentration result in 0.08–0.33 µg m^{-3}, while the maximum estimates result in 0.39–2.83 µg m^{-3}. The best estimates (0.09–0.71 µg m^{-3}) should deliver the most reasonable results for the BC mass concentration estimates for the exhaust plume and the contrail sequences.

Table 18. *BC mass concentration estimates for the 5 considered contrail and aircraft exhaust plume sequences for stp conditions assuming a density ρ = 1,800 kg m^{-3}. The schematics illustrate the respective approaches used for the minimum estimate, the best estimate and the maximum estimate (see Section 3.4.5).*

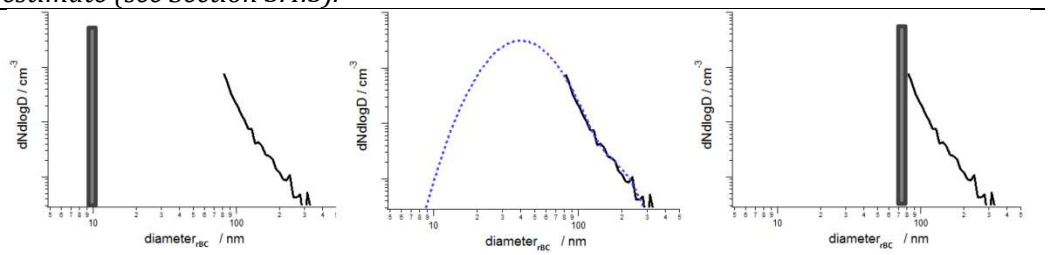

Contrail/ exhaust sequence	Minimum estimate (10 nm; ρ = 1,800 kg m^{-3}) / µg m^{-3}	Best estimate (ρ = 1,800 kg m^{-3}) / µg m^{-3}	Maximum estimate (75 nm; ρ = 1,800 kg m^{-3}) / µg m^{-3}
1 (#110916b)	0.33	**0.71**	1.50
2 (#110916b)	0.08	**0.52**	2.83
3 (#110916b)	0.08	**0.17**	0.89
4 (#110916b)	0.11	**0.21**	0.62
5 (#110924a)	0.05	**0.09**	0.39

In sequences 3 and 4, besides the freshly emitted aircraft exhausts, the Pagami Creek fire plume was present, biasing the aviation-related BC mass concentrations. As a consequence, the BC mass concentration caused by the aircraft has to be assumed to be lower. Because the Pagami Creek fire had BC mass concentrations of 0.03–0.35 µg m^{-3} (median: 0.16 µg m^{-3}), during sequences 3 and 4, the Pagami Creek fire plume contribution to the derived BC mass concentrations can be approximated to 14–100% (best estimates: 94% and 76% for sequence 3 and 4, respectively). However, comparing the BC number size distributions of all five contrail and exhaust sequences, the interference of the Pagami Creek fire plume is not clearly discernible in Figure 86, implying that the BC number size distributions for the aircraft exhaust plumes and the Pagami Creek fire plume are similar. The BC number size distribution for sequence 4 measured within the Pagami Creek fire plume (see Section 4.3) shown in Figure 86, confirms this similarity. No significant differences are discernible, though the forest fire plume seems to have increased concentrations in the size range of 80–200 nm. However, the CMD_1 lies within the *CMD*s observed for the aircraft exhausts and contrails.

In addition, in comparison to all contrail and aircraft exhaust, despite of the transportation of 3–4 days and the resulting dilution, sequences of the Pagami Creek fire plume still exhibited BC mass concentrations comparably high as the BC mass concentrations observed in fresh aircraft exhaust plumes and contrails. Nevertheless, due to the multitude of commercial flights, aviation needs to be considered as a relevant and permanent source of BC in the upper troposphere, obviously discernible in the estimate for civil aviation in the year 2005 with a total flight distance of 407 · 10^{8} km (Lee et al., 2010).

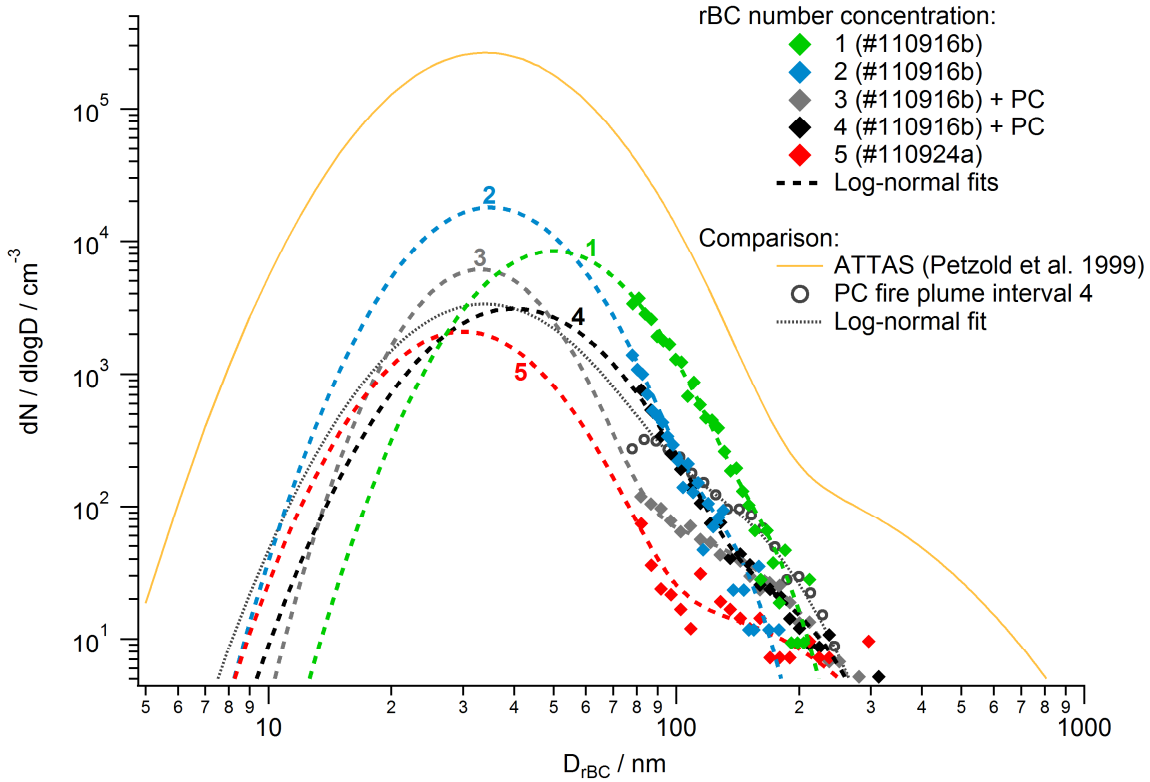

Figure 86. *BC number size distributions (stp) for the 5 considered contrail and aircraft exhaust sequences (Figure 85). Diamonds represent the SP2 rBC measurements and dashed lines the extrapolation by log-normal fits (Section 3.4.5). During sequences 3 and 4 simultaneously the Pagami Creek (PC) fire plume was measured, which biased the BC measurements. For comparison, a BC number size distribution measured in the Pagami Creek fire plume (grey circles) and the related fit (grey dotted line) is shown as well as a size distribution for the exhaust plume (dilution factor: 197) of the ATTAS aircraft at FL 260 (Petzold et al., 1999).*

A sophisticated analysis of plume ages can be done following Schumann et al. (1998). For this study, the uncertainties for the BC mass concentration estimates are already large (see Table 18). Thus, detailed analysis of the dilution and the age of the plumes, causing further uncertainties, would not result in a better understanding of the presented data. A more simplified and qualitative approach applied for the observed plumes uses the CO_2 mixing ratio. Thereby, an indication for the dilution is given by ΔCO_2 (Table 17), describing the difference of the maximum CO_2 value observed in the exhaust to the mean background CO_2 mixing ratio. ΔCO_2 is in agreement with the estimated BC mass concentrations, indicating the presence of higher BC mass concentrations in less diluted exhaust plumes. For the exhaust plume sequence 2, ΔCO_2 is not significantly increased. This might be caused by CO_2 sampling artifacts due to the high fluctuations within the exhaust plume or due to data analysis issues. More precisely, the used CO_2 instrument has a low sampling frequency which cannot resolve the highly fluctuating CO_2 concentrations. In addition, high pressure fluctuations might cause a rejection of the data due to quality assurance procedures. Thus, artifacts due to the CO_2 measurement have to be considered. Consequently, the presented values represent minimal estimates for ΔCO_2. The plumes analyzed in this study are estimated to be older than 20 s, and probably even older than 100 s.

The results for BC number size distributions and BC mass concentrations of the aircraft exhaust plumes and contrails can be compared to results from Petzold et al. (1999). They probed in-flight the exhaust of the ATTAS aircraft in roughly 8 km altitude 237 m behind the aircraft. The BC number size distribution, shown in Figure 86, exhibits a similar structure compared to the results of this study with a CMD_1 of 34 nm. However, they measured consistently higher concentrations, resulting in BC mass concentrations of 9.6–12.7 µg m^{-3}, which are far higher compared to the results of this study (best estimate: 0.09–0.71 µg m^{-3}). The difference can be attributed to the dilution of the respective plumes, which is small in the case of the ATTAS aircraft due to the sampling distance of just 237 m and the related plume age of < 2 s, while the plumes analyzed in this study are much older (see above).

Stettler et al. (2013b) and references therein report that BC emitted by aircraft engines can be characterized as having a BC number size distribution with a *CMD* in the range 10–40 nm and a *GSD* in the range 1.3–2.3. These findings give evidence that the method applied in this study for contrails of the described age provides reasonable results for the BC number size distribution (*CMD*: 30–55 nm; *GSD*: 1.4–1.5) and increases the reliability of this method.

Based on the presented BC number size distribution, the BC mass size distribution can be derived, assuming an BC density of 1,800 µg m^{-3}: in Figure 87 the measured rBC mass size distributions and the log-normal fits are shown. Here the differences between the respective exhaust plumes and contrails are distinctly discernible. While the sequences 1 and 2 (no contrail formation) exhibit monomodal structures, the sequences 3, 4 and 5 show bimodal structures. This is an indication for a processing of the BC particles due to supersaturational conditions. Possibly these conditions lead to an accumulation of the BC particles. However, in sequences 3 and 4, the presence of the forest fire plume promotes this bimodal structure. But the fact that this structure also is determined for an unbiased sequence (sequence 5), underlines the hypothesis of accumulation processes induced by supersaturation.

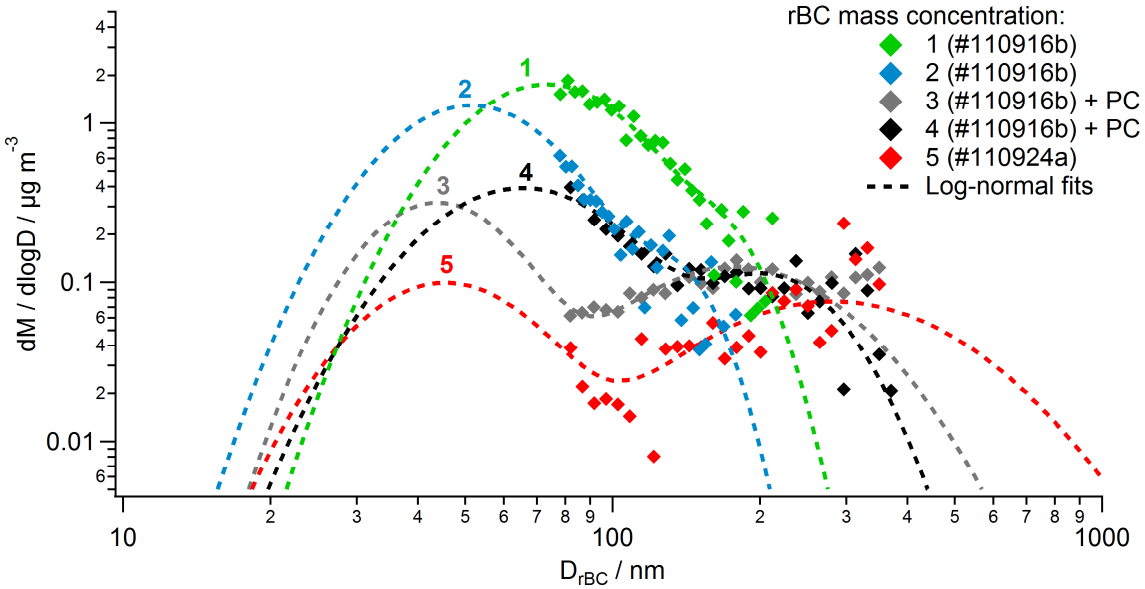

Figure 87. *BC mass size distributions (stp) for the 5 considered contrail and aircraft exhaust sequences (see Figure 85). Diamonds represent the SP2 measurements and dashed lines represent the converted log-normal fits of the BC number size distributions from Figure 86 assuming 1,800 µg m^{-3} for the BC particle density. During sequences 3 and 4 simultaneously the Pagami Creek (PC) fire plume was measured, biasing the measurements.*

The presented estimates clarify the relevance of aviation as a source of BC in the atmosphere. Besides the direct effect based on emissions of BC particles, aviation-induced BC particles play a significant role for the formation processes of contrails and contrail-induced cirrus clouds. These processes are not treated in this study. Further information on contrails and contrail induced cirrus clouds can be found, for example, in Schumann et al. (2012). However, this approach and the use of the SP2 delivers relevant information on the BC load in aircraft exhausts and should be developed further to reduce the uncertainties of the BC emissions of aviation and to study the respective processes.

5 Summary and conclusion

This thesis addresses the investigation of black carbon (BC) aerosol layers at mid-latitudes based on airborne in-situ observations during CONCERT 2011 in order to provide a comprehensive data set to investigate the relevance of atmospheric BC. Therefore, in this study the Single Particle Soot Photometer (SP2), based on laser-induced incandescence, was carefully prepared and characterized and for the first time operated onboard the research aircraft Falcon. The major findings and their implications are summarized in the following:

Atmospheric aerosol distribution at mid-latitudes in September 2011
Based on 11 research flights conducted during CONCERT 2011, the aerosol burden within the vertical column of the troposphere and the UTLS region over Europe in September 2011 is derived. The BC mass concentration spreads over three orders of magnitude, showing a large variability within the free troposphere, while the highest concentrations ($\sim$ 1 µg m^{-3}) are observed in the PBL and slightly above. The comparison to model results shows good agreement for altitudes < 7 km, while above that significant deviations are observed, possibly caused by specific meteorological conditions and transport patterns of the air masses during the campaign. These findings imply the need for further airborne measurements of the vertical profiles of BC aerosol to identify the mechanisms, affecting the BC distribution in the atmosphere and causing the observed deviations at higher altitudes.

Aerosol layer characteristics at mid-latitudes in September 2011
During CONCERT 2011 highly variable aerosol layers were observed in roughly 10% of the flight time above the PBL, contributing to the above mentioned variability in the free troposphere and UTLS region. Most of the layers are present at altitudes < 7 km and their vertical depth is predominantly < 4 km. The frequency and distribution of the aerosol layer observations agrees with long-term aerosol layer observations above Europe reported it the literature, giving further evidence for representative results from this study. Based on trajectories, the aerosol layers observed during CONCERT 2011 were allocated to main source regions like the marine boundary layer (MBL), the planetary boundary layer (PBL) of Europe and northern Africa, volcanic emissions, long-range transport from North America and forest fires. The different types of aerosol layers were characterized with respect to their microphysical properties, such as rBC mass size distributions, total rBC mass concentrations, total particle number size distributions and mixing states. The major findings on the characteristics of BC-containing aerosol layers are:

- The average rBC mass concentrations observed in the aerosol layers range from < 5 ng m^{-3} to > 400 ng m^{-3} (stp), exhibiting a factor of about 100 between the highest and lowest concentrations. Aerosol layers attributed to the MBL and volcanic ash plumes show low average rBC mass concentrations (< 20 ng m^{-3}), substantially less than e.g. a volcanic ash plume mixed with fresh PBL aerosol (up to 300 ng m^{-3}). Aged lofted PBL aerosol layers have average rBC mass concentrations between 70 ng m^{-3} to above 280 ng m^{-3}, while the average rBC mass concentrations of the forest fire layer sequences range between roughly 30 ng m^{-3}

and 350 ng m^{-3}. For the observed aerosol layers, the BC mass size distributions are parameterized by log-normal distributions with mass median diameters up to 188 nm.

- Derived total particle number concentrations of the observed aerosol layers, including BC-containing and BC-free particles, vary with almost two orders of magnitude. The total particle number size distributions show monomodal or bimodal structures in the Aitken and accumulation mode size range, while no significant amount of coarse mode particles was observed. Fresh volcanic ash aerosol shows a similar bimodal structure as the observed forest fire plumes, though with far higher concentrations and count median diameters (*CMD*) shifted towards smaller particle sizes. In aged PBL and aged MBL aerosol layers the bimodal structure is just slightly discernible or not present. Based on the data of 32.3 hours during 11 research flights, this study presents a generic range of size distributions, which can be expected for the different aerosol types for September in Central Europe.

- To assess the mixing state of individual aerosol particles, for the BC-containing particles of the observed aerosol layers the coating thickness is derived. BC particles measured in the forest fire plumes show 40–220 nm thick coatings, with a maximum of about 80–160 nm. For all other sources the maxima of the coating thickness histograms are < 50 nm and with maximum coating thicknesses of about 180 nm, implying generally similar coating processes taking place for BC from all described sources. This stable coating thickness distribution for aged aerosol layers observed above Central Europe differs significantly from the coating thicknesses of fresh PBL aerosol, which is relevant for the modification of the absorption of the BC core due to the lensing effect. These results can help to reduce uncertainties associated with the particle mixing of BC-containing particles.

- The median color ratios observed in the forest fire aerosol layers are distinctly higher compared to the color ratios observed in the sparse aerosol layers, featuring a high similarity. This indicates an averagely higher boiling point temperature of BC particles in forest fire plumes probably associated with different BC material formed during forest fires.

Characteristics of absorbing forest fire aerosol layers

In the framework of the CONCERT 2011 campaign, an intense elevated forest fire aerosol layer (Pagami Creek fire plume) was observed over northeast Germany on 16 September 2011 at an altitude of 10–12 km using aerosol airborne in-situ measurements of the DLR research aircraft Falcon and a ground-based lidar (TROPOS Leipzig). In addition, a second forest fire aerosol layer (Canada forest fire plume) was observed in the lower troposphere (2.2–3.4 km a.s.l.) on the same day. Back trajectories and dispersion simulations are conducted to determine the sources of the aerosol layers. In the following, the major findings on the characteristics of these two absorbing forest fire aerosol layers (main focus: Pagami Creek fire plume) will be summarized (see also Dahlkötter et al., 2014):

- The observed aerosol layers are attributed to the Pagami Creek fire in Minnesota, USA, and a forest fire in Canada. The attribution to the Pagami Creek fire is supported by e.g. the measured lidar linear depolarization ratio (6–8% at 532 nm), indicating a forest fire source.

- The total rBC mass concentrations of the aged (3–4 days old) Pagami Creek fire plume and the Canada forest fire plume are 0.033–0.348 µg m^{-3} (median: 0.159 µg m^{-3}; stp)

and 0.101 µg m^{-3} (median; stp), respectively, comparable to rBC mass concentrations typical for a moderately polluted PBL. The *MMD*s of the Pagami Creek fire plume rBC size distribution range between 120 nm and 160 nm, while the Canada forest fire plume exhibits a *MMD* of 188 nm. The observed variations are caused partly by the burning conditions and partly by different processes during transport, such as dilution or wet removal. In the forest fire plumes BC contributes to only a minor fraction of all aerosol particles (average rBC volume fractions in the SP2 size range in the Pagami Creek fire plume: 2.5–3.9%).

- To account for all particles, including BC-containing and BC-free particles, total aerosol number size distributions are calculated for the forest fire plumes. In contrast to a background air sample showing a monomodal total number size distribution, the Pagami Creek fire plume shows a bimodal number size distribution with a pronounced accumulation and Aitken mode. The Canada forest fire plume shows consistently lower concentrations but a similar size distribution, however with increasingly merging modes and shifted towards smaller particle sizes. Biomass burning number size distributions reported in the literature agree with the observations made for the Pagami Creek and the Canada forest fire plume, indicating similar source materials, environmental and burning conditions and transport patterns. The findings on the forest fire plumes analyzed in this study underline the general relationship of an increase in the *CMD* and a decrease of the geometric standard deviation (*GSD)* of the accumulation mode of total number size distributions of boreal forest fire aerosol with increasing plume age reported in the literature. However, the associated ages of the plumes deviate slightly from dependency of *CMD*, *GSD* and plume age shown in Weinzierl (2007) and references therein.

- The BC particles in the Pagami Creek fire plume show coating thicknesses of roughly 40–220 nm with a maximum between 80 nm and 160 nm (medians: 105–136 nm), whereas the majority of coated particles in fresh PBL aerosol exhibits coatings predominantly < 65 nm (median: < 20 nm). Most likely the coating consists of a mix of organic and inorganic species, which has an impact on the BC radiative forcing, on the BC hygroscopicity, and on the efficiency to act as cloud condensation or ice nuclei. Resulting from small rBC diameters and large coating thicknesses, shell-core ratios of up to 7.4 with median shell/core diameter ratios of D_P/D_{rBC} = 3.7, 2.8 and 2.4 at D_{rBC} = 90 nm, 130 nm and 170 nm, respectively, were determined for the Pagami Creek fire plume. For the Canada forest fire plume slightly smaller D_P/D_{rBC} ratios (maximum: 7.2; median: 2.9) were derived. Besides the accumulation of coating material during the almost four-day transport, most likely, major parts of the coating were condensed on the BC particles during or shortly after the burning event. This assumption is in agreement with observations reported in the literature, showing that shortly after the forest fire BC particles are already thickly coated.

- This study shows that the majority of the rBC-containing particles observed in the Pagami Creek fire plume disintegrated in the SP2 laser beam. This process is an indication of very thickly coated rBC cores or rBC cores located eccentrically, near the surface or at the surface of rBC-free particles. The observed number fraction of disintegrating particles is primarily a function of overall particle size, indicating that disintegration was possibly just the result of very thick coatings. The question if disintegrating particles are uniquely or predominantly associated with biomass burning aerosol remains to be addressed. The fact, that biomass burning BC-particles often exhibit thick coatings might be a reason for preferential occurrence of disintegrating particles in biomass burning aerosol, supported by

the absence of disintegrating particles in all other aerosol layers observed during CONCERT 2011. Aside from Sedlacek et al. (2012), observing similar high fraction of disintegrating particles in a biomass burning aerosol at the ground, this study shows for the first time the existence of disintegrating BC particles in high-altitude BC layers.

- The bulk absorption coefficient σ_{abs} of the Pagami Creek fire plume is between 0.6 Mm^{-1} and 15.0 Mm^{-1} (median: 4.9 Mm^{-1}; stp) at 530 nm wavelength. The calculated absorption coefficient of the pure BC cores $\sigma_{abs,rBC}$ at 550 nm wavelength is 0.2–3.0 Mm^{-1} (median: 1.2 Mm^{-1}; stp), implying that uncoated BC particles contribute 13–47% to the bulk absorption. In comparison, for the Canada forest fire plume $\sigma_{abs,rBC}$ (0.6–0.9 Mm^{-1}; stp) contributes 17–38% to σ_{abs} (2.4–3.6 Mm^{-1}; stp). The remaining fraction of the absorption (53–87%) can be explained by a combination of the following mechanisms: 1) A large fraction of absorbing OC, e.g. BrC, contributes significantly to the absorption, though it is less absorbing. 2) Coatings on the BC particles enhance their absorption significantly. 3) Absorbing soil dust particles are possibly lifted together with the smoke particles during the intense forest fire events. The bulk Ångström exponent of absorption $å_{abs}$ is for the Pagami Creek fire plume and the Canada forest fire plume 1.7–3.4 (median: 2.7) and 1.2–1.8, respectively. The difference to the expected $å_{abs}$ for pure BC ($å_{abs} \approx 1$) underlines that, besides BC, other wavelength-dependent absorbing components contribute to the bulk absorption. The imaginary part of the refractive index k at 530 nm wavelength derived for the bulk aerosol emphasizes the presented findings: for the Pagami Creek fire plume k is 0.010–0.023 (median: 0.015), while for the Canada forest fire plume k is 0.039–0.059. Due to a possible bias of organic aerosols on the absorption measurements, the presented values (σ_{abs}, $å_{abs}$, k) should be considered with caution as maximum estimates.

In conclusion, the microphysical properties of the observed extended forest fire plumes obtained within these case studies clarify the relevance of forest fire aerosol layers in the troposphere and the UTLS region. The highly variable particle composition, mixing state and concentrations increase the heterogeneity of biomass burning plumes. This has a manifold of impacts on the radiation budget of the atmosphere, which are not yet fully understood. Consequently, this study enables to assess the impact of light-absorbing aerosol layers on the radiation budget using radiation transfer calculations. However, to globalize the BC mass import to the upper troposphere and to minimize uncertainties of model estimates, additional in-situ measurements of aerosol layers similar to the presented layers and additional studies of the processes of aerosol transport by pyro-convection to the UTLS region are necessary.

Sources contributing to the BC load in the UTLS region

- This thesis presents a rough estimate of the BC mass import due to the Pagami Creek fire to the UTLS region above Europe (1–126 Mg BC; best estimate: 25 Mg BC) and compares it with the daily BC emissions of global aviation (12 – 55 Mg BC). A further estimate shows that about $2 \cdot 10^3$–$9 \cdot 10^4$ Mg BC was emitted by 17 pyro-convective events in the USA and Canada in 2002 to the UTLS region, which is of the same magnitude as annual emissions of BC from aviation. Thereby, the estimated highlight the relevance of forest fires to act as a potential BC source for the upper free troposphere.

- Aside from the BC mass import of forest fires, in this thesis the import by aviation is determined by probing aircraft exhaust plumes during CONCERT 2011 and a method to

derive BC mass size distributions is presented. The range of the rBC mass concentration in the exhaust plume sequences is derived (best estimates: 0.09–0.71 μg m^{-3}), which is the same magnitude as the concentrations in the aged and diluted Pagami Creek fire plume. Nevertheless, due to the multitude of commercial flights, aviation is a relevant source of BC in the upper troposphere and plays a significant role for the formation processes of contrails and contrail induced cirrus clouds. The presented approach and the use of the SP2 delivers relevant information on the BC load in aircraft exhausts and should be developed further to reduce the uncertainties of the BC emissions of aviation and to study the particular processes.

Perspective

The SP2, certificated and characterized for airborne in-situ measurements in the framework of this study, was operated since CONCERT 2011 frequently onboard the Falcon, e.g. during the DC3 field experiment or the SALTRACE field experiment, and will be operated also on the research aircraft HALO in the near future.

The detailed data and findings obtained within this study, especially with respect to BC in aerosol layers, will be used for radiation transfer calculations to assess the impact of elevated absorbing aerosol layers at mid-latitudes on the radiative budget. This will be done within the framework of the Helmholtz young investigators group AerCARE, working on the impact of aerosol layers on the atmosphere and climate characterized by aircraft, satellites and radiative transfer models, in which this study was performed. In addition, several open questions still need to be addressed.

First comparisons of the measured BC and the modeled BC were presented in this thesis. To improve the understanding of BC in the atmosphere, further comparison studies are planned.

Further studies should examine the number of pyro-convection events, relevant mechanism to transport large amounts of forest fire aerosol and BC to the upper troposphere and even to the stratosphere. This will help to confirm the estimates presented in this study and to clarify the relevance of forest fires for the BC load in the UTLS region.

The findings about disintegrating BC particles show that these particles were found abundantly in forest fire plumes. However, further measurements in other forest fire plumes of different ages are needed to investigate the fraction and the specific structures of such disintegrating BC particles in more detail. This will help to understand the relevance of disintegrating particles on the radiative transfer and on microphysical and chemical mixing processes.

The SP2 allows deriving advanced information on the BC emission of aviation. Further developments of the method presented in this study will allow a detailed analysis of the age of the exhaust plumes, providing size resolved data on BC-containing particles as a function of dilution and aging. Thus, detailed information on aviation emission factors can be obtained and can be used to reduce the uncertainties of the existing emission factors.

As described, BC measurements in clouds are suspected of being subjected to measurement artifacts. Further examinations of this issue, for example, by investigating the color ratio measured with the SP2, will help to reduce the uncertainty and might help to solve this problem.

Appendix

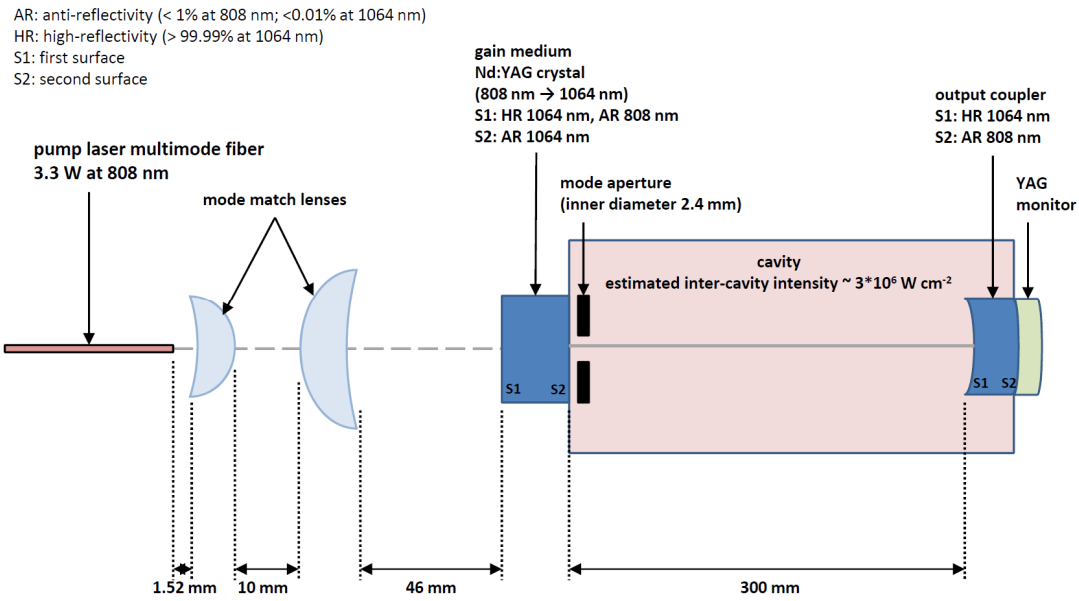

Appendix 1. *Schematic cross-sectional view of the laser system in the Single Particle Soot Photometer (SP2). Adopted from DMT (2012).*

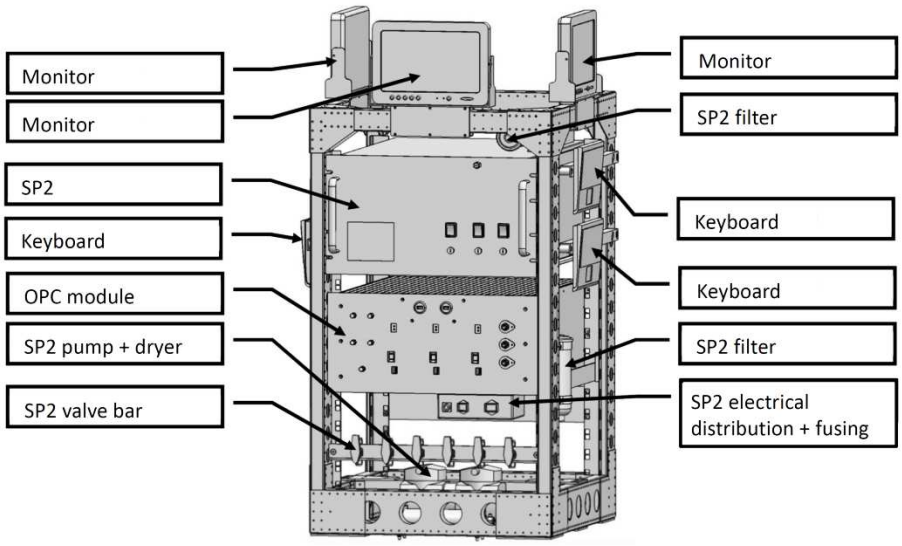

Appendix 2. *SP2 mounted in a standard Falcon rack. The OPC module contains two SKY-OPCs and computers for the data acquisition of wing-mounted instruments. Adopted from Enviscope (2011).*

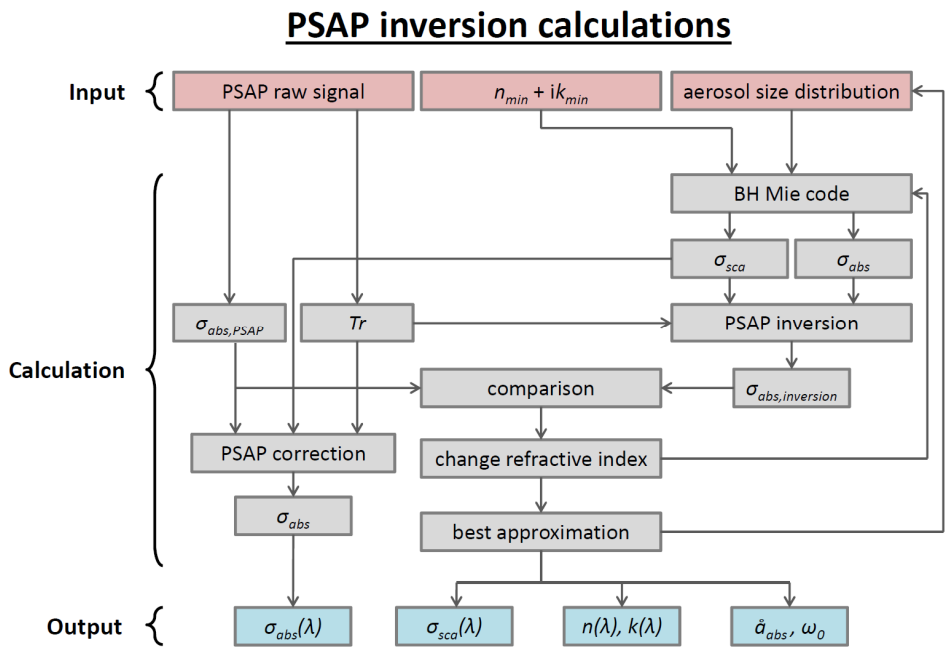

Appendix 3. *Detailed iterative PSAP inversion calculations used for the determination of optical and microphysical aerosol properties, adopted from Veira (2011).*

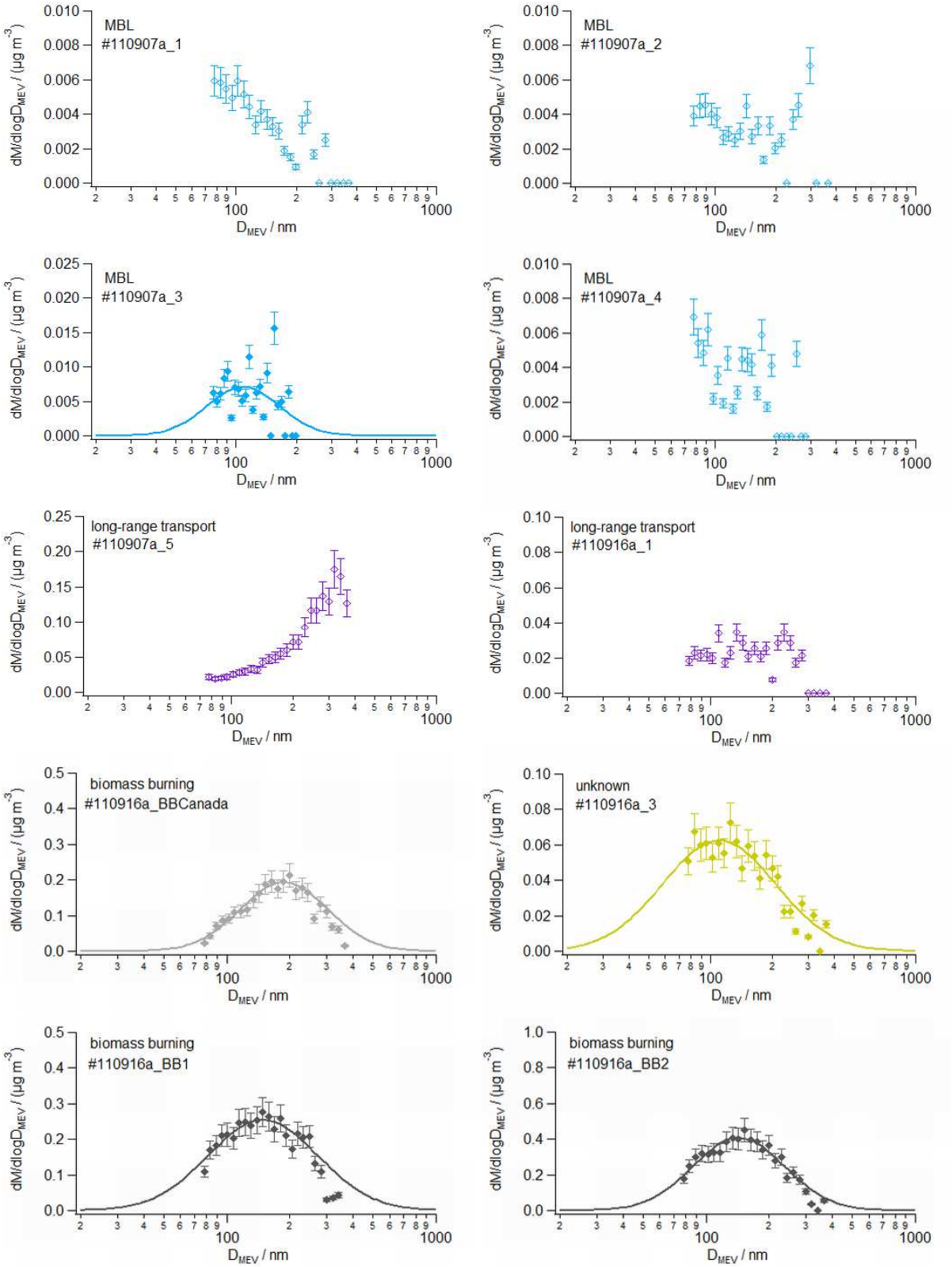

Appendix 4a. *rBC mass size distribution of every measurement sequence (Table 10). Diamonds represent the measurements. Log-normal fits (solid lines) were added if applicable (see Section 3.3.1). Error bars represent 15% uncertainty.* $D_{MEV} \triangleq D_{rBC}$.

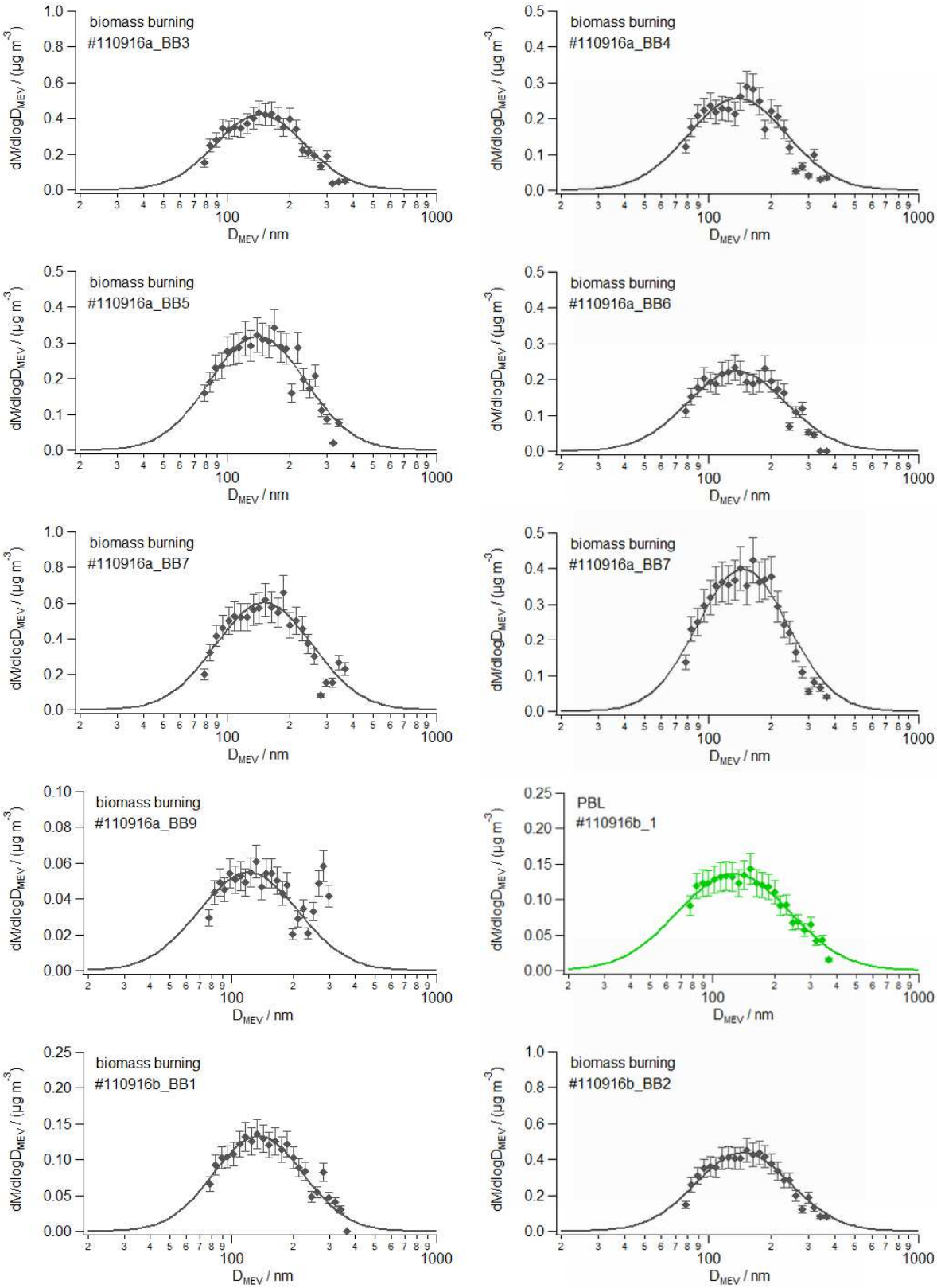

Appendix 4b. *rBC mass size distribution of every measurement sequence (Table 10). Diamonds represent the measurements. Log-normal fits (solid lines) were added if applicable (see Section 3.3.1). Error bars represent 15% uncertainty.* $D_{MEV} \triangleq D_{rBC}$.

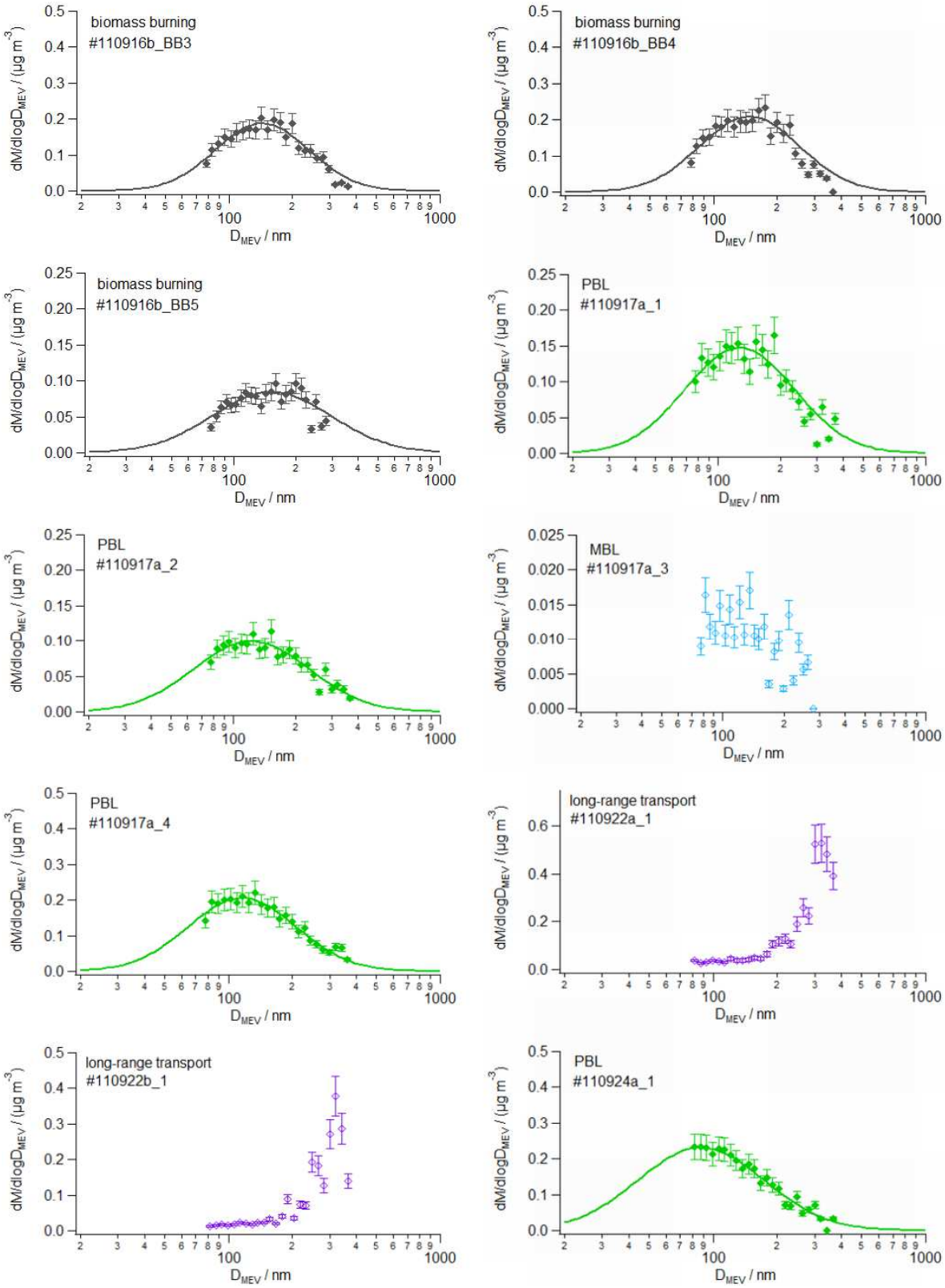

Appendix 4c. *rBC mass size distribution of every measurement sequence (Table 10). Diamonds represent the measurements. Log-normal fits (solid lines) were added if applicable (see Section 3.3.1). Error bars represent 15% uncertainty.* $D_{MEV} \triangleq D_{rBC}$.

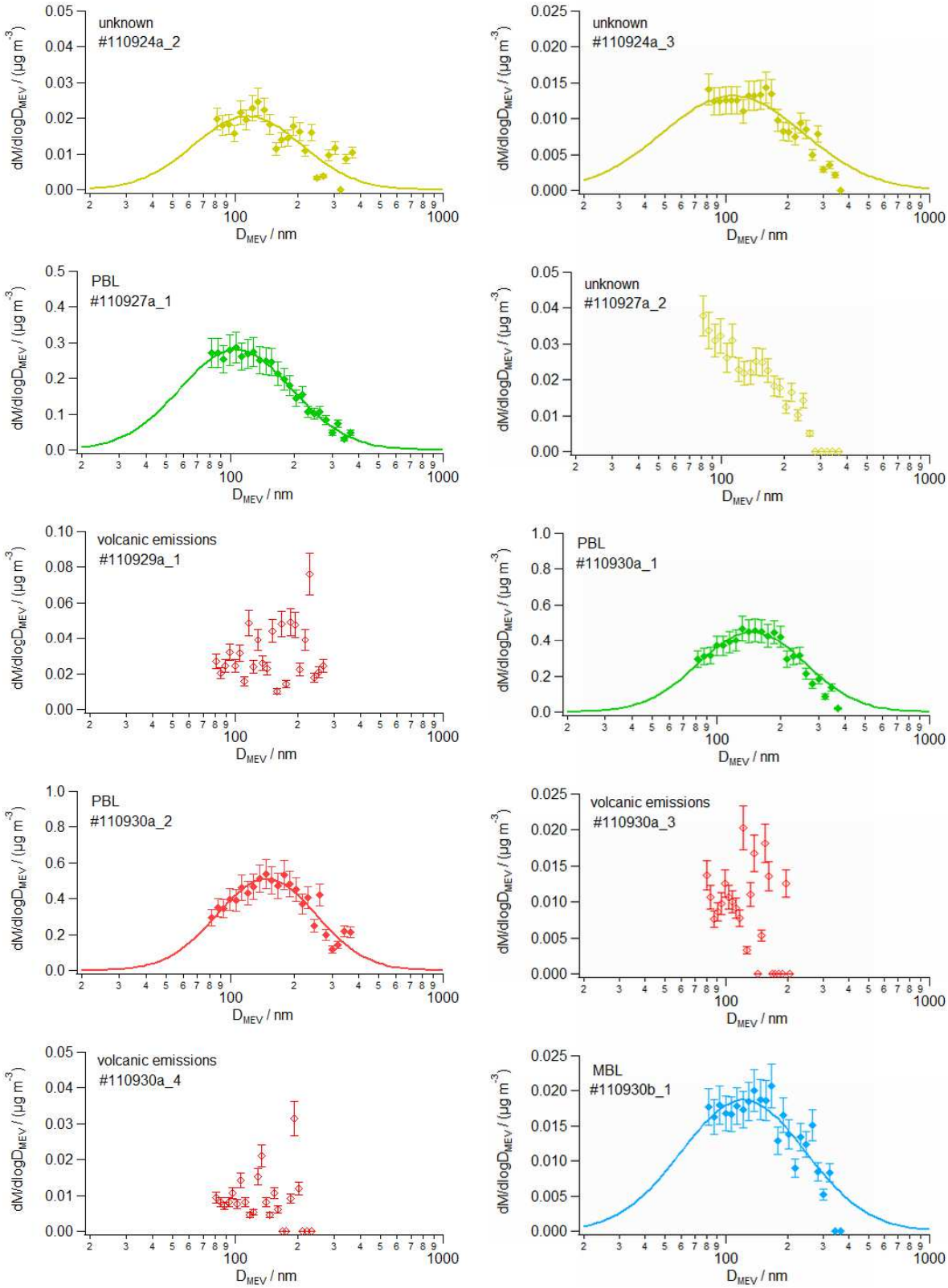

Appendix 4d. *rBC mass size distribution of every measurement sequence (Table 10). Diamonds represent the measurements. Log-normal fits (solid lines) were added if applicable (see Section 3.3.1). Error bars represent 15% uncertainty.* $D_{MEV} \triangleq D_{rBC}$.

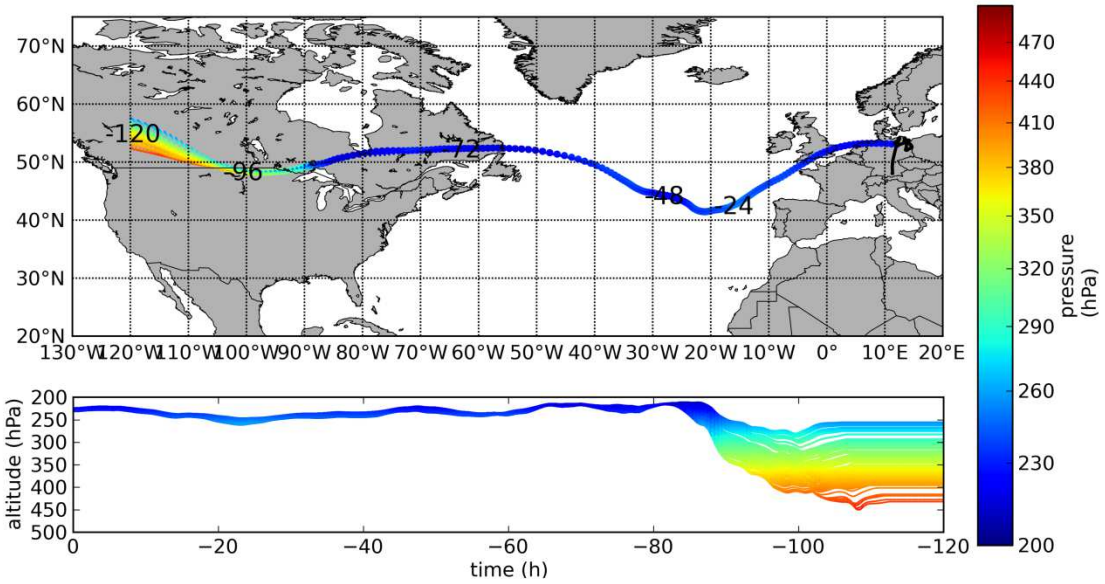

Appendix 5. *Backward trajectories of the observed Pagami Creek fire aerosol layer sequence 3 (see Figure 63) calculated with FLYTUL with color-coded pressure altitude. The age of the trajectory is indicated by numbers. The bottom panel shows the altitude evolution of the particular trajectories.*

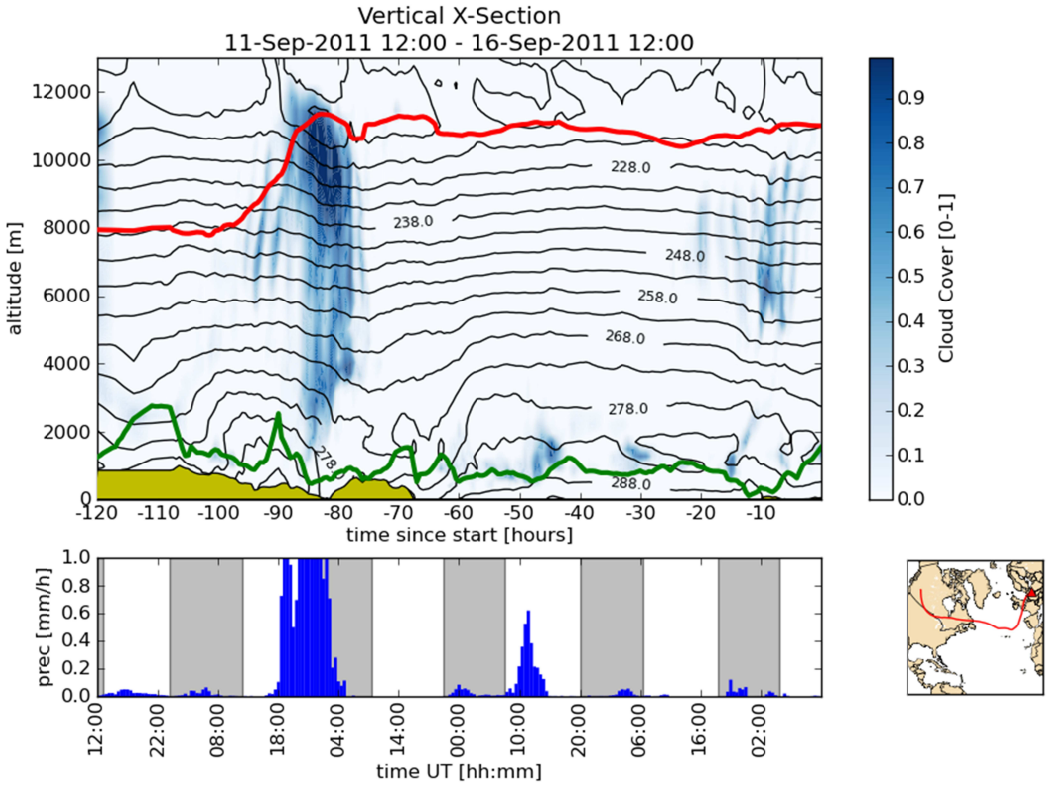

Appendix 6. *Meteorological conditions for the mean trajectory (red line) shown in Appendix 5. In the upper panel the cloud cover is color-coded (black lines: ambient temperature; green line: boundary layer height; yellow plane: ground level height). The bottom panel shows the precipitation (at the ground) along the trajectory. When formed below the altitude of the trajectory, the amount of precipitation modifying the air mass along might be smaller.*

References

Ackerman, A. S., Toon, O. B., Stevens, D. E., Heymsfield, A. J., Ramanathan, V., and Welton, E. J.: Reduction of tropical cloudiness by soot, Science, 288, 1042-1047, doi: 10.1126/science.288.5468.1042, 2000.

Ackerman, T. P., and Toon, O. B.: Absorption of visible radiation in atmosphere containing mixtures of absorbing and nonabsorbing particles, Applied Optics, 20, 3661-3668, doi: 10.1364/ao.20.003661, 1981.

Adachi, K., Chung, S. H., and Buseck, P. R.: Shapes of soot aerosol particles and implications for their effects on climate, Journal of Geophysical Research-Atmospheres, 115, D15206, doi: 10.1029/2009JD012868, 2010.

Addlesee, A. J.: Anisokinetic sampling of aerosol at a slot intake, Journal of Aerosol Science, 11, 483-493, doi: 10.1016/0021-8502(80)90121-4, 1980.

Akagi, S. K., Yokelson, R. J., Wiedinmyer, C., Alvarado, M. J., Reid, J. S., Karl, T., Crounse, J. D., and Wennberg, P. O.: Emission factors for open and domestic biomass burning for use in atmospheric models, Atmos. Chem. Phys., 11, 4039-4072, doi: 10.5194/acp-11-4039-2011, 2011.

Akagi, S. K., Craven, J. S., Taylor, J. W., McMeeking, G. R., Yokelson, R. J., Burling, I. R., Urbanski, S. P., Wold, C. E., Seinfeld, J. H., Coe, H., Alvarado, M. J., and Weise, D. R.: Evolution of trace gases and particles emitted by a chaparral fire in California, Atmos. Chem. Phys., 12, 1397-1421, doi: 10.5194/acp-12-1397-2012, 2012.

Alexander, D. T. L., Crozier, P. A., and Anderson, J. R.: Brown carbon spheres in East Asian outflow and their optical properties, Science, 321, 833-836, doi: 10.1126/science.1155296, 2008.

Andreae, M. O., Rosenfeld, D., Artaxo, P., Costa, A. A., Frank, G. P., Longo, K. M., and Silva-Dias, M. A. F.: Smoking rain clouds over the Amazon, Science, 303, 1337-1342, doi: 10.1126/science.1092779, 2004.

Andreae, M. O., and Gelencser, A.: Black carbon or brown carbon? The nature of light-absorbing carbonaceous aerosols, Atmos. Chem. Phys., 6, 3131-3148, doi: 10.5194/acp-6-3131-2006, 2006.

Andreae, M. O.: Aerosols before pollution, Science, 315, 50-51, doi: 10.1126/science.1136529, 2007.

Andreae, M. O., and Rosenfeld, D.: Aerosol-cloud-precipitation interactions. Part 1. The nature and sources of cloud-active aerosols, Earth-Science Reviews, 89, 13-41, doi: 10.1016/j.earscirev.2008.03.001, 2008.

Aquila, V.: Global model studies on the distribution and composition of potential atmospheric ice nuclei, Ph.D., Fakultät für Physik, Ludwig-Maximilians-Universität München, München, 141 pp., 2009.

Aquila, V., Hendricks, J., Lauer, A., Riemer, N., Vogel, H., Baumgardner, D., Minikin, A., Petzold, A., Schwarz, J. P., Spackman, J. R., Weinzierl, B., Righi, M., and Dall'Amico, M.: MADE-in: a new aerosol microphysics submodel for global simulation of insoluble particles and their mixing state, Geoscientific Model Development, 4, 325-355, doi: 10.5194/gmd-4-325-2011, 2011.

Ban-Weiss, G. A., Cao, L., Bala, G., and Caldeira, K.: Dependence of climate forcing and response on the altitude of black carbon aerosols, Climate Dynamics, 38, 897-911, doi: 10.1007/s00382-011-1052-y, 2012.

Barnaba, F., Angelini, F., Curci, G., and Gobbi, G. P.: An important fingerprint of wildfires on the European aerosol load, Atmos. Chem. Phys., 11, 10487-10501, doi: 10.5194/acp-11-10487-2011, 2011.

Bauer, S. E., Menon, S., Koch, D., Bond, T. C., and Tsigaridis, K.: A global modeling study on carbonaceous aerosol microphysical characteristics and radiative effects, Atmos. Chem. Phys., 10, 7439-7456, doi: 10.5194/acp-10-7439-2010, 2010.

Baumgardner, D., Dye, J. E., Gandrud, B. W., and Knollenberg, R. G.: Interpretation of measurements made by the Forward Scattering Spectrometer Probe (FSSP-300) during the Airborne Arctic Stratospheric Expedition Journal of Geophysical Research-Atmospheres, 97, 8035-8046, doi: 10.1029/91JD02728, 1992.

Baumgardner, D., Kok, G., and Raga, G.: Warming of the Arctic lower stratosphere by light absorbing particles, Geophysical Research Letters, 31, 4 pp., L06117 doi: 10.1029/2003gl018883, 2004.

Baumgardner, D., Subramanian, R., Twohy, C., Stith, J., and Kok, G.: Scavenging of black carbon by ice crystals over the northern Pacific, Geophysical Research Letters, 35, 5 pp., L22815 doi: 10.1029/2008gl035764, 2008.

Baumgardner, D., Brenguier, J. L., Bucholtz, A., Coe, H., DeMott, P., Garrett, T. J., Gayet, J. F., Hermann, M., Heymsfield, A., Korolev, A., Kraemer, M., Petzold, A., Strapp, W., Pilewskie, P., Taylor, J., Twohy, C., Wendisch, M., Bachalo, W., and Chuang, P.: Airborne instruments to measure atmospheric aerosol particles, clouds and radiation: A cook's tour of mature and emerging technology, Atmospheric Research, 102, 10-29, doi: 10.1016/j.atmosres.2011.06.021, 2011.

Baumgardner, D., Popovicheva, O., Allan, J., Bernardoni, V., Cao, J., Cavalli, F., Cozic, J., Diapouli, E., Eleftheriadis, K., Genberg, P. J., Gonzalez, C., Gysel, M., John, A., Kirchstetter, T. W., Kuhlbusch, T. A. J., Laborde, M., Lack, D., Mueller, T., Niessner, R., Petzold, A., Piazzalunga, A., Putaud, J. P., Schwarz, J., Sheridan, P., Subramanian, R., Swietlicki, E., Valli, G., Vecchi, R., and Viana, M.: Soot reference materials for instrument calibration and intercomparisons: a workshop summary with recommendations, Atmos. Meas. Tech., 5, 1869-1887, doi: 10.5194/amt-5-1869-2012, 2012.

Belyaev, S. P., and Levin, L. M.: Techniques for collection of representative aerosol samples, Aerosol Science 5, 325-338, doi: 10.1016/0021-8502(74)90130-X, 1974.

Bohren, C. F., and Huffman, D. R.: Absorption and scattering of light by small particles, John Wiley & Sons, Inc. , New York, USA, 530 pp., 1983.

Bond, T. C., Anderson, T. L., and Campbell, D.: Calibration and intercomparison of filter-based measurements of visible light absorption by aerosols, Aerosol Sci. Technol., 30, 582-600, doi: 10.1080/027868299304435, 1999.

Bond, T. C., Streets, D. G., Yarber, K. F., Nelson, S. M., Woo, J. H., and Klimont, Z.: A technology-based global inventory of black and organic carbon emissions from combustion, Journal of Geophysical Research-Atmospheres, 109, D14203, doi: 10.1029/2003jd003697, 2004.

Bond, T. C., and Bergstrom, R. W.: Light absorption by carbonaceous particles: An investigative review, Aerosol Sci. Technol., 40, 27-67, doi: 10.1080/02786820500421521, 2006.

Bond, T. C., Doherty, S. J., Fahey, D. W., Forster, P. M., Berntsen, T., DeAngelo, B. J., Flanner, M. G., Ghan, S., Kärcher, B., Koch, D., Kinne, S., Kondo, Y., Quinn, P. K., Sarofim, M. C., Schultz, M. G., Schulz, M., Venkataraman, C., Zhang, H., Zhang, S., Bellouin, N., Guttikunda, S. K., Hopke, P. K., Jacobson, M. Z., Kaiser, J. W., Klimont, Z., Lohmann, U., Schwarz, J. P., Shindell, D., Storelvmo, T., Warren, S. G., and Zender, C. S.: Bounding the role of black carbon in the climate system: A scientific assessment, Journal of Geophysical Research: Atmospheres, 118, 5380–5552, doi: 10.1002/jgrd.50171, 2013.

Brock, C. A., Cozic, J., Bahreini, R., Froyd, K. D., Middlebrook, A. M., McComiskey, A., Brioude, J., Cooper, O. R., Stohl, A., Aikin, K. C., de Gouw, J. A., Fahey, D. W., Ferrare, R. A., Gao, R. S., Gore, W., Holloway, J. S., Hübler, G., Jefferson, A., Lack, D. A., Lance, S., Moore, R. H., Murphy, D. M., Nenes, A., Novelli, P. C., Nowak, J. B., Ogren, J. A., Peischl, J., Pierce, R. B., Pilewskie, P., Quinn, P. K., Ryerson, T. B., Schmidt, K. S., Schwarz, J. P., Sodemann, H., Spackman, J. R., Stark, H., Thomson, D. S., Thornberry, T., Veres, P., Watts, L. A., Warneke, C., and Wollny, A. G.: Characteristics, sources, and transport of aerosols measured in spring 2008 during the aerosol, radiation, and cloud processes affecting Arctic Climate (ARCPAC) Project, Atmos. Chem. Phys., 11, 2423-2453, doi: 10.5194/acp-11-2423-2011, 2011.

Browse, J., Carslaw, K. S., Arnold, S. R., Pringle, K., and Boucher, O.: The scavenging processes controlling the seasonal cycle in Arctic sulphate and black carbon aerosol, Atmos. Chem. Phys., 12, 6775-6798, doi: 10.5194/acp-12-6775-2012, 2012.

Buseck, P. R., and Posfai, M.: Airborne minerals and related aerosol particles: Effects on climate and the environment, Proceedings of the National Academy of Sciences of the United States of America, 96, 3372-3379, doi: 10.1073/pnas.96.7.3372, 1999.

Cappa, C. D., Lack, D. A., Burkholder, J. B., and Ravishankara, A. R.: Bias in filter-based aerosol light absorption measurements due to organic aerosol loading: Evidence from laboratory measurements, Aerosol Sci. Technol., 42, 1022-1032, doi: 10.1080/02786820802389285, 2008.

Cappa, C. D., Onasch, T. B., Massoli, P., Worsnop, D. R., Bates, T. S., Cross, E. S., Davidovits, P., Hakala, J., Hayden, K. L., Jobson, B. T., Kolesar, K. R., Lack, D. A., Lerner, B. M., Li, S.-M., Mellon, D., Nuaaman, I., Olfert, J. S., Petaja, T., Quinn, P. K., Song, C., Subramanian, R., Williams, E. J., and Zaveri, R. A.: Radiative Absorption Enhancements Due to the Mixing State of Atmospheric Black Carbon, Science, 337, 1078-1081, doi: 10.1126/science.1223447, 2012.

Chýlek, P., Srivastava, V., Pinnick, R. G., and Wang, R. T.: Scattering of electromagnetic waves by composite spherical particles: Experiment and effective medium approximations, Applied Optics, 27, 2396-2404, doi: 10.1364/AO.27.002396, 1988.

Clarke, A. D., Charlson, R. J., and Ogren, J. A.: Stratospheric aerosol light absorption before and after El Chichon, Geophysical Research Letters, 10, 1017-1020, doi: 10.1029/GL010i011p01017, 1983.

Clarke, A. D.: A thermo-optic technique for in situ analysis of size-resolved aerosol physicochemistry, Atmospheric Environment Part a-General Topics, 25, 635-644, doi: 10.1016/0960-1686(91)90061-b, 1991.

Cohn, S. A., and Angevine, W. M.: Boundary Layer Height and Entrainment Zone Thickness Measured by Lidars and Wind-Profiling Radars, Journal of Applied Meteorology, 39, 1233-1247, doi: 10.1175/1520-0450(2000)039<1233:blhaez>2.0.co;2, 2000.

Corradini, S., Spinetti, C., Carboni, E., Tirelli, C., Buongiorno, M. F., Pugnaghi, S., and Gangale, G.: Mt. Etna tropospheric ash retrieval and sensitivity analysis using Moderate Resolution Imaging Spectroradiometer measurements, Journal of Applied Remote Sensing, 2, 023550, doi: 10.1117/1.3046674, 2008.

Cross, E. S., Onasch, T. B., Ahern, A., Wrobel, W., Slowik, J. G., Olfert, J., Lack, D. A., Massoli, P., Cappa, C. D., Schwarz, J. P., Spackman, J. R., Fahey, D. W., Sedlacek, A., Trimborn, A., Jayne, J. T., Freedman, A., Williams, L. R., Ng, N. L., Mazzoleni, C., Dubey, M., Brem, B., Kok, G., Subramanian, R., Freitag, S., Clarke, A., Thornhill, D., Marr, L. C., Kolb, C. E., Worsnop, D. R., and Davidovits, P.: Soot Particle Studies - Instrument Inter-Comparison - Project Overview, Aerosol Sci. Technol., 44, 592-611, doi: 10.1080/02786826.2010.482113, 2010.

Cruz, C. N., and Pandis, S. N.: The effect of organic coatings on the cloud condensation nuclei activation of inorganic atmospheric aerosol, Journal of Geophysical Research: Atmospheres, 103, 13111-13123, doi: 10.1029/98jd00979, 1998.

Dahlkötter, F., Griessbaum, F., Schmidt, A., and Klemm, O.: Direct measurement of CO2 and particle emissions from an urban area, Meteorologische Zeitschrift, 19, 565-575, doi: 10.1127/0941-2948/2010/0492, 2010.

Dahlkötter, F., Gysel, M., Sauer, D., Minikin, A., Baumann, R., Seifert, P., Ansmann, A., Fromm, M., Voigt, C., and Weinzierl, B.: The Pagami Creek smoke plume after long-range transport to the upper troposphere over Europe – aerosol properties and black carbon mixing state, Atmos. Chem. Phys., 14, 6111-6137, doi: 10.5194/acp-14-6111-2014, 2014.

Damoah, R., Spichtinger, N., Forster, C., James, P., Mattis, I., Wandinger, U., Beirle, S., Wagner, T., and Stohl, A.: Around the world in 17 days - hemispheric-scale transport of forest fire smoke from Russia in May 2003, Atmos. Chem. Phys., 4, 1311-1321, doi: 10.5194/acp-4-1311-2004, 2004.

Damoah, R., Spichtinger, N., Servranckx, R., Fromm, M., Eloranta, E. W., Razenkov, I. A., James, P., Shulski, M., Forster, C., and Stohl, A.: A case study of pyro-convection using transport model and remote sensing data, Atmos. Chem. Phys., 6, 173-185, doi: 10.5194/acp-6-173-2006, 2006.

de Graaf, M., Stammes, P., Torres, O., and Koelemeijer, R. B. A.: Absorbing Aerosol Index: Sensitivity analysis, application to GOME and comparison with TOMS, Journal of Geophysical Research-Atmospheres, 110, D01201, doi: 10.1029/2004jd005178, 2005.

Dentener, F., Kinne, S., Bond, T., Boucher, O., Cofala, J., Generoso, S., Ginoux, P., Gong, S., Hoelzemann, J. J., Ito, A., Marelli, L., Penner, J. E., Putaud, J. P., Textor, C., Schulz, M., van der Werf, G. R., and Wilson, J.: Emissions of primary aerosol and precursor gases in the years 2000 and 1750 prescribed data-sets for AeroCom, Atmos. Chem. Phys., 6, 4321-4344, doi: 10.5194/acp-6-4321-2006, 2006.

Diehl, T., Heil, A., Chin, M., Pan, X., Streets, D., Schultz, M., and Kinne, S.: Anthropogenic, biomass burning, and volcanic emissions of black carbon, organic carbon, and SO_2 from 1980 to 2012 for hindcast model experiments, Atmos. Chem. Phys. Discuss., 12, 24895-24954, doi: 10.5194/acpd-12-24895-2012, 2012.

DMT (Droplet Measurement Technologies): Single Particle Soot Photometer (SP2) Laser Alignment Manual (DOC-0229), Boulder, Manual, 28 pp., 2009.

DMT (Droplet Measurement Technologies): Single Particle Soot Photometer (SP2) Operator Manual (DOC-0171), Boulder, Manual, 51 pp., 2012.

Draxler, R. R., and Hess, G. D.: Description of the HYSPLIT_4 modelling system, NOAA Technical Memorandum ERL ARL-224, Air Resources Laboratory, Silver Spring, Maryland, 1997.

Draxler, R. R., and Hess, G. D.: An overview of the HYSPLIT_4 modelling system for trajectories, dispersion, and deposition, Australian Meteorological Magazine, 47, 295-308, 1998.

Ebert, M., Weinbruch, S., Rausch, A., Gorzawski, G., Hoffmann, P., Wex, H., and Helas, G.: Complex refractive index of aerosols during LACE 98 as derived from the analysis of individual particles, Journal of Geophysical Research-Atmospheres, 107, 8121, doi: 10.1029/2000jd000195, 2002.

Enviscope (Enviscope GmbH): Declaration of Design and Performance für Modifikation FALCON_SP (DDP #: 74912_FALCON_SP_20110515), Frankfurt, Certification, 20 pp., 2011.

Fenn, R. W., Shettle, E. P., Hering, W. S., and Johnson, R. W.: Atmospheric optical properties and meteorological conditions, Atmospheric Environment, 15, 1911-1918, doi: 10.1016/0004-6981(81)90225-0, 1981.

Fernald, F. G.: Analysis of atmospheric lidar observations: some comments, Applied Optics, 23, 652-653, doi: 10.1364/AO.23.000652, 1984.

Fiebig, M.: Das troposphaerische Aerosol in mittleren Breiten - Mikrophysik, Optik und Klimaantrieb am Beispiel der Feldstudie LACE 98, Ph.D., Fakultät für Physik, Ludwig-Maximilians-Universität München, Oberpfaffenhofen, 259 pp., 2001.

Fiebig, M., Petzold, A., Wandinger, U., Wendisch, M., Kiemle, C., Stifter, A., Ebert, M., Rother, T., and Leiterer, U.: Optical closure for an aerosol column: Method, accuracy, and inferable properties applied to a biomass-burning aerosol and its radiative forcing, Journal of Geophysical Research-Atmospheres, 107, 8130, doi: 10.1029/2000jd000192, 2002.

Fiebig, M., Stohl, A., Wendisch, M., Eckhardt, S., and Petzold, A.: Dependence of solar radiative forcing of forest fire aerosol on ageing and state of mixture, Atmos. Chem. Phys., 3, 881-891, doi: 10.5194/acp-3-881-2003, 2003.

Fierz, M., Vernooij, M. G. C., and Burtscher, H.: An improved low-flow thermodenuder, Journal of Aerosol Science, 38, 1163-1168, doi: 10.1016/j.jaerosci.2007.08.006, 2007.

Fromm, M., Bevilacqua, R., Servranckx, R., Rosen, J., Thayer, J. P., Herman, J., and Larko, D.: Pyro-cumulonimbus injection of smoke to the stratosphere: Observations and impact of a super blowup in northwestern Canada on 3-4 August 1998, Journal of Geophysical Research-Atmospheres, 110, D08205, doi: 10.1029/2004jd005350, 2005.

Fromm, M., Shettle, E. P., Fricke, K. H., Ritter, C., Trickl, T., Giehl, H., Gerding, M., Barnes, J. E., O'Neill, M., Massie, S. T., Blum, U., McDermid, I. S., Leblanc, T., and Deshler, T.: Stratospheric impact of the Chisholm pyrocumulonimbus eruption: 2. Vertical profile perspective, Journal of Geophysical Research: Atmospheres, 113, D08203, doi: 10.1029/2007jd009147, 2008.

Fromm, M., Lindsey, D. T., Servranckx, R., Yue, G., Trickl, T., Sica, R., Doucet, P., and Godin-Beekmann, S. E.: THE UNTOLD STORY OF PYROCUMULONIMBUS, Bulletin of the American Meteorological Society, 91, 1193-1209, doi: 10.1175/2010bams3004.1, 2010.

Gao, R. S., Schwarz, J. P., Kelly, K. K., Fahey, D. W., Watts, L. A., Thompson, T. L., Spackman, J. R., Slowik, J. G., Cross, E. S., Han, J. H., Davidovits, P., Onasch, T. B., and Worsnop, D. R.: A novel method for estimating light-scattering properties of soot aerosols using a modified single-particle soot photometer, Aerosol Sci. Technol., 41, 125-135, doi: 10.1080/02786820601118398, 2007.

Gatebe, C. K., Varnai, T., Poudyal, R., Ichoku, C., and King, M. D.: Taking the pulse of pyrocumulus clouds, Atmospheric Environment, 52, 121-130, doi: 10.1016/j.atmosenv.2012.01.045, 2012.

Gayet, J. F., Auriol, F., Minikin, A., Strom, J., Seifert, M., Krejci, R., Petzold, A., Febvre, G., and Schumann, U.: Quantitative measurement of the microphysical and optical properties of cirrus clouds with four different in situ probes: Evidence of small ice crystals, Geophysical Research Letters, 29, 2230, doi: 10.1029/2001gl014342, 2002.

Giglio, L., Descloitres, J., Justice, C. O., and Kaufman, Y. J.: An enhanced contextual fire detection algorithm for MODIS, Remote Sensing of Environment, 87, 273-282, doi: 10.1016/s0034-4257(03)00184-6, 2003.

Grimm (Grimm Aerosol Technik GmbH & Co. KG): Aerosolspektrometer SERIE 1.129 “SKY-OPC“, Ainring, Manual, 36 pp., 2007.

Groß, S., Esselborn, M., Weinzierl, B., Wirth, M., Fix, A., and Petzold, A.: Aerosol classification by airborne high spectral resolution lidar observations, Atmos. Chem. Phys., 13, 2487-2505, doi: 10.5194/acp-13-2487-2013, 2013.

Gysel, M., Laborde, M., Olfert, J. S., Subramanian, R., and Groehn, A. J.: Effective density of Aquadag and fullerene soot black carbon reference materials used for SP2 calibration, Atmos. Meas. Tech., 4, 2851-2858, doi: 10.5194/amt-4-2851-2011, 2011.

Gysel, M., and Laborde, M. (Paul Scherrer Institute): Manual for PSI's SP2 Toolkit by Martin Gysel & Marie Laborde, Manual, 64 pp., 2012.

Gysel, M., Laborde, M., Mensah, A. A., Corbin, J. C., Keller, A., Kim, J., Petzold, A., and Sierau, B.: Technical Note: The single particle soot photometer fails to reliably detect PALAS soot nanoparticles, Atmos. Meas. Tech., 5, 3099-3107, doi: 10.5194/amt-5-3099-2012, 2012.

Hamburger, T.: Aerosol microphysical properties during anticyclonic flow conditions over Europe, Ph.D., Fakultät für Physik, Ludwig-Maximilians-Universität München, München, 193 pp., 2010.

Hamburger, T., McMeeking, G., Minikin, A., Birmili, W., Dall'Osto, M., O'Dowd, C., Flentje, H., Henzing, B., Junninen, H., Kristensson, A., de Leeuw, G., Stohl, A., Burkhart, J. F., Coe, H., Krejci, R., and Petzold, A.: Overview of the synoptic and pollution situation over Europe during the EUCAARI-

LONGREX field campaign, Atmos. Chem. Phys., 11, 1065-1082, doi: 10.5194/acp-11-1065-2011, 2011.

Hansen, J., Sato, M., Kharecha, P., and von Schuckmann, K.: Earth's energy imbalance and implications, Atmos. Chem. Phys., 11, 13421-13449, doi: 10.5194/acp-11-13421-2011, 2011.

Haywood, J., and Boucher, O.: Estimates of the direct and indirect radiative forcing due to tropospheric aerosols: A review, Reviews of Geophysics, 38, 513-543, doi: 10.1029/1999rg000078, 2000.

Haywood, J. M., Osborne, S. R., Francis, P. N., Keil, A., Formenti, P., Andreae, M. O., and Kaye, P. H.: The mean physical and optical properties of regional haze dominated by biomass burning aerosol measured from the C-130 aircraft during SAFARI 2000, Journal of Geophysical Research-Atmospheres, 108, 8473, doi: 10.1029/2002jd002226, 2003.

Heimerl, K.: Characterisation of the DLR Single Particle Soot Photometer and its Sensitivity to Different Absorbing Aerosol Types, Diploma, Fakultät für Physik, Ludwig-Maximilians-Universität München, München, 87 pp., 2011.

Hendricks, J., Karcher, B., Dopelheuer, A., Feichter, J., Lohmann, U., and Baumgardner, D.: Simulating the global atmospheric black carbon cycle: a revisit to the contribution of aircraft emissions, Atmos. Chem. Phys., 4, 2521-2541, doi: 10.5194/acp-4-2521-2004, 2004.

Hinds, W. C.: Aerosol Technology: Properties, Behaviour, and Measurement of Airborne Particles, 2nd ed., John Wiley & Sons, Inc. , New York, USA, 464 pp., 1999.

Hoose, C., and Möhler, O.: Heterogeneous ice nucleation on atmospheric aerosols: a review of results from laboratory experiments, Atmos. Chem. Phys., 12, 9817-9854, doi: 10.5194/acp-12-9817-2012, 2012.

Horvath, H.: Atmsopheric light absorption - A review, Atmospheric Environment Part a-General Topics, 27, 293-317, doi: 10.1016/0960-1686(93)90104-7, 1993.

Hussein, T., Dal Maso, M., Petaja, T., Koponen, I. K., Paatero, P., Aalto, P. P., Hameri, K., and Kulmala, M.: Evaluation of an automatic algorithm for fitting the particle number size distributions, Boreal Environment Research, 10, 337-355, 2005.

IPCC: Climate Change 2007: The Physical Science Basis. Contribution of Working Group I to the Fourth Assessment Report of the Intergovernmental Panel on Climate Change, [Solomon, S., Qin, D., Manning, M., Chen, Z., Marquis, M., Averyt, K. B., Tignor, M., and Miller, H. L. (eds.)], Cambridge University Press, Cambridge, United Kingdom and New York, NY, USA, 2007.

Jacobson, M. Z.: Strong radiative heating due to the mixing state of black carbon in atmospheric aerosols, Nature, 409, 695-697, doi: 10.1038/35055518, 2001.

Jaenicke, R.: Atmospheric aerosols and global climate, Journal of Aerosol Science, 11, 577-588, doi: 10.1016/0021-8502(80)90131-7, 1980.

Jeßberger, P., Voigt, C., Schumann, U., Sölch, I., Schlager, H., Kaufmann, S., Petzold, A., Schäuble, D., and Gayet, J.-F.: Aircraft type influence on contrail properties, Atmos. Chem. Phys. Discuss., 13, 13915-13966, doi: 10.5194/acpd-13-13915-2013, 2013.

Jost, H.-J., Drdla, K., Stohl, A., Pfister, L., Loewenstein, M., Lopez, J. P., Hudson, P. K., Murphy, D. M., Cziczo, D. J., Fromm, M., Bui, T. P., Dean-Day, J., Gerbig, C., Mahoney, M. J., Richard, E. C., Spichtinger, N., Pittman, J. V., Weinstock, E. M., Wilson, J. C., and Xueref, I.: In-situ observations of mid-latitude forest fire plumes deep in the stratosphere, Geophysical Research Letters, 31, L11101, doi: 10.1029/2003gl019253, 2004.

Jurkat, T., Voigt, C., Arnold, F., Schlager, H., Aufmhoff, H., Schmale, J., Schneider, J., Lichtenstern, M., and Doernbrack, A.: Airborne stratospheric ITCIMS measurements of SO2, HCl, and HNO3 in the aged plume of volcano Kasatochi, Journal of Geophysical Research-Atmospheres, 115, D00L17, doi: 10.1029/2010jd013890, 2010.

Justice, C. O., Giglio, L., Korontzi, S., Owens, J., Morisette, J. T., Roy, D., Descloitres, J., Alleaume, S., Petitcolin, F., and Kaufman, Y.: The MODIS fire products, Remote Sensing of Environment, 83, 244-262, doi: 10.1016/s0034-4257(02)00076-7, 2002.

Kahnert, M., Nousiainen, T., Lindqvist, H., and Ebert, M.: Optical properties of light absorbing carbon aggregates mixed with sulfate: assessment of different model geometries for climate forcing calculations, Optics Express, 20, 10042-10058, doi: 10.1364/OE.20.010042, 2012.

Kaspari, S. D., Schwikowski, M., Gysel, M., Flanner, M. G., Kang, S., Hou, S., and Mayewski, P. A.: Recent increase in black carbon concentrations from a Mt. Everest ice core spanning 1860-2000 AD, Geophysical Research Letters, 38, L04703, doi: 10.1029/2010gl046096, 2011.

Kaufman, Y. J., Tanre, D., and Boucher, O.: A satellite view of aerosols in the climate system, Nature, 419, 215-223, doi: 10.1038/nature01091, 2002.

Kirchstetter, T. W., Novakov, T., and Hobbs, P. V.: Evidence that the spectral dependence of light absorption by aerosols is affected by organic carbon, Journal of Geophysical Research-Atmospheres, 109, D21208, doi: 10.1029/2004jd004999, 2004.

Kirchstetter, T. W., and Thatcher, T. L.: Contribution of organic carbon to wood smoke particulate matter absorption of solar radiation, Atmos. Chem. Phys., 12, 6067-6072, doi: 10.5194/acp-12-6067-2012, 2012.

Klett, J. D.: Stable analytical inversion solution for processing lidar returns, Applied Optics, 20, 211-220, doi: 10.1364/ao.20.000211, 1981.

Knorr, W., Lehsten, V., and Arneth, A.: Determinants and predictability of global wildfire emissions, Atmos. Chem. Phys., 12, 6845-6861, doi: 10.5194/acp-12-6845-2012, 2012.

Kondo, Y., Matsui, H., Moteki, N., Sahu, L., Takegawa, N., Kajino, M., Zhao, Y., Cubison, M. J., Jimenez, J. L., Vay, S., Diskin, G. S., Anderson, B., Wisthaler, A., Mikoviny, T., Fuelberg, H. E., Blake, D. R., Huey, G., Weinheimer, A. J., Knapp, D. J., and Brune, W. H.: Emissions of black carbon, organic, and inorganic aerosols from biomass burning in North America and Asia in 2008, Journal of Geophysical Research-Atmospheres, 116, D08204, doi: 10.1029/2010jd015152, 2011a.

Kondo, Y., Sahu, L., Moteki, N., Khan, F., Takegawa, N., Liu, X., Koike, M., and Miyakawa, T.: Consistency and Traceability of Black Carbon Measurements Made by Laser-Induced Incandescence, Thermal-Optical Transmittance, and Filter-Based Photo-Absorption Techniques, Aerosol Sci. Technol., 45, 295-312, doi: 10.1080/02786826.2010.533215, 2011b.

Kübbeler, M., Hildebrandt, M., Meyer, J., Schiller, C., Hamburger, T., Jurkat, T., Minikin, A., Petzold, A., Rautenhaus, M., Schlager, H., Schumann, U., Voigt, C., Spichtinger, P., Gayet, J. F., Gourbeyre, C., and Kraemer, M.: Thin and subvisible cirrus and contrails in a subsaturated environment, Atmos. Chem. Phys., 11, 5853-5865, doi: 10.5194/acp-11-5853-2011, 2011.

Kulkarni, P., Baron, P. A., and Willeke, K.: Aerosol Measurement: Principles, Techniques, and Applications, 3rd ed., John Wiley & Sons, Hoboken, USA, 900 pp., 2011.

Laborde, M., Mertes, P., Zieger, P., Dommen, J., Baltensperger, U., and Gysel, M.: Sensitivity of the Single Particle Soot Photometer to different black carbon types, Atmos. Meas. Tech., 5, 1031-1043, doi: 10.5194/amt-5-1031-2012, 2012a.

Laborde, M., Schnaiter, M., Linke, C., Saathoff, H., Naumann, K. H., Moehler, O., Berlenz, S., Wagner, U., Taylor, J. W., Liu, D., Flynn, M., Allan, J. D., Coe, H., Heimerl, K., Dahlkötter, F., Weinzierl, B., Wollny, A. G., Zanatta, M., Cozic, J., Laj, P., Hitzenberger, R., Schwarz, J. P., and Gysel, M.: Single Particle Soot Photometer intercomparison at the AIDA chamber, Atmos. Meas. Tech., 5, 3077-3097, doi: 10.5194/amt-5-3077-2012, 2012b.

Laborde, M., Crippa, M., Tritscher, T., Jurányi, Z., Decarlo, P. F., Temime-Roussel, B., Marchand, N., Eckhardt, S., Stohl, A., Baltensperger, U., Prévôt, A. S. H., Weingartner, E., and Gysel, M.: Black carbon physical properties and mixing state in the European megacity Paris, Atmos. Chem. Phys., 13, 5831-5856, doi: 10.5194/acp-13-5831-2013, 2013.

Lack, D. A., Cappa, C. D., Covert, D. S., Baynard, T., Massoli, P., Sierau, B., Bates, T. S., Quinn, P. K., Lovejoy, E. R., and Ravishankara, A. R.: Bias in filter-based aerosol light absorption measurements due to organic aerosol loading: Evidence from ambient measurements, Aerosol Sci. Technol., 42, 1033-1041, doi: 10.1080/02786820802389277, 2008.

Lack, D. A., Langridge, J. M., Bahreini, R., Cappa, C. D., Middlebrook, A. M., and Schwarz, J. P.: Brown carbon and internal mixing in biomass burning particles, Proceedings of the National Academy of Sciences of the United States of America, 109, 14802-14807, doi: 10.1073/pnas.1206575109, 2012.

Lack, D. A., and Langridge, J. M.: On the attribution of black and brown carbon light absorption using the Ångström exponent, Atmos. Chem. Phys., 13, 10535-10543, doi: 10.5194/acp-13-10535-2013, 2013.

Lafon, S., Sokolik, I. N., Rajot, J. L., Caquineau, S., and Gaudichet, A.: Characterization of iron oxides in mineral dust aerosols: Implications for light absorption, Journal of Geophysical Research-Atmospheres, 111, D21207, doi: 10.1029/2005jd007016, 2006.

Lavoue, D., Liousse, C., Cachier, H., Stocks, B. J., and Goldammer, J. G.: Modeling of carbonaceous particles emitted by boreal and temperate wildfires at northern latitudes, Journal of Geophysical Research-Atmospheres, 105, 26871-26890, doi: 10.1029/2000jd900180, 2000.

Lee, D. S., Fahey, D. W., Forster, P. M., Newton, P. J., Wit, R. C. N., Lim, L. L., Owen, B., and Sausen, R.: Aviation and global climate change in the 21st century, Atmospheric Environment, 43, 3520-3537, doi: 10.1016/j.atmosenv.2009.04.024, 2009.

Lee, D. S., Pitari, G., Grewe, V., Gierens, K., Penner, J. E., Petzold, A., Prather, M. J., Schumann, U., Bais, A., Berntsen, T., Iachetti, D., Lim, L. L., and Sausen, R.: Transport impacts on atmosphere and climate: Aviation, Atmospheric Environment, 44, 4678-4734, doi: 10.1016/j.atmosenv.2009.06.005, 2010.

Lieke, K., Kandler, K., Scheuvens, D., Emmel, C., Von Glahn, C., Petzold, A., Weinzierl, B., Veira, A., Ebert, M., Weinbruch, S., and Schuetz, L.: Particle chemical properties in the vertical column based on aircraft observations in the vicinity of Cape Verde Islands, Tellus Series B-Chemical and Physical Meteorology, 63, 497-511, doi: 10.1111/j.1600-0889.2011.00553.x, 2011.

Liu, B. Y. H., Zhang, Z. Q., and Kuehn, T. H.: A numerical study of inertial errors in anisokinetic sampling, Journal of Aerosol Science, 20, 367-380, doi: 10.1016/0021-8502(89)90012-8, 1989.

Liu, D., Flynn, M., Gysel, M., Targino, A., Crawford, I., Bower, K., Choularton, T., Juranyi, Z., Steinbacher, M., Huglin, C., Curtius, J., Kampus, M., Petzold, A., Weingartner, E., Baltensperger, U., and Coe, H.: Single particle characterization of black carbon aerosols at a tropospheric alpine site in Switzerland, Atmos. Chem. Phys., 10, 7389-7407, doi: 10.5194/acp-10-7389-2010, 2010.

Liu, D., Allan, J., Whitehead, J., Young, D., Flynn, M., Coe, H., McFiggans, G., Fleming, Z. L., and Bandy, B.: Ambient black carbon particle hygroscopic properties controlled by mixing state and composition, Atmos. Chem. Phys., 13, 2015-2029, doi: 10.5194/acp-13-2015-2013, 2013.

Liu, L., and Mishchenko, M. I.: Scattering and radiative properties of complex soot and soot-containing aggregate particles, Journal of Quantitative Spectroscopy & Radiative Transfer, 106, 262-273, doi: 10.1016/j.jqsrt.2007.01.020, 2007.

Lohmann, U., and Feichter, J.: Global indirect aerosol effects: a review, Atmos. Chem. Phys., 5, 715-737, doi: 10.5194/acp-5-715-2005, 2005.

Lohmann, U., and Hoose, C.: Sensitivity studies of different aerosol indirect effects in mixed-phase clouds, Atmos. Chem. Phys., 9, 8917-8934, doi: 10.5194/acp-9-8917-2009, 2009.

Luderer, G., Trentmann, J., Hungershöfer, K., Herzog, M., Fromm, M., and Andreae, M. O.: Small-scale mixing processes enhancing troposphere-to-stratosphere transport by pyro-cumulonimbus storms, Atmos. Chem. Phys., 7, 5945-5957, doi: 10.5194/acp-7-5945-2007, 2007.

Lukacs, H., Gelencser, A., Hammer, S., Puxbaum, H., Pio, C., Legrand, M., Kasper-Giebl, A., Handler, M., Limbeck, A., Simpson, D., and Preunkert, S.: Seasonal trends and possible sources of brown carbon based on 2-year aerosol measurements at six sites in Europe, Journal of Geophysical Research-Atmospheres, 112, D23s18, doi: 10.1029/2006jd008151, 2007.

Martins, J. V., Artaxo, P., Hobbs, P. V., Liousse, C., Cachier, H., Kaufman, Y., and Plana-Fattori, A.: Particle size distributions, elemental compositions, carbon measurements, and optical properties of smoke from biomass burning in the Pacific Northwest of the United States. , Biomass burning and global change, 2, 716-732, 1996.

Martins, J. V., Artaxo, P., Liousse, C., Reid, J. S., Hobbs, P. V., and Kaufman, Y. J.: Effects of black carbon content, particle size, and mixing on light absorption by aerosols from biomass burning in Brazil, Journal of Geophysical Research: Atmospheres, 103, 32041-32050, doi: 10.1029/98jd02593, 1998.

Mattis, I., Mueller, D., Ansmann, A., Wandinger, U., Preissler, J., Seifert, P., and Tesche, M.: Ten years of multiwavelength Raman lidar observations of free-tropospheric aerosol layers over central Europe: Geometrical properties and annual cycle, Journal of Geophysical Research-Atmospheres, 113, D20202, doi: 10.1029/2007jd009636, 2008.

McMeeking, G. R.: The optical, chemical, and physical properties of aerosols and gases emitted by the laboratory combustion of wildland fuels. , Ph.D., Department of Atmospheric Sciences, Colorado State University, 321 pp., 2008.

McMeeking, G. R., Hamburger, T., Liu, D., Flynn, M., Morgan, W. T., Northway, M., Highwood, E. J., Krejci, R., Allan, J. D., Minikin, A., and Coe, H.: Black carbon measurements in the boundary layer over western and northern Europe, Atmos. Chem. Phys., 10, 9393-9414, doi: 10.5194/acp-10-9393-2010, 2010.

McMeeking, G. R., Good, N., Petters, M. D., McFiggans, G., and Coe, H.: Influences on the fraction of hydrophobic and hydrophilic black carbon in the atmosphere, Atmos. Chem. Phys., 11, 5099-5112, doi: 10.5194/acp-11-5099-2011, 2011.

Metcalf, A. R., Craven, J. S., Ensberg, J. J., Brioude, J., Angevine, W., Sorooshian, A., Duong, H. T., Jonsson, H. H., Flagan, R. C., and Seinfeld, J. H.: Black carbon aerosol over the Los Angeles Basin during CalNex, Journal of Geophysical Research-Atmospheres, 117, D00v13, doi: 10.1029/2011jd017255, 2012.

Mie, G.: Beiträge zur Optik trüber Medien, speziell kolloidaler Metalllösungen Ann. Phys., 330, 377-445, doi: 10.1002/andp.19083300302, 1908.

Minikin, A., Petzold, A., Ström, J., Krejci, R., Seifert, M., van Velthoven, P., Schlager, H., and Schumann, U.: Aircraft observations of the upper tropospheric fine particle aerosol in the Northern and Southern Hemispheres at midlatitudes, Geophysical Research Letters, 30, 1503, doi: 10.1029/2002gl016458, 2003.

Minikin, A., Petzold, A., Weinzierl, B., and Gayet, J.-F.: In Situ Measurement Methods for Atmospheric Aerosol Particles and Cloud Elements, in: Atmospheric Physics, edited by: Schumann, U., Research Topics in Aerospace, Springer Berlin Heidelberg, 297-315, doi: 10.1007/978-3-642-30183-4_18, 2012.

Mishchenko, M. I., Liu, L., Travis, L. D., and Lacis, A. A.: Scattering and radiative properties of semi-external versus external mixtures of different aerosol types, Journal of Quantitative Spectroscopy & Radiative Transfer, 88, 139-147, doi: 10.1016/j.jqsrt.2003.12.032, 2004.

Möhler, O., Nink, A., Saathoff, H., Schaefers, S., Schnaiter, M., Schock, W., and Schurath, U.: The Karlsruhe aerosol chamber facility AIDA: Technical description and first results of homogeneous and heterogeneous ice nucleation experiments, in: Workshop on Ion-Aerosol-Cloud Interactions, edited by: Kirkby, J., C E R N Reports, 7, 163-168, 2001.

Möhler, O., Buttner, S., Linke, C., Schnaiter, M., Saathoff, H., Stetzer, O., Wagner, R., Kramer, M., Mangold, A., Ebert, V., and Schurath, U.: Effect of sulfuric acid coating on heterogeneous ice nucleation by soot aerosol particles, Journal of Geophysical Research-Atmospheres, 110, D11210, doi: 10.1029/2004jd005169, 2005.

Möhler, O., Benz, S., Saathoff, H., Schnaiter, M., Wagner, R., Schneider, J., Walter, S., Ebert, V., and Wagner, S.: The effect of organic coating on the heterogeneous ice nucleation efficiency of mineral dust aerosols, Environmental Research Letters, 3, 025007, doi: 10.1088/1748-9326/3/2/025007, 2008.

Moosmüller, H., Chakrabarty, R. K., and Arnott, W. P.: Aerosol light absorption and its measurement: A review, Journal of Quantitative Spectroscopy & Radiative Transfer, 110, 844-878, doi: 10.1016/j.jqsrt.2009.02.035, 2009.

Moteki, N., and Kondo, Y.: Effects of mixing state on black carbon measurements by laser-induced incandescence, Aerosol Sci. Technol., 41, 398-417, doi: 10.1080/02786820701199728, 2007.

Moteki, N., and Kondo, Y.: Dependence of Laser-Induced Incandescence on Physical Properties of Black Carbon Aerosols: Measurements and Theoretical Interpretation, Aerosol Sci. Technol., 44, 663-675, doi: 10.1080/02786826.2010.484450, 2010.

Moteki, N., Kondo, Y., and Nakamura, S.: Method to measure refractive indices of small nonspherical particles: Application to black carbon particles, Journal of Aerosol Science, 41, 513-521, doi: 10.1016/j.jaerosci.2010.02.013, 2010.

Moteki, N., Kondo, Y., Oshima, N., Takegawa, N., Koike, M., Kita, K., Matsui, H., and Kajino, M.: Size dependence of wet removal of black carbon aerosols during transport from the boundary layer to the free troposphere, Geophysical Research Letters, 39, L13802, doi: 10.1029/2012gl052034, 2012.

Müller, D., Ansmann, A., Mattis, I., Tesche, M., Wandinger, U., Althausen, D., and Pisani, G.: Aerosol-type-dependent lidar ratios observed with Raman lidar, Journal of Geophysical Research-Atmospheres, 112, D16202, doi: 10.1029/2006jd008292, 2007.

Onasch, T. B., Trimborn, A., Fortner, E. C., Jayne, J. T., Kok, G. L., Williams, L. R., Davidovits, P., and Worsnop, D. R.: Soot Particle Aerosol Mass Spectrometer: Development, Validation, and Initial Application, Aerosol Sci. Technol., 46, 804-817, doi: 10.1080/02786826.2012.663948, 2012.

Oshima, N., Kondo, Y., Moteki, N., Takegawa, N., Koike, M., Kita, K., Matsui, H., Kajino, M., Nakamura, H., Jung, J. S., and Kim, Y. J.: Wet removal of black carbon in Asian outflow: Aerosol Radiative Forcing in East Asia (A-FORCE) aircraft campaign, Journal of Geophysical Research-Atmospheres, 117, D03204, doi: 10.1029/2011jd016552, 2012.

Ouimette, J. R., and Flagan, R. C.: The extinction coefficient of multicomponent aerosols, Atmospheric Environment, 16, 2405-2419, doi: 10.1016/0004-6981(82)90131-7, 1982.

Patterson, E. M.: Measurements of the imaginary part of the refractive index between 300 and 700 nm for Mount St. Helens ash, Science, 211, 836-838, doi: 10.1126/science.211.4484.836, 1981.

Patterson, E. M., Pollard, C. O., and Galindo, I.: Optical properties of the ash from El Chichon volcano, Geophysical Research Letters, 10, 317-320, doi: 10.1029/GL010i004p00317, 1983.

Petzold, A., Strom, J., Schröder, F. P., and Karcher, B.: Carbonaceous aerosol in jet engine exhaust: emission characteristics and implications for heterogeneous chemical reactions, Atmospheric Environment, 33, 2689-2698, doi: 10.1016/s1352-2310(98)00314-8, 1999.

Petzold, A., Fiebig, M., Flentje, H., Keil, A., Leiterer, U., Schroder, F., Stifter, A., Wendisch, M., and Wendling, P.: Vertical variability of aerosol properties observed at a continental site during the

Lindenberg Aerosol Characterization Experiment (LACE 98), Journal of Geophysical Research-Atmospheres, 107, 8128, doi: 10.1029/2001jd001043, 2002.

Petzold, A., Stein, C., Nyeki, S., Gysel, M., Weingartner, E., Baltensperger, U., Giebl, H., Hitzenberger, R., Dopelheuer, A., Vrchoticky, S., Puxbaum, H., Johnson, M., Hurley, C. D., Marsh, R., and Wilson, C. W.: Properties of jet engine combustion particles during the PartEmis experiment: Microphysics and Chemistry, Geophysical Research Letters, 30, 1719, doi: 10.1029/2003gl017283, 2003.

Petzold, A., Weinzierl, B., Huntrieser, H., Stohl, A., Real, E., Cozic, J., Fiebig, M., Hendricks, J., Lauer, A., Law, K., Roiger, A., Schlager, H., and Weingartner, E.: Perturbation of the European free troposphere aerosol by North American forest fire plumes during the ICARTT-ITOP experiment in summer 2004, Atmos. Chem. Phys., 7, 5105-5127, doi: 10.5194/acp-7-5105-2007, 2007.

Petzold, A., Rasp, K., Weinzierl, B., Esselborn, M., Hamburger, T., Dörnbrack, A., Kandler, K., Schutz, L., Knippertz, P., Fiebig, M., and Virkkula, A.: Saharan dust absorption and refractive index from aircraft-based observations during SAMUM 2006, Tellus Series B-Chemical and Physical Meteorology, 61, 118-130, doi: 10.1111/j.1600-0889.2008.00383.x, 2009.

Petzold, A., Veira, A., Mund, S., Esselborn, M., Kiemle, C., Weinzierl, B., Hamburger, T., Ehret, G., Lieke, K., and Kandler, K.: Mixing of mineral dust with urban pollution aerosol over Dakar (Senegal): impact on dust physico-chemical and radiative properties, Tellus Series B-Chemical and Physical Meteorology, 63, 619-634, doi: 10.1111/j.1600-0889.2011.00547.x, 2011.

Petzold, A., and Kärcher, B.: Aerosols in the Atmosphere, in: Atmospheric Physics, edited by: Schumann, U., Research Topics in Aerospace, Springer Berlin Heidelberg, 37-53, doi: 10.1007/978-3-642-30183-4_3, 2012.

Petzold, A., Ogren, J. A., Fiebig, M., Laj, P., Li, S. M., Baltensperger, U., Holzer-Popp, T., Kinne, S., Pappalardo, G., Sugimoto, N., Wehrli, C., Wiedensohler, A., and Zhang, X. Y.: Recommendations for reporting "black carbon" measurements, Atmos. Chem. Phys., 13, 8365-8379, doi: 10.5194/acp-13-8365-2013, 2013.

Pöschl, U.: Atmospheric aerosols: Composition, transformation, climate and health effects, Angewandte Chemie-International Edition, 44, 7520-7540, doi: 10.1002/anie.200501122, 2005.

Posfai, M., Simonics, R., Li, J., Hobbs, P. V., and Buseck, P. R.: Individual aerosol particles from biomass burning in southern Africa: 1. Compositions and size distributions of carbonaceous particles, Journal of Geophysical Research-Atmospheres, 108, 8483, doi: 10.1029/2002jd002291, 2003.

Posfai, M., Gelencser, A., Simonics, R., Arato, K., Li, J., Hobbs, P. V., and Buseck, P. R.: Atmospheric tar balls: Particles from biomass and biofuel burning, Journal of Geophysical Research-Atmospheres, 109, D06213, doi: 10.1029/2003jd004169, 2004.

Pratt, K. A., Murphy, S. M., Subramanian, R., DeMott, P. J., Kok, G. L., Campos, T., Rogers, D. C., Prenni, A. J., Heymsfield, A. J., Seinfeld, J. H., and Prather, K. A.: Flight-based chemical characterization of biomass burning aerosols within two prescribed burn smoke plumes, Atmos. Chem. Phys., 11, 12549-12565, doi: 10.5194/acp-11-12549-2011, 2011.

Prospero, J. M., Ginoux, P., Torres, O., Nicholson, S. E., and Gill, T. E.: Environmental characterization of global sources of atmospheric soil dust identified with the Nimbus 7 Total Ozone Mapping Spectrometer (TOMS) absorbing aerosol product, Reviews of Geophysics, 40, 1002, doi: 10.1029/2000rg000095, 2002.

Quennehen, B., Schwarzenboeck, A., Schmale, J., Schneider, J., Sodemann, H., Stohl, A., Ancellet, G., Crumeyrolle, S., and Law, K. S.: Physical and chemical properties of pollution aerosol particles transported from North America to Greenland as measured during the POLARCAT summer campaign, Atmos. Chem. Phys., 11, 10947-10963, doi: 10.5194/acp-11-10947-2011, 2011.

Quennehen, B., Schwarzenboeck, A., Matsuki, A., Burkhart, J. F., Stohl, A., Ancellet, G., and Law, K. S.: Anthropogenic and forest fire pollution aerosol transported to the Arctic: observations from the POLARCAT-France spring campaign, Atmos. Chem. Phys., 12, 6437-6454, doi: 10.5194/acp-12-6437-2012, 2012.

Quinn, P. K., Bates, T. S., Coffman, D. J., and Covert, D. S.: Influence of particle size and chemistry on the cloud nucleating properties of aerosols, Atmos. Chem. Phys., 8, 1029-1042, doi: 10.5194/acp-8-1029-2008, 2008.

Raes, F., VanDingenen, R., Cuevas, E., VanVelthoven, P. F. J., and Prospero, J. M.: Observations of aerosols in the free troposphere and marine boundary layer of the subtropical Northeast Atlantic: Discussion of processes determining their size distribution, Journal of Geophysical Research-Atmospheres, 102, 21315-21328, doi: 10.1029/97jd01122, 1997.

Raes, F., Van Dingenen, R., Vignati, E., Wilson, J., Putaud, J. P., Seinfeld, J. H., and Adams, P.: Formation and cycling of aerosols in the global troposphere, Atmospheric Environment, 34, 4215-4240, doi: 10.1016/s1352-2310(00)00239-9, 2000.

Ramanathan, V., and Carmichael, G.: Global and regional climate changes due to black carbon, Nature Geoscience, 1, 221-227, doi: 10.1038/ngeo156, 2008.

Reid, J. S., Eck, T. F., Christopher, S. A., Koppmann, R., Dubovik, O., Eleuterio, D. P., Holben, B. N., Reid, E. A., and Zhang, J.: A review of biomass burning emissions part III: intensive optical properties of biomass burning particles, Atmos. Chem. Phys., 5, 827-849, doi: 10.5194/acp-5-827-2005, 2005a.

Reid, J. S., Koppmann, R., Eck, T. F., and Eleuterio, D. P.: A review of biomass burning emissions part II: intensive physical properties of biomass burning particles, Atmos. Chem. Phys., 5, 799-825, doi: 10.5194/acp-5-799-2005, 2005b.

Riemer, N., Vogel, H., and Vogel, B.: Soot aging time scales in polluted regions during day and night, Atmos. Chem. Phys., 4, 1885-1893, doi: 10.5194/acp-4-1885-2004, 2004.

Righi, M., Hendricks, J., and Sausen, R.: The global impact of the transport sectors on atmospheric aerosol: simulations for year 2000 emissions, Atmos. Chem. Phys., 13, 9939-9970, doi: 10.5194/acp-13-9939-2013, 2013.

Rocadenbosch, F., Md Reba, M. N., Sicard, M., and Comerón, A.: Practical analytical backscatter error bars for elastic one-component lidar inversion algorithm, Applied Optics, 49, 3380-3393, doi: 10.1364/AO.49.003380, 2010.

Rose, M.: Long-range transport of BC into the Arctic during ACCESS 2012, Master thesis (in preparation), Fakultät für Physik, Ludwig-Maximilians-Universität München, München, 2014.

Rosenfeld, D., Fromm, M., Trentmann, J., Luderer, G., Andreae, M. O., and Servranckx, R.: The Chisholm firestorm: observed microstructure, precipitation and lightning activity of a pyro-cumulonimbus, Atmos. Chem. Phys., 7, 645-659, doi: 10.5194/acp-7-645-2007, 2007.

Russell, P. B., Bergstrom, R. W., Shinozuka, Y., Clarke, A. D., DeCarlo, P. F., Jimenez, J. L., Livingston, J. M., Redemann, J., Dubovik, O., and Strawa, A.: Absorption Angstrom Exponent in AERONET and related data as an indicator of aerosol composition, Atmos. Chem. Phys., 10, 1155-1169, doi: 10.5194/acp-10-1155-2010, 2010.

Saathoff, H., Naumann, K. H., Schnaiter, M., Schock, W., Mohler, O., Schurath, U., Weingartner, E., Gysel, M., and Baltensperger, U.: Coating of soot and (NH4)(2)SO4 particles by ozonolysis products of alpha-pinene, Journal of Aerosol Science, 34, 1297-1321, doi: 10.1016/s0021-8502(03)00364-1, 2003.

Sahu, L. K., Kondo, Y., Moteki, N., Takegawa, N., Zhao, Y., Cubison, M. J., Jimenez, J. L., Vay, S., Diskin, G. S., Wisthaler, A., Mikoviny, T., Huey, L. G., Weinheimer, A. J., and Knapp, D. J.: Emission characteristics of black carbon in anthropogenic and biomass burning plumes over California during ARCTAS-CARB 2008, Journal of Geophysical Research-Atmospheres, 117, D16302, doi: 10.1029/2011jd017401, 2012.

Satheesh, S. K., and Moorthy, K. K.: Radiative effects of natural aerosols: A review, Atmospheric Environment, 39, 2089-2110, doi: 10.1016/j.atmosenv.2004.12.029, 2005.

Scarnato, B. V., Vahidinia, S., Richard, D. T., and Kirchstetter, T. W.: Effects of internal mixing and aggregate morphology on optical properties of black carbon using a discrete dipole approximation model, Atmos. Chem. Phys., 13, 5089-5101, doi: 10.5194/acp-13-5089-2013, 2013.

Schmale, J., Schneider, J., Jurkat, T., Voigt, C., Kalesse, H., Rautenhaus, M., Lichtenstern, M., Schlager, H., Ancellet, G., Arnold, F., Gerding, M., Mattis, I., Wendisch, M., and Borrmann, S.: Aerosol layers from the 2008 eruptions of Mount Okmok and Mount Kasatochi: In situ upper troposphere and lower stratosphere measurements of sulfate and organics over Europe, Journal of Geophysical Research-Atmospheres, 115, D00l07, doi: 10.1029/2009jd013628, 2010.

Schmale, J.: Aircraft-based in-situ aerosol mass spectrometry: Chemical characterization and source identification of submicron particulate matter in the free and upper troposphere and lower stratosphere, Ph.D., Fachbereich Physik, Mathematik und Informatik, Johannes Gutenberg-Universität Mainz, Mainz, 249 pp., 2011.

Schmidt, L.: Charakterisierung und Erprobung des optischen Aerosolspektrometers UHSAS-A für den Betrieb auf dem Forschungsflugzeug HALO, Diploma, Fakultät für Physik, Ludwig-Maximilians-Universität München, München, 89 pp., 2009.

Schumann, U., Schlager, H., Arnold, F., Baumann, R., Haschberger, P., and Klemm, O.: Dilution of aircraft exhaust plumes at cruise altitudes, Atmospheric Environment, 32, 3097-3103, doi: 10.1016/s1352-2310(97)00455-x, 1998.

Schumann, U., Mayer, B., Gierens, K., Unterstrasser, S., Jessberger, P., Petzold, A., Voigt, C., and Gayet, J. F.: Effective Radius of Ice Particles in Cirrus and Contrails, Journal of the Atmospheric Sciences, 68, 300-321, doi: 10.1175/2010jas3562.1, 2011.

Schumann, U., Graf, K., Mannstein, H., and Mayer, B.: Contrails: Visible Aviation Induced Climate Impact, in: Atmospheric Physics, edited by: Schumann, U., Research Topics in Aerospace, Springer Berlin Heidelberg, 239-257, doi: 10.1007/978-3-642-30183-4_15, 2012.

Schumann, U., Jeßberger, P., and Voigt, C.: Contrail ice particles in aircraft wakes and their climatic importance, Geophysical Research Letters, 40, 2867-2872, doi: doi:10.1002/grl.50539, 2013.

Schwarz, J. P., Gao, R. S., Fahey, D. W., Thomson, D. S., Watts, L. A., Wilson, J. C., Reeves, J. M., Darbeheshti, M., Baumgardner, D. G., Kok, G. L., Chung, S. H., Schulz, M., Hendricks, J., Lauer, A., Karcher, B., Slowik, J. G., Rosenlof, K. H., Thompson, T. L., Langford, A. O., Loewenstein, M., and Aikin, K. C.: Single-particle measurements of midlatitude black carbon and light-scattering aerosols from the boundary layer to the lower stratosphere, Journal of Geophysical Research-Atmospheres, 111, D16207, doi: 10.1029/2006jd007076, 2006.

Schwarz, J. P., Gao, R. S., Spackman, J. R., Watts, L. A., Thomson, D. S., Fahey, D. W., Ryerson, T. B., Peischl, J., Holloway, J. S., Trainer, M., Frost, G. J., Baynard, T., Lack, D. A., de Gouw, J. A., Warneke, C., and Del Negro, L. A.: Measurement of the mixing state, mass, and optical size of individual black carbon particles in urban and biomass burning emissions, Geophysical Research Letters, 35, L13810, doi: 10.1029/2008gl033968, 2008a.

Schwarz, J. P., Spackman, J. R., Fahey, D. W., Gao, R. S., Lohmann, U., Stier, P., Watts, L. A., Thomson, D. S., Lack, D. A., Pfister, L., Mahoney, M. J., Baumgardner, D., Wilson, J. C., and Reeves, J. M.: Coatings and their enhancement of black carbon light absorption in the tropical atmosphere, Journal of Geophysical Research-Atmospheres, 113, 10, doi: D03203 10.1029/2007jd009042, 2008b.

Schwarz, J. P., Spackman, J. R., Gao, R. S., Perring, A. E., Cross, E., Onasch, T. B., Ahern, A., Wrobel, W., Davidovits, P., Olfert, J., Dubey, M. K., Mazzoleni, C., and Fahey, D. W.: The Detection Efficiency of the Single Particle Soot Photometer, Aerosol Sci. Technol., 44, 612-628, doi: 10.1080/02786826.2010.481298, 2010a.

Schwarz, J. P., Spackman, J. R., Gao, R. S., Watts, L. A., Stier, P., Schulz, M., Davis, S. M., Wofsy, S. C., and Fahey, D. W.: Global-scale black carbon profiles observed in the remote atmosphere and compared to models (vol 37, art L18812 , 2010), Geophysical Research Letters, 37, L23804, doi: 10.1029/2010gl046007, 2010b.

Sedlacek, A. J., III, Lewis, E. R., Kleinman, L., Xu, J., and Zhang, Q.: Determination of and evidence for non-core-shell structure of particles containing black carbon using the Single-Particle Soot Photometer (SP2), Geophysical Research Letters, 39, L06802, doi: 10.1029/2012gl050905, 2012.

Seinfeld, J. H.: Atmospheric chemistry and physics of air pollution, John Wiley & Sons, Inc., New York, USA, 761 pp., 1986.

Seinfeld, J. H., and Pandis, S. N.: Atmospheric Chemistry and Physics - From Air Pollution to Climate Change 2nd ed., John Wiley & Sons, Inc. , New York, USA, 1232 pp., 2006.

Sem, G. J.: Design and performance characteristics of three continuous-flow condensation particle counters: a summary, Atmospheric Research, 62, 267-294, doi: 10.1016/s0169-8095(02)00014-5, 2002.

Sheridan, P. J., Arnott, W. P., Ogren, J. A., Andrews, E., Atkinson, D. B., Covert, D. S., Moosmuller, H., Petzold, A., Schmid, B., Strawa, A. W., Varma, R., and Virkkula, A.: The Reno Aerosol Optics Study: An evaluation of aerosol absorption measurement methods, Aerosol Sci. Technol., 39, 1-16, doi: 10.1080/027868290901891, 2005.

Shiraiwa, M., Kondo, Y., Iwamoto, T., and Kita, K.: Amplification of Light Absorption of Black Carbon by Organic Coating, Aerosol Sci. Technol., 44, 46-54, doi: 10.1080/02786820903357686, 2010.

Slowik, J. G., Cross, E. S., Han, J.-H., Kolucki, J., Davidovits, P., Williams, L. R., Onasch, T. B., Jayne, J. T., Kolb, C. E., and Worsnop, D. R.: Measurements of Morphology Changes of Fractal Soot Particles using Coating and Denuding Experiments: Implications for Optical Absorption and Atmospheric Lifetime, Aerosol Sci. Technol., 41, 734-750, doi: 10.1080/02786820701432632, 2007a.

Slowik, J. G., Cross, E. S., Han, J. H., Davidovits, P., Onasch, T. B., Jayne, J. T., WilliamS, L. R., Canagaratna, M. R., Worsnop, D. R., Chakrabarty, R. K., Moosmüller, H., Arnott, W. P., Schwarz, J. P., Gao, R. S., Fahey, D. W., Kok, G. L., and Petzold, A.: An inter-comparison of instruments measuring black carbon content of soot particles, Aerosol Sci. Technol., 41, 295-314, doi: 10.1080/02786820701197078, 2007b.

Spichtinger, N., Damoah, R., Eckhardt, S., Forster, C., James, P., Beirle, S., Marbach, T., Wagner, T., Novelli, P. C., and Stohl, A.: Boreal forest fires in 1997 and 1998: a seasonal comparison using transport model simulations and measurement data, Atmos. Chem. Phys., 4, 1857-1868, doi: 10.5194/acp-4-1857-2004, 2004.

Stein, C., Schröder, F., and Petzold, A.: The condensation particle size analyzer: A new instrument for the measurement of ultrafine aerosol size distributions, J. Aerosol Sci., 32, 381-382, 2001.

Stephens, M., Turner, N., and Sandberg, J.: Particle identification by laser-induced incandescence in a solid-state laser cavity, Applied Optics, 42, 3726-3736, doi: 10.1364/AO.42.003726, 2003.

Stettler, M. E. J., Boies, A. M., Petzold, A., and Barrett, S. R. H.: Global Civil Aviation Black Carbon Emissions, Environ. Sci. Technol., 47, 10397-10404, doi: 10.1021/es401356v, 2013a.

Stettler, M. E. J., Swanson, J. J., Barrett, S. R. H., and Boies, A. M.: Updated Correlation Between Aircraft Smoke Number and Black Carbon Concentration, Aerosol Sci. Technol., 47, 1205-1214, doi: 10.1080/02786826.2013.829908, 2013b.

Stith, J. L., Twohy, C. H., DeMott, P. J., Baumgardner, D., Campos, T., Gao5, R.-S., and Anderson, J.: Scavenging of biomass burning refractory black carbon and ice nuclei in a Western Pacific extratropical storm, 2011.

Stohl, A., Andrews, E., Burkhart, J. F., Forster, C., Herber, A., Hoch, S. W., Kowal, D., Lunder, C., Mefford, T., Ogren, J. A., Sharma, S., Spichtinger, N., Stebel, K., Stone, R., Strom, J., Torseth, K., Wehrli, C., and Yttri, K. E.: Pan-Arctic enhancements of light absorbing aerosol concentrations due to North American boreal forest fires during summer 2004, Journal of Geophysical Research-Atmospheres, 111, D22214, doi: 10.1029/2006jd007216, 2006.

Stohl, A., Forster, C., Huntrieser, H., Mannstein, H., McMillan, W. W., Petzold, A., Schlager, H., and Weinzierl, B.: Aircraft measurements over Europe of an air pollution plume from Southeast Asia - aerosol and chemical characterization, Atmos. Chem. Phys., 7, 913-937, doi: 10.5194/acp-7-913-2007, 2007.

Takemura, T., Nozawa, T., Emori, S., Nakajima, T. Y., and Nakajima, T.: Simulation of climate response to aerosol direct and indirect effects with aerosol transport-radiation model, Journal of Geophysical Research-Atmospheres, 110, D02202, doi: 10.1029/2004jd005029, 2005.

Tesche, M., Gross, S., Ansmann, A., Mueller, D., Althausen, D., Freudenthaler, V., and Esselborn, M.: Profiling of Saharan dust and biomass-burning smoke with multiwavelength polarization Raman lidar at Cape Verde, Tellus Series B-Chemical and Physical Meteorology, 63, 649-676, doi: 10.1111/j.1600-0889.2011.00548.x, 2011.

Trentmann, J., Luderer, G., Winterrath, T., Fromm, M., nbsp, D, Servranckx, R., Textor, C., Herzog, M., Graf, H. F., Andreae, M., and O: Modeling of biomass smoke injection into the lower stratosphere by a large forest fire (Part I): reference simulation, Atmos. Chem. Phys., 6, 5247-5260, doi: 10.5194/acp-6-5247-2006, 2006.

Trickl, T., Giehl, H., Jäger, H., and Vogelmann, H.: 35 yr of stratospheric aerosol measurements at Garmisch-Partenkirchen: from Fuego to Eyjafjallajökull, and beyond, Atmos. Chem. Phys., 13, 5205-5225, doi: 10.5194/acp-13-5205-2013, 2013.

Turquety, S., Logan, J. A., Jacob, D. J., Hudman, R. C., Leung, F. Y., Heald, C. L., Yantosca, R. M., Wu, S., Emmons, L. K., Edwards, D. P., and Sachse, G. W.: Inventory of boreal fire emissions for North America in 2004: Importance of peat burning and pyroconvective injection, Journal of Geophysical Research: Atmospheres, 112, D12S03, doi: 10.1029/2006jd007281, 2007.

Twomey, S.: Influence of pollution on the shortwave albedo of clouds, Journal of the Atmospheric Sciences, 34, 1149-1152, doi: 10.1175/1520-0469(1977)034<1149:tiopot>2.0.co;2, 1977.

van der Werf, G. R., Randerson, J. T., Giglio, L., Collatz, G. J., Kasibhatla, P. S., and Arellano Jr, A. F.: Interannual variability in global biomass burning emissions from 1997 to 2004, Atmos. Chem. Phys., 6, 3423-3441, doi: 10.5194/acp-6-3423-2006, 2006.

Veira, A.: Dakar's urban pollution plume: A SAMUM-II case study on the plume structure and the influence of urban emissions on dust physico-chemical and radiative properties, Diploma, Fakultät für Physik, Ludwig-Maximilians-Universität München, München, 151 pp., 2011.

Vignati, E., Wilson, J., and Stier, P.: M7: An efficient size-resolved aerosol microphysics module for large-scale aerosol transport models, Journal of Geophysical Research: Atmospheres, 109, D22202, doi: 10.1029/2003jd004485, 2004.

Vignati, E., Karl, M., Krol, M., Wilson, J., Stier, P., and Cavalli, F.: Sources of uncertainties in modelling black carbon at the global scale, Atmos. Chem. Phys., 10, 2595-2611, doi: 10.5194/acp-10-2595-2010, 2010.

Virkkula, A., Ahlquist, N. C., Covert, D. S., Arnott, W. P., Sheridan, P. J., Quinn, P. K., and Coffman, D. J.: Modification, calibration and a field test of an instrument for measuring light absorption by particles, Aerosol Sci. Technol., 39, 68-83, doi: 10.1080/027868290901963, 2005.

Virkkula, A.: Correction of the Calibration of the 3-wavelength Particle Soot Absorption Photometer (3λ PSAP), Aerosol Sci. Technol., 44, 706-712, doi: 10.1080/02786826.2010.482110, 2010.

Voigt, C., Schumann, U., Jurkat, T., Schaeuble, D., Schlager, H., Petzold, A., Gayet, J. F., Kraemer, M., Schneider, J., Borrmann, S., Schmale, J., Jessberger, P., Hamburger, T., Lichtenstern, M., Scheibe, M., Gourbeyre, C., Meyer, J., Kübbeler, M., Frey, W., Kalesse, H., Butler, T., Lawrence, M. G., Holzaepfel,

F., Arnold, F., Wendisch, M., Doepelheuer, A., Gottschaldt, K., Baumann, R., Zoeger, M., Soelch, I., Rautenhaus, M., and Doernbrack, A.: In-situ observations of young contrails - overview and selected results from the CONCERT campaign, Atmos. Chem. Phys., 10, 9039-9056, doi: 10.5194/acp-10-9039-2010, 2010.

Voigt, C., Schumann, U., Jessberger, P., Jurkat, T., Petzold, A., Gayet, J. F., Kraemer, M., Thornberry, T., and Fahey, D. W.: Extinction and optical depth of contrails, Geophysical Research Letters, 38, L11806, doi: 10.1029/2011gl047189, 2011.

Volz, F. E.: Infrared optical constants of ammonium sulfate, saharan dust, volcanic pumice, and flyash, Applied Optics, 12, 564-568, doi: 10.1364/AO.12.000564, 1973.

Wagner, R., Linke, C., Naumann, K.-H., Schnaiter, M., Vragel, M., Gangl, M., and Horvath, H.: A review of optical measurements at the aerosol and cloud chamber AIDA, Journal of Quantitative Spectroscopy & Radiative Transfer, 110, 930-949, doi: 10.1016/j.jqsrt.2009.01.026, 2009.

Weigel, R., Borrmann, S., Kazil, J., Minikin, A., Stohl, A., Wilson, J. C., Reeves, J. M., Kunkel, D., de Reus, M., Frey, W., Lovejoy, E. R., Volk, C. M., Viciani, S., D'Amato, F., Schiller, C., Peter, T., Schlager, H., Cairo, F., Law, K. S., Shur, G. N., Belyaev, G. V., and Curtius, J.: In situ observations of new particle formation in the tropical upper troposphere: the role of clouds and the nucleation mechanism, Atmos. Chem. Phys., 11, 9983-10010, doi: 10.5194/acp-11-9983-2011, 2011.

Weinzierl, B.: Radiatively-driven processes in forest fire and desert dust plumes, Ph.D., Fakultät für Physik, Ludwig-Maximilians-Universität München, München, 177 pp., 2007.

Weinzierl, B., Petzold, A., Esselborn, M., Wirth, M., Rasp, K., Kandler, K., Schuetz, L., Koepke, P., and Fiebig, M.: Airborne measurements of dust layer properties, particle size distribution and mixing state of Saharan dust during SAMUM 2006, Tellus Series B-Chemical and Physical Meteorology, 61, 96-117, doi: 10.1111/j.1600-0889.2008.00392.x, 2009.

Weinzierl, B., Sauer, D., Esselborn, M., Petzold, A., Veira, A., Rose, M., Mund, S., Wirth, M., Ansmann, A., Tesche, M., Gross, S., and Freudenthaler, V.: Microphysical and optical properties of dust and tropical biomass burning aerosol layers in the Cape Verde region-an overview of the airborne in situ and lidar measurements during SAMUM-2, Tellus Series B-Chemical and Physical Meteorology, 63, 589-618, doi: 10.1111/j.1600-0889.2011.00566.x, 2011.

Weinzierl, B., Sauer, D., Minikin, A., Reitebuch, O., Dahlkötter, F., Mayer, B., Emde, C., Tegen, I., Gasteiger, J., Petzold, A., Veira, A., Kueppers, U., and Schumann, U.: On the visibility of airborne volcanic ash and mineral dust from the pilot's perspective in flight, Physics and Chemistry of the Earth, 45-46, 87-102, doi: 10.1016/j.pce.2012.04.003, 2012.

Wendisch, M., Coe, H., Baumgardner, D., Brenguier, J.-L., Dreiling, V., Fiebig, M., Formenti, P., Hermann, M., Krämer, M., Levin, Z., Maser, R., Mathieu, E., Nacass, P., Noone, K., Osborne, S., Schneider, J., Schütz, L., Schwarzenböck, A., Stratmann, F., and Wilson, J. C.: Aircraft Particle Inlets: State-of-the-Art and Future Needs, AMERICAN METEOROLOGICAL SOCIETY, 89-91, doi: 10.1175/BAMS-85-1-89, 2004.

Whitby, K. T.: The physical characteristics of sulfur aerosols, Atmospheric Environment (1967), 12, 135-159, doi: 10.1016/0004-6981(78)90196-8, 1978.

Wiedinmyer, C., Akagi, S. K., Yokelson, R. J., Emmons, L. K., Al-Saadi, J. A., Orlando, J. J., and Soja, A. J.: The Fire INventory from NCAR (FINN): a high resolution global model to estimate the emissions from open burning, Geoscientific Model Development, 4, 625-641, doi: 10.5194/gmd-4-625-2011, 2011.

Winter, B., and Chýlek, P.: Contribution of sea salt aerosol to the planetary clear-sky albedo, Tellus Series B-Chemical and Physical Meteorology, 49, 72-79, doi: 10.1034/j.1600-0889.49.issue1.5.x, 1997.

Yin, Y., Chen, Q., Jin, L., Chen, B., Zhu, S., and Zhang, X.: The effects of deep convection on the concentration and size distribution of aerosol particles within the upper troposphere: A case study, Journal of Geophysical Research: Atmospheres, 117, D22202, doi: 10.1029/2012jd017827, 2012.

Symbols

Symbol	Definition
A	Area
$å_{abs}$	Ångström exponent of absorption
$å_{ext}$	Ångström exponent of extinction
$å_{sca}$	Ångström exponent of scattering
B	Spectral radiance of a blackbody
c	Speed of light in vacuum ($2.9979 \cdot 10^{8}$ m s^{-1})
C_{abs}	Absorption cross-section
C_{ext}	Extinction cross-section
$C_{geometric}$	Geometric cross-section
CMD	Count median diameter
C_{sca}	Scattering cross-section
Δ_{coat}	Coating thickness
D_{BC}	Mass equivalent diameter of BC core
$D_{cutoff,50}$	Cutoff diameter of the aerosol inlet
D_{MEV}	Mass equivalent diameter ($\triangleq D_{rBC}$)
D_P	Aerosol particle (optical) diameter
D_{rBC}	Mass equivalent diameter of rBC core
$E(D_P)$	Aerosol inlet sampling efficiency
$f(Tr)$	PSAP transmission correction function
GSD	Geometric standard deviation
h	Planck's constant ($6.626 \cdot 10^{-34}$ J s)
I	Attenuated intensity of light
I_0	Incident intensity of light
k	Imaginary part of complex refractive index
k_B	Boltzmann constant ($1.381 \cdot 10^{-23}$ J K^{-1})
m	Complex refractive index
M	Mass concentration
MMD	Mass median diameter
MMR	Mass mixing ratio
n	Real part of complex refractive index
N	Number concentration
p	Pressure
Q	Flow
Q_{abs}	Absorption efficiency
Q_{ext}	Extinction efficiency
Q_{sca}	Scattering efficiency
RH	Relative humidity

Symbol	Definition
r_P	Radius of entire particle
r_{rBC}	Radius of rBC particle core
s	PSAP scattering correction factor
T	Temperature
Tr	Transmission
V	Volume
λ	Wavelength
ρ	Density
σ_0	Uncorrected PSAP response
σ_{abs}	Absorption coefficient
$\sigma_{abs,PSAP}$	PSAP signal
σ_{ext}	Extinction coefficient
σ_{sca}	Scattering coefficient
ω_0	Single-scattering albedo

Abbreviations

Abbreviation	Meaning
ACCESS	Arctic Climate Change Economy and Society project
AIDA	Aerosol Interaction and Dynamics in the Atmosphere (aerosol chamber)
APD	Avalanche photodiode
ARL	Air Resources Laboratory
a.u.	Arbitrary units
AVHRR	Advanced Very High Resolution Radiometer
BC	Black carbon
BID	Broadband incandescence detector
BrC	Brown carbon
CCN	Cloud condensation nuclei
CFS	Canadian Forest Service
CNC	Condensation Nucleus Counter
CONCERT 2011	CONtrail and Cirrus ExpeRimenT (2011)
CPC	Condensation Particle Counter
CPSA	Condensation Particle Size Analyzer
DFG	Deutsche Forschungsgemeinschaft
DLR	Deutsches Zentrum für Luft- und Raumfahrt (German Aerospace Center)
DMA	Differential Mobility Analyzer
DMT	Droplet Measurement Technologies
ECMWF	European Centre for Medium-Range Weather Forecasts
EMC	Electromagnetic Compatibility
FLYTUL	FLight analYsis Tool Using LAGRANTO
FSSP	Forward Scattering Spectrometer Probe
GEOS-5	Goddard Earth Observing System Model, Version 5
GFS	Global Forecast System
HYSPLIT	HYbrid Single-Particle Lagrangian Integrated Trajectory model
IABG	Industrieanlagen-Betriebsgesellschaft mbH
TROPOS	Leibniz Institute for Tropospheric Research
IN	Ice nuclei
IPCC	Intergovernmental Panel on Climate Change
KIT	Karlsruhe Institute of Technology
LAC	Light absorbing carbon
LEO	Leading edge only
LGGE	Laboratoire de Glaciologie et Géophysique de l'Environnement
LIDAR	Light detection and ranging
LSD	Light scattering detector
MBL	Marine boundary layer

Abbreviation	Meaning
MODIS	Moderate Resolution Imaging Spectroradiometer
MPI	Max Planck Institute for Chemistry
NID	Narrowband incandescence detector
NOAA	National Oceanic and Atmopheric Administration
OC	Organic carbon
OPC	Optical Particle Counter
PAH	Polycyclic aromatic hydrocarbons
PBL	Planetary boundary layer
PCASP	Passive Cavity Aerosol Spectrometer Probe
PMT	Photomultiplier tube
PSAP	Particle Soot Absorption Photometer
PSD	Position-sensitive detector
PSI	Paul Scherrer Institute
PSL	Polystyrene latex sphere
rBC	Refractive black carbon
SOOT-11	SP2 inter-comparison campaign
SP2	Single Particle Soot Photometer
SP-AMS	Soot-Particle Aerosol Mass Spectrometer
stp	Standard temperature and pressure (273.15 K, 1013.25 hPa)
TD	Thermal denuder
TEAPD	Two-element avalanche photodiode
TEM	Transversal electromagnetic mode
UHSAS-A	Ultra-High Sensitivity Aerosol Spectrometer Airborne
UMN	University of Manchester
UTLS	Upper troposphere lower stratosphere
YAG	Yttrium Aluminium Garnet

List of publications

Name, Vorname: **Dahlkötter, Florian**

Professur: **Lehrstuhl für Atmosphärische Umweltforschung (Prof. Dr. H. P. Schmid)**

An den
Dekan der
Fakultät Wissenschaftszentrum Weihenstephan für
Ernährung, Landwirtschaft und Umwelt

Weihenstephan

Veröffentlichungen aus dem Themenkreis der Dissertation

Gemäß § 6 Abs. 1 Satz 2 der aktuellen Promotionsordnung der TUM zeige ich hiermit an, dass ich Veröffentlichungen aus dem Themenkreis meiner Dissertation vorgenommen habe.

_____ _____

Datum Unterschrift

Publikationen aus dem Themenkreis der Dissertation:

peer-reviewed:

Dahlkötter, F., Gysel, M., Sauer, D., Minikin, A., Baumann, R., Seifert, P., Ansmann, A., Fromm, M., Voigt, C., and Weinzierl, B.: The Pagami Creek smoke plume after long-range transport to the upper troposphere over Europe – aerosol properties and black carbon mixing state, Atmos. Chem. Phys., 14, 6111-6137, doi: 10.5194/acp-14-6111-2014, 2014.

Konferenzbeiträge:

Dahlkötter, F., Weinzierl, B., Sauer, D., Minikin, A., Gysel, M., Ansmann, A., Voigt, C.: Biomass burning layers over Central Europe: First results, European Research Course on Atmospheres (ERCA2012), Grenoble, France, *poster presentation*, 2012.

Dahlkötter, F., Weinzierl, B., Sauer, D., Minikin, A., Baumann, R., Gysel, M., Voigt, C., Ansmann, A.: Airborne measurements of biomass burning layers over Central Europe: A case study, European Aerosol Conference *(*EAC) 2012, Granada, Spain, *oral presentation*, 2012.

Dahlkötter, F., Weinzierl, B., Sauer, D., Minikin, A., Baumann, R., Gysel, M., Voigt, C., Ansmann, A.: Airborne measurements of biomass burning layers over Central Europe: A case study, 2011 DMT SP2 User's Group Workshop 2012, Boulder, Colorado, USA, *oral presentation*, 2012.

Weitere (peer-reviewed) Publikationen (<u>nicht</u> aus dem Themenkreis der Dissertation):

Laborde, M., Schnaiter, M., Linke, C., Saathoff, H., Naumann, K. H., Moehler, O., Berlenz, S., Wagner, U., Taylor, J. W., Liu, D., Flynn, M., Allan, J. D., Coe, H., Heimerl, K., **Dahlkötter, F.**, Weinzierl, B., Wollny, A. G., Zanatta, M., Cozic, J., Laj, P., Hitzenberger, R., Schwarz, J. P., and Gysel, M.: Single Particle Soot Photometer intercomparison at the AIDA chamber, Atmos. Meas. Tech., 5, 3077-3097, doi: 10.5194/amt-5-3077-2012, 2012

Weinzierl, B., Sauer, D., Minikin, A., Reitebuch, O., **Dahlkötter, F.**, Mayer, B., Emde, C., Tegen, I., Gasteiger, J., Petzold, A., Veira, A., Kueppers, U., and Schumann, U.: On the visibility of airborne volcanic ash and mineral dust from the pilot's perspective in flight, Physics and Chemistry of the Earth, 45-46, 87-102, doi: 10.1016/j.pce.2012.04.003, 2012.